Università degli Studi di Genova

Scuola di Dottorato di
Scienze e Tecnologie per l'Ingegneria

Dottorato di Ricerca in Geofisica

Tesi di Dottorato - XXV ciclo

Settore scientifico disciplinare: FIS/06

The Planetary Boundary Layer: from statistical characterization to dynamic model

Candidata: Elena Costa Frola

Tutor interno: Prof. Daniele Spallarossa

Tutor esterno: Prof. Andrea Mazzino

Contents

Ringraziamenti

Desidero ringraziare primi fra tutti i coordinatori del corso di Dottorato di Geofisica, Prof. Claudio Eva e Prof. Daniele Spallarossa, quest'ultimo anche tutor nell'ultimo periodo del mio percorso, per la loro disponibilità.
Esprimo la mia riconoscenza ai tutor, Prof. Corrado Ratto e Prof. Roberto Festa, che si sono succeduti nei primi due anni del mio studio, e al Prof. Andrea Mazzino per essere stati punto di riferimento della mia attività.
Ringrazio il Dipartimento di Fisica dell'Università degli Studi di Genova per aver messo a mia disposizione locali e strumentazione con cui ho potuto lavorare.
Desidero esprimere la mia riconoscenza all'ISAC-CNR di Torino e in particolare al Prof. Enrico Ferrero, che mi ha consentito di utilizzare dati oggetto del mio studio.
Ringrazio il Prof. Carlo Cravero e il Consorzio SIRE di Savona per avermi fornito competenze e strumentazione indispensabili alla mia ricerca.
Esprimo riconoscenza all'Ing. Mauro Carretta del Consorzio SIRE per avermi trasmesso conoscenze tecniche utili alla mia attività, all'Ing. Paolo Macelloni e all'Ing. Giuseppe Briasco per la cordialità con cui mi hanno accolta nei loro uffici.
Da ultimo, ma non per importanza, voglio esprimere la mia gratitudine ad amici e parenti, che mi hanno incoraggiata nella mia ricerca; un particolare ringraziamento spetta ai miei genitori, che mi hanno sempre sostenuta.

Anknowlodgements

First of all, I would like to thank all coordinators of Geophysics Doctorate, Prof. Claudio Eva and Prof. Daniele Spallarossa, this last one was also my tutor in my last period of study, for their helpfulness.
I wish also to show my gratitude to my tutors, Prof. Corrado Ratto and Prof. Roberto Festa, who followed one another in my first two years of study, as well as Prof. Andrea Mazzino for having been the reference point of my activity.
My thanks go to the Physics Department of Genoa University for having provided me with the rooms and devices which I could use to work.
I wish also to express my gratitude to ISAC-CNR of Turin, especially to Prof. Enrico Ferrero, who allowed me to use the data, which were the subject of my study.
I would like to express my acknowledgments to Prof. Carlo Cravero and Consortium SIRE of Savona for having provided me with the indispensable competences and instruments for my research.
I wish also to thank Eng. Mauro Carretta of the Consortium SIRE for having passed me his technical skills which were so useful for my activity, Eng. Paolo Macelloni and Eng. Giuseppe Briasco for their friendliness when they welcomed me into their offices.
Last, but not least, I would like to express my best gratitude to all my friends and relatives who encouraged me to carry out this research; a special thank goes to my parents who always supported me.

Riassunto

La Tesi di Dottorato tratta delle proprietà dello Strato Limite Atmosferico (Planetary Boundary Layer, PBL), sviluppando due importanti tematiche, che interessano la Geofisica:

- la turbolenza atmosferica in area urbana;
- il comportamento del vento su orografia complessa.

Il primo dei due argomenti è relativo alle proprietà statistiche del flusso atmosferico nello Strato Limite Urbano, esaminate con l'utilizzo di misure dirette. Il secondo è pertinente alla previsione della dinamica del flusso atmosferico in area con particolare orografia, analizzata mediante un approccio numerico.
Obiettivo del primo dei due argomenti è lo studio delle proprietà della turbolenza atmosferica con particolare attenzione per la statistica delle fluttuazioni di temperatura in relazione alla stabilità atmosferica e la ricerca delle relative leggi di scala.
La caratterizzazione delle proprietà statistiche delle fluttuazioni di temperatura trova diverse applicazioni in ambito meteorologico, fra le principali lo studio delle parametrizzazioni dei modelli di turbolenza in simulazioni del flusso atmosferico. Dette parametrizzazioni permettono di rappresentare quanto succede alle piccole scale, noto il comportamento del sistema fisico alle scale maggiori.
La peculiarità dell'attività risiede nel fatto che fornisce una verifica delle proprietà statistiche delle fluttuazioni di temperatura mediante l'utilizzo di misure dirette raccolte in un dataset di grandi dimensioni. Ho, quindi, confrontato i risultati della mia analisi con la trattazione teorica [14] e i risultati ricavati da esperimenti numerici precedenti alla mia ricerca [5], [6].
Nel mio lavoro ho utilizzato misure ottenute dalla campagna sperimentale condotta negli anni 2007 e 2008 nella città di Torino nell'ambito del progetto CIPE della Regione Piemonte 'Studio modellistico e sperimentale della turbolenza atmosferica e della dispersione di inquinanti 2006-2008' [12].
Il dataset, fornitomi dall'ISAC del CNR di Torino (Prof. E. Ferrero), è costituito da circa un anno di misure dei campi di vento e di temperatura rilevate in una centralina del CNR, posta alla periferia della città e dotata di anemometri dislocati a tre quote (5 m, 9 m e 25 m). Gli strumenti effettuano misure delle tre componenti della velocità del vento e della temperatura con una frequenza di 20 Hz, fornendo in un'ora 72000 dati per ogni grandezza fisica.
La disponibilità di un dataset di tali dimensioni, ha permesso uno studio differenziato mese per mese per il periodo dal 01/02/2007 al 29/02/2008.

Il flusso, analizzato mediante il numero di Reynolds, è risultato essere più turbolento all'aumentare della quota dell'anemometro nei mesi più caldi, probabilmente a causa di una turbolenza di origine termica, mentre nei mesi freddi questo comportamento è legato ad una maggiore turbolenza di origine meccanica.
La variabilità della temperatura segue mediamente il ciclo diurno ad ogni quota e per ogni mese. Si è potuta osservare nei mesi estivi una ridotta discrepanza tra le temperature misurate alle diverse quote, essendo l'atmosfera rimescolata.
La stabilità atmosferica è stata valutata mediante il calcolo di un indicatore che coinvolge i valori del lapse rate ambientale e del lapse rate adiabatico; nel caso di stratificazione stabile dell'atmosfera l'indice corrisponde al quadrato della frequenza di Brunt-Väisälä [28]. Mediamente lo Strato Limite Atmosferico conta un maggior numero di eventi a stratificazione instabile rispetto a quella stabile e pertanto la statistica a disposizione per la caratterizzazione delle fluttuazioni termiche nel caso di PBL instabile risulta essere più ricca di quella relativa al caso di PBL stabile.
L'analisi delle funzioni di densità di probabilità delle fluttuazioni di temperatura ha permesso di esaminare le proprietà statistiche della turbolenza. Lo studio distingue le variazioni termiche di bassa entità da quelle di valore maggiore al variare della stabilità atmosferica. Relativamente alle prime si è potuto verificare il comportamento lineare degli esponenti da assegnare alla separazione spaziale tra gli anemometri, individuato sia teoricamente che da simulazioni numeriche. In merito alle fluttuazioni di temperatura più forti detto andamento non è rispettato dai risultati di esperimenti numerici, che hanno individuato una discrepanza tra la previsione teorica e i dati forniti da simulazioni numeriche. Con il mio lavoro ho dato conferma alle prove di carattere numerico evidenziando, mediante l'analisi delle misure del dataset, il fenomeno citato, noto come intermittenza, e relativa saturazione.
Pertanto, è stata trovata una legge di scala sia per le fluttuazioni di temperatura deboli che per quelle più intense. Entrambe risultano verificate nella maggior parte dei mesi analizzati sia per i casi di atmosfera instabile che per i casi di atmosfera stabile.
In merito al secondo tema della mia attività di ricerca, il comportamento del vento su orografia complessa, l'obiettivo è la realizzazione di campi di vento ad alta risoluzione.
Attualmente si possono ottenere grandezze meteorologiche con risoluzione orizzontale dell'ordine del chilometro. Distribuzioni di vento a risoluzioni più elevate possono avere svariate applicazioni, ad esempio possono servire alla valutazione del potenziale eolico di una zona geografica, allo studio della dispersione di inquinanti in atmosfera, all'esame della propagazione di incendi.
Con questa finalità, si è impostata la procedura per nidificare un modello di fluidodinamica computazionale (CFD) in un modello meteorologico a mesoscala [18].
Il modello di previsione meteorologica a mesoscala WRF, di cui ho utilizzato i dati, è stato fornito dal Dipartimento di Fisica (Università degli Studi di Genova). I pacchetti informatici usati nel calcolo fluidodinamico ad alta risoluzione, SOLID WORKS, GAMBIT, ICEM, CFX, FLUENT, sono stati messi a disposizione dal Consorzio SIRE (Prof. C. Cravero).
L'area di studio comprende la provincia di Genova e si estende in coordinate geografiche da 44,357° a 44,537° in latitudine e da 8,664° a 9,117° in longitudine,

coprendo una superficie di 19610 m in latitudine e di 35640 m in longitudine; verticalmente si estende fino a 3500 m s.l.m..
Per la simulazione di fluidodinamica computazionale sono state costruite due griglie di calcolo non strutturate (mediante SOLID WORKS, GAMBIT, ICEM), con celle di prismi e tetraedri: una rada con 6650057 elementi, l'altra più fitta con 13146002 elementi. Non fornendo quest'ultima risultati migliori della prima rispetto alle tempistiche di calcolo richieste, si è adoperato il grigliato a risoluzione inferiore, con passo di 80 m in superficie e 600 m sulle facce laterali e su quella superiore del dominio di studio.
Poichè nella regione esaminata la provenienza media del vento degli strati atmosferici più bassi risulta frequente dal settore di Nord-Est, specialmente in autunno e inverno, è stata scelta come caso-studio una simulazione di un'ora (h 00 del giorno 01/11/2009) con questa configurazione meteorologica.
Il calcolo di fluidodinamica computazionale è stato impostato stazionario, isotermo, incomprimibile ed i modelli di turbolenza scelti sono stati il $k-\omega$ e il $k-\epsilon$ [1].
Sono state svolte simulazioni differenti nella definizione delle condizioni al contorno (mediante CFX e FLUENT) e si è verificato che assegnare alle facce laterali del dominio della simulazione CFD le velocità del vento ottenute da WRF nei relativi nodi vincola pesantemente il calcolo. Sia assegnando a tutte e quattro le facce laterali che attribuendole a tre o due di esse, le distribuzioni spaziali del vento fornite dalle procedure numeriche non risultano fisicamente accettabili. Solamente assegnando valori medi delle velocità del vento di WRF a tutte le facce laterali si hanno in uscita al calcolo fluidodinamico campi di vento realistici rispetto all'orografia dell'area di interesse. Come atteso, si è evidenziato che le principali valli genovesi influenzano il campo di vento.
Ripetendo la simulazione con quest'ultima impostazione per dieci istanti orari successivi, si sono confrontati i valori ottenuti dalla procedura di fluidodinamica computazionale con quelli previsti dal modello meteorologico e i dati rilevati presso il Centro Funzionale (Genova) di ARPA Liguria. Intensità e direzione della velocità del vento fornite dal modello CFD sono in buon accordo con le misure dirette, che si discostano maggiormente dai valori simulati da WRF. Si può concludere, quindi, che la procedura di fluidodinamica computazionale permette di individuare fenomeni a piccola scala non prevedibili mediante il modello meterologico a mesoscala.

Abstract

My Thesis deals with the properties of Planetary Boundary Layer and it concerns two important geophysical subjects:

- atmospheric turbulence in urban area;
- behaviour of the wind over complex orography.

The first topic concerns the statistical features of Urban Boundary Layer; they are analysed by direct measurements. The second one pertains to forecast of dynamics of atmospheric flow in an area with particular orography; it is studied by numerical approach.

The purpose of the first subject is the study of properties of atmospheric turbulence with particular attention for statistics of temperature fluctuations in relations to atmospheric stability and the research of scale properties.

The characterization of statistical features has various applications in the meteorological sector, for example the parameterizations of turbulence models are required in simulations of atmospheric flow. The relations of parameterization permit to perform the behaviour at small scales, when the behaviour of physical system is known at large scales.

The peculiarity of activity is due to the fact that it provides a verification of the statistical properties of temperature fluctuations obtained by direct measures of a dataset with big dimension and I compared the results of my analysis with the theory [14] and the results of the numerical experiments [5], [6].

In my work I used the measures of the experimental campaign conducted in Turin in 2007 and 2008, relating to CIPE project of Piedmont region 'Modeling and experimental study about the atmospheric turbulence and pollutant dispersion 2006-2008' [12].

The dataset, given by ISAC of Turin CNR (Prof. E. Ferrero), includes measurements of wind velocity and temperature detected in CNR station, located at outskirt of the town with an equipment of three anemometers at elevations of 5 m, 9 m and 25 m. The devices provide the measure of the wind components and the temperature with a frequency of 20 Hz. Therefore, they give 72000 data in an hour for every physical quantity.

The rich statistics permits to carry out a study, differentiated month by month, during the period from 01/02/2007 to 29/02/2008, in order to compare the properties searched for the various periods of study.

The flow, studied by Reynolds number, is more turbulent at high elevations of anemometer during warmer months, probably because of turbulence of thermal origin; whereas in colder months this behaviour is caused by turbulence of mechanical

origin.
The variability of the temperature follows a daily cycle at every height and for every month. During summer months it is possible to observe a small discrepancy among the temperatures measured at different elevations, because the atmosphere is more mixed.
The atmospheric stability is analysed by computation of an indicator, that uses the environmental and the adiabatic lapse rate. The index corresponds to the square of Brunt-Väisälä frequency or buoyancy frequency in the case of stable atmospheric stratification [28]. On average, the Planetary Boundary Layer counts a bigger number of events with unstable stratification in comparison to the ones with stable stratification; therefore, the statistics for the study of temperature fluctuations in unstable conditions is richer than the other one.
The analysis of probability density functions of temperature fluctuations permits to examine the statistical properties of turbulence. The study distinguishes between small and big temperature variations, changing the conditions of atmospheric stability. Concerning the first ones, I could verify the linear behaviour of exponent, that must be assigned to spatial separations among the elevations of anemometers. This trend is observed in theoretical considerations and in numerical experiments, too. Relating to strong temperature fluctuations, this behaviour does not occur in numerical experiments, allowing to individuate a discrepancy between theoretical prevision and results of numerical simulations. In my research, I confirmed the numerical tests: the analysis of measurements of dataset allowed to individuate the phenomenon known as intermittency and relative saturation.
Therefore, a scale law was found for weak temperature fluctuations and strong ones, too. Both are verified in the most part of analysed months for the cases of unstable atmosphere and for the cases of stable atmosphere.
As to the second topic of my research, the behaviour of wind over complex orography, the goal is to achieve wind fields with high resolution.
Currently, it is possible to obtain meteorological quantities with horizontal resolution in order of kilometres. Distributions of the wind with higher resolution can have various applications, for example they can be useful for the evaluation of wind energy potential in geographic area, the study of pollutant dispersion in atmosphere and the examination of fire propagation.
With this purpose, a procedure for nesting of Computational Fluid Dynamics (CFD) model in mesoscale meteorological model is set [16], [18].
The mesoscale meteorological model WRF, from which I used the data, belongs to the Physics Department (University of Genoa). The softwares used in fluid dynamics computation with high resolution, SOLID WORKS, GAMBIT, ICEM, CFX, FLUENT, were provided by Consortium SIRE (Prof. C. Cravero).
The domain of study covers Genoa province. Its horizontal extension is of 19610 m in latitude and 35640 m in longitude; whereas, in vertical direction, local orography considered, it extends up to an elevation of 3500 m a.s.l..
For the CFD procedure the domain is discretized by two unstructured meshes (by SOLID WORKS, GAMBIT, ICEM). They are built by tetrahedrons and prism cells with different resolution: a coarse grid with 6650057 elements, a thick one with 13146002 elements. The latest one does not provide better results, therefore I used

a grid with lower resolution, with grid pitch of 80 m over the surface and grid pitch of 600 m over lateral faces and top one of the domain.
Since in the examined region the wind direction in low atmospheric layers is often North-East, especially in autumn and in winter, I chose as case-study an hour (h 00 of day 01/11/2009) with this meteorological configuration.
The computation was stationary, isothermal with temperature of 280 K and incompressible. The fluid was set as ideal gas and the chosen turbulence models were $k - \omega$ and $k - \epsilon$ [1].
I carried out some simulations differentiated by definition of boundary conditions (by CFX and FLUENT) and I verified that the assignation of WRF wind velocity to nodes of lateral faces influences the computation very much. If the punctual velocities are assigned to lateral faces, the wind fields obtained by numerical procedures are not acceptable. Instead, if the WRF average velocities are assigned, the outputs of fluid dynamics computation are realistic in comparison to the orography of the examined zone. As expected, it is possible to observe that the main Genoa valleys influence the wind fields.
Repeating the simulation with the latest statement for ten following hours, I was able to compare the values simulated by CFD procedure with the ones obtained by WRF and the ones measured by Functional Center (Genoa) of ARPA Liguria.
A good agreement beetwen the results of computational fluid dynamics simulations and measurements is observed. Instead, there is a bigger discrepancy beetwen the measures and the data obtained by meteorological model. Therefore, I can conclude that CFD procedure permits to detect phenomena at a small scale, that cannot be identified by mesoscale meteorological model.

Introduction

My Thesis deals with two important geophysical subjects:

- analysis of atmospheric turbulence in Urban Boundary Layer;
- study of wind fields over complex terrain.

They concern the properties of Planetary Boundary Layer (PBL) and I have in mind to search for its characterizations. In detail, the first topic is related to the statistical analysis of PBL in urban area and the second one concerns the forecast of single events in dynamics of lower layers of Troposphere and in particular in PBL.
The purpose of the first subject is the study of some properties of turbulence in Urban Boundary Layer and in particular the research of statistical characteristics of temperature fluctuations with the change of atmospheric stability conditions. Regarding this last matter, some scale properties were individuated by numerical experiments [5], [6]. In my Thesis, I have in mind to search an evidence of these properties by using data measured directly over complex terrain.
The characterization of statistical feature of temperature fluctuations has various applications in meteorology, for example in the study of parameterizations in turbulence models. The turbulence parameterizations permit to perform the behaviour at small scales, when the behaviour of physical sistem is known at large scales.
In this analysis I could use a dataset obtained by experimental campaign conducted in Turin in years 2007 and 2008. The dataset includes measurements of wind velocity and temperature, sampled with frequency of 20 Hz by three anemometers at elevations of 5 m, 9 m and 25 m over the terrain in Surface Layer.
The rich statistics permits to execute a month-by-month differentiated study in order to compare the properties investigated in the various periods of study.
At the beginning, I have in mind to characterize the properties of the atmospheric flow calculating the Reynolds number and executing a first analysis of temperature by calculation of its hourly average and standard deviation.
In the study of atmospheric stability, I calculated various indicators in order to individuate a useful instrument to show a condition of atmosphere stratification in Urban Boundary Layer. Besides, this index must be used in the following analysis concerning the behaviour of temperature fluctuations. In this perspective, I individuated the index that shows better the daily variability of atmospheric stability. It uses environmental lapse rate and adiabatic lapse rate and it corresponds to the square of Brunt-Väisälä frequency or buoyancy frequency in the case of a stable atmospheric stratification.
In the analyses described above, a representation of typical day for every month can

be useful to carry out a comparison of the different periods.
In order to study the features of temperature fluctuations, the behaviour of small and big temperature difference are distinguished at the change of atmospheric stability. I have in mind to search for a scale laws for every case and verify the different characteristics. In detail, the goal concerning the weak temperature fluctuations is the check of linear behaviour of exponents for spatial separations among the anemometers; the purpose relevant to strong temperature fluctuations is the individuation of phenomenon of intermittency saturation.
The aim of the second subject, the study of wind fields over complex terrain, is the achievement of wind fields with high resolution.
Currently, we can obtain meteorological quantities with a resolution in order of kilometres, in my research I would like to achieve the numerical procedure for realization of wind fields with better resolution. The latest ones have various applications, for example they can become useful for the evaluation of wind energy potential in geographic area, the study of pollutant dispersion in atmosphere, the examination of fire propagation.
Therefore, the object of my work is the nesting of Computational Fluid Dynamics (CFD) model in mesoscale meteorological model.
The meteorological model provides fields of various quantities, for example wind velocity, temperature, pressure, density, every hour over pressure levels with low resolutions. These ones are used in statement of CFD model to obtain wind fields with higher resolution.
The meteorological model used is WRF and the CFD software are CFX and FLUENT.
The domain of study covers Genoa province. Its horizontal extension is of 19610 m in latitude and 35640 m in longitude; whereas, in vertical direction, local orography considered, it extends up to an elevation of 3500 m a.s.l..
For the CFD procedure the domain is discretized by two unstructured meshes. They are built by tetrahedrons and prism cells with different resolution, in order to have a comparison of output of simulations executed with different grids.
The computations are set stationary, isothermal, incompressible and the turbulence model is based on RANS equations. In this statement the Navier-Stokes equations describing the atmospheric flow are averaged and the computational timetables are lower than ones of other CFD approaches. Besides, the choise of this turbulence models is common for various geophysical study [16], [18].
I examined the simulations relevant to an hour (h 00 of 01/11/2009) as case-study, because it is representative of particular meteorological configuration that interests the considered area. The wind direction is in North-East sector at lower elevations and it is frequent in autumn and in winter in Liguria region.
The simulations are differentiated in the choice of boundary conditions in order to identify a computation configuration, allowing to obtain realistic wind fields over a region with particular orography.
At first, the wind velocity provided by meteorological model is assigned as boundary conditions in its nodes located on later faces of domain. The simulations are carried out using both meshes. Since the thicker grid does not provide better results than the other one, the following computations are executed with coarser grid. These

ones are obtained with simplified boundary conditions: the wind velocity assigned to lateral faces is an average of wind velocity obtained by meterological model. In both statements, the number of lateral faces constrained by meteorological model velocity are changed in order to individuate the better configuration. Eventually, the configuration providing more realistic results is individuated by simulation with wind velocity, calculated as an average of the meteorological model velocity, assigned to four lateral faces.
The last one is repeated for the following hourly instants and the results of the calculations are compared with the data obtained by meteorological model and the direct measurements in an inner point of domain, next to Functional Center of ARPAL. In this way, we can have a check of simulations results by measured data.
In summary, the outline of Thesis is divided in two parts: the first one concerns the theme of atmospheric turbulence in Urban Boundary Layer and it is described in Chapter 1 and Chapter 2; the second one deals with the study of wind fields over complex terrain and it is reported in Chapter 3, Chapter 4 and Chapter 5.
In detail, for the first subject in Chapter 1 there is a theoretical treatment of atmospheric turbulence, and in Chapter 2 the analysis of the phenomenon by using the data measured is presented; for the second topic in Chapter 3 the fundamentals of modelling of atmospheric flow used in my work are reported, in Chapter 4 the nesting of CFD model in meteorological model is described and in Chapter 5 the variations of previous CFD statement and simulations of the following hourly instant are presented.

Chapter 1

Atmospheric turbulence

1.1 Introduction

In this chapter the principia of atmospheric turbulence are described. Further I pay attention to the characteristics of Planetary Boundary Layer, a relevant part of Earth atmosphere interested by turbulent flows, and the conditions of stability of the above mentioned Planetary Boundary Layer.
Here, the fundamentals of Komlmogorov's 1941 Theory are explained and, then, I introduced the phenomena of scale invariance and intermittency, that concern both the velocity and the temperature fields. Finally the statistics of temperature and its fluctuations are shown.
The analysis of turbulence is subject dealt by different applied sciences, in particular the objects of my study are Atmosphere Physics, Fluid Dynamics and Computational Fluid Dynamics. In the latest one the choice of turbulence model is very important in numerical simulations.

1.2 Planetary Boundary Layer

The Planetary Boundary Layer, shortly PBL, is the lowest layer of Troposphere. The Troposphere extends up to 11 km in elevation over the Earth's surface (figure 1.1). It is divided in:

- Free Atmosphere;
- Planetary Boundary Layer.

The Planetary Boundary Layer is distinguished from the Free Atmosphere for different aspects:

- friction: it is insignificant and the little energy is dissipated in the Free Atmosphere, whereas it is considerable and energy dissipation is high in the Planetary Boundary Layer;
- turbulence: it is present in the clouds and near the jet stream in the Free Atmosphere, whereas it is an important phenomenon in the Planetary Boundary Layer;

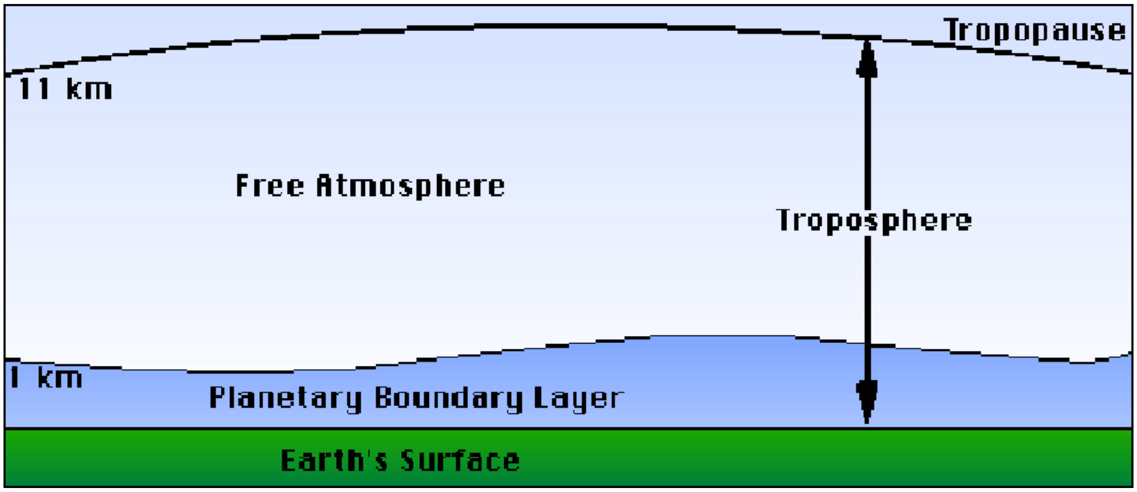

Figure 1.1: Division of Trophosphere: Free Atmosphere and Planetary Boundary Layer [28].

- thickness: the Free Atmosphere extends between 8 km and 18 km, while the Planetary Boundary Layer has an elevation between 100 m and 3000 m over the ground with diurnal variation;
- mixing: it is essentially horizontal with a small molecular diffusion in the Free Atmosphere, whereas it occurs both in horizontal and in vertical directions in the Planetary Boundary Layer.

In detail, the Planetary Boundary Layer is the part of Troposphere near the Earth's surface with depth variable in space and in time: it can change from some hundreds metres to a few kilometres. Its configuration depends primarily on the daily cycle of sun forcing and on meteorological conditions.
The Planetary Boundary Layer can be defined as atmosphere layer influenced directly by Earth's surface and it reacts to surface forcing in time scale of order of an hour or smaller [28].
The main influences of Earth's surface are frictional drag, terrain roughness, radiative flows, evapotraspiration, sensitive heat, latent heat and pollutant emissions.
The Earth's surface absorbs the sun radiation and sends it out in a long time in different ways: radiation in infrared light, sensitive heat or latent heat. The energy transfer is partially operated by turbulent flows, that allow the exchange of sensitive heat, latent heat, momentum, diffusion of air costituents and pollutants.

1.2.1 Diurnal cycle of Planetary Boundary Layer

The Planetary Boundary Layer follows a diurnal cycle, due to solar forcing; it can be divided into four main layers (1.2):

- Surface Layer;

- Mixed Layer;
- Residual Layer;
- Stable Layer.

In detail, each part is described in succession.

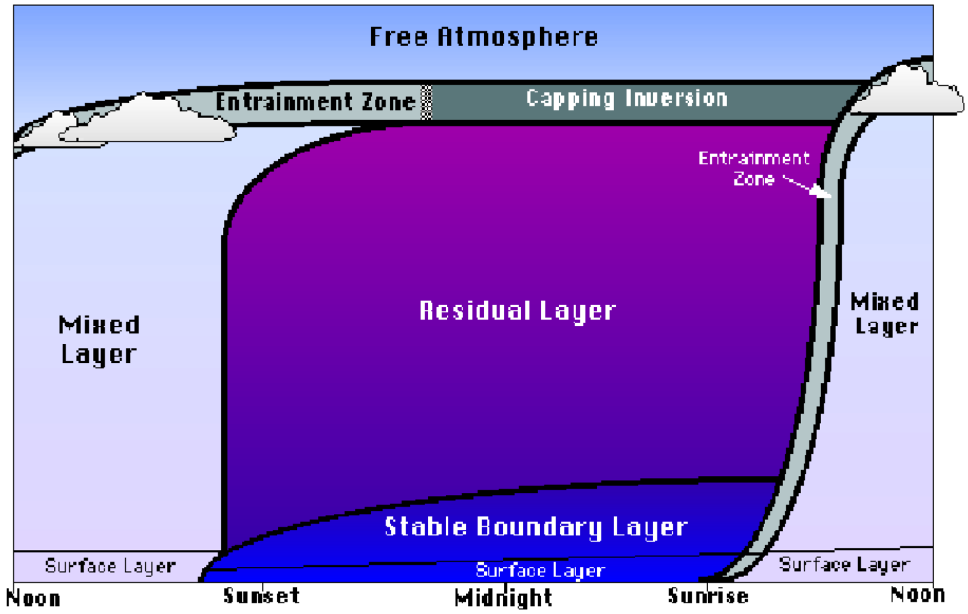

Figure 1.2: Structure of Planetary Boundary Layer [28].

The Surface Layer (shortly SL) is the sub-layer closest to the Earth with a relatively constant elevation during the day, varying less than 10 % of its thickness. Its height is about 10 % of the global elevation of Planetary Boundary Layer. In the part nearest to the surface, the molecular viscosity is an important cause of turbulence. Above the Surface Layer there are Mixed Layer (shortly ML) or Stable Layer (shortly SL), depending on the temperature structure of PBL.
The temperature of Planeary Boundary layer is influenced mainly by solar radiation. The warming of Earth's surface during the dayligh heats up the overhanging air and it causes the formation of an unstable atmosphere layer, known as Convective Boundary Layer (shorty CBL) .
The Convective Boundary Layer is split into three parts: the Surface Layer, the Mixed Layer and the Entrainment Layer (shortly EL). The Mixed Layer is characterized by a vertical mixing of air, due essentially to convective motion, while the Entrainment Layer is a transition layer located between Mixed Layer and Free Atmosphere.
The nocturnal cooling causes a decrease of turbulence, developed in the Planetary Boundary Layer; during the night the Stable Nocturnal Boundary Layer (known as Stable Boundary Layer, shortly SNL) develops itself near to the ground. It is characterized by lighter winds and weaker turbulence than those existing in the Mixed

Layer. Above the Stable Boundary Layer there is a part of Planetary Boundary Layer, knows as Residual Layer (shortly RS), where a turbulent mixing of diurnal hours remains in a stratification almost neutral [28].

1.3 Atmospheric stability

The static stability of a fluid does not depend on the mechanical features of the fluid, but it is related to buoyancy. It is due to differences of density inside the fluid. A fluid is statically stable when a denser layer is placed below a lighter one, whereas the opposite configuration defines the unstable case. In the second situation, vertical motions form themselves, because they try to take back the fluid in an equilibrium condition.
The stability of the air is a characteristic of the atmosphere that determines a lot of phenomena, in relation to vertical movements of air masses.
The conditions of stability and instability of the air depend on the so-called environmental lapse rate and the dry adiabatic lapse rate.
The environmental lapse rate is defined as follows

$$\gamma = -\frac{dT}{dz} \tag{1.1}$$

where T is the temperature and z the vertical coordinate.
The dry adiabatic lapse rate si defined as follows

$$\gamma_d = \Big(-\frac{dT}{dz}\Big)_a = \frac{g}{C_p} \tag{1.2}$$

where g is the gravitational acceleration and C_p is the specific heat of dry air at constant pressure.
This expression is derived by the first principle of thermodynamics, applied to an adiabatic transformation. We assume that a dry air parcel moves fastly without heat exchanges with the surrounding environment and therefore the transformation is considered adiabatic.
The relation between the environmental lapse rate γ and the adiabatic lapse rate γ_d determines the different conditions of static stability of the atmosphere [28].
We can suppose that an air parcel has a little displacement upwards, that does not influence the surrounding environment. Therefore the Archimedes' Law allows to derive the behaviour of the parcel. At the beginning the parcel has the same temperature of the surrounding environment. If the process is considered adiabatic, it is characterized by the adiabatic lapse rate γ_d, whereas the transformation of the surrounding environment is ruled by the lapse rate γ. After this movement, the air parcel may have different temperature in comparison to the one of the environment, estimated at the same elevation. The difference between these temperatures is positive if $\gamma > \gamma_d$ and it is negative if $\gamma < \gamma_d$.
In the first situation, under condition of constant pressure, the air parcel will have a density smaller than the environment one. By means of the buoyancy it will be subjected to a further movement upwards and in this condition the atmospheric

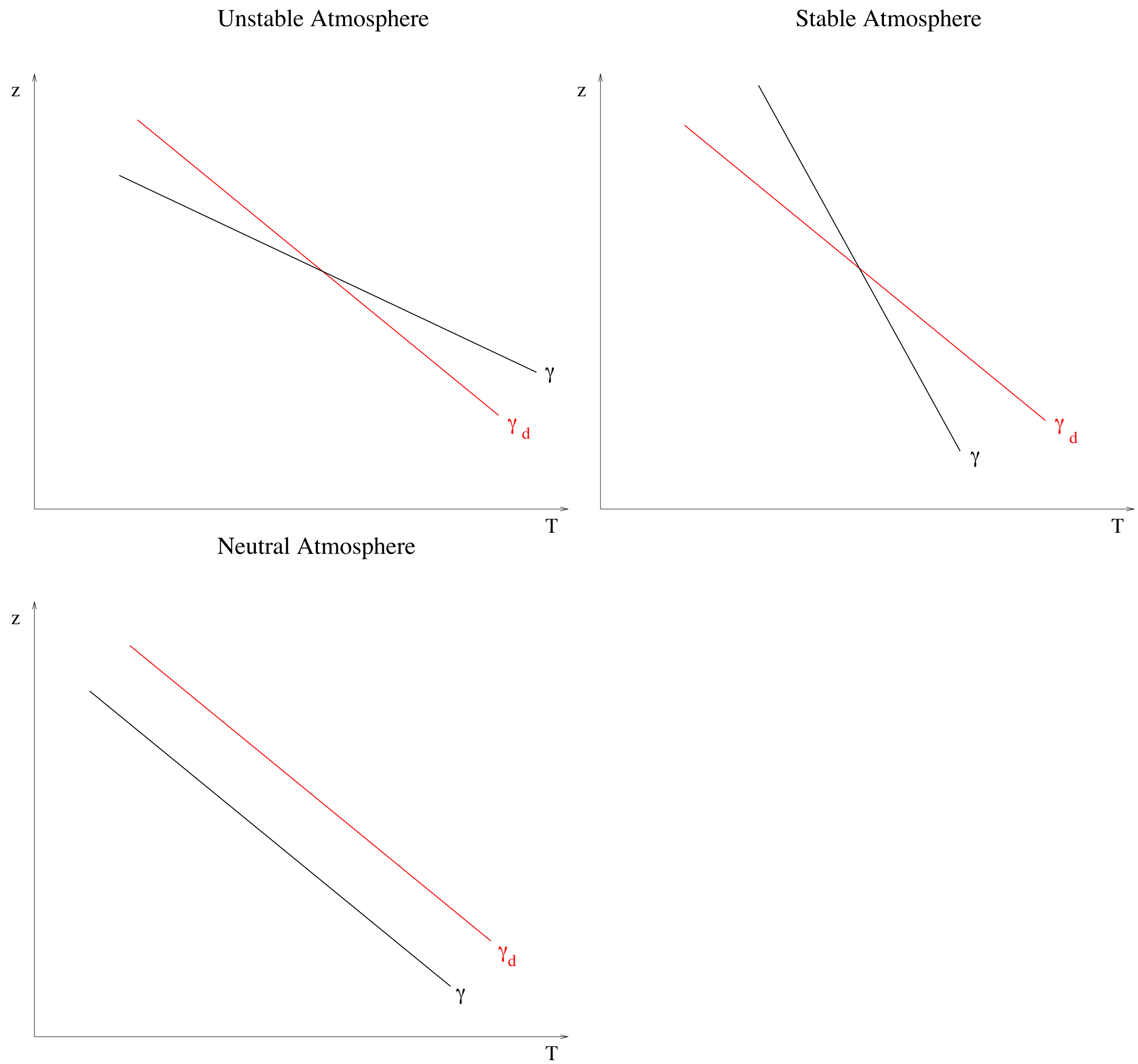

Figure 1.3: Atmospheric stability.

layer is statically unstable.
In the second situation, the air parcel will have larger density than that of the environment and in this condition the atmospheric layer is statically stable.
The condition corresponding to the same density between the air parcel and the surrounding environment results in $\gamma = \gamma_d$ and the atmospheric layer is statically neutral, because the buoyancy is equal to zero (figure 1.3).
In the Surface Layer another indicator of the condition of atmospheric stability is represented by the turbulent flow of sensible heat H_0, defined by the relation

$$H_0 = \rho C_p cov(w, T) \tag{1.3}$$

where ρ is the density of the air, C_p is the specific heat at constant pressure and $cov(w, T)$ is the covariance between the third component of wind velocity w and the temperature T.
During the sunny day hours, when the solar energy is sufficient to develop large convective eddies, H_0 and $cov(w, T)$ are positive and the atmosphere is in unstable

conditions.
On the contrary, the atmospheric stable situations often occur during not-windy night hours and the values of H_0 and $cov(w,T)$ are negative.
Finally, the adiabatic situations correspond to transitions from convective conditions to stable ones and H_0 and $cov(w,T)$ are equal to zero [22].

1.4 Fundamentals of atmospheric turbulence

Turbulence is an irregular motion of fluids, that occurs when fluid particles move along solid surfaces. The physical observable change in chaotic both in space and time coordinates under turbulent conditions.
Therefore, the nature of the turbulence requires a statistical study and a probabilistic description [28].
Atmospheric turbulence is caused by nonlinear effects, that are combined with non-local effects originated by the pressure. The equations ruling space and time evolution of an incompressible flow are the so-called Navier-Stokes equations

$$\frac{\partial \boldsymbol{v}}{\partial t} + \boldsymbol{v} \cdot \boldsymbol{\partial} \boldsymbol{v} = -\frac{1}{\rho}\boldsymbol{\partial} p + \nu \boldsymbol{\partial}^2 \boldsymbol{v} + \boldsymbol{f} \tag{1.4}$$

$$\boldsymbol{\partial} \cdot \boldsymbol{v} = 0 \tag{1.5}$$

where $\boldsymbol{v}$ is the flow velocity, ρ the fluid density, p the pressure, ν the kinematic viscosity and $\boldsymbol{f}$ the external forcing.
The turbulence is defined by eddies of various sizes, that interact with each other and with average velocity. This system is characterized by a kinetic turbulent energy for unit mass k and its rate of dissipation ϵ, defined as follows

$$k = \frac{1}{2}(\overline{(u-u_a)^2} + \overline{(v-v_a)'^2} + \overline{(w-w_a)^2}) \tag{1.6}$$

$$\epsilon = \frac{dk}{dt} \tag{1.7}$$

where $\boldsymbol{v}(u,v,w)$ is the local velocity, $\boldsymbol{v_a}(u_a,v_a,w_a)$ is the average velocity and the horizontal bar represents the average operation.
The emergence of turbulence depends on the value assumed by the dimensionless number, Reynolds number, defined as

$$Re = \frac{Lv}{\nu} \tag{1.8}$$

where L, v are respectively the characteristic length and velocity scales and ν is the kinematic viscosity. This last one is associated to dynamic viscosity μ, as shown in the following relation

$$\nu = \frac{\mu}{\rho} \tag{1.9}$$

with ρ the fluid density.
Low values of Reynolds number characterize a laminar flow, while large values are distinctive of turbulent flow.
In atmosphere the turbulent flow is caused by different forcings. Some of these are:

- heating of the ground, caused by sun radiation, that determines the movement of air mass (thermal currents);
- friction of the ground, that influences the average flow and determines the wind shear;
- presence of obstacles (trees, buildings,...), that perturbs the average wind and determines the leeward eddies;
- emission of pollutant, natural or anthropogenic.

Therefore, the atmospheric turbulence is usually divided in:

- thermal turbulence;
- mechanical turbulence.

The first one is caused by the difference of temperature between the surface and the surrounding air layer, that is essentially determined by sun radiation and it occurs during the daylight. The second one is due to wind shear and also by the presence of obstacles on the ground and it can persist during the night, too [14].

1.5 Scales of turbulence

The turbulent flow is described by set of eddies of various dimensions and its study requires the definition of scale lengths, that correspond to the dimension of the same eddies. They are:

- L integral scale;
- μ Kolmogorov scale;
- η Taylor scale.

In detail, the integral scale L is connected to eddies of the biggest dimensions and it is calculated as follows

$$L = \int_0^{+\infty} \frac{R(r)}{R(0)}\, dr \tag{1.10}$$

where $R(r)$ is the cross-correlation function of the velocity, defined in the following way

$$R(r) = \overline{(v(\boldsymbol{x}) - v_a(\boldsymbol{x}))\,(v(\boldsymbol{x}+\boldsymbol{r}) - v_a(\boldsymbol{x}+\boldsymbol{r})} \tag{1.11}$$

The length scale L represents the largest distance, within which the velocities of turbulent flows are correlated. It is the lowest limit of space interval, where energy input causes the energy cascade, known as Richardson cascade (figure 1.4).
The Kolmogorov scale μ is defined as follows

$$\mu = \left(\frac{\nu}{\epsilon}\right)^{\frac{1}{4}} \tag{1.12}$$

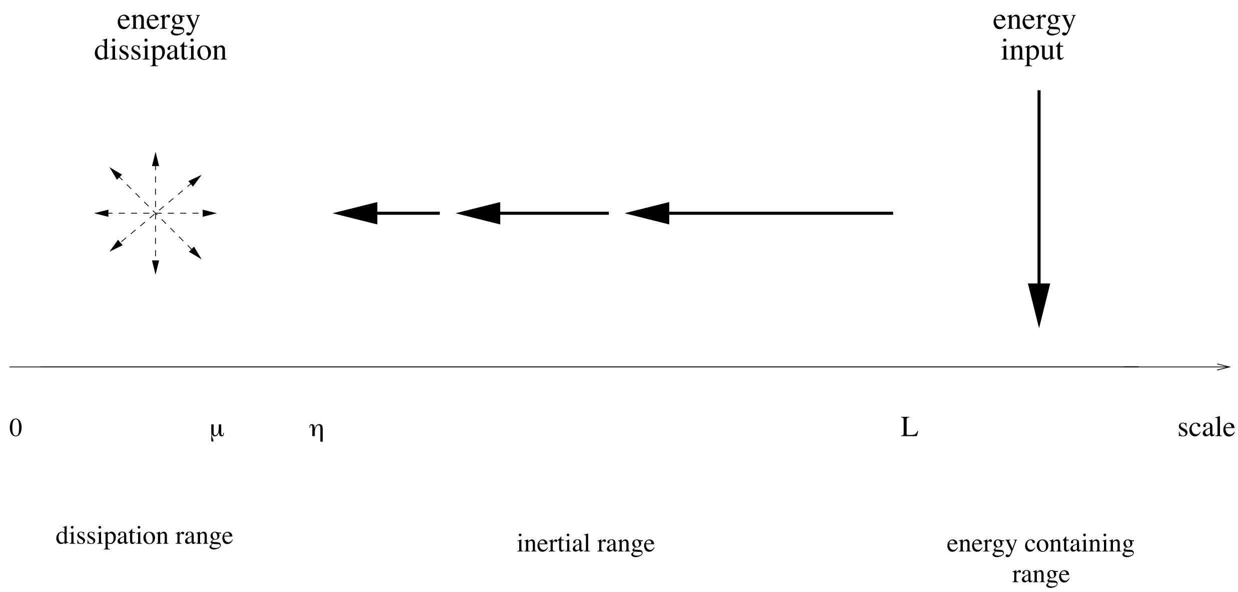

Figure 1.4: Energy cascade of Richardson [26].

The length scales μ and L define respectively the ultraviolet scale and infrared scale. They characterized the lower and upper extremes of equilibrium range $[\mu, L]$, wherein the First Hypotesis of Kolmogorov's 1941 Theory is valid.
It assures that, under condition of statistical omogeneity and isotropy and for large Reynolds numbers, the average properties of every turbulent flow are determined by the kinematic viscosity ν of the fluid and by the turbulent kinetic energy k.
The Second Hypotesis of Kolmogorov's 1941 Theory assures existance of a range of scales where energy flux flows at a constant rate. This range is known as inertial range, $[\eta, L]$, where η is the Taylor scale or dissipative scale, and is defined as follows

$$\eta = \left(\frac{\nu\, k}{\epsilon}\right)^{\frac{1}{2}} \tag{1.13}$$

Below η energy is dissipated due to molecular viscosity. This means that the cascade process occuring in the inertial range and stops at η [26].

1.6 Kolmogorov's 1941 Theory

The Kolmogorov's 1941 Theory, briefly K41, shows a formalization of phenomena that concerning the transfer of energy from large to small spatial scales, introduced in previous section 1.5. It is also known as a mean average theory, because it neglets the fluctuations.
The turbulence is a chaotic phenomenon and for this reason its study needs a statistical approach. The study of inertial range uses the probability distributions of velocity fluctuation and its momentum of various orders.
The velocity fluctuation between two points $\boldsymbol{x_1}$ and $\boldsymbol{x_2}$ at the time t is $\delta_r \boldsymbol{v}$; it is defined as follows

$$\delta_r \boldsymbol{v} = \boldsymbol{v}(\boldsymbol{x_2}, t) - \boldsymbol{v}(\boldsymbol{x_1}, t) \tag{1.14}$$

where $\boldsymbol{r}$ is the distance between the points $\boldsymbol{x_1}$ and $\boldsymbol{x_2}$.
The velocity momentum of order p is

$$\langle(\delta_r \mathbf{v})^p\rangle = \langle(\mathbf{v}(\mathbf{x_2}, t) - \mathbf{v}(\mathbf{x_1}, t))^p\rangle \tag{1.15}$$

Starting from this last expression (1.15), the longitudinal structure function of order p, $S_p^L(r)$, is made up in the following way

$$S_p^L(r) = \langle(\delta_r \mathbf{v})^p\rangle_{//} = \langle[(\mathbf{v}(\mathbf{x_2}, t) - \mathbf{v}(\mathbf{x_1}, t)) \cdot \widehat{\mathbf{r}}]^p\rangle \tag{1.16}$$

with $\widehat{\mathbf{r}} = \frac{\boldsymbol{r}}{r}$ is the unit vector that indicates the direction between the points $\boldsymbol{x_1}$ and $\boldsymbol{x_2}$.
If we tries to write the equations for the p-order structure functions, the famous closure problem rises, i.e. the equation for S_p^L involves S_{p+1}^L. The only exception is for $p = 3$ for which an equation in closed form can be derived, and its solution provides

$$S_3^L(r) = -\frac{4}{5}\overline{\epsilon}r \tag{1.17}$$

where $\overline{\epsilon} = \int_0^k F(k')dk'$ is the forcing term.
The equation (1.17), known as four-fifth law, is obtained from Navier-Stokes equations [14]. Following remarks are worth discussing:

- the negative sign shows that the energy flows from the largest to the smallest scales (phenomenon also known as direct cascade). It occurs in the three-dimensional space, whereas in the two-dimensional space the expression of longitudinal structure function of order three, $S_3^L(r)$, is

$$S_3^L(r) = \frac{4}{3}\overline{\epsilon}r \tag{1.18}$$

- a weak dependence on the system forcing is present in term $\overline{\epsilon}$. Therefore, the law has a universal character with respect to the forcing class;

- the dependence has a power law, behaviour that ensures a scale invariance.

1.7 Scale invariance and intermittency

Because of the chaotic nature of turbulence and the proliferation of degrees of freedom, statistical tools must be utilized to deal with it.
According to K41 Theory, the determination of scaling behaviour for generic order p of the structure function can be obtained by means simple dimensional consideration (power counting). This occurs because the K41 Theory is a mean field theory.
From the four-fifth law we have

$$\langle(\delta_r \mathbf{v})^3\rangle_{//} \propto \overline{\epsilon}r \tag{1.19}$$

$$\langle(\delta_r \mathbf{v})\rangle_{//} \propto \overline{\epsilon}^{\frac{1}{3}}r^{\frac{1}{3}} \tag{1.20}$$

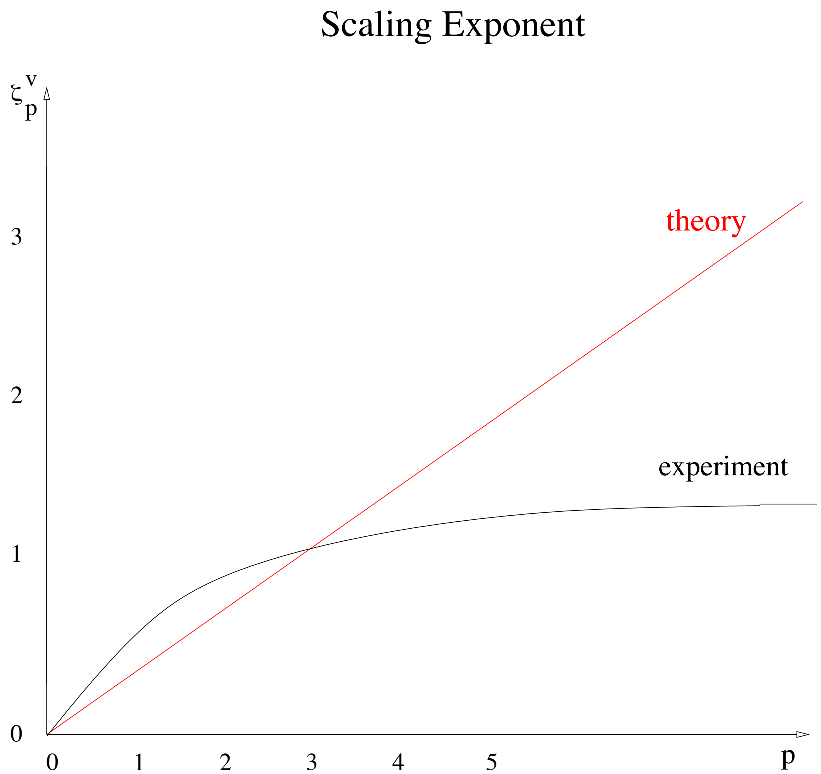

Figure 1.5: Scaling exponent ζ_p^v provided by Kolmogorov's Theory is shown by a red line, the one obtained by numerical experiments is shown by black line.

The equation for structure functions $S_p^L(r)$ of general order p is then derived dimensionally

$$S_p^L(r) = \langle (\delta_r \mathbf{v})^p \rangle_{//} = C_p \,\overline{\epsilon}^{\zeta_p^v} r^{\zeta_p^v} \tag{1.21}$$

where C_p is a constant and $\zeta_p^v = \frac{p}{3}$ is the scaling exponent, i.e. the scaling exponent has a linear behaviour with the order p [22].
Such prediction is not observed in numerical simulations, with the exception of the case $p = 3$, for which there is an agreement between the theory and the numerical simulations.

The difference between the scaling exponents, obtained by K41 Theory, and the ones obtained by numerical experiments, shown in figure 1.5, is known as intermittency. From a physical point of view this means that the energy is dissipated in a domain having a nontrivial (i.e. fractal or multifractal) structure [14]. The trend of ζ_p^v for high values of p becomes constant in the experiments and the limit value of ζ_p^v for large p is usually called z_∞^v. This phenomenon is known as intermittency saturation. Finally, we can also say that the probability density function of fluctuations of velocity is non-Gaussian and it explains the discrepancy between the scaling exponents derived by the K41 Theory and those obtained by means of experiments [5], [6].

1.8 Temperature

In the analysis of turbulence, it is also interesting to study the temperature and relative fluctuations in addition to velocity and its fluctuations.
The behaviour of temperature $T(\boldsymbol{x}, t)$ is described by the following equation

$$\partial_t T(\boldsymbol{x}, t) + \boldsymbol{v}(\boldsymbol{x}, t) \cdot \boldsymbol{\partial} T(\boldsymbol{x}, t) = D_0 \partial^2 T(\boldsymbol{x}, t) + f(\boldsymbol{x}, t) \tag{1.22}$$

where D_0 is the thermal diffusivity coefficient and $f(\boldsymbol{x}, t)$ represents the external forcing that can be individuated in possible sources or sink of heat, located in the domain.
The behaviour of temperature can be passive or active.
When the temperature behaves as a passive scalar, it does not influence the velocity field. It occurs especially if Planetary Boundary Layer has neutral stratification.
On the contrary, when the temperature has a role of active scalar, it affects the velocity field especially by means of the contribution of the buoyancy [26].
In both cases, in the Planetary Boundary Layer strong temperature fluctuations are observed.
Similarly to theoretical treatment of velocity, temperature fluctuation $\delta_r T$ between two points $\boldsymbol{x_1}$ and $\boldsymbol{x_2}$ at the time t is defined as follows

$$\delta_r T = T(\boldsymbol{x_2}, t) - T(\boldsymbol{x_1}, t) \tag{1.23}$$

Temperature fluctuations affect the whole range of spatial scales, from the largest to the smallest scales of motion.
If the temperature is a passive scalar, there is a prediction for the scaling exponents of the velocity and temperature fluctuations. They follow from the Yaglom Law and the following relations are found:

$$(\delta_r \boldsymbol{v})_{//} \sim r^h \tag{1.24}$$
$$\delta_r T \sim r^{\frac{1-h}{2}} \tag{1.25}$$

where h is a scaling exponent obtained from fractal model [14]. In the particular case of $h = \frac{1}{3}$, we obtain

$$(\delta_r \boldsymbol{v})_{//} \sim r^{\frac{1}{3}} \tag{1.26}$$
$$\delta_r T \sim r^{\frac{1}{3}} \tag{1.27}$$

Such prediction is known as Kolmogorov - Obukhov - Corssin prediction (KOC51 Theory).

1.8.1 Global scalar invariance and its violations

The treatment of temperature field is similar to the one of velocity. We can understand the statistical properties of this field, if we analyse the structure function $S_p(r)$

$$S_p(r) = \langle (\delta_r T)^p \rangle \tag{1.28}$$

Small temperature fluctuations are captured by low values of order p, whereas large temperature fluctuations are associated to high values of order p.
If the fluctuation $\delta_r T$ is scalar invariant under the transformation $r \to \lambda r$, there is a number $\mu(\lambda, p)$ such that $\frac{S_p(r\lambda)}{S_p(r)} = \mu(\lambda, p)$ does not depend on the separation r. This characteristic is verified if the structure function is

$$S_p(r) = A_p r^{\zeta_p^T} \tag{1.29}$$

where A_p is a coefficient and ζ_p^T is the scaling exponent [14].
A proportional relation may be derived from espressions (1.28) and (1.29); it is written in the following way

$$\langle(\delta_r T)^p\rangle \sim r^{\zeta_p^T} \tag{1.30}$$

Upon the condition that ζ_p^T is a linear function of order p, $\zeta_p^T = \beta p$, we can speak of the global scale invariance. This means that scale invariance is valid for each type of fluctuation, from the smallest to the largest fluctuations.
Indeed, if we define the fluctuation as $[S_p(r)]^{\frac{1}{p}}$, the ratio $\frac{[S_p(r)]^{\frac{1}{p}}}{[S_p(r\lambda)]^{\frac{1}{p}}}$ does not depend on the scale r and on the order p.
Upon the condition that ζ_p^T is a nonlinear function of p, we can speak of local scale invariance or anomalous scaling or intermittency, similarly to the analysis of velocity. In this case the ratio $\frac{[S_p(r)]^{\frac{1}{p}}}{[S_p(r\lambda)]^{\frac{1}{p}}} = \lambda^{\zeta_p^T} p$ does not depend on the scale r, but it depends on the order p. Only the fluctuations with the same strenght reproduce themselves at smaller scales in a self-similar fashion, it does not occur for temperature fluctuations with different intensity.
The behaviour of scaling exponent ζ_p^T is similar to the one of velocity fluctuations. Its qualitative trend is shown is figure 1.6.
Indeed, in analogy of the case of the velocity, in correspondence of large p we can observe an asymptotic behaviour of the scaling exponent ζ_p^T. It assumes an approximately constant value $\zeta_p^T = \zeta_\infty$ for large values of p. In analogy to the velocity behaviour, this phenomenon is known as saturation of intermittency [6].

1.8.2 Statistics of temperature fluctuations

The study of the scale invariance and the intermittency needs the statistic tool of probability density function of temperature fluctuations $P(\delta_r T)$.
In particular, the analysis of the cores of probability density function of temperature fluctuations allows to identify the properties of the weak temperaure fluctuations, whereas the analysis of the tails of probability density function allows to show the features of the strong temperature fluctuations.
The global scale invariance is characterized by the following rescaling property of probability density function

$$P(\delta_r T) = r^{-\beta} \widetilde{P}\Big(\frac{\delta_r T}{r^\beta}\Big) \tag{1.31}$$

This means that for each scale r, the relative fluctuation $\delta_r T$ is controlled by the same function $\widetilde{P}\big(\frac{\delta_r T}{r^\beta}\big)$. The exponent β represents the information about the effects

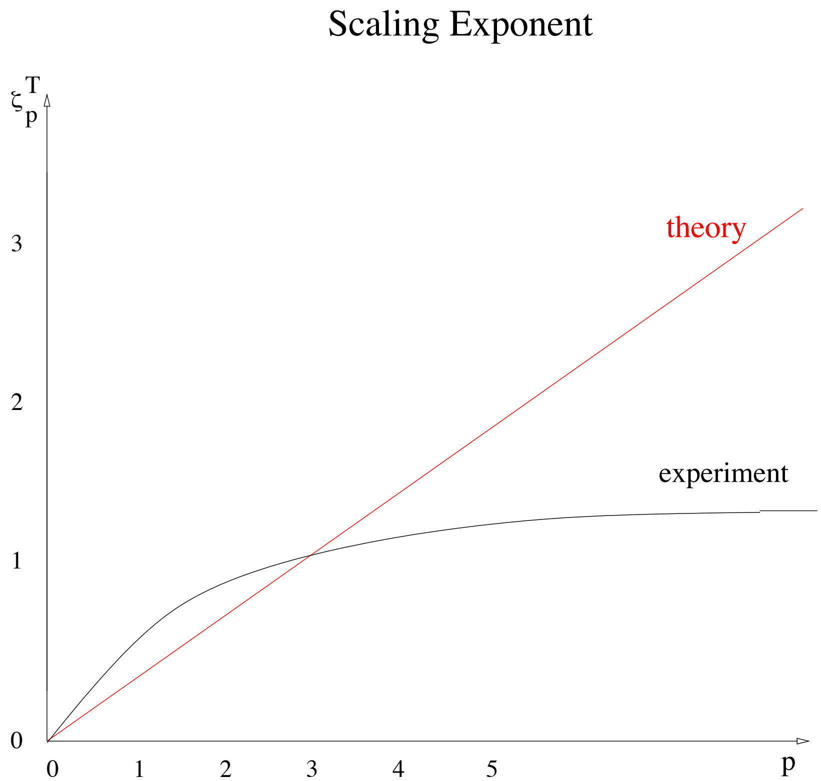

Figure 1.6: Scaling exponent ζ_p^T provided by Kolmogorov - Obukhov - Corssin Theory is shown by a red line, the one obtained by numerical experiments is shown by a black line.

of the scale.
For the study of intermittency, the probability density functions have not a relation with global rescaling, but they admit an appropriate rescaling relation only for the probability density function tails, written in the following way

$$P(\delta_r T) = \frac{r^{z_\infty}}{\sigma} Q\Big(\frac{\delta_r T}{\sigma}\Big) \tag{1.32}$$

where Q is a function which does not depend on distance r, and σ is the root mean square of temperature field.
The expression (1.32) is valid for $|\delta_r T| > \lambda\sigma$ with $\lambda > 1$. This condition, that represents the strong temperature fluctuations, is used to analyse the behaviour of the probability density function tails.
We can consider the cumulated probabilities in correspondence to the large temperature variances $Prob[|\delta_r T| > \lambda\sigma]$, it is written as follows

$$Prob[|\delta_r T| > \lambda\sigma] \equiv \int_{-\infty}^{-\lambda\sigma} P(\delta_r T)\, d(\delta_r T) + \int_{\lambda\sigma}^{+\infty} P(\delta_r T)\, d(\delta_r T) \tag{1.33}$$

where $P(\delta_r T)$ is the same as espression (1.32) , with $|\delta_r T| > \lambda\sigma$ and $\lambda > 1$.
An asymptotic relation for $Prob[|\delta_r T|$ is obtained

$$Prob[|\delta_r T| > \lambda\sigma] \sim r^{\zeta_\infty} \tag{1.34}$$

The value of scaling exponent ζ_∞ can be derived by the slope of $\log\{Prob[|\delta_r T| > \lambda\sigma]\}$ versus $\log r$ [5].

1.8.3 Connection between the statistics of temperature fluctuations and geometry

There is a link between the statistics of temperature fluctuations and geometry, that concerns the intermittency saturation.
The scaling exponent ζ_∞, that shows the intermittency saturation, is related to the fractal dimension D_F of the set containing the strong temperature fluctuations.
Operating in two-dimensional space, the strong temperature fluctuations can be schematized by discontinuity points of step functions. The discontinuity points are located by given coordinates in appropriate plane; for simplicity reason it is possible to choose a plane with a constant coordinate (for example with fixed z) in a usual three-dimensional space.
The ensemble of all discontinuity points defines the set S hosting large temperature fluctuations. Roughly, S is formed by intersection of a two-dimensional plane with the plume interfaces, across which strong temperature jumps occur.
A useful indicator to characterize the geometrical properties of set S is the fractal dimension D_F. The fundamental steps to define D_F are recalled as follows [14]:

- take the boxes of side r in order to cover the whole plane considered before and denote with N_{tot} the total number of the boxes;
- define the function $N(r)$ as the number of boxes containing at least one point of S;
- for sufficiently small values of r, we can expect a power-law behaviour for $N(r)$ in the form $N(r) \sim r^{-D_F}$; it defines the fractal dimension of S.

Given the fractal dimension D_F, we were able to compute the probability $Prob[|\delta_r T| > \lambda\sigma]$ with $\lambda > 1$ of having large temperature jumps in a certain distance r. Indeed, using the definition of probability

$$Prob[|\delta_r T| > \lambda\sigma] = \frac{N(r)}{N_{tot}} \tag{1.35}$$

with $N(r) \sim r^{-D_F}$ representing the favorable cases and $N_{tot} \sim r^{-2}$ the possible ones in two-dimensional space, we shall obtain

$$Prob[|\delta_r T| > \lambda\sigma] \sim r^{2-D_F} \tag{1.36}$$

From the comparison of the expressions (1.34) and (1.36) it follows the relation $\zeta_\infty = 2 - D_F$ for a particular two-dimensional situation. It can be extended to general case of any set S in three-dimensional ordinary space, where we have the $N_{tot} \sim r^{-3}$ relation.
Therefore, it is possible to obtain the relation between the intermittency saturation exponent ζ_∞ and the fractal dimensions D_F of the set containing the large temperature fluctuations as follows

$$\zeta_\infty = 3 - D_F \tag{1.37}$$

where D_F is the fractal dimension of the considered set S [5].

Chapter 2

Temperature in Urban Boundary Layer

2.1 Introduction

In my research I used a dataset of velocity and temperature, I received from the National Research Council of Turin.
The dataset is obtained by direct measurements carried out in Turin during an experimental campaign. It was organized within the project of Piedmont region 'Model and experimental study of atmospheric turbulence and dispersion of pollutants, 2006-2008' with collaboration of National Research Council of Turin, Department of Physics of Turin University and Regional Agency for the Protection of the Environment of Piedmont.
The measurements relate to a long period: from January 2007 to March 2008. Therefore, the statistical study is possible and it is very useful in the analysis of atmospheric turbulence. Indeed, the nature the phenomenon needs statistical tools to identify its main characteristics.
I analysed the main features of temperature, measured by three sonic anemometers with location in the suburbs of Turin. I repeated the same analysis scheme for every month of the whole period, looking for analogies and differences for every month and any relations among the months of the same meteorological season.
In the first time, I examined the average temperature and relevant standard deviation to obtain a general indication concerning the daily trend.
Then, I studied the properties of atmospheric stability, using three different indicators; among them I chose an indicator to characterize the stratification of Planetary Boundary Layer.
Last but not least, because this matter concerns my research about the atmospheric turbulence, I paid attention to temperature fluctuations with the purpose of identifying their scaling properties in relation to Kolmogorov-Obukhov-Corssin Theory of 1951.
The characterization, provided by Theory KOC51, is not always verified by numerical experiments; only for weak temperature fluctuations there is an agreement between theory and numerical experiments [5], [6], while for strong temperature fluctuations there is a discrepancy between the previsions of Kolmogorov-Obukhov-

Corssin Theory and the results of numerical experiments.
In my research, there is a comparison between the theoretical expectations and the elaborations from measured data.
In detail, I analysed the temperature fluctuations in referring to the conditions of atmospheric stability, because the different stratification of the Planetary Boundary Layer influences the behaviour of the statistics of this variable.
This study has important conseguences in areas of interest not only theoretical, but practical too.
In the analysis of temperature fluctuations, I searched the scaling properties, that have connections with intrinsic structure of the atmospheric turbulence. Besides they permit to obtain the parameterization relations. The latest ones are necessary in fluid dynamics computations and in meteorological simulations.
For example, in Computational Fluid Dynamics, the scaling relations are required in closure of turbulence model in Large Eddy Simulations (LES) and in simulations using the Reynolds-averaged Navier-Stokes (RANS) equations.
In meteorological models, the statistics of temperature fluctuations is required in parameterizations of small scale motion in atmospheric turbulence, subsequently the flow at large scale is known. They are used for meteorological forecast and climatological analysis.

2.2 Dataset

The data of temperature examined were measured in an urban meteorological station in Turin (Strada delle Cacce) from January 2007 to March 2008 [12].
The measurement station belongs to the Physics Department of Turin University, in an area owned by National Research Council. It is located in the southern outskirts of the town, on grassy, flat terrain surrounded by buildings (figure 2.1).
In the middle of the station there is a 25 m mast (figure 2.2). Tree anemometes, by means of which the temperatures are detected, are located on it at different heights: 5 m, 9 m and 25 m. So there is a dataset with three sequences of temperature: one for each instrument.
The frequency of measurement sampling of the anemometers is 20 Hz. Therefore, every hour contains 72000 data for every device, but sometimes the data are not available.
The mechanism of measuring is not easy. Every anemometer starts sending continuously the data at constant rate to a computer located in the station, then the communication between the two devices are established. The acquisition software writes the data in a lot of small files; it is programmed to close a file every four hours, so that the risk of data loss in case of blackout is minimized. When a file is closed, the communication is interrupted and it is re-established when a new file is opened and the writing of the data restarts.
These operations can require a variable time amount, during which the software tries to communicate with the instruments. If the connection is not re-established quickly, the transmission of the data between the anemometers and the calculator cannot occur and the relevant data get lost.
For this reason, the percentage of available data of every instrument may change

Figure 2.1: CNR station map (Turin, Strada delle Cacce).

in various months and among the anemometers. In detail, the percentage of data obtained is shown in the table 2.1.
The data of anemometer located at elevation of 5 m are available, in comparison to possible measurements of the whole period, in percentage bigger than 60 % for twelve months. The exceptions are February 2007, May 2007 and June 2007.
The functionality of anemometer at 9 m is similar to the one of the instrument at 5 m; the months with the percentage of available data lower than 60 % are January 2007, March 2007 and April 2007.
On the contrary the months with the percentage of available data larger than 60 % are more numerous for the instrument at 25 m. At this elevation the missing data have a bigger percentage than 40 % of the whole period only in December 2007 and March 2008.
The majority of the months have available data in a bigger percentage than 60 % at the same time in all the anemometers; therefore, this fact does not occur for six months: January 2007, February 2007, May 2007, June 2007, December 2007 and March 2008. In particular, in September 2007, October 2007, January 2008 and February 2008 there are available data in a bigger percentage than 90 % of the possible total measurements.
In my research, the period from 01/02/2007 to 29/02/2008 is analysed in detail and in the following figures I show the behaviour of the examined aspects only for some months. In particular I have chosen the months in which the properties of

Figure 2.2: CNR station mast (pointing North).

atmospheric turbulence are more evident.

2.3 Characterization of turbulence

The analysis of turbulence begin with the calculation of Reynolds number Re (1.8). It is used to understand the features of the flow, in particular to distinguish laminar flow compared to turbulent flow.
The dimensionless indicator Re is calculated using an air kinematic viscosity $\nu = 1.45 \cdot 10^{-5} Pa\, s$, derived from values concerning air of density $\rho = 1.225 \frac{kg}{m^3}$ and dynamic viscosity $\mu = 1.78 \cdot 10^{-5} \frac{m2}{s}$. Besides, in the expression (1.8), L is substituted by the height of the anemometer considered and v is estimated as hourly-averaged velocity.
The values of Reynolds number are calculated for a typical day of each month of the whole period. They allow to show a typical situation of the flow, that occurs every month.
In a typical day of every month, Reynolds number increases with the height. In particular, Re value is lower than $1 \cdot 10^6$ at heights of 5 m and 9 m, while at 25 m it is bigger than $1 \cdot 10^6$ (figure 2.3).
Especially in May 2007, June 2007 and July 2007 the values of Re are greater than in other periods for the anemometer at 25 m. During late spring and summer the atmosphere is particulary well mixed and the turbulence is predominantly of thermal nature.

Table 2.1: Percentage of data available for every anemometer at CNR station mast. The elevation of anemometers is indicated.

month	data at 5 m (%)	data at 9 m (%)	data at 25 m(%)
January 2007	89	47	99
February 2007	20	97	98
March 2007	96	57	98
April 2007	90	56	97
May 2007	36	86	97
June 2007	31	97	97
July 2007	68	95	95
August 2007	70	96	98
September 2007	94	97	96
October 2007	94	97	98
November 2007	94	88	63
December 2007	98	87	43
January 2008	97	97	95
February 2008	97	95	96
March 2008	97	99	12

In February 2007, March 2007 and April 2007, Re at height of 25 m is great. In this period the turbulence could be produced by mechanical and thermal instabilities [28].
Using the data of every anemometer, the trend of Reynolds number shows greater values during the hours of daylight, especially from 10 h to 20 h. In particular, for the months of spring and summer, the maximun is bigger than in other months. This supports the hypothesis that the turbulence of thermal origin has more evident effects than the mechanical one.

2.4 Trend of temperature

The temperatures, measured by anemometers, are corrected from the empirical equations of different devices. They derived from the empirical calibration of the instruments and they are different for the anemometers, because these relations consider the distinctive features of the devices and their locations [21].
For the anemometer at elevation of 5 m, the relations used are

$$c_5 = (1.001\, T_5^{meas})^{0.5} \tag{2.1}$$

$$\begin{aligned} T_5 = {} & 2.294 \cdot 10^{-18}\, (-394.691 + c_5)^2\, (-287.607 + c_5)^2 \\ & [136717 + (-735.740 + c_5)\, c_5]^2\, [100033 + (-628.922 + c_5)\, c_5]^2 \end{aligned} \tag{2.2}$$

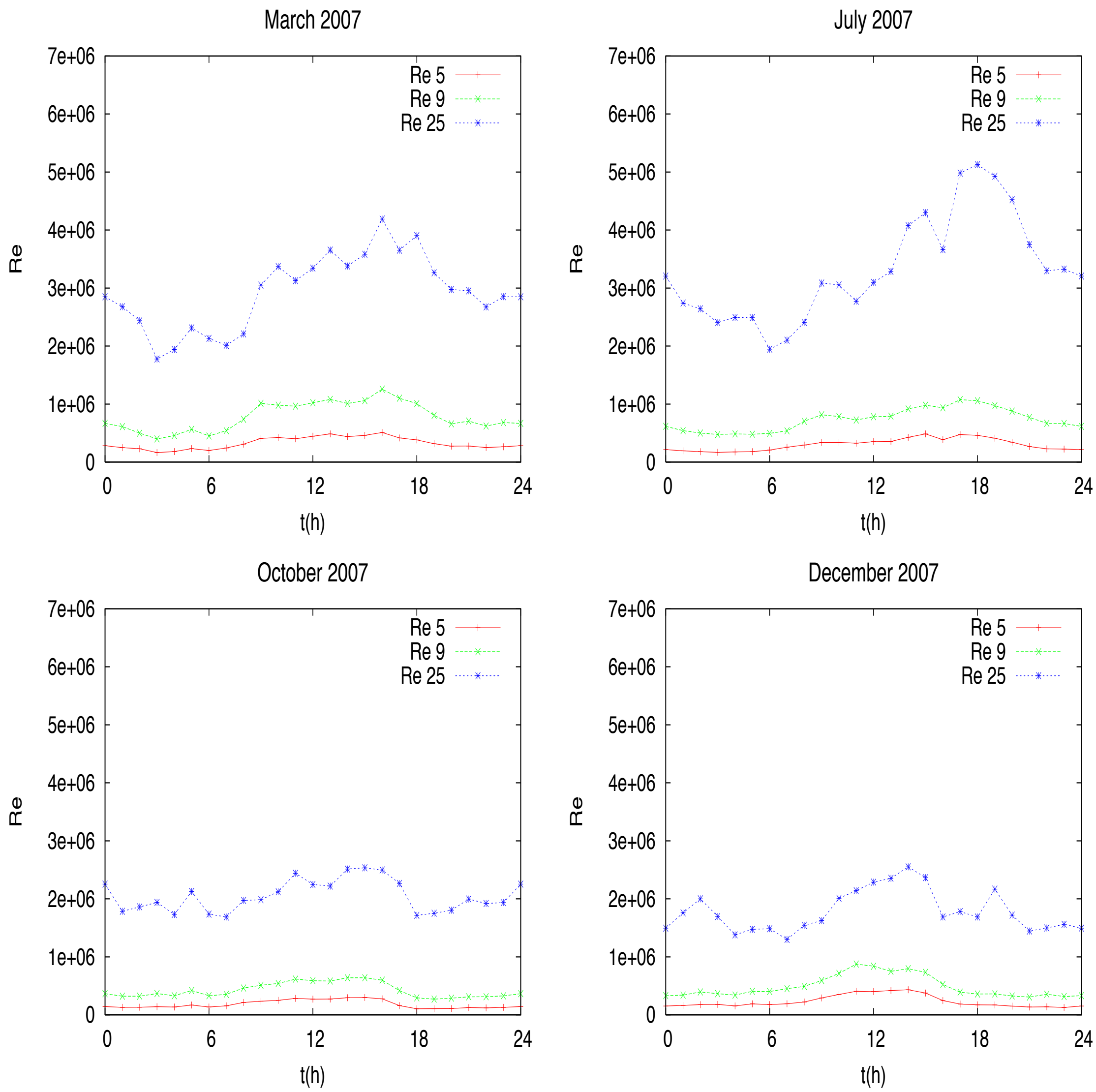

Figure 2.3: Hourly-averaged Reynolds number of a characteristic day for each month. In the figure the elevation of anemometers is indicated in metres.

where T_5^{meas} is the temperature measured by anemometer at height of 5 m and T_5 is the corrected temperature.
For the anemometer at elevation of 9 m, the equations are

$$c_9 = (1.001\, T_9^{meas})^{0.5} \tag{2.3}$$

$$T_9 = 1.324 \cdot 10^{-23} \, (-13672.700 + c_9)^2 \, (-403.036 + c_9)^2$$
$$[134881 + (-728.382 + c_9)\, c_9]^2 \, [93519.400 + (-609.324 + c_9)\, c_9]^2 \tag{2.4}$$

where T_9^{meas} is the temperature measured by anemometer at height of 9 m and T_9 is the corrected temperature.
Finally, the equations used for data at elevation of 25 m are

$$c_{25} = (1.001\, T_{25}^{meas})^{0.5} \tag{2.5}$$

$$T_{25} = 4.158 \cdot 10^{-19} \left[172984 + (-831.017 + c_{25})\, c_{25}\right]^2$$
$$\left[129220 + (-712.237 + c_{25})\, c_{25}\right]^2 \left[94732.000 + (-613.836 + c_{25})\, c_{25}\right]^2 \quad (2.6)$$

where T_{25}^{meas} is the temperature measured by anemometer at height of 25 m and T_{25} is the corrected temperature.
In my study the values of temperature T_5, T_9 and T_{25} are used. I calculated the average temperature for every hour, using 72000 data measured in an hour and the relevant standard deviation.
Then the hourly-averaged temperature in relation to all days of each month and its standard deviation are examined to know the trend of the variable studied in my research.

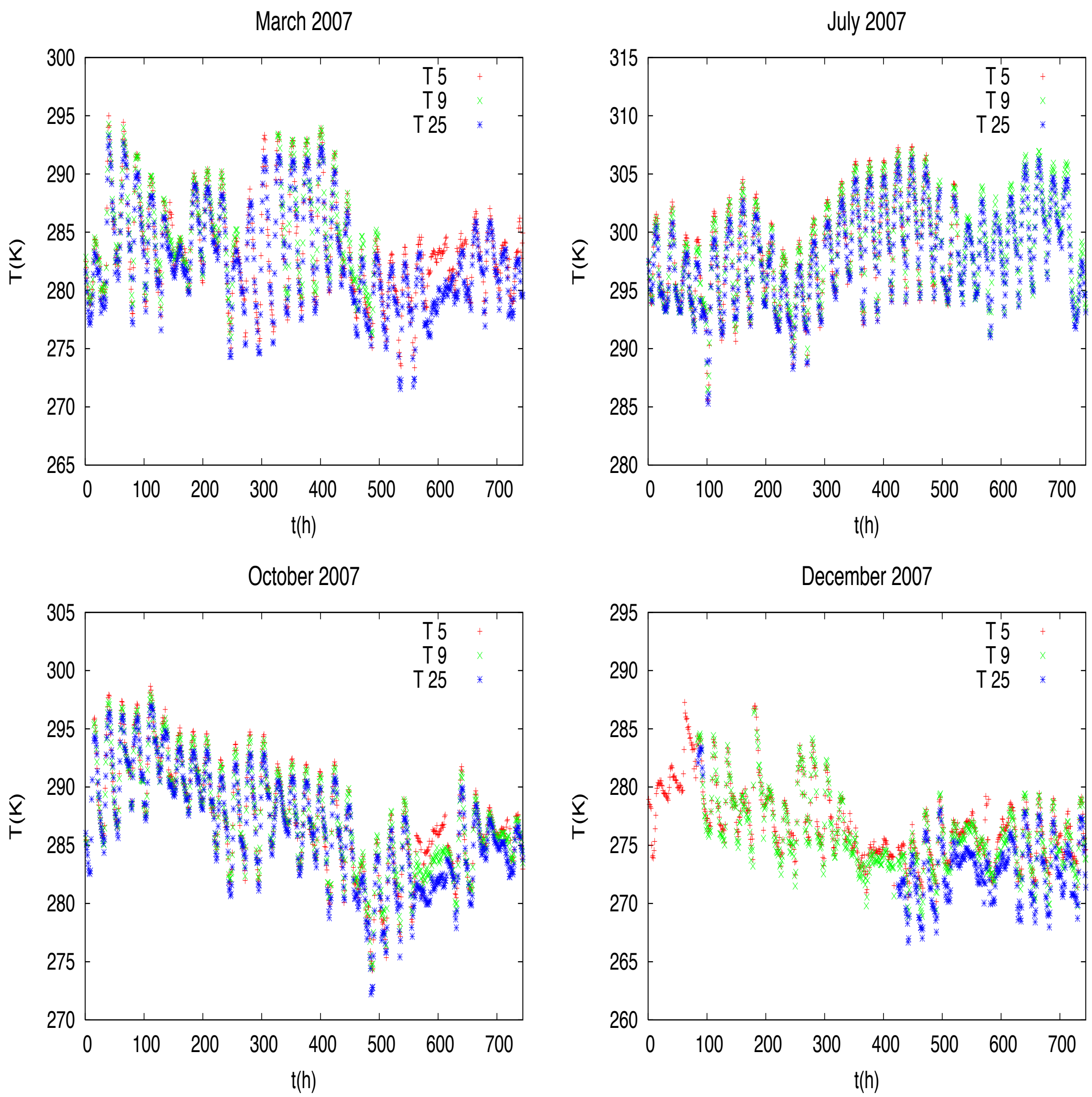

Figure 2.4: Hourly-averaged temperature for each month. In the figure the elevation of anemometers is indicated in metres.

In the analysis of the temperature averaged in one hour (figure 2.4), it is possible to observe the daily trend during all months for each anemometer. It is shown also

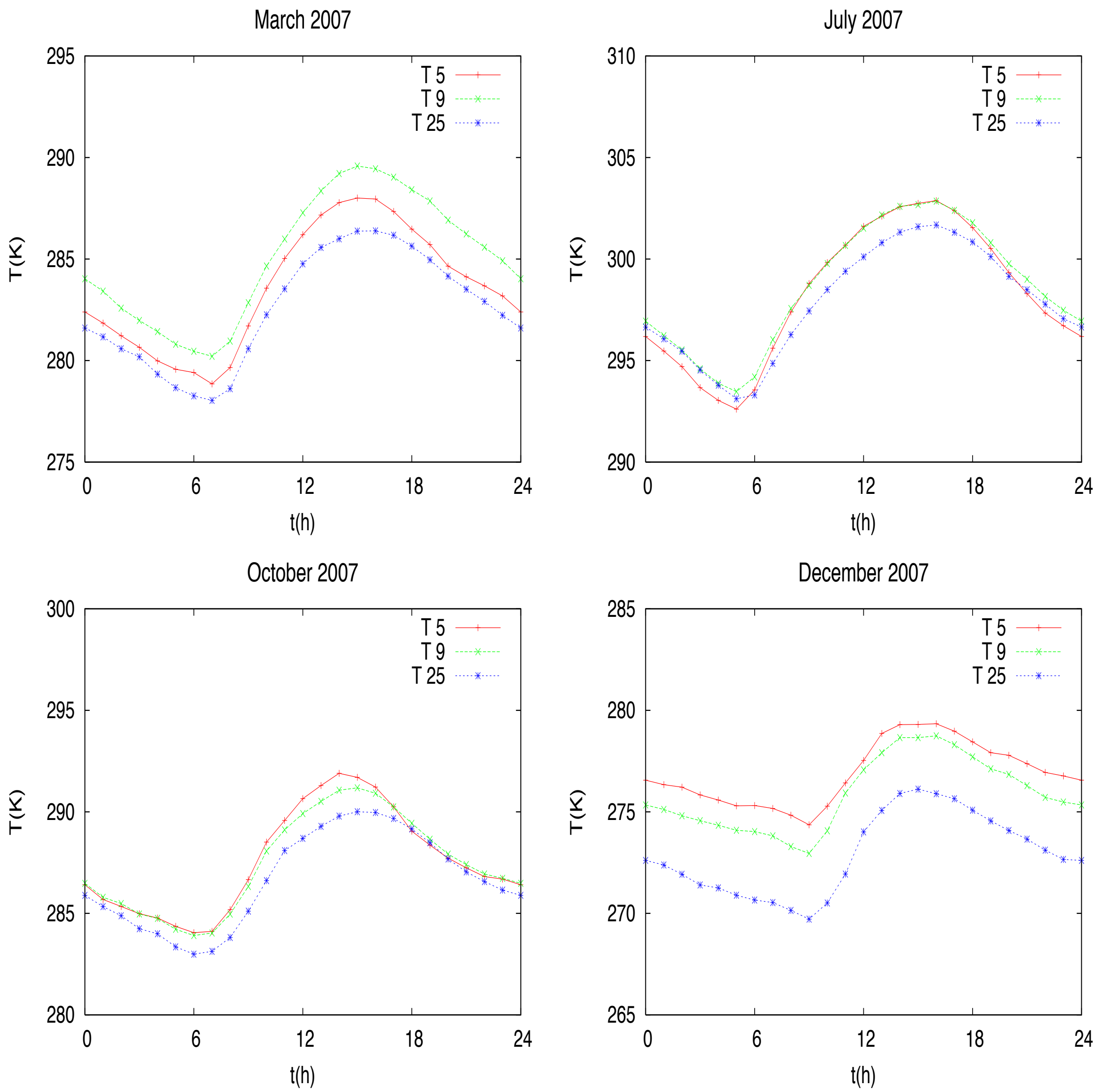

Figure 2.5: Hourly-averaged temperature for each month. In the figure the elevation of anemometers is indicated in metres.

in the graphics of the temperature of a characteristic day (figure 2.5).
The temperature decreases overall with the height, but there are some cases (March 2007 and April 2007), in which the temperature measured by anemometer at 9 m is greater than the one detected by anemometer at 5 m. Probably, these events are caused by a temperature inversion at low height; they are in large number, in fact this trend is shown in the analysis of the temperature of a typical day again.
During July 2007, August 2007 and September 2007, the differences among the three anemometers are the smallest. This is a clear sign of the enhanced atmospheric mixing, occurring mainly in summer. In other months, in particular in December 2007 and January 2008, the differences of temperature are more evident, in particular between the anemomenters at 5 m and 9 m compared to the device at 25 m. Indeed, the distance between the instruments located at 5 m and 9 m is smaller than the

distance between one of the lower anemometers and the anemometer located at 25 m.

In the analysis of the daily trend of the temperature, it is possible to observe that the variable follows the typical daily trend in the whole period. In particular, it takes smaller values in the first hours of the day and at night, whereas in the central hours of the day it has bigger values, reaching its maximum from 12 h to 18 h.

The lower values of temperature during daily trend are measured from 6 h to 10 h in the winter months, whereas during other periods of the year smaller values are present from 4 h to 8 h.

Therefore, the behaviour of hourly-averaged temperature confirms that in the trend of this variable the solar forcing is the most important one compared with other forcings.

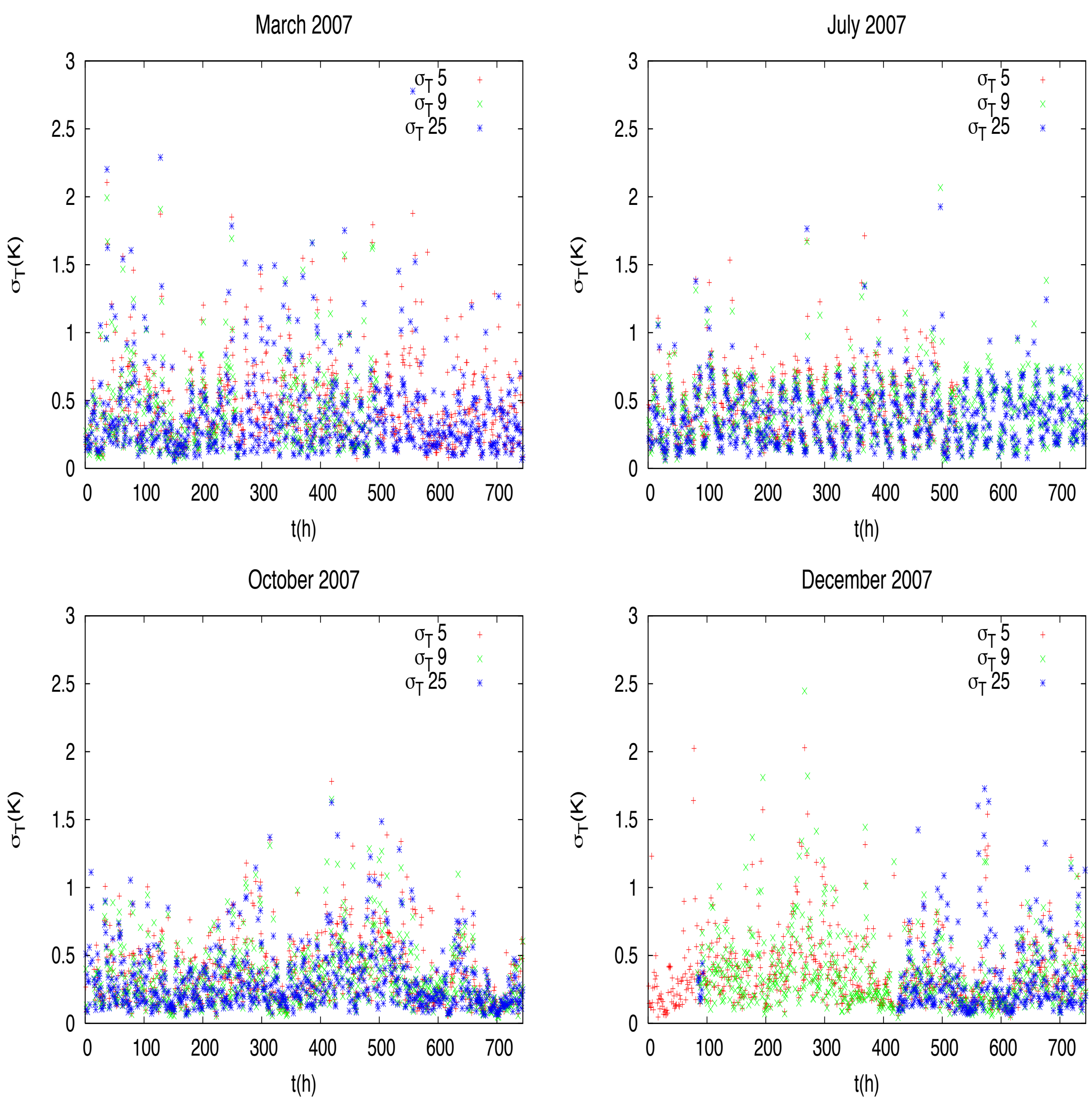

Figure 2.6: Hourly-averaged temperature standard deviation for each month. In the figure the elevation of anemometers is indicated in metres.

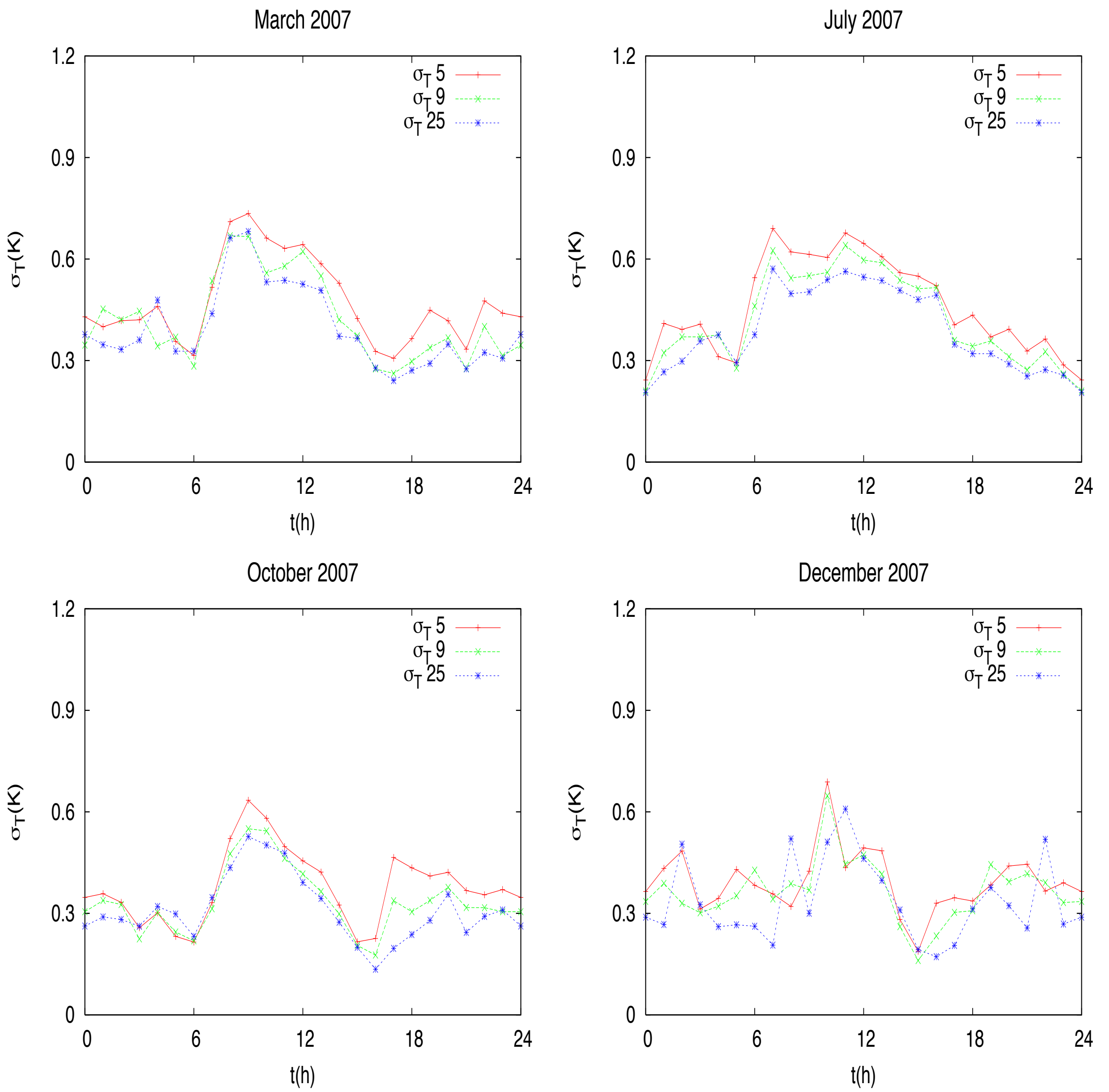

Figure 2.7: Hourly-averaged temperature standard deviation of a characteristic day for each month. In the figure the elevation of anemometers is indicated in metres.

In the analysis of standard deviation of temperature, there are not particular differences among the months. Indeed, the trends of the temperature standard deviation (figure 2.6) are similar in comparison with all months.
Comparing the trends of different anemometers, the values of this variable are often bigger for anemometers at elevation of 5 m and 9 m. The temperature measured by anemometers located at lower heights has a greater variance at lower heights, because this variable mainly depends on changes of forcing originated near the surface.
Also the hourly-averaged temperature standard deviation does not show particular differences in the months. On average, in the typical day (figure 2.7) it is greater in the central hours of the day, from 8 h to 14 h, whereas it is lower in the first and in the last hours of the day, respectively from 0 h to 6 h and from 18 h to 24 h. This

trend occurs for every device.
Therefore, the thermal turbulence existing mainly during the central hours of the day, has greater effects than the turbulence of mechanical origin, that occurs especially during the night.

2.5 Indices of atmospheric stability

The different events of atmospheric stability are characterized by relation between the environmental lapse rate $\gamma = -\frac{dT}{dz}$ and the adiabatic lapse rate γ_d, as discussed in section 1.3. The conditions of different state of atmospheric stability, explained in the previous chapter, are:

- $\gamma < \gamma_d$ for stable atmospheric stratification;
- $\gamma > \gamma_d$ for unstable atmospheric stratification;
- $\gamma = \gamma_d$ for neutral atmospheric stratification.

In my analysis three indices to characterize the atmopheric stability are calculated. They are:

- $\gamma_d - \gamma$ with $\gamma_d = 9.8 \cdot 10^{-3}\,\frac{K}{m}$;
- $\alpha = \frac{g\,(\gamma_d - \gamma)}{\overline{T}}$ with $g = 9.8\,\frac{m}{s^2}$ gravitational acceleration, $\overline{T}$ average temperature;
- $\frac{z}{L}$ with z height over the ground and L Monin-Obukhov length.

In detail, I explain here the variables present in the definitions of the indicators and the method to estimate them.
The environmental lapse rate γ is estimated as ratio of finite differences

$$\gamma = -\frac{T_i - T_j}{z_i - z_j} \tag{2.7}$$

where T_i and T_j are temperatures at the relative heigths of z_i and z_j, with (i, j)=(5, 9), (9, 25), (5, 25).
This variable is used in the computation of the first two indices ($\gamma_d - \gamma$ and α). In addition, calculating the second index, the temperature $\overline{T}$ is estimated as hourly average.
Therefore, considering the above mentioned conditions of atmospheric stability, it is possible to obtain the following relations to individuate the atmospheric stratification:

- $\gamma_d - \gamma$ and α are positive in atmosphere with stable stratification;
- $\gamma_d - \gamma$ and α are negative in atmosphere with unstable stratification;
- $\gamma_d - \gamma$ and α are equal to zero in atmosphere with neutral stratification.

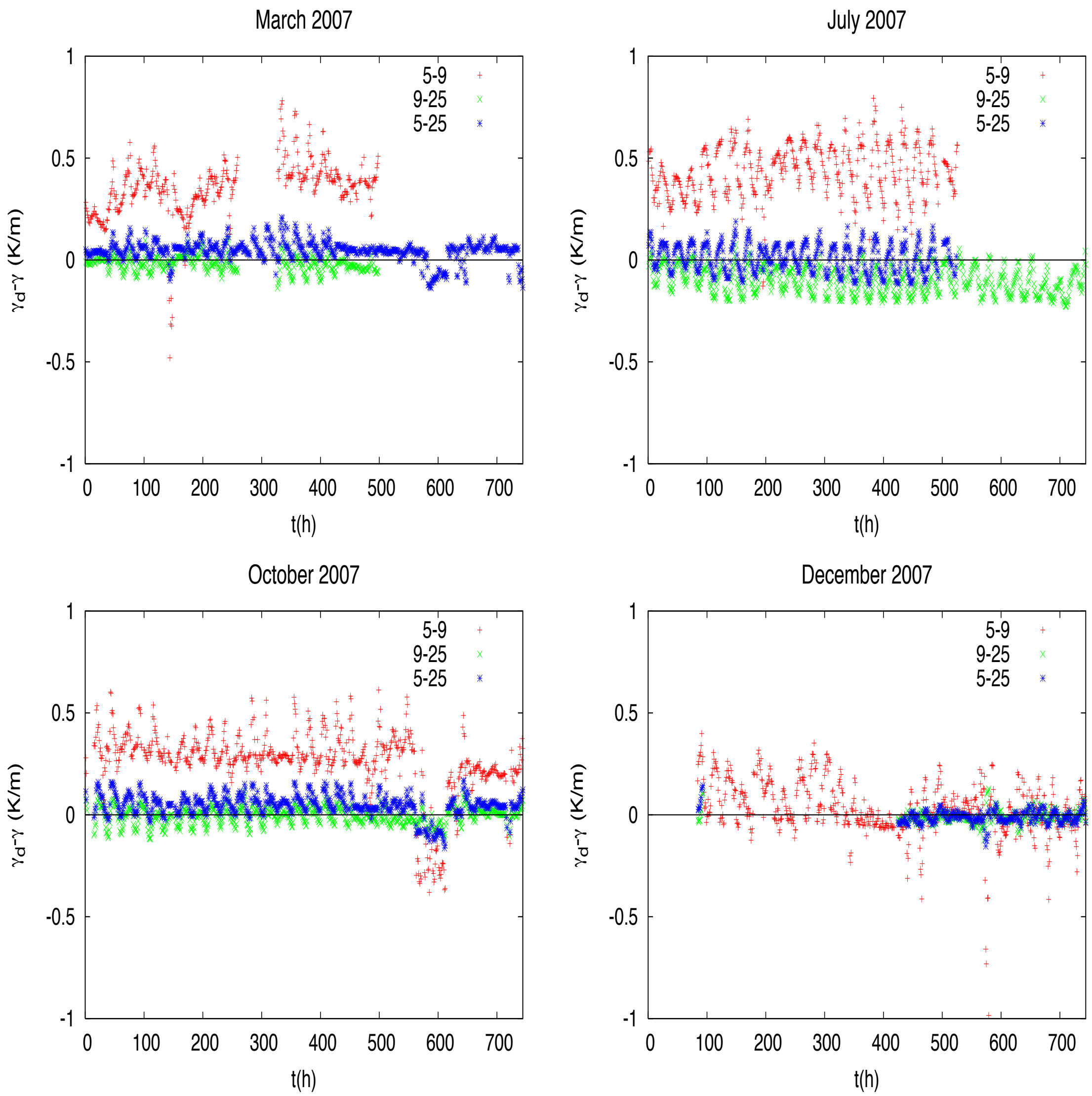

Figure 2.8: Hourly-averaged difference between adiabatic lapse rate γ_d and environmental lapse rate γ for each month. In the figure the elevation of anemometers is indicated in metres.

In particular, index α is the square of Brunt-Väisälä frequency or buoyancy frequency in the case of the stable atmospheric stratification. This frequency corresponds to the frequency at which a parcel oscillates vertically within a statically stable environment [22].
In the computation of the third indicator, the height z is substituted by the elevation of considered anemometer, and the Monin-Obukhov length L is calculated by the relation below

$$L = -\frac{\rho\, C_p\, \overline{T}\, u_*^3}{k\, g\, H_0} \tag{2.8}$$

where ρ is the density of the air , $C_p = 1005 \frac{J}{kg\,K}$ is the specific heat at constant pressure, $\overline{T}$ is the the hourly-averaged temperature, u_* is the friction velocity, $k = 0.4$

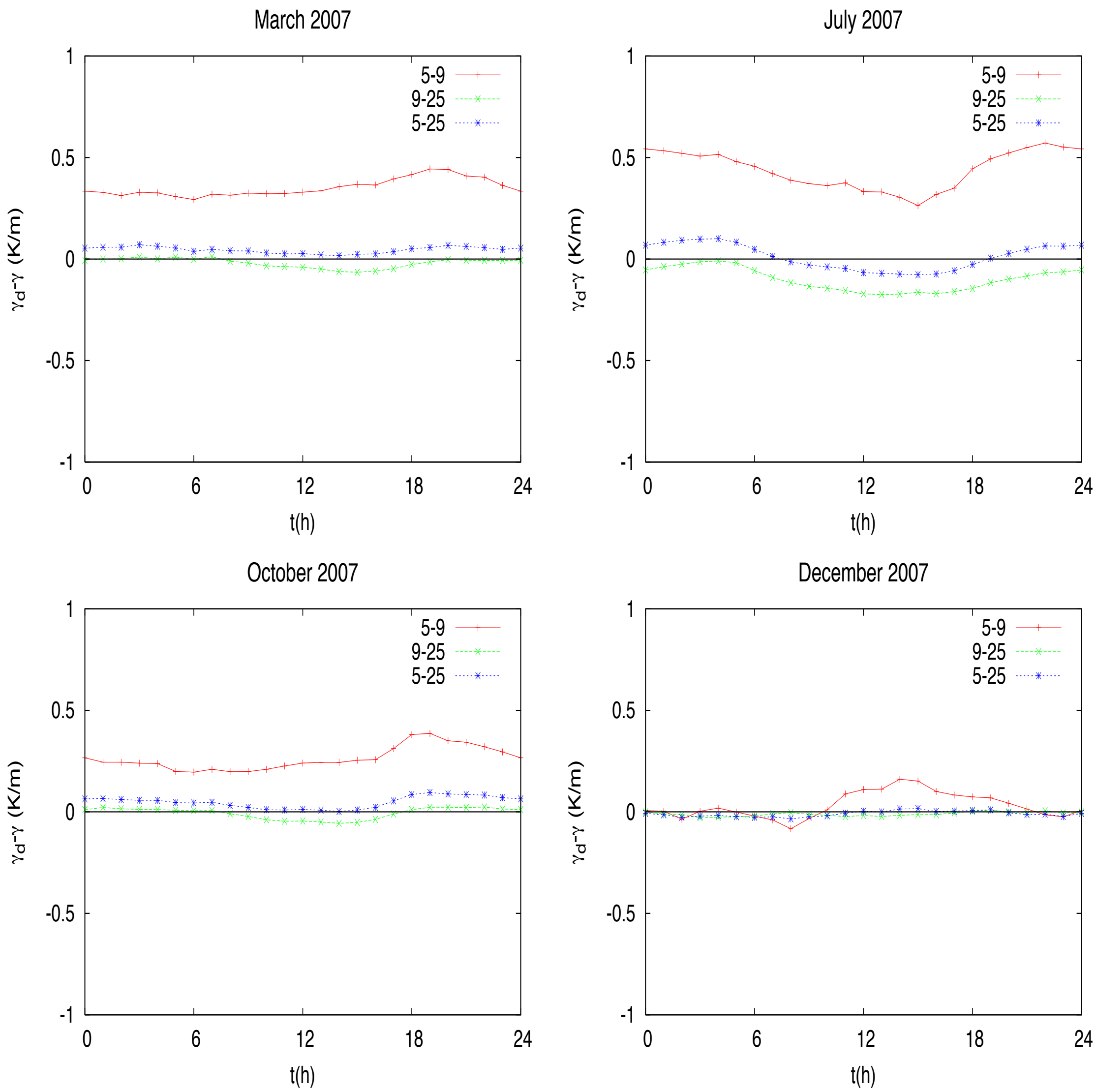

Figure 2.9: Hourly-averaged difference between adiabatic lapse rate γ_d and environmental lapse rate γ of a characteristic day for each month. In the figure the elevation of anemometers is indicated in metres.

is the Von Karman constant, $g = 9.8\,\frac{m}{s^2}$ is the gravitational acceleration and H_0 is the the sensible heat.
Replacing the expression of sensible heat H_0 (1.3) in the definition of the Monin-Obukhov length L, this parameter is calculated by the relation below

$$L = -\frac{\overline{T}\,u_*^3}{k\,g\,cov(w,T)} \tag{2.9}$$

Besides, the friction velocity u_* is estimated by the following relation

$$u_* = (cov(u,w)^2 + cov(v,w)^2)^{\frac{1}{4}} \tag{2.10}$$

where $cov(u,w)$ is the covariance between the components of wind velocity u and w, $cov(v,w)$ is the covariance between the components of wind velocity v and w [17].

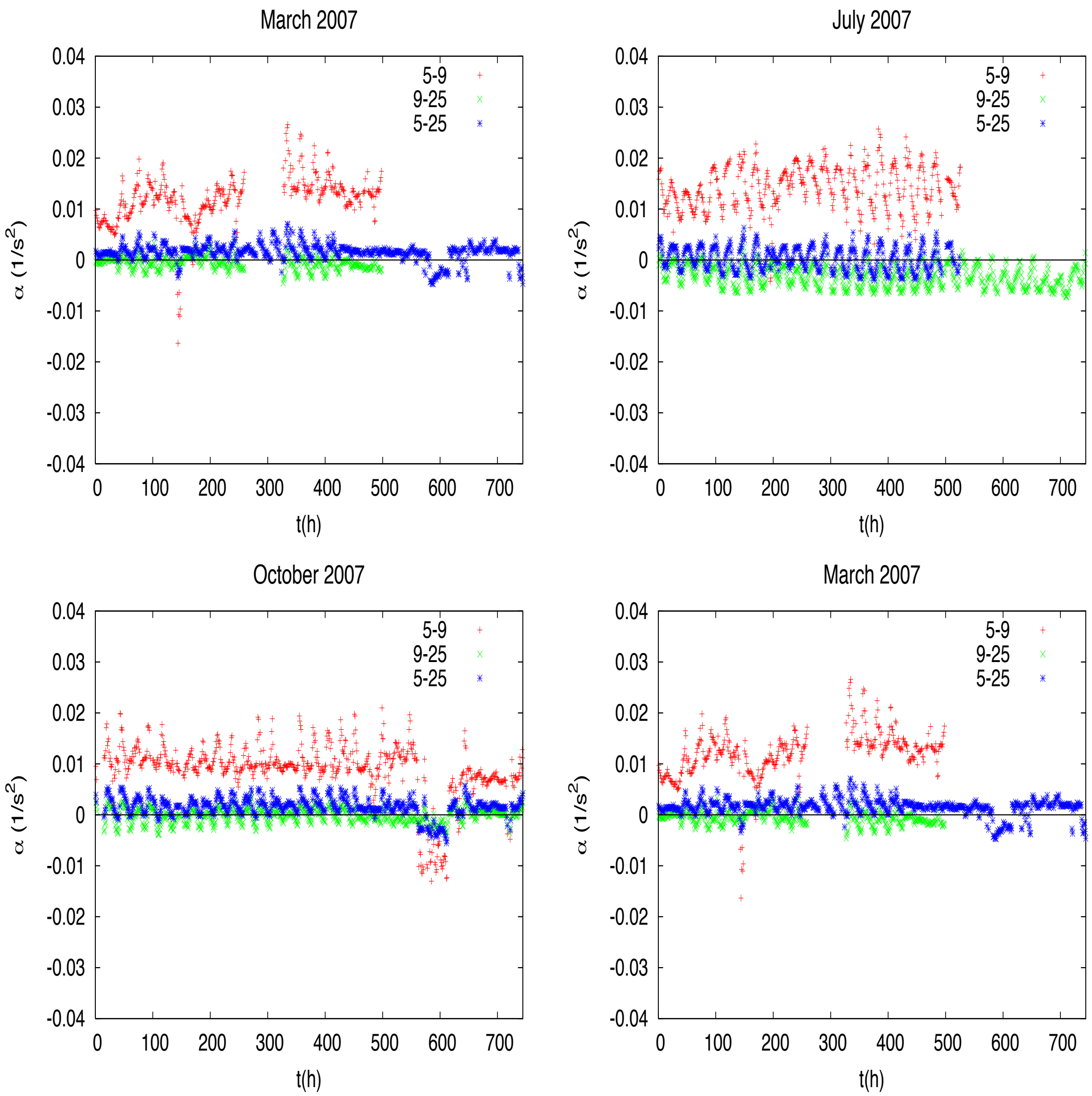

Figure 2.10: Hourly-averaged index α for each month: $\alpha = \frac{g\,(\gamma_d - \gamma)}{\overline{T}}$, with g gravitational acceleration, $\overline{T}$ hourly-averaged temperature, γ_d adiabatic lapse rate and γ environmental lapse rate. In the figure the elevation of anemometers is indicated in metres.

The marker L is a scaling parameter, in which u_* and $cov(w, T)$ are the indicators respectively of the mechanical and thermal forcings in the turbulence of the Surface Layer. In fact, L represents the altitude at which mechanical and thermal turbulence have equivalent magnitude and this value has a magnitude order equal to the one of the Surface Layer extension.
The conditions of atmospheric stability, explained in section 1.3, using the sign of H_0 or equal to $cov(w, T)$, are shortly:

- $H_0 < 0$, $cov(w, T) < 0$ for stable atmospheric stratification;
- $H_0 > 0$, $cov(w, T) > 0$ for unstable atmospheric stratification;

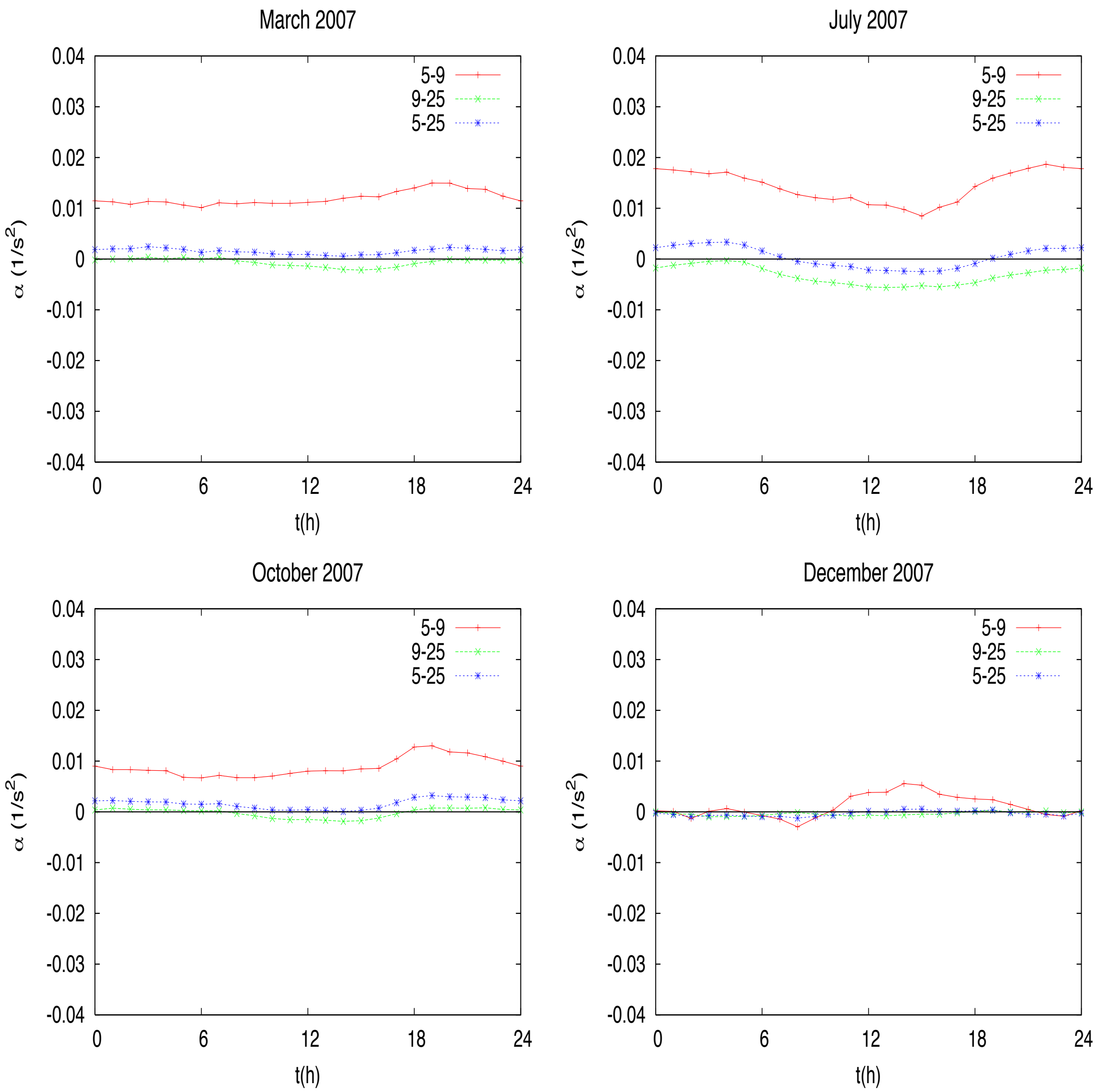

Figure 2.11: Hourly-averaged index α of a characteristic day for each month: $\alpha = \frac{g\,(\gamma_d - \gamma)}{\overline{T}}$, with g gravitational acceleration, $\overline{T}$ hourly-averaged temperature, γ_d adiabatic lapse rate and γ environmental lapse rate. In the figure the elevation of anemometers is indicated in metres.

- $H_0 = 0$, $cov(w, T) = 0$ for neutral atmospheric stratification.

Therefore, the conditions relevant to the atmospheric stability, obtained by using the indicator $\frac{z}{L}$, are as follows:

- $\frac{z}{L} > 0$ in atmosphere with stable stratification;
- $\frac{z}{L} < 0$ in atmosphere with unstable stratification;
- $\frac{z}{L} = 0$ in atmosphere with neutral stratification.

I calculate both the mean of each hourly-averaged index and the averaged index of all days of each month in order to get a typical day for all months.

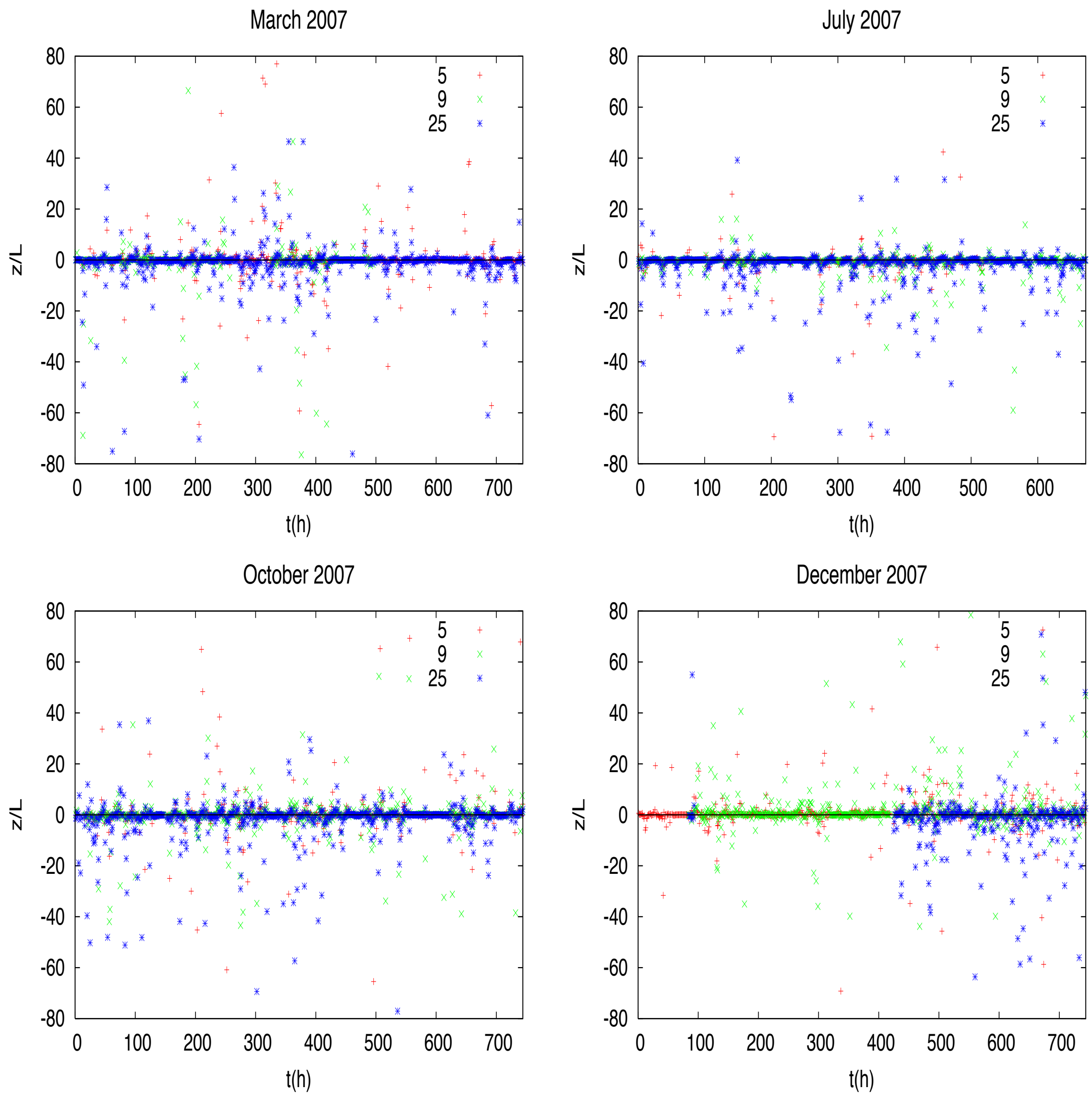

Figure 2.12: Hourly-averaged ratio of the height z to length of Monin-Obukhov L for each month. In the figure the elevation of anemometers is indicated in metres.

In the analysis of the indices, it is possible to observe, as expected, similarity between $\gamma_d - \gamma$ and α. Generally, they have a regular behaviour, both in the trends obtained by computation of these parameters for every hour of the month (figures 2.8 and 2.10) and in the trends representing of the typical day for the whole month (figures 2.9 and 2.11).
The indices estimated by means of the difference between the heights of 9 m and 25 m, 5 m and 25 m are analogous and their values are small than the ones of the index calculated by the difference between the heights of 5 m and 9 m.
These considerations are applied to the months from March 2007 to July 2007 and to months of October 2007 and November 2007. In August 2007, September 2007 and December 2007 the values of these indices, calculated between the different heights, have a small difference.

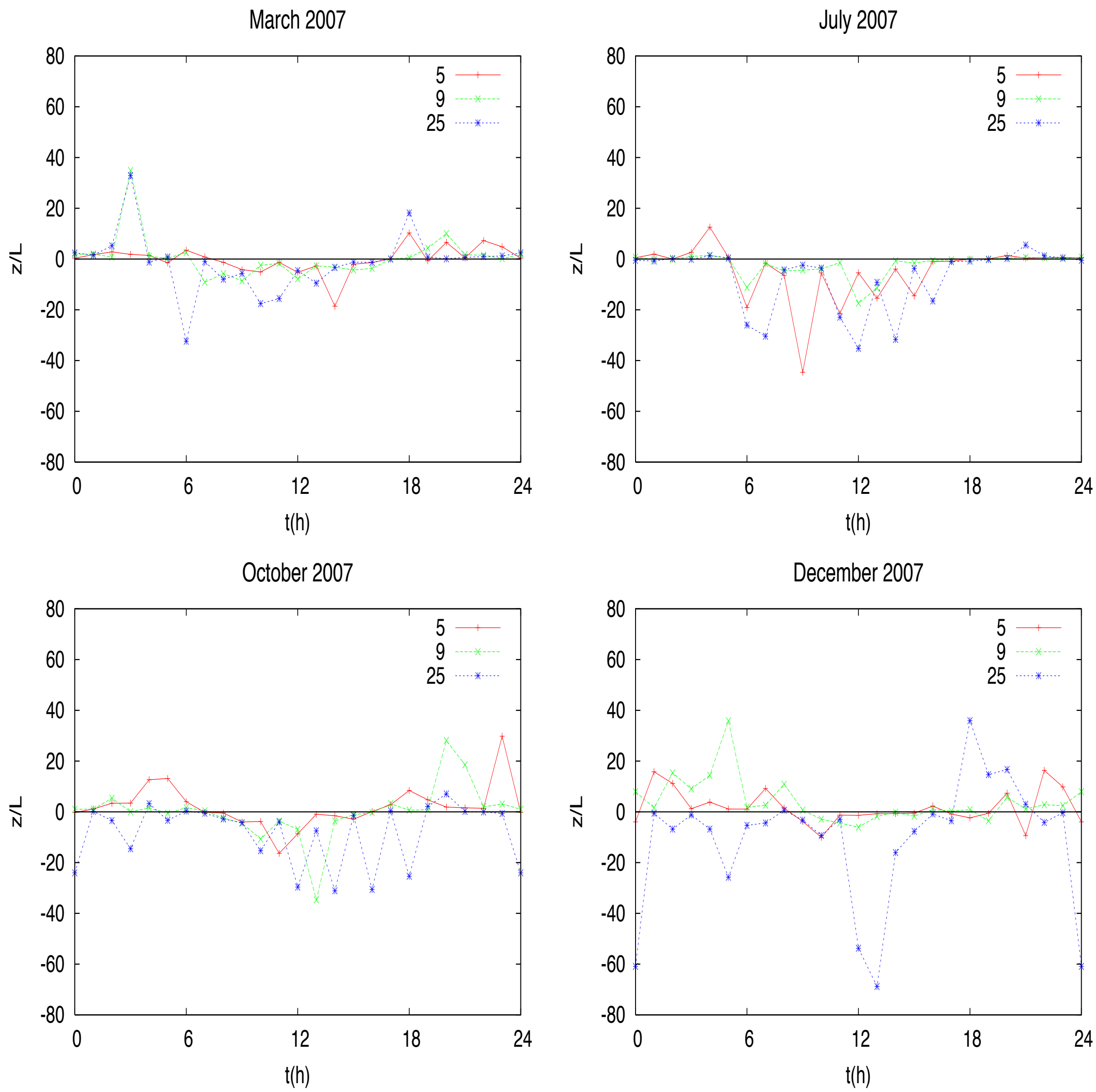

Figure 2.13: Hourly-averaged ratio of the height z to length of Monin-Obukhov L of a characteristic day for each month. In the figure the elevation of anemometers is indicated in metres.

The trend of the index $\frac{z}{L}$ shows a smaller regularity than the other indices, both in the trends obtained by computation of these parameter for every hour of the month (figure 2.12) and in the trends representing of the typical day for the whole month (figure 2.13).

On average, the condition of stable atmospheric stratification occurs more frequently during the day than at night. Events of atmospheric instability obviously have an opposite distribution.

Therefore, I choose the parameter α, similar to $\gamma_d - \gamma$, as an index of reference. In particular, α calculated by difference between the heights of 9 m and 25 m is selected, because its value is generally included between the others and it can show better the condition of atmospheric stratification.

Table 2.2: Percentage of atmospheric stability and instability events, obtained by index $\alpha = \frac{g\,(\gamma_d - \gamma)}{\overline{T}}$.

month	stability (%)	instability (%)	all events
February 2007	67.2	32.8	46800000
March 2007	27.3	72.7	30816000
April 2007	19.6	80.4	29016000
May 2007	27.9	72.1	46152000
June 2007	10.8	89.2	49896000
July 2007	7.1	92.9	51840000
August 2007	30.1	69.9	52200000
September 2007	13.2	86.8	50112000
October 2007	47.0	53.0	51768000
November 2007	43.4	56.6	29664000
December 2007	25.4	74.6	23256000
January 2008	2.0	98.0	51120000
February 2008	28.5	71.5	47664000

The cases of atmosferic stability and instability are estimated by this index (table 2.2). The number of all events is low in March 2007, April 2007, November 2007 and December 2007; while the months with a richer statistics are June 2007, July 2007, August 2007, September 2007, October 2007 and January 2008.
While for summer months this is easily explained in term of persistent convective activity, for January 2008 the frequent instability probably has a mechanically generated origin [17].
The condition of atmospheric stability is prevailing in February 2007 with a bigger percentage than 50 %; its value is great for October 2007 and November 2007, but the percentage is lower than 50 %.
The number of stable stratification events is smaller than the one of unstable stratification events: the percentage of stable stratification events is 26 % and the percentage of unstable stratification events is 74 % of the total cases.

2.6 Temperature fluctuations

The aim of my research is here to investigate the statistics of temperature fluctuations, starting from the temperatures measured by the anemometers in relation to different conditions of atmospheric stability.
Temperature fluctuations are defined here in the following way.
I define the normalized deviation from the hourly-averaged temperature as

$$\tau = \frac{T - \overline{T}}{\sigma_T} \tag{2.11}$$

where T is the value of the temperature corrected by relations (2.1)-(2.6) of section 2.4, $\overline{T}$ and σ_T are respectively the hourly-averaged temperature and its standard deviation.
The variable τ is calculated for all measurements of the dataset.
A space fluctuation, replacing the expression (1.23), is now defined as

$$\Delta\tau_{i,j} = \tau_i - \tau_j \tag{2.12}$$

with (i, j)=(5, 9), (9, 25), (5, 25) indicating the heights (in metres) of the considered anemometers.
Therefore, the relations (1.25) and (1.30) are replaced respectively by

$$\Delta_r\tau \sim r^{\beta} \tag{2.13}$$

and

$$< (\Delta_r\tau)^p >\sim r^{\zeta_p} \tag{2.14}$$

where β and ζ_p are the new exponents. The scaling exponent ζ_p substitutes ζ_p^T of section 1.8.

Table 2.3: Values of β for atmospheric instability and stability cases, individuated by atmospheric stability index α.

month	instability	stability
February 2007	0.33	0.40
March 2007	0.30	0.30
April 2007	0.33	0.33
May 2007	0.30	0.30
June 2007	0.40	0.30
July 2007	0.35	0.35
August 2007	0.40	0.40
September 2007	0.30	0.30
October 2007	0.33	0.30
November 2007	0.25	0.25
December 2007	0.15	0.20
January 2008	0.20	0.20
February 2008	0.20	0.25

The probability density function is now $P(\Delta_r\tau)$ and the relation (1.31) becomes

$$P(\Delta_r\tau) = r^{-\beta}\widetilde{P}\Big(\frac{\Delta_r\tau}{r^{\beta}}\Big) \tag{2.15}$$

where **r** is the distance between two anemometers; the value of r is 4 m when the data considered are measured by anemometers at 5 m at 9 m, it is 20 m when the

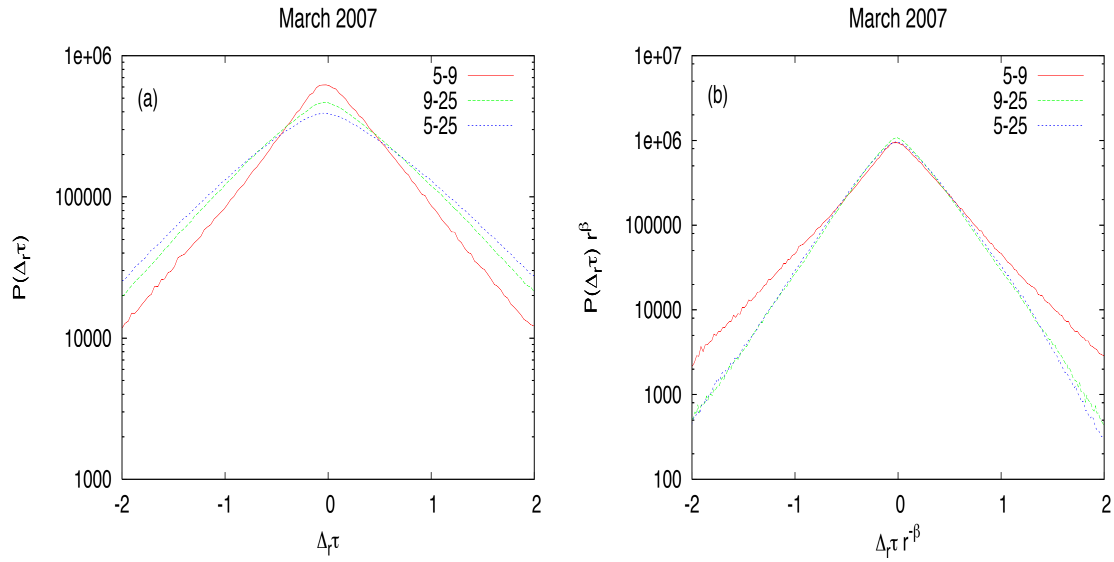

Figure 2.14: *March 2007.* Probability density function $P(\Delta_r\tau)$ of difference of τ, calculated between two anemometers located at 5 m and 9 m, at 9 m and 25 m, at 5 m and 25 m in unstable atmosphere. a) $P(\Delta_r\tau)$s are shown without rescaling. b) $P(\Delta_r\tau)$s are multiplied by the factor r^β and $\Delta_r\tau$ is multiplied by the factor $r^{-\beta}$ with r the distance between two anemometers and $\beta \sim 0.30$. In the figure the elevation of anemometers is indicated in metres.

data considered are measured by anemometer at 5 m at 25 m, and it is 16 m when the data considered are measured by anemometers at 9 m at 25 m.
Probability density functions of $\Delta_r\tau$, $P(\Delta_r\tau)$s, are analysed for the conditions of unstable atmosphere and stable atmosphere to verify the scale invariance in relation to linear behaviour of temperature fluctuation moments with low order and the intermittancy saturation in relation to behaviour of temperature fluctuation moments with high order [14].
In the study of scale invariance, as a continuation of the previous works [5] and [6], I search the positive number β such that the cores of curves, obtained by the quantities $P(\Delta_r\tau)r^\beta$ versus $r^{-\beta}$, collapse one on the other for different r.
The events are associated to the stability parameter α: $\alpha < 0$ for unstable atmosphere and $\alpha > 0$ for stable atmosphere.
The analisys is repeated for every month of the studied period.
In particular, from figure 2.14 to figure 2.17, events of atmospheric instability are presented, and in the following figures, from figure 2.18 to figure 2.21, the cases of atmospheric stability are shown. In every picture, the first graphic representation (figure (a)) is the $P(\Delta_r\tau)$ without rescaling and the second graphic representation (figure (b)) is $P(\Delta_r\tau)$ with rescaling: $P(\Delta_r\tau)r^\beta$ as a function of $\Delta_r\tau r^{-\beta}$.
The cores of $P(\Delta_r\tau)r^\beta$ collapse in a good way in the cases of the atmospheric instability and stability with different values of β. This β value changes during the months (table 2.3), but the variation of its value is very small.
In detail, the analysis of every month can be summarized as follows:

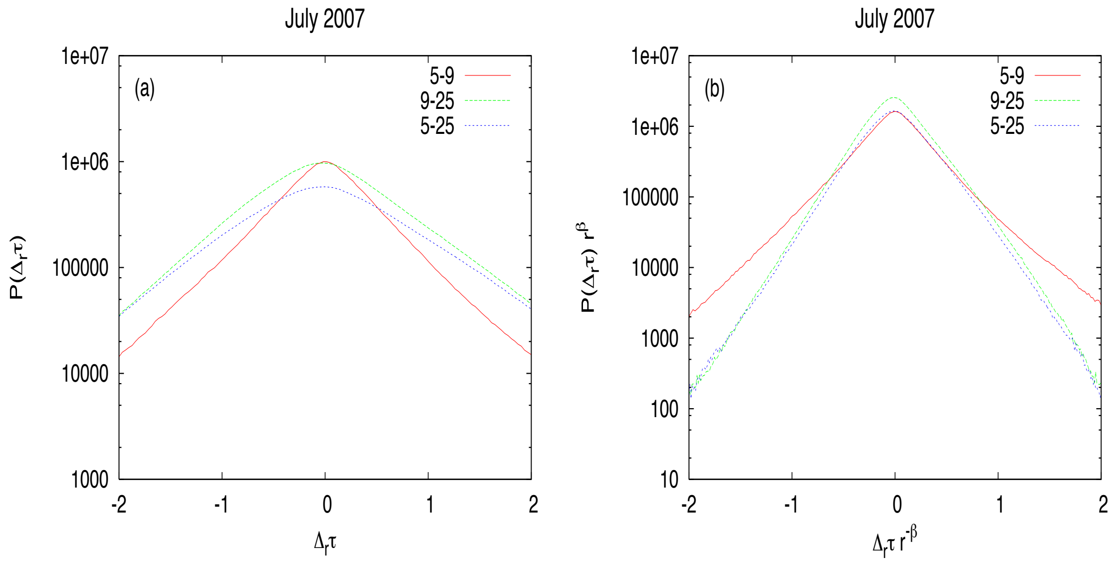

Figure 2.15: *July 2007*. Probability density function $P(\Delta_r\tau)$ of difference of τ, calculated between two anemometers located at 5 m and 9 m, at 9 m and 25 m, at 5 m and 25 m in unstable atmosphere. a) $P(\Delta_r\tau)$s are shown without rescaling. b) $P(\Delta_r\tau)$s are multiplied by the factor r^β and $\Delta_r\tau$ is multiplied by the factor $r^{-\beta}$ with r the distance between two anemometers and $\beta \sim 0.35$. In the figure the elevation of anemometers is indicated in metres.

- *February 2007*. Only two rescalings of $P(\Delta_r\tau)$, obtained by differences between 5 m and 9 m, 5 m and 25 m, collapse for $\alpha < 0$ with $\beta = 0.33$ and for $\alpha > 0$ with $\beta = 0.40$;
- *March 2007*. The rescalings of $P(\Delta_r\tau)$ collapse for $\alpha < 0$ and $\alpha > 0$ with $\beta = 0.30$;
- *April 2007*. The rescalings of $P(\Delta_r\tau)$ collapse for $\alpha < 0$ and $\alpha > 0$ with $\beta = 0.33$;
- *May 2007*. Only two rescalings of $P(\Delta_r\tau)$, obtained by differences between 5 m and 9 m, 5 m and 25 m, collapse for $\alpha < 0$ and $\alpha > 0$ with $\beta = 0.30$;
- *June 2007*. Only two rescalings of $P(\Delta_r\tau)$, obtained by differences between 5 m and 9 m, 5 m and 25 m, collapse for $\alpha < 0$ with $\beta = 0.40$ and for $\alpha > 0$ with $\beta = 0.30$;
- *July 2007*. Only two rescalings of $P(\Delta_r\tau)$, obtained by differences between 5 m and 9 m, 5 m and 25 m, collapse for $\alpha < 0$ and $\alpha > 0$ with $\beta = 0.35$;
- *August 2007*. Only two rescalings of $P(\Delta_r\tau)$, obtained by differences between 5 m and 9 m, 5 m and 25 m, collapse for $\alpha < 0$ and $\alpha > 0$ with $\beta = 0.40$;
- *September 2007*. The rescalings of $P(\Delta_r\tau)$ collapse for $\alpha < 0$ and $\alpha > 0$ with $\beta = 0.30$;

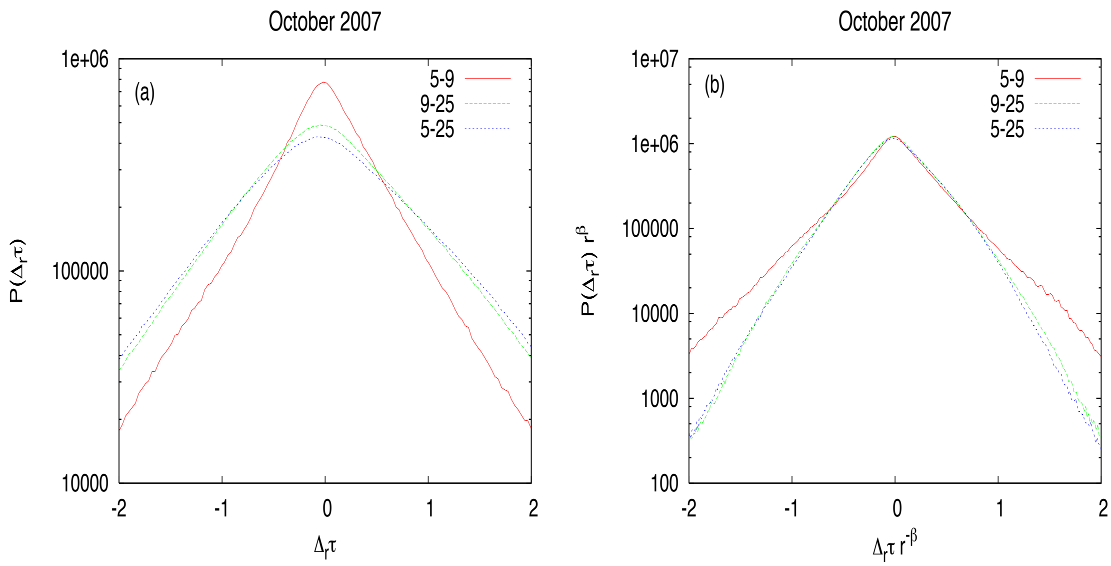

Figure 2.16: *October 2007.* Probability density function $P(\Delta_r\tau)$ of difference of τ, calculated between two anemometers located at 5 m and 9 m, at 9 m and 25 m, at 5 m and 25 m in unstable atmosphere. a) $P(\Delta_r\tau)$s are shown without rescaling. b) $P(\Delta_r\tau)$s are multiplied by the factor r^β and $\Delta_r\tau$ is multiplied by the factor $r^{-\beta}$ with r the distance between two anemometers and $\beta \sim 0.33$. In the figure the elevation of anemometers is indicated in metres.

- *October 2007.* The rescalings of $P(\Delta_r\tau)$ collapse for $\alpha < 0$ with $\beta = 0.33$ and for $\alpha > 0$ with $\beta = 0.30$;
- *November 2007.* The rescalings of $P(\Delta_r\tau)$ collapse for $\alpha < 0$ and for $\alpha > 0$ with $\beta = 0.25$;
- *December 2007.* The rescalings of $P(\Delta_r\tau)$ collapse for $\alpha < 0$ with $\beta = 0.15$ and for $\alpha > 0$ with $\beta = 0.20$;
- *January 2008.* The rescalings of $P(\Delta_r\tau)$ collapse for $\alpha < 0$ and $\alpha > 0$ with $\beta = 0.20$;
- *February 2007.* The rescalings of $P(\Delta_r\tau)$ collapse for $\alpha < 0$ with $\beta = 0.20$ and for $\alpha > 0$ with $\beta = 0.25$.

On average, there is not a difference of β values between unstable atmosphere and stable atmosphere: the value of β is 0.30 both for unstable atmosphere and stable atmosphere, in according to values obtained in previous works [5] and [6]. Besides, the variability of the exponent is similar in case of atmospheric instability and stability: the standard deviation of β is 0.08 in unstable conditions and it is 0.06 for stable conditions.
It is possible conclude that the exponent β does not depend on the value of r in the Surface Layer and it changes a little between the different cases of atmospheric stability: in different periods it is the same for unstable and stable situations.

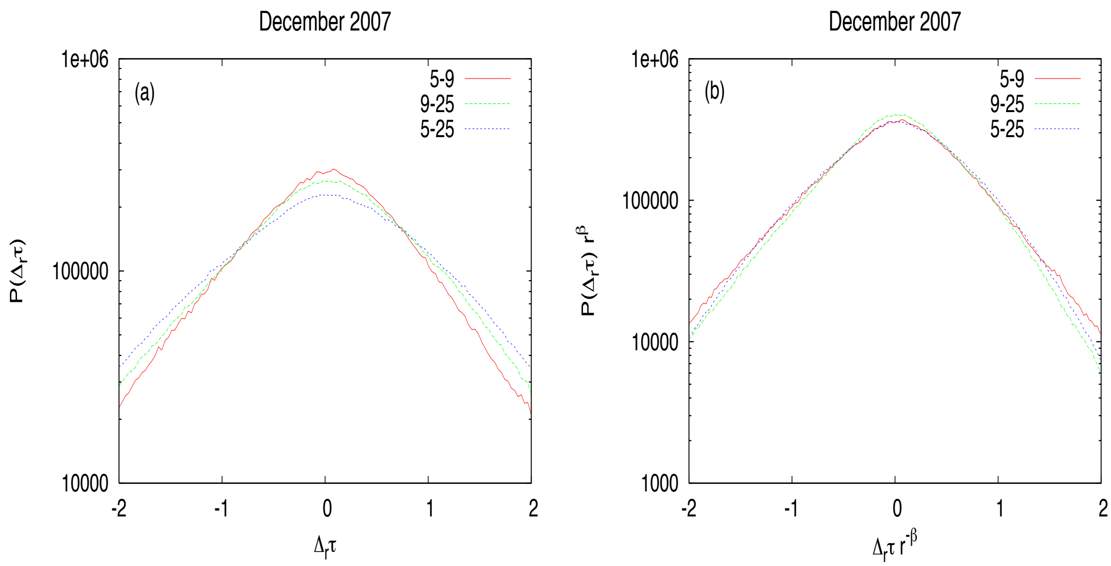

Figure 2.17: *December 2007.* Probability density function $P(\Delta_r\tau)$ of difference of τ, calculated between two anemometers located at 5 m and 9 m, at 9 m and 25 m, at 5 m and 25 m in unstable atmosphere. a) $P(\Delta_r\tau)$s are shown without rescaling. b) $P(\Delta_r\tau)$s are multiplied by the factor r^β and $\Delta_r\tau$ is multiplied by the factor $r^{-\beta}$ with r the distance between two anemometers and $\beta \sim 0.15$. In the figure the elevation of anemometers is indicated in metres.

Table 2.4: Values of ζ_∞ for atmospheric instability and stability cases, individuated by atmospheric stability index α.

month	instability	stability
February 2007	0.6	0.5
March 2007	0.6	0.6
April 2007	0.6	0.6
May 2007	0.6	0.6
June 2007	0.8	0.7
July 2007	0.7	0.6
August 2007	1.0	0.8
September 2007	0.6	0.6
October 2007	0.6	0.8
November 2007	0.6	0.5
December 2007	0.3	0.4
January 2008	0.5	0.3
February 2008	0.4	0.5

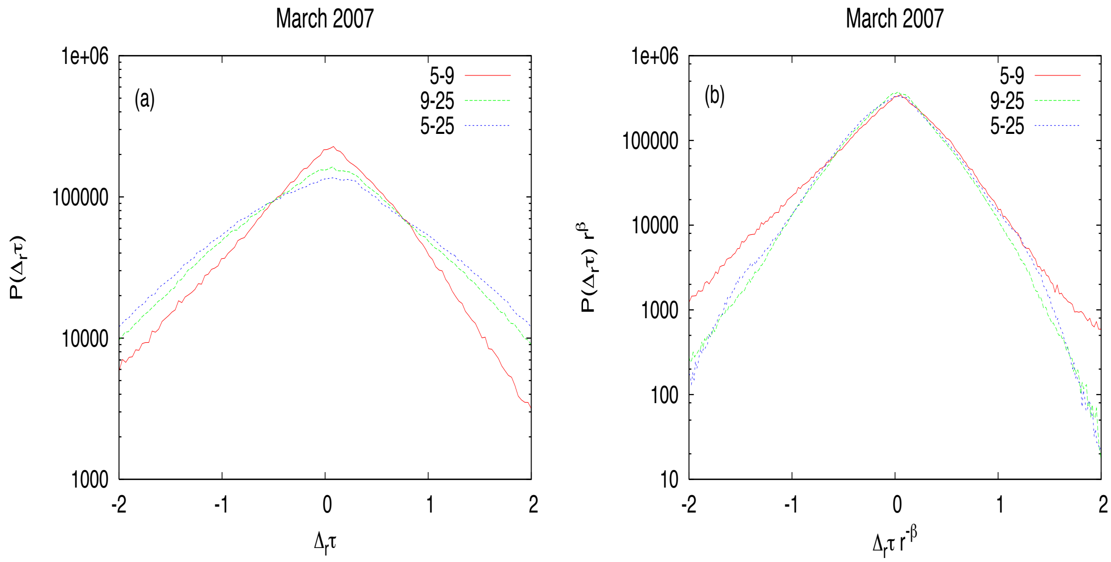

Figure 2.18: *March 2007.* Probability density function $P(\Delta_r\tau)$ of difference of τ, calculated between two anemometers located at 5 m and 9 m, at 9 m and 25 m, at 5 m and 25 m in stable atmosphere. a) $P(\Delta_r\tau)$s are shown without rescaling. b) $P(\Delta_r\tau)$s are multiplied by the factor r^β and $\Delta_r\tau$ is multiplied by the factor $r^{-\beta}$ with r the distance between two anemometers and $\beta \sim 0.30$. In the figure the elevation of anemometers is indicated in metres.

Then, I study the intermittancy saturation and I search for the positive number ζ_∞, such that the tails of the curves, obtained by $P(\Delta_r\tau)r^{-\zeta_\infty}$ versus r, collapse for different r. The method of analysis is similar to the previous one.
In particular, from figure 2.22 to figure 2.25 events of atmospheric instability are presented, and in the following figures, from figure 2.26 to figure 2.29, the cases of atmospheric stability are shown. In every picture, the first graphic representation (figure (a)) is the $P(\Delta_r\tau)$ without rescaling and the second graphic representation (figure (b)) is $P(\Delta_r\tau)$ with rescaling: $P(\Delta_r\tau)r^{-\zeta_\infty}$ as a function of $\Delta_r\tau$.
The tails of $P(\Delta_r\tau)r^{-\zeta_\infty}$ collapse in a good way in cases of atmospheric instability and stability with different values of ζ_∞. This parameter changes during the months (table 2.4), but the variation of its value is very small.
In detail, the analysis of every month can be summarized as follows:

- *February 2007.* Only two rescalings of $P(\Delta_r\tau)$, obtained by differences between 5 m and 9 m, 5 m and 25 m, collapse for $\alpha < 0$ with $\zeta_\infty = 0.6$ and $\alpha > 0$ with $\zeta_\infty = 0.5$;

- *March 2007.* The rescalings of $P(\Delta_r\tau)$ collapse for $\alpha < 0$ and $\alpha > 0$ with $\zeta_\infty = 0.6$;

- *April 2007.* The rescalings of $P(\Delta_r\tau)$ collapse for $\alpha < 0$ with $\zeta_\infty = 0.6$ and partially for $\alpha < 0$ with the same value of ζ_∞;

- *May 2007.* Only two rescalings of $P(\Delta_r\tau)$, obtained by differences between 5

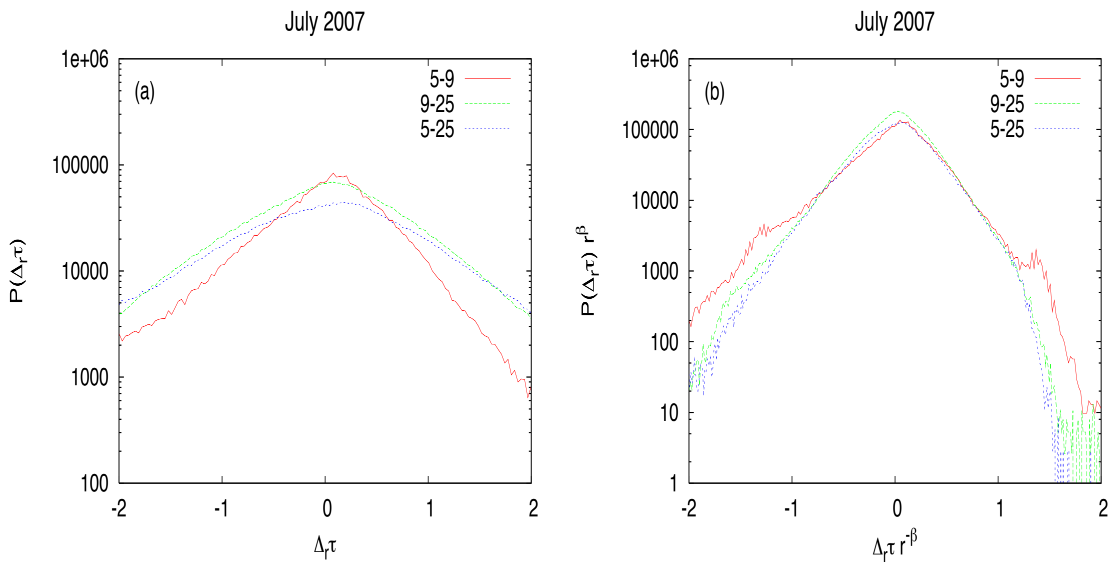

Figure 2.19: *July 2007.* Probability density function $P(\Delta_r\tau)$ of difference of τ, calculated between two anemometers located at 5 m and 9 m, at 9 m and 25 m, at 5 m and 25 m in stable atmosphere. a) $P(\Delta_r\tau)$s are shown without rescaling. b) $P(\Delta_r\tau)$s are multiplied by the factor r^{β} and $\Delta_r\tau$ is multiplied by the factor $r^{-\beta}$ with r the distance between two anemometers and $\beta \sim 0.35$. In the figure the elevation of anemometers is indicated in metres.

m and 9 m, 5 m and 25 m, collapse for $\alpha < 0$ with $\zeta_\infty = 0.6$; all the rescalings of $P(\Delta\tau)$ for $\alpha < 0$ collapse with $\zeta\infty = 0.6$;

- *June 2007.* Only two rescalings of $P(\Delta_r\tau)$, obtained by differences between 5 m and 9 m, 5 m and 25 m, collapse for $\alpha < 0$ with $\zeta_\infty = 0.8$ and partially for $\alpha > 0$ with $\zeta_\infty = 0.7$;

- *July 2007.* The rescalings of $P(\Delta_r\tau)$ collapse for $\alpha < 0$ with $\zeta_\infty = 0.7$ and partially for $\alpha > 0$ with $\zeta_\infty = 0.6$;

- *August 2007.* The rescalings of $P(\Delta_r\tau)$ collapse for $\alpha < 0$ with $\zeta_\infty = 1.0$ and $\alpha > 0$ with $\zeta_\infty = 0.8$;

- *September 2007.* The rescalings of $P(\Delta_r\tau)$ collapse for $\alpha < 0$ with $\zeta_\infty = 0.6$ and partially for $\alpha > 0$ with the same value of ζ_∞;

- *October 2007.* The rescalings of $P(\Delta_r\tau)$ collapse for $\alpha < 0$ with $\zeta\infty = 0.6$ and for $\alpha > 0$ with $\zeta_\infty = 0.8$;

- *November 2007.* The rescalings of $P(\Delta_r\tau)$ collapse for $\alpha < 0$ with $\zeta_\infty = 0.6$ and partially for $\alpha > 0$ with $\zeta_\infty = 0.5$;

- *December 2007.* The rescalings of $P(\Delta_r\tau)$ collapse for $\alpha < 0$ with $\zeta_\infty = 0.3$ and for $\alpha > 0$ with $\zeta_\infty = 0.4$;

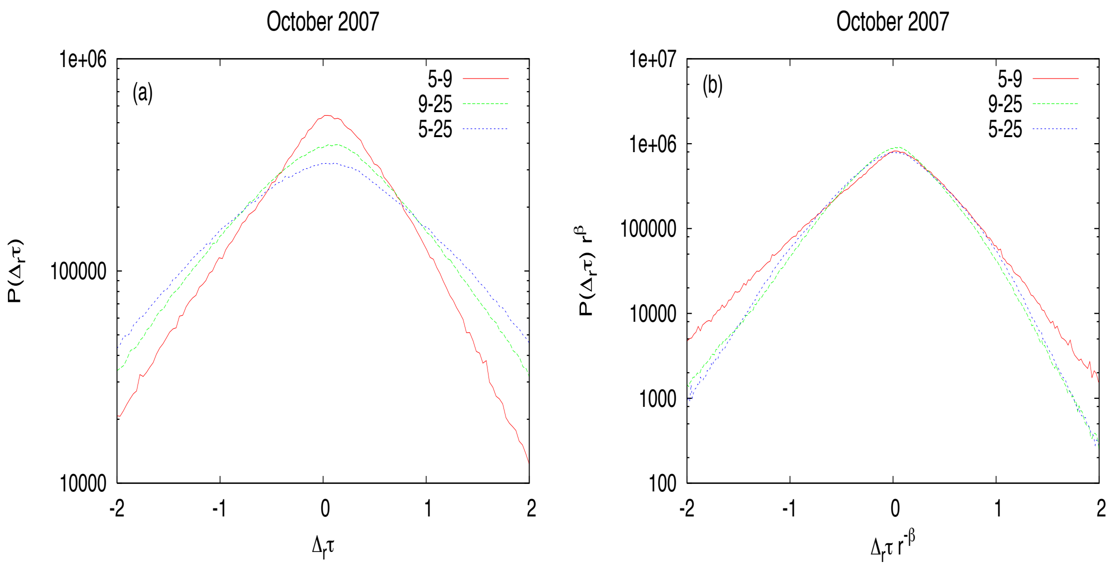

Figure 2.20: *October 2007.* Probability density function $P(\Delta_r\tau)$ of difference of τ, calculated between two anemometers located at 5 m and 9 m, at 9 m and 25 m, at 5 m and 25 m in stable atmosphere. a) $P(\Delta_r\tau)$s are shown without rescaling. b) $P(\Delta_r\tau)$s are multiplied by the factor r^β and $\Delta_r\tau$ is multiplied by the factor $r^{-\beta}$ with r the distance between two anemometers and $\beta \sim 0.30$. In the figure the elevation of anemometers is indicated in metres.

- *January 2008.* The rescalings of $P(\Delta_r\tau)$ collapse for $\alpha < 0$ with $\zeta_\infty = 0.5$ and partially for $\alpha > 0$ with $\zeta_\infty = 0.3$;

- *February 2008.* The rescalings of $P(\Delta_r\tau)$ collapse for $\alpha < 0$ with $\zeta_\infty = 0.4$ and partially for $\alpha > 0$ with $\zeta_\infty = 0.5$.

On average, the value of ζ_∞ is 0.6 both for unstable atmosphere and stable atmosphere, according to the values obtained in precedent works [5] and [6]. The variability of the exponent is greater in case of instability than in case of stability: the standard deviation of ζ_∞ is 0.2 in unstable conditions and it is 0.1 for stable conditions.
Like β, the exponent ζ_∞ does not depend on the value of r in a Surface Layer and it changes a little between the different cases of stability atmosphere: in various period it is the same for unstable and stable atmosphere.
Finally, about the connection between the statistics of temperature fluctuations and geometry (section 1.8.3), I calculate the fractal dimension D_F for each set containing the strong temperature fluctuations by the exponent ζ_∞. Its value can be obtained by relation 1.37 and it is about 2.4. Similar to the scaling exponent ζ_∞, the value of this parameter is indipendent from the conditions of atmospheric stability.

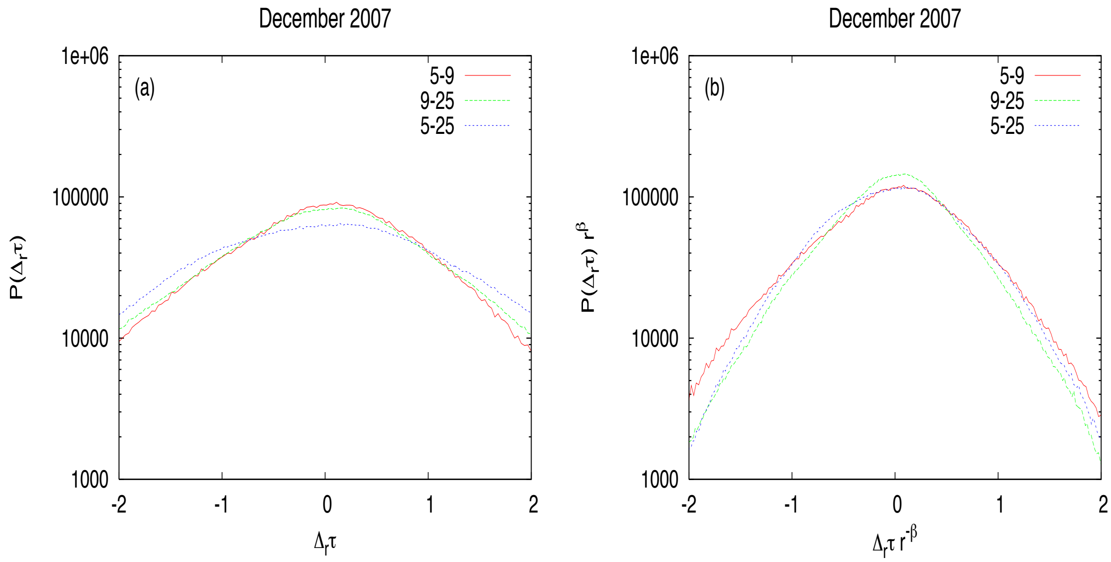

Figure 2.21: *December 2007.* Probability density function $P(\Delta_r\tau)$ of difference of τ, calculated between two anemometers located at 5 m and 9 m, at 9 m and 25 m, at 5 m and 25 m in stable atmosphere. a) $P(\Delta_r\tau)$s are shown without rescaling. b) $P(\Delta_r\tau)$s are multiplied by the factor r^{β} and $\Delta_r\tau$ is multiplied by the factor $r^{-\beta}$ with r the distance between two anemometers and $\beta \sim 0.20$. In the figure the elevation of anemometers is indicated in metres.

2.7 Conclusion

In the first analyis, I studied the daily trends of the meteorological variables of Reynolds number, temperature and atmospheric stability indicators. I chose the index to show conditions of atmospheric stability and subsequently I examined the statistics of temperature fluctuations.
In the study of temperature fluctuations statistics the scaling exponents are identified in relation with conditions of atmospheric stability.
The trends of Reynolds numbers and temperature show that the solar daily cycle influences these physical variables, used in meteorological studies. As expected, it is possible to notice that the turbulence, examined by Reynolds number, is characterized by two aspects, mechanical and thermal. Both of them are mainly connected with the daily trend of this variable. Similar behaviours are underlined by the values of Reynolds number obtained from the measurements of each anemometer and in particular using the data of the instrument at the highest elevation.
The temperature follows a behaviour analogous to Reynolds number one. The differences among these variables, obtained from the measurements of anemometers at different heights, decrease partially in the spring and summer months; during this period the atmosphere is particularly well mixed and it is possible to observe bigger values of Reynolds number.
The behaviour of atmospheric stability index, α parameter, confirms this hypothesis. In fact, it takes larger values in summer months and smaller in winter ones,

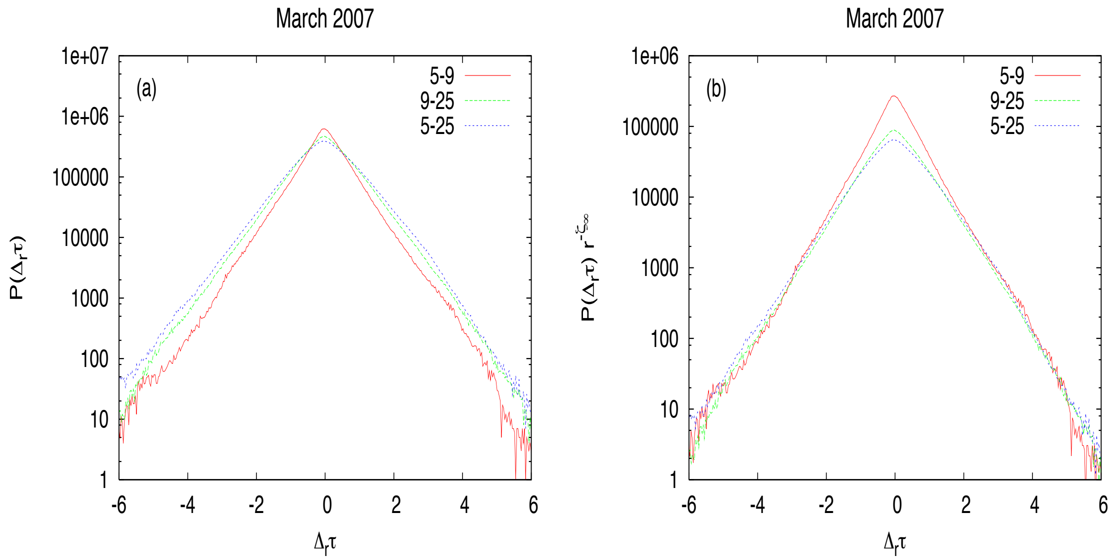

Figure 2.22: *March 2007.* Probability density function $P(\Delta_r\tau)$ of difference of τ, calculated between two anemometers located at 5 m and 9 m, at 9 m and 25 m, at 5 m and 25 m in unstable atmosphere. a) $P(\Delta_r\tau)$s are shown without rescaling. b) $P(\Delta_r\tau)$s are multiplied by the factor $r^{-\zeta_\infty}$ with r the distance between two anemometers and $\zeta_\infty \sim 0.6$. In the figure the elevation of anemometers is indicated in metres.

with the only exception of January 2008. In this winter month, the turbulence is supposed to have an essentially mechanical nature and it is possible to think that this form of turbulence determines considerable effects on the value of atmospheric stability indicator.
Moreover, it is possible observe that atmospheric turbulence and stability follows the daily cicle. In particular, the turbulence of thermal origin is more frequent if it is compared to the one of mechanical origin. It is identified by smaller values of stability index during the hours around midday and in the first hours of the afternoon. It is verified especially during spring and summer months.
The indicator of atmospheric stability was selected among various parameters, considering the daily cycle, in fact the chosen index follows the expected daily trend. Furthermore, it permits to observe that the frequency of atmospheric instability conditions is greater than the one of atmospheric stability conditions. Indeed, the effects of thermal and mechanical turbulence existing in various meteorological situations, influence the values of atmospheric stability index and this allows to conclude that the situations of unstable stratification of atmosphere are more frequent than the ones of stable atmospheric stratification.
In the analysis of the temperature fluctuations, I considered the distinction between the atmosphere with stable stratification and the one with unstable stratification. The statistics for the study of stable atmosphere counts a smaller number of events than the one of unstable atmosphere; but the dataset is very great and this allows to use enough data for a statistical study of both configurations of atmospheric strati-

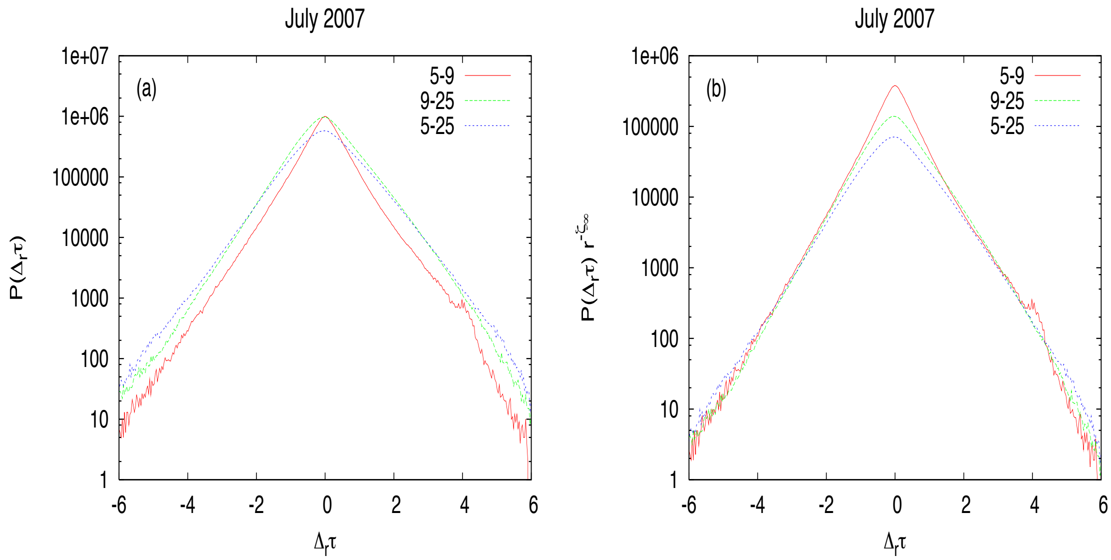

Figure 2.23: *July 2007.* Probability density function $P(\Delta_r\tau)$ of difference of τ, calculated between two anemometers located at 5 m and 9 m, at 9 m and 25 m, at 5 m and 25 m in unstable atmosphere. a) $P(\Delta_r\tau)$s are shown without rescaling. b) $P(\Delta_r\tau)$s are multiplied by the factor $r^{-\zeta_\infty}$ with r the distance between two anemometers and $\zeta_\infty \sim 0.7$. In the figure the elevation of anemometers is indicated in metres.

fication.
In this investigation I was able to find scaling characteristics previously elaborated by numerical experiments about atmosphere with unstable stratification [5], [6]. In my analysis, I could confirm these scaling properties for unstable atmosphere and moreover I also extended them to the atmosphere with stable stratification, using a dataset with a large number of measurements of temperature.
Both weak and large temperature fluctuations verify the scaling properties obtained by numerical elaborations, as mentioned above.
In particular, I verified the property of scale invariance for the small temperature fluctuation by searching for appropriate exponent β. Its average value has not considerable difference between the events of unstable and stable atmospheric stratification. I found $\beta = 0.30$ for unstable and stable atmosphere. This value is consistent with the scaling exponent individuated by the precedent computational experiments.
Therefore, it is possible to conclude that for weak temperature fluctuations, the elaborations of data measured and the ones of previous numerical computations follow the Theory KOC51. Both analyses provide a similar scaling exponent, and in my research I verified that it does not depend on conditions of atmospheric stability.
Besides, for strong temperature fluctuations I found a scaling exponent ζ_∞, that allows to affirm that the saturation of intermittency is verified by means of direct measurements for both unstable and stable atmospheric stratification.
For both atmospheric configurations, I found the same average value of scaling

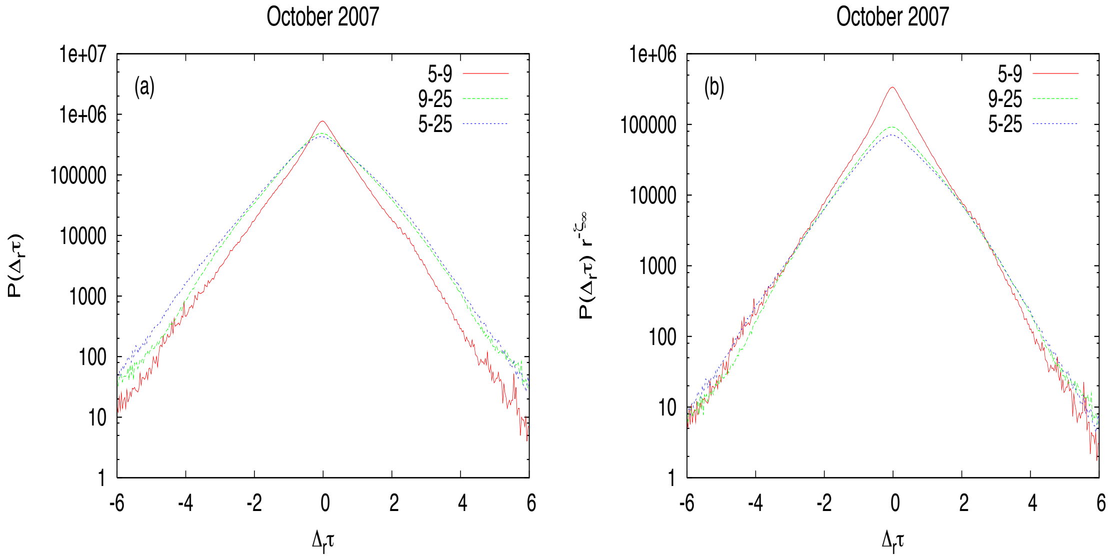

Figure 2.24: *October 2007.* Probability density function $P(\Delta_r\tau)$ of difference of τ, calculated between two anemometers located at 5 m and 9 m, at 9 m and 25 m, at 5 m and 25 m in unstable atmosphere. a) $P(\Delta_r\tau)$s are shown without rescaling. b) $P(\Delta_r\tau)$s are multiplied by the factor $r^{-\zeta_\infty}$ with r the distance between two anemometers and $\zeta_\infty \sim 0.6$. In the figure the elevation of anemometers is indicated in metres.

exponent $\zeta_\infty = 0.6$, that is compatible with the value computed by numerical elaborations.

Hence, it is possible to conclude that the large temperature fluctuations have an opposite behaviour from the one of small temperature fluctuations. For the large temperature fluctuations, the elaborations of measured data and the ones of numerical computations do not follow the Theory KOC51. Both analyses permit to underline the phenomenon of intermittency saturation and they provide a similar scaling exponent, and in my research I verified that it does not depend on the conditions of atmospheric stability.

Furthermore, the fractal dimension of set containing the strong temperature fluctuations derived by the scaling exponent of intermittency saturation, does not depend on the stability conditions of atmospheric stratification. Its value is $D_F = 2.4$ and it is consistent with the one found in previous works.

As a conclusion of my research, I can state that the exponent β and ζ_∞, that are characteristics respectively of the weak and strong temperature fluctuations, are indipendent from the conditions of atmospheric stability. Consequently, they can be considered as a property of the layer of atmosphere near Earth's surface.

As to the connection between the temperature fluctuations and geometry of the flow, the latest assertion suggests to consider the field of temperature fluctuation as bifractal object. It is the simplest multifractal object, by which it is possible to describe the geometrical characteristic of atmospheric turbulence.

This result is obtained using measurement in Surface Layer, but it could be inter-

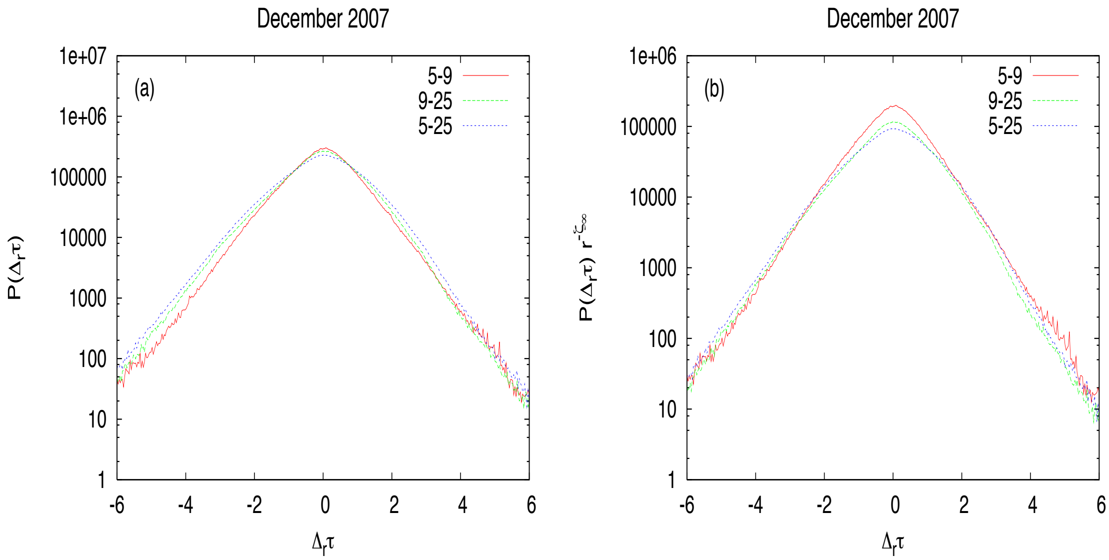

Figure 2.25: *December 2007.* Probability density function $P(\Delta_r \tau)$ of difference of τ, calculated between two anemometers located at 5 m and 9 m, at 9 m and 25 m, at 5 m and 25 m in unstable atmosphere. a) $P(\Delta_r \tau)$s are shown without rescaling. b) $P(\Delta_r \tau)$s are multiplied by the factor $r^{-\zeta_\infty}$ with r the distance between two anemometers and $\zeta_\infty \sim 0.3$. In the figure the elevation of anemometers is indicated in metres.

esting to have further measured data at a higher elevation and to verify that this statement can be extrapolated to every heights of Planetary Boundary Layer, using direct measurement in a way similar to my analysis.

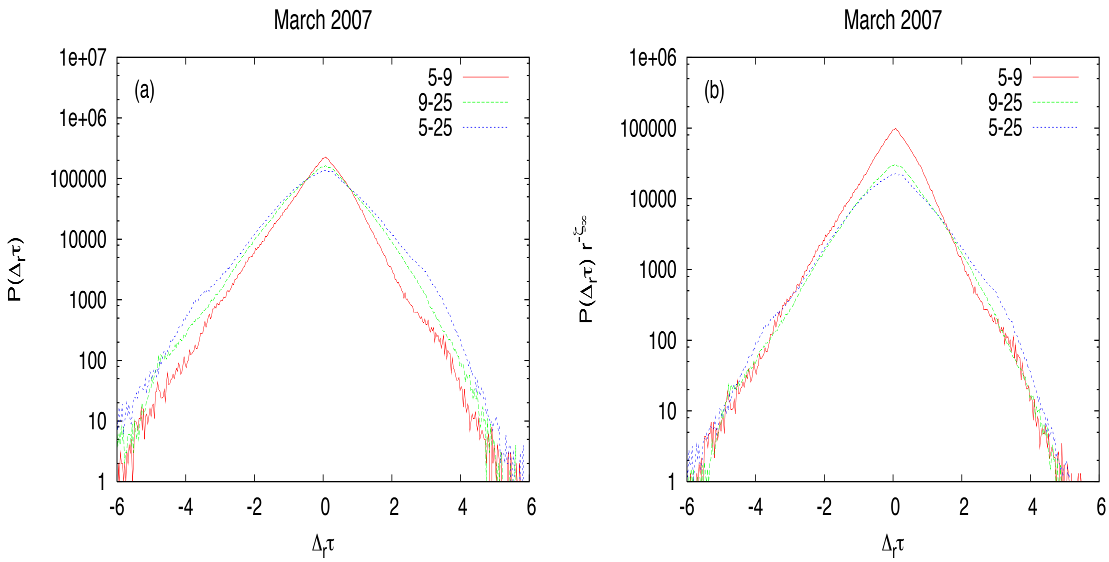

Figure 2.26: *March 2007.* Probability density function $P(\Delta_r\tau)$ of difference of τ, calculated between two anemometers located at 5 m and 9 m, at 9 m and 25 m, at 5 m and 25 m in stable atmosphere. a) $P(\Delta_r\tau)$s are shown without rescaling. b) $P(\Delta_r\tau)$s are multiplied by the factor $r^{-\zeta_\infty}$ with r the distance between two anemometers and $\zeta_\infty \sim 0.6$. In the figure the elevation of anemometers is indicated in metres.

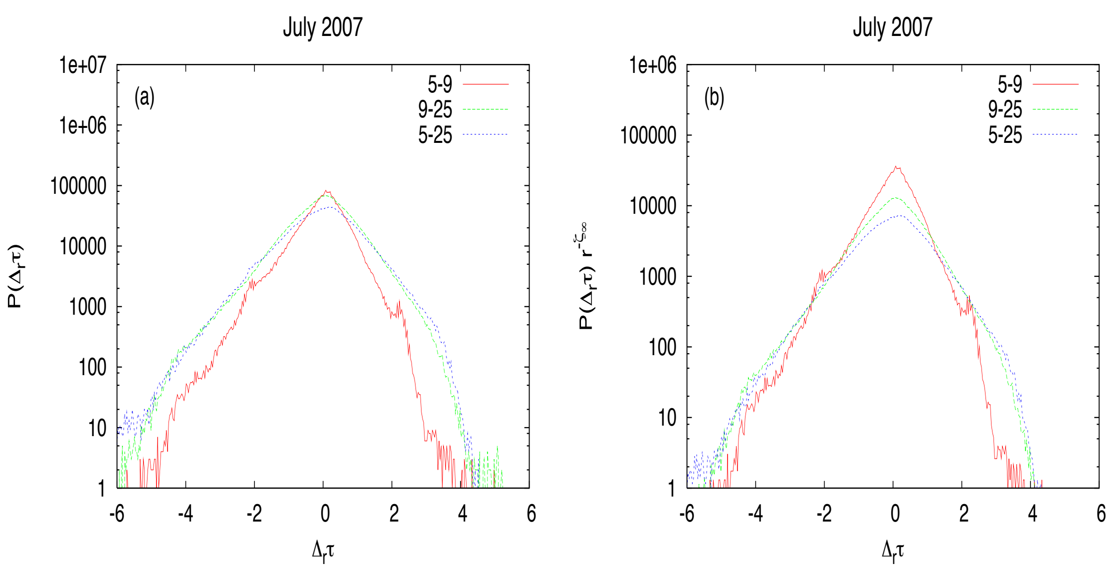

Figure 2.27: *July 2007.* Probability density function $P(\Delta_r\tau)$ of difference of τ, calculated between two anemometers located at 5 m and 9 m, at 9 m and 25 m, at 5 m and 25 m in stable atmosphere. a) $P(\Delta_r\tau)$s are shown without rescaling. b) $P(\Delta_r\tau)$s are multiplied by the factor $r^{-\zeta_\infty}$ with r the distance between two anemometers and $\zeta_\infty \sim 0.6$. In the figure the elevation of anemometers is indicated in metres.

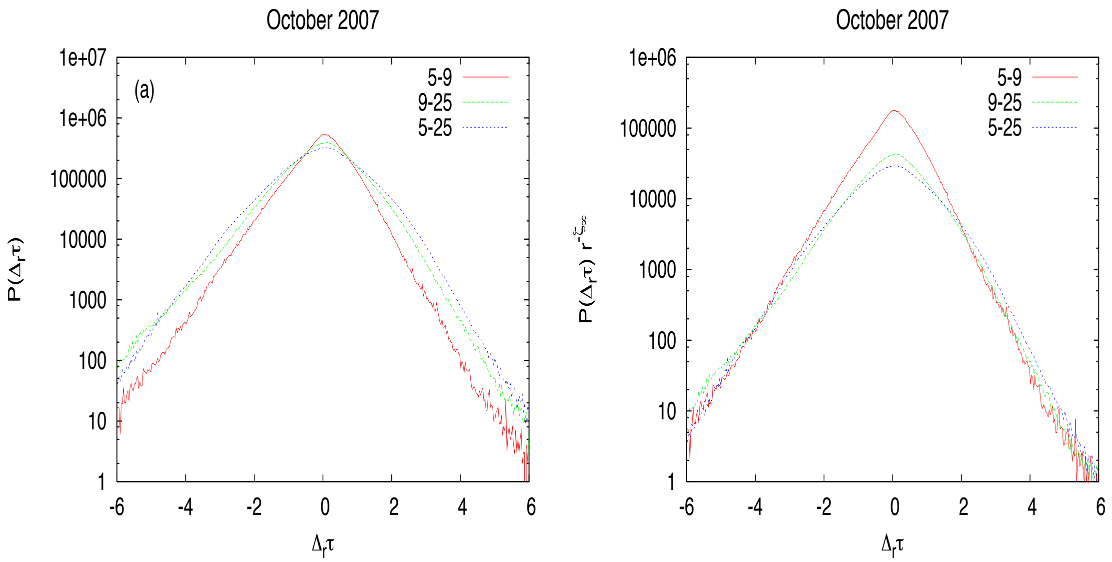

Figure 2.28: *October 2007.* Probability density function $P(\Delta_r\tau)$ of difference of τ, calculated between two anemometers located at 5 m and 9 m, at 9 m and 25 m, at 5 m and 25 m in stable atmosphere. a) $P(\Delta_r\tau)$s are shown without rescaling. b) $P(\Delta_r\tau)$s are multiplied by the factor $r^{-\zeta_\infty}$ with r the distance between two anemometers and $\zeta_\infty \sim 0.8$. In the figure the elevation of anemometers is indicated in metres.

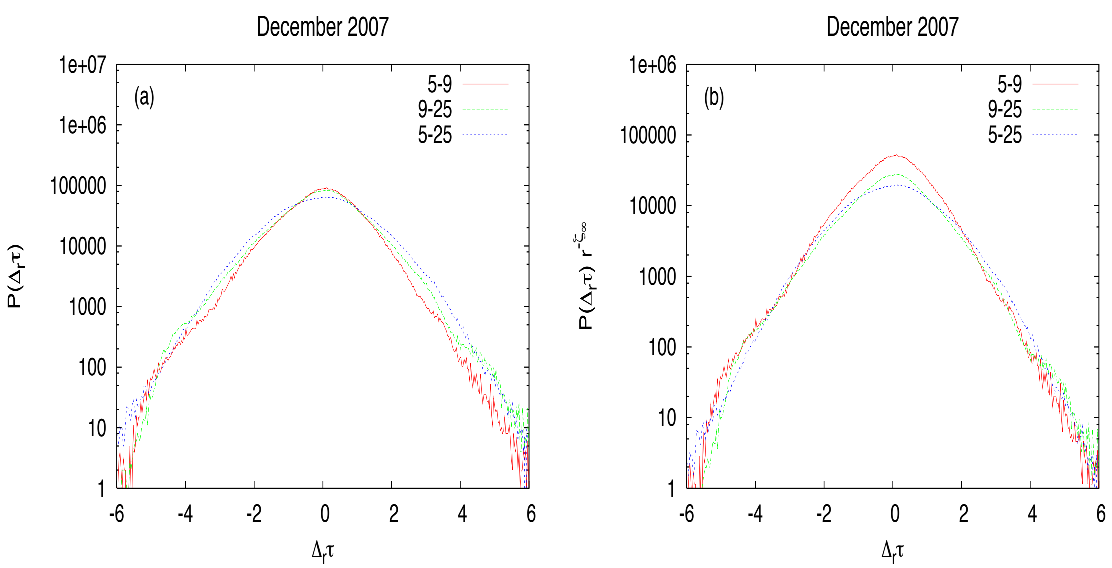

Figure 2.29: *December 2007.* Probability density function $P(\Delta_r\tau)$ of difference of τ, calculated between two anemometers located at 5 m and 9 m, at 9 m and 25 m, at 5 m and 25 m in stable atmosphere. a) $P(\Delta_r\tau)$s are shown without rescaling. b) $P(\Delta_r\tau)$s are multiplied by the factor $r^{-\zeta_\infty}$ with r the distance between two anemometers and $\zeta_\infty \sim 0.4$. In the figure the elevation of anemometers is indicated in metres.

Chapter 3

Modelling of flows in the Atmospheric Boundary Layer

3.1 Introduction

In this chapter, I introduce the mathematical model used in my study. The general elements about Fluid Dynamics are shown briefly, and particular attention is given to its applications in Meteorology and in Computational Fluid Dynamics (shortly CFD). Finally, the informatic packages employed are presented.

3.2 Mathematical model

The mathematical model, used in my Thesis, is based on the principia of the Fluid Dynamics. It is a part of Fluid Mechanics, that deals with the fluid flows. In my Thesis the study of fluid flows in atmosphere is treated.
The Fluid Dynamics involves fundamental elements of Mechanics and Thermodynamics in addition to costitutive equations of the fluid; the last ones are the empirical laws that describe the behaviour of the fluid [17].
The primitive equations of Fluid Dynamics are the Navier-Stokes equations. They are conservation rules and they are expressed in Lagrangian formalism as follows:

- the continuity equation, that is the mass conservation law, is

$$\frac{d\rho}{dt} = -\rho \boldsymbol{\partial} \cdot \boldsymbol{v} + q \tag{3.1}$$

  with ρ fluid density, $\boldsymbol{v}$ fluid velocity and q density of mass source;

- the Second Law of Dynamics in vector form, that is the momentum conservation law, is

$$\frac{d\boldsymbol{v}}{dt} = \boldsymbol{g} - 2\boldsymbol{\Omega} \times \boldsymbol{v} - \frac{1}{\rho}\boldsymbol{\partial} p + \frac{1}{\rho}\boldsymbol{\partial} \cdot \mathcal{T} \tag{3.2}$$

  with $\boldsymbol{g}$ gravitational acceleration, Ω Earth's angular rotation velocity, p atmospheric pressure and $\mathcal{T}$ tensor of viscous stress. The last term of the equation represents the effects of momentum and vorticity diffusivity, namely the conversion of mechanical energy in heat, that in macroscopic terms are characterized by fluid viscosity;

- the energy conservation equation, that corresponds to the First Law of Thermodynamics, is

$$\frac{de}{dt} = -\frac{p}{\rho}\boldsymbol{\partial} \cdot \boldsymbol{v} - \frac{1}{\rho}\boldsymbol{\partial} \cdot \boldsymbol{j} + \frac{1}{\rho}\mathcal{T} : \mathcal{D} \tag{3.3}$$

  with e internal specific energy, $\boldsymbol{j}$ heat current density and $\mathcal{D}$ tensor of deformation. On the right-hand side of the equation, the first and second terms describe the transformation of work and heat, while the third one is related to the conversion of kinetic energy in heat. It is a dissipative term and it equal to zero, when the fluid is ideal and without viscosity ($\mathcal{T} = 0$).

The Navier-Stokes equations show a problem of closure, because there are six unknowns (density ρ, three components of velocity $\boldsymbol{v}(u, v, w)$, temperature T, pressure p) in three equations: two of them are in scalar form (equations (3.1), (3.3)) and one is in vectorial form (equation (3.2)), that corresponds to three scalar equations, one for each velocity component. Therefore we have six unknowns in five scalar equations.
The previous equations must be used with the characterization of the fluid by costitutive relations:

$$s = s(e, \rho) \tag{3.4}$$
$$\mathcal{T} = \mathcal{T}(\mathcal{D}) \tag{3.5}$$
$$\boldsymbol{j} = \boldsymbol{j}(\boldsymbol{\partial} T) \tag{3.6}$$

with s specific entropy.
Besides, in order to solve a Fluid Dynamics problem, it is necessary to define

- the initial conditions, namely the value at initial time ($\rho(\boldsymbol{x}, 0)$, $\boldsymbol{v}(\boldsymbol{x}, 0)$, $e(\boldsymbol{x}, 0)$);
- the boundary conditions, namely relation of unknows ($\rho(\boldsymbol{x}, t)$, $\boldsymbol{v}(\boldsymbol{x}, t)$, $e(\boldsymbol{x}, t)$) on the border of the domain.

The problem associated to equations (3.1), (3.2), (3.3) is nonlinear and there is not a general mathematical method to solve nonlinear problem. It is possible to solve by means of numerical techniques in Computational Fluid Dynamics.
In some cases the conditions of the problem can be semplified; for example, if the fluid has a constant density or it is not viscous, flow is isothermal or isoentropic, an analytic solution of the equations system can be found. Besides, when the fluid is not viscous, $\mathcal{T} = 0$, the semplified system is known as system of Eulero equations.

3.3 Meteorology

The Navier-Stokes equations are fundamental in the Meteorology. This subject is a sector of the Atmosphere Science and studies the phenomena that occur in Earth's

atmosphere in order to get a characterization of the climate and to obtain weather forecast [8].
It includes several study fields, for example:

- dynamic meteorology, that analyses the formation and development of data observed;
- synoptic meteorology, that studies the evolution of atmospheric conditions in larger spatial scales than 1000 km. It uses weather charts and information derived by experiments;
- satellite meteorology, that uses data of remote sensing;
- radar meterology, that makes use of radar data in order to have weather forecast;
- agrometeorology, that studies the connections between weather and agriculture;
- environmental meteorology, that analyses the pollutant dynamics.

One of the most important products of meteorology study is weather forecast. It is based on experimental and theoretical aspects; the last ones derive from fundamentals of Atmosphere Science [15].
A weather forecast is the result of a sequential procedure. It is characterized by the following parts:

- observation and measure of atmospheric phenomena, in particular estimation of temperature, humidity, pressure, sun radiation, velocity and direction of the wind;
- analysis and elaboration of data;
- forecast, using measures as initial conditions and mathematical model to advance in time the measured initial conditions.

Besides, the weather forecast is characterized by spatial extension and time interval of forecast [7].
As to spatial extension, the weather forecast is classified in the following way:

- local;
- national;
- continental;
- global.

As to time interval of forecast, it is classified in:

- now-casting, less than 24 hours;
- short time-limit, 24-72 hours;

- middle time-limit, less than a week;
- long time-limit, 1-2 weeks;
- seasonal forecast, with the aim of identifying the seasonal climate trend.

3.4 Computational Fluid Dynamics

The numerical methods to solve the system of equations (3.1), (3.2), (3.3) are developed in the discipline of Computional Fluid Dynamics (CFD).
It had its origins in aeronautics field in the seventies, and then the competences were transferred in the industrial sector of turbomachinery in the eighties with more elaborated structures than the first applications in aircraft simulations. Nowadays its applications are various, some sectors are:

- aeronautics;
- turbomachinery;
- combustion analysis;
- tecniques of flux control;
- study of environmental flux;
- pollution dispersion;
- wind engineering.

The numerical techniques are complementary to experimental analysis: the measures provide singular values, while the computational analysis gives a global overview. These approches are combined to study a problem, and it is possible to compare a general solution with particular measurements, that are obtained in some locations and not in every part of the studied domain [31].
Once the fluid dynamics problem is assigned, the following operative outline can be obtained:

- selection of physical-mathematical model suitable to the situation in pre-processing;
- definition of calculation domain and boundary conditions in pre-processing;
- dicretisation of computational domain and mesh generation in pre-processing;
- choice of discretization method and appropriate numerical scheme to be defined in the flow-solver;
- analysis of the solution and identification of significative results in post-processing.

3.5 Discretization of Navier-Stokes equations

The system of Partial Differential Equations (3.1), (3.2), (3.3) must be discretized before beginning the flow-solver of CFD simulation [1].
There are three techniques of discretizations:

- finite difference method (FDM);
- finite volume method (FVM);
- finite element method (FEM).

The finite difference method is the simplest technique of discretization for the ordinary differential and partial differential equations. The fundamental idea of this method is to write the derivative by incremental ratio and to write the function by the development of Taylor series.
For example, the derivative of the first order, in the uniform discretization, can be written in the following ways:

- forward form
$$\frac{\partial u}{\partial x} = \frac{u(x+\Delta x) - u(x)}{\Delta x} \tag{3.7}$$
where Δx is a parameter of discretization
- backward form
$$\frac{\partial u}{\partial x} = \frac{u(x) - u(x-\Delta x)}{\Delta x} \tag{3.8}$$
- central form

$$\frac{\partial u}{\partial x} = \frac{u(x+\Delta x) - u(x-\Delta x)}{2\Delta x} \tag{3.9}$$

The finite volume method is an ordinary technique used in CFD. It can be used for structured and unstructured meshes. It is used in many Computational Fluid Dynamics packages.
Its name refers to the small control volume, that is surrounding each node point on a mesh. The equations (3.1), (3.2), (3.3) must be written in eulerian reference system and the integral form can be used [29].
For example, the continuity equation (3.1) can be written in the conservative way

$$\frac{\partial \rho}{\partial t} + \boldsymbol{\partial} \cdot (\rho \boldsymbol{v}) = q \tag{3.10}$$

In the integral three-dimensional form the equation (3.10) becomes

$$\int_V \frac{\partial \rho}{\partial t}\, dV + \int_V \boldsymbol{\partial} \cdot (\rho \boldsymbol{v})\, dV = \int_V q\, dV \tag{3.11}$$

In the hypothesis that the volume V does not change in time $\left(\frac{\partial V}{\partial t} = 0\right)$, V has a small extension and ρ e q are invariant in time, the result is

$$\frac{\partial \rho}{\partial t} + \frac{1}{V}\int_V \boldsymbol{\partial} \cdot (\rho \boldsymbol{v})\, dV = q \tag{3.12}$$

and by applying the divergence theorem, the volume integral is replaced by the surface integral

$$\frac{\partial \rho}{\partial t} + \frac{1}{V}\int_S \rho \boldsymbol{v} \cdot \boldsymbol{n}\, dS = q \tag{3.13}$$

where S is the boundary surface of volume V.
In equation (3.13), the integral can be substituted by summation

$$\int_S \rho \boldsymbol{v} \cdot \boldsymbol{n}\, dS = \sum_1^n (\overline{\rho\, u}\, S_x + \overline{\rho\, v}\, S_y + \overline{\rho\, w}\, S_z) \tag{3.14}$$

where $(\overline{\rho\, u}, \overline{\rho\, v}, \overline{\rho\, w})$ is the average flux of density calculated by techniques of approximation (cell vertex or cell centred).
The finite element method is used in partial differential equations and in integral equations. Its solution approach is based on the elimination of differential form and it renders steady the problem. This method transforms systems of partial differential equations in ordinary differential equations, that can be solved by standard techniques.
The calculation scheme must have some properties:

- consistency, namely the discretization form must have a small deviation with the original equations system;
- stability, namely the error of iteration scheme is minimum;
- convergence, namely the solution of numerical scheme must be near the solution of the original equations system;
- boundedness, namely the solution of computation is limited by physical values.

3.6 Turbulence Modelling

In the CFD procedure, a particular importance is assigned to the choice of the turbulence modelling. This is very important, because it characterizes the computation and it influences the timetable of the solution running.
There are three techniques for the turbulence modelling:

- direct numerical simulation (DNS);
- Reynolds averaged Navier-Stokes equations (RANS equations);
- large eddy simulation (LES).

In DNS the Navier-Stokes equations are solved without approximations to determine the wind velocity field $\mathbf{v}(\mathbf{x}, t)$ for each realization of the flow. Since all length scales have to be solved, DNS is computationally expensive and the computational cost becomes very large if the turbulence is developed. For this reason the approach is

restricted to flows with low or moderate Reynolds numbers.
In the RANS method a Reynolds decomposition can be used, writing every unknown by sum of a mean and a fluctuation. The RANS equations contain a further unknown called Reynolds stresses tensor, which is due to all scales of motion and needs to be modelled in order to close the equations system. The advantage of RANS method in comparison of other models is that RANS equations allow to treat the turbulence as a steady phenomenon, so even unsteady flows are studied as steady ones.
The RANS equations models are classified by the number of additional differential equations needed to close the original equations system (3.1), (3.2), (3.3). Some turbulence models used to close RANS equations are:

- algebraic or zero-equation model: mixing length;
- one-equation model: Spalart-Allmaras;
- two-equations models: $k-\epsilon$ (standard, RNG, realizable) and $k-\omega$ (standard, SST);
- five-equations model (in two-dimensional simulations) and seven-equations model (in three-dimensional simulations): Reynolds Stress Model.

The LES is a form of turbulence calculation between DNS and RANS methods. LES equations are solved for a velocity field $\mathbf{v}(\mathbf{x})$ of large scale filtered in the space $\mathbf{v}\widetilde{(\mathbf{x}}, t)$. In this method the large-scale motion is simulated, while the smaller-scales motion is modelled. The timetable for this computation is large [22].
In the following sections, I describe the turbulence modelling of RANS equations, used in my work.

3.6.1 RANS equations

The Reynolds-averaged Navier-Stokes (RANS) equations are time-averaged equations of motion for fluid flow. These equations can be used to have a whole knowledge of the properties of turbulence flow, obtained by averaged solutions of the Navier-Stokes equations.
In this section, the RANS equations for a stationary and incompressible flow of Newtonian fluid are described.
The Navier-Stokes equation is written in the following way

$$\partial_t \mathbf{v} + \mathbf{v} \cdot \boldsymbol{\partial} \mathbf{v} = -\frac{\boldsymbol{\partial} p}{\varrho} + \nu \boldsymbol{\partial}^2 \mathbf{v} + \mathbf{f} \tag{3.15}$$

$$\boldsymbol{\partial} \cdot \mathbf{v} = 0 \tag{3.16}$$

with $\mathbf{f}$ general body-force term.
In order to obtain the RANS equations it is possible to use the Reynolds decomposition for the velocity field $\mathbf{v}(\mathbf{x}, t)$, the pressure p and the body-force $\mathbf{f}$, written as follows

$$\mathbf{v}(\mathbf{x}, t) = \overline{\mathbf{v}(\mathbf{x})} + \mathbf{v}'(\mathbf{x}, t) \tag{3.17}$$

$$p(\mathbf{x},t) = \overline{p(\mathbf{x})} + p'(\mathbf{x},t) \tag{3.18}$$

$$\mathbf{f}(\mathbf{x},t) = \overline{\mathbf{f}(\mathbf{x})} + \mathbf{f}'(\mathbf{x},t) \tag{3.19}$$

where $\overline{\mathbf{v}(\mathbf{x})}$, $\overline{p(\mathbf{x})}$ and $\overline{\mathbf{f}(\mathbf{x})}$ are respectively time averaged velocity, time averaged pressure and time averaged force, while $\mathbf{v}'(\mathbf{x},t)$, $p'(\mathbf{x},t)$ and $\mathbf{f}'(\mathbf{x},t)$ are the fluctuating parts of the above-written greatnesses.
In this way there is the assumption that the time-dependent turbulent (chaotic) velocity fluctuations can be separated from the mean flow velocity $\overline{\mathbf{v}}$, that is indipendent of the time [13].
By replacing the Reynolds decompositions (3.17), (3.18) and (3.19) in the Navier-Stokes equations (3.15) and (3.16), the results is

$$\begin{aligned} \partial_t(\overline{\mathbf{v}}+\mathbf{v}') + (\overline{\mathbf{v}}+\mathbf{v}')\cdot\boldsymbol{\partial}(\overline{\mathbf{v}}+\mathbf{v}') &= -\frac{\boldsymbol{\partial}(\overline{p}+p')}{\varrho} + \nu\boldsymbol{\partial}^2(\overline{\mathbf{v}}+\mathbf{v}') + (\overline{\mathbf{f}}+\mathbf{f}') && (3.20)\\ \boldsymbol{\partial}\cdot(\overline{\mathbf{v}}+\mathbf{v}') &= 0 && (3.21)\end{aligned}$$

Since $\overline{\mathbf{v}}$ is indipendent from t, by definition, the first term in equation (3.20) is equal to zero. After the expansion of the dot product on the left-hand side it is possible to write

$$\partial_t\mathbf{v}'+\overline{\mathbf{v}}\cdot\boldsymbol{\partial}\overline{\mathbf{v}}+\overline{\mathbf{v}}\cdot\boldsymbol{\partial}\mathbf{v}'+\mathbf{v}'\cdot\boldsymbol{\partial}\overline{\mathbf{v}}+\mathbf{v}'\cdot\boldsymbol{\partial}\mathbf{v}' = -\frac{\boldsymbol{\partial}(\overline{p}+p')}{\varrho}+\nu\boldsymbol{\partial}^2(\overline{\mathbf{v}}+\mathbf{v}')+(\overline{\mathbf{f}}+\mathbf{f}') \tag{3.22}$$

Afterwards, by deriving the time-averaged entire equation (3.22) and the following equation is obtained

$$\overline{\partial_t\mathbf{v}'}+\overline{\overline{\mathbf{v}}\cdot\boldsymbol{\partial}\overline{\mathbf{v}}}+\overline{\overline{\mathbf{v}}\cdot\boldsymbol{\partial}\mathbf{v}'}+\overline{\mathbf{v}'\cdot\boldsymbol{\partial}\overline{\mathbf{v}}}+\overline{\mathbf{v}'\cdot\boldsymbol{\partial}\mathbf{v}'} = -\frac{\overline{\boldsymbol{\partial}(\overline{p}+p')}}{\varrho}+\nu\overline{\boldsymbol{\partial}^2(\overline{\mathbf{v}}+\mathbf{v}')}+\overline{(\overline{\mathbf{f}}+\mathbf{f}')} \tag{3.23}$$

In the linear terms of the right-hand side of the previous equation (3.23) time averaging and spatial differentiation can be commuted, and in the first term of the left-hand side of the same equation temporal averaging and differentiaton can be commuted and, using the Reynolds decomposition, the result is

$$\overline{\partial_t\mathbf{v}'} = \partial_t\overline{\mathbf{v}'} = 0 \tag{3.24}$$

Considering the third term of the equation (3.23) and using the time average, the following relations are obtained

$$\begin{aligned} \overline{\overline{\mathbf{v}}\cdot\boldsymbol{\partial}\mathbf{v}'} &= \lim_{T\to+\infty}\int_0^T \overline{\mathbf{v}}\cdot\boldsymbol{\partial}\mathbf{v}'\,dt && (3.25)\\ &= \overline{\mathbf{v}}\cdot\lim_{T\to+\infty}\frac{\int_0^T\boldsymbol{\partial}\mathbf{v}'\,dt}{T} && (3.26)\\ &= \overline{\mathbf{v}}\cdot\boldsymbol{\partial}\lim_{T\to+\infty}\frac{\int_0^T\mathbf{v}'\,dt}{T} && (3.27)\\ &= \mathbf{v}'\cdot\boldsymbol{\partial}\overline{\mathbf{v}'} = 0 && (3.28)\end{aligned}$$

The second equality (3.26) can be written because $\overline{\mathbf{v}}$ is indipendent of t. Similarly, the third equality (3.27) occurs because $\boldsymbol{\partial}$ is an operator, that is also indipendent

of t and finally the equality (3.28) is obtained considering the features of Reynolds decomposition. Following a similar analysis, it is possible to operate with the term $\mathbf{v}' \cdot \boldsymbol{\partial}\overline{\mathbf{v}}$ of the equation (3.23) with the same resulting.
The term $\overline{(\overline{\mathbf{f}} + \mathbf{f}')}$ is equal to $\overline{\mathbf{f}}$ for the properties of Reynolds decomposition. So the equation (3.23) becomes

$$\overline{\overline{\mathbf{v}} \cdot \boldsymbol{\partial}\overline{\mathbf{v}}} + \overline{\mathbf{v}' \cdot \boldsymbol{\partial}\mathbf{v}'} = -\frac{\boldsymbol{\partial}\overline{p}}{\varrho} + \nu\boldsymbol{\partial}^2\overline{\mathbf{v}} + \overline{\mathbf{f}} \tag{3.29}$$

Averaging the Navier-Stokes equation (3.21), the result is

$$\boldsymbol{\partial} \cdot \overline{\overline{\mathbf{v}}} + \boldsymbol{\partial} \cdot \overline{\mathbf{v}'} = 0 \tag{3.30}$$

Using the Reynolds relation $\overline{\mathbf{v}} = \overline{\overline{\mathbf{v}}}$, from the equation (3.30) we write

$$\boldsymbol{\partial}\overline{\mathbf{v}} = -\boldsymbol{\partial}\overline{\mathbf{v}'} \tag{3.31}$$

From the equation (3.31) the next relations can be derived

$$\overline{\boldsymbol{\partial}\overline{\mathbf{v}}^2} = \boldsymbol{\partial}\overline{\overline{\mathbf{v}}^2} = \boldsymbol{\partial}\overline{\mathbf{v}}^2 \tag{3.32}$$

$$\overline{\boldsymbol{\partial}\mathbf{v}'^2} = \boldsymbol{\partial}\overline{\mathbf{v}'^2} \tag{3.33}$$

As a consequence of these identities (3.32) and (3.33) we can write the equation (3.29) in the following way

$$\boldsymbol{\partial}\overline{\mathbf{v}}^2 + \boldsymbol{\partial}\overline{\mathbf{v}'^2} = -\frac{\boldsymbol{\partial}\overline{p}}{\varrho} + \nu\boldsymbol{\partial}^2\overline{\mathbf{v}} + \overline{\mathbf{f}} \tag{3.34}$$

This equation (3.34) is a typical form in which the Reynolds averaged Navier-Stokes equation is shown [19].

3.7 Models and softwares

For my Thesis, I used the data of meteorological model, WRF, of the Department of Physics (University of Genoa) and I used CFD softwares, CFX and FLUENT, of Consortium SIRE (Dynamics Simulation and Virtual Reality of Savona). Besides, to display the results of CFD simulations, I utilized a free software, PARAVIEW.
For the geometrical aspects of the study, some softwares, SOLID WORKS, GAMBIT and ICEM, were made available by Consortium SIRE.

3.7.1 WRF

WRF (Weather Research and Forecasting), used by Department of Physics [25], is a model for the simulation of atmospheric systems. It was developed with the collaboration of the American Governative Agencies and Research Groups: for example, NCAR (National Center for Atmospheric Research), NOAA (National Oceanic and Atmospheric Administration), AFWA (Air Force Weather Agency), NRL (Naval

Research Laboratory), FAA (Federal Aviation Administration), Oklahoma University, involving research agencies world wide.
It is free and available on line, at wrf-model.org/index.php.
It is used in different fields, for example:

- meteorological forecasting;
- simulation with coupling of atmosphere - ocean;
- studies of meteorological models;
- studies of parameterization and data assimilation.

It has two non-hydrostatic cores, WRF-ARW and WRF-NMM, with differences in numerical formulation, kind of coordinates and mesh. In this way, WRF can operate with various space resolutions: from thousand kilometres to thousand metres.
The simulation needs boundary and initial conditions, extracted from global records of reanalysis CFSR of NCEP (National Center for Environmental Prediction), agency of NOAA. This database covers the period 1979 - 2010; it has variables defined on meshes with size 0.5 ° in latitude and longitude and with time resolution of 1 h.

3.7.2 CFX

CFX is a commercial software of Computational Fluid Dynamics; it is useful for flow simulations in different fields:

- aerodynamics;
- turbomachinery;
- combustions;
- applications to industrial component;
- enviromental flows;
- fluid-structure interaction.

The software, available at SIRE, is the ANSYS-CFX version [2]. It was created with CFX-4, that in its turn came from Flow3D and TASCflow.
Flow3D was used by Autority of Atomic Energy in United Kingdom (UKAEA) in the eighties, whereas TASCflow was developed by Advanced Scientific Computing (ASC) in Waterloo (Canada).
CFX solver uses a system of multiple-meshes with discretization of partial differential equations of the system by finite volume method. Its simulations can be both steady (independent of time) and unsteady (in evolution with time) and it can operate with different convergence schemes.
This software permits to analyse laminar and turbulent flows. It solves turbulent motions by different models:

- RANS (Reynolds-averaged Navier-Stokes) equations;

- LES (large eddy simulation);
- DES (detached eddy simulation).

For the RANS Equations there are various schemes of closure of the problem:

- $k - \epsilon$;
- $k - \omega$;
- SST;
- Reynolds-Stress Model.

Every simulation needs boundary and initial conditions.
The software is divided in three parts:

- CFX-PRE: it is used to import the mesh to choose model options and to set boundary conditions;
- CFX-SOLVER: it is used to execute the calculation;
- CFX-POST: it is used to analyse the results of the calculation.

3.7.3 FLUENT

Fluent software is a sophisticated numerical and robust solver, that uses the finite volumes and allows to obtain accurate results for a large range of flows. It is available on Windows, Linux and Unix platforms.
Advanced parallel processing can efficiently utilize multiple, multiple-core processors in a single machine and in a multiple machines in a network. Dynamic load balancing automatically detects and analyses parallel performance and adjusts the distribution of computational cells among the processors so that a balanced load is shared by CPU, even when complex physical models are in use.
Different situations are simulated by FLUENT. It allows to work in two-dimensional and three-dimensional geometry.

Important physical aspects are introduced, for example: heat transfer, sources of mass, momentum, energy and noise. The models for various flow regimes are specified:

- laminar (only for smooth flows);
- viscous.

The turbulence models available in FLUENT are the following ones:

- large eddy simulation (LES);
- detached eddy simulation (DES);
- Spalart-Allmaras;

- k-ϵ standard;
- k-ϵ realizable;
- k-ϵ RNG;
- k-ω standard;
- k-ω SST;
- Reynolds stress.

This software uses complex geometries and meshes:

- various and mixed meshes (structured, unstructured and hybrid);
- sliding meshes;
- mixing-plane model, where the mesh boundaries are time averaged;
- dynamic and deforming meshes;
- free surfaces.

The reference frames can be:

- inertial (stationary or moving);
- non-inertial (rotating and accelerating);
- multiple with meshes in relative motion.

Working with this software, quantitative analysis and flow visualizations can be obtained. Therefore, we have:

- two-dimensional plots of values of primitive and derived quantities;
- surface and volume integrals fluxes and averages;
- temporal variation of primitive and derived quantities;
- Fourier analysis.

The output of FLUENT simulation can be exported in different format and analysed by CFX-POST (section 3.7.2) and PARAVIEW (section 3.7.4).

3.7.4 PARAVIEW

PARAVIEW is a software useful for data analysis and visualization of data with high level of detail. It can manage dataset by distribuited data processing sources. It was created thanks to the scientific collaboration between Kitware, Inc and Los Alamoss National Laboratory in 2000 with the goal to build an open source package able of managing dataset of big dimensions and obtaining relative graphic visualizations. Then, the elaboration of the program included other laboratories and research groups, for example Sandia National Labs, CsimSoft.
The software enables different applications:

- management of complex geometries with structured and unstructured meshes;
- handling of datase and its elaborations;
- visualization of data in different graphic methods.

PARAVIEW can import output data from CFX in EnSight format.

3.7.5 Geometrical softwares

SOLID WORKS, GAMBIT and ICEM are used to build the geometry of domain and to create the mesh for CFD simulations.
SOLID WORKS is a CAD (Computer-Aided Design) package, whereas GAMBIT and ICEM are useful to build the mesh. In particular, it is possible to use GAMBIT to define the surfaces of the domain boundary easily, while ICEM can be used to obtain the mesh.
ICEM, available at SIRE, is the version ANSYS-ICEM [4]. It provides different kinds of mesh:

- hexahedral;
- tetrahedral;
- prismatic;
- mixed.

The grids can be structured and unstructured, they can cover surfaces and volumes. The module TETRA/PRISM of ANSYS-ICEM uses a recursive approach, it generates eight tetrahedral elements for each partitioning until it covers the whole volume. Extrusion of the prism-layers is made by definition of the number of layers, the height of the first layer (or the height of the entire block of prism-layers) and the expansion ratio. The distribution of these cells may be anisotropic.
The algorithm of this plan is patch-indipendent: it is not affected by geometrical defects, therefore time-saving is obtained.
Moreover, qualitative and quantitative control of the mesh, smoothing algorithm and possibility of rebuilding the mesh assure good quality of the mesh.

Chapter 4

Nidification of a CFD model in a meteorological model

4.1 Introduction

This study concerns the subject of Computational Fluid Dynamics and Meteorology. It is developed by collaboration between the Group of Atmospheric Physics of Department of Physiscs (University of Genoa) and the Consortium SIRE (Dynamics Simulation and Virtual Reality of Savona).
The goal is the nidification of a model of Computational Fluid Dynamics (CFX and FLUENT) of SIRE in mesoscale meteorological model (WRF) of Department of Physics.
WRF renders meteorological variables, while the CFD softwares permit to have wind velocity fields with good resolution. The knowledge of wind velocity provides a lot of applications, for example:

- calculation of wind power in a given area;
- study of pollutants dispersion in atmosphere;
- study of fire propagation.

In this chapter I use the CFD software of CFX. Therefore, I use the output of WRF as boundary conditions of CFX to have wind fields with high resolution on an area including Genoa city.
For this purpose, a domain of study is defined and relevant mesh is built by geometrical softwares (SOLID WORKS, GAMBIT and ICEM) with attention to the orography of studied area.
Moreover, the numerical simulation is verified, comparing its results with direct measurements of wind. These are provided by meteorological station of ARPAL, located in Genoa.

4.2 Measurement station

Physics Department has a dataset of wind measured hourly during 2009 by a meteorological station of ARPAL (Regional Agency for Environmental Protection -

Liguria).
The measurement station provides intensity and direction of the wind and it is located near the Functional Center of ARPAL in Genoa (figure 4.1).

Figure 4.1: Meteorological station. Functional Center - ARPAL. Genoa.

Its geographical coordinates are

- latitude: 44.40035 °
- longitude: 8.94591 °
- altitude: 30 m a.s.l.

4.3 Domain

The domain, the first simulations are performed, has a horizontal surface of 19610 m in latitude and 35640 m in longitude. Its extremes are:

- latitude: from 44.357 ° to 44.537 °
- longitude: from 8.664 ° to 9.117 °

This area, where Genoa is located, shows a complex orography (figure 4.2), that influences intensity and direction of the wind.

4.4 Geometry

The surface of domain is discretized in point (28997) in three-dimensional system of orthogonal cartesian coordinates. In this way it is used in simulation of Computational Fluid Dynamics (figure 4.3).
Geographical coordinate of longitude corresponds to axis x, latitude to axis y and altitude to axis z. In particular:

- axis x: grid step = 132 m, total number = 271;

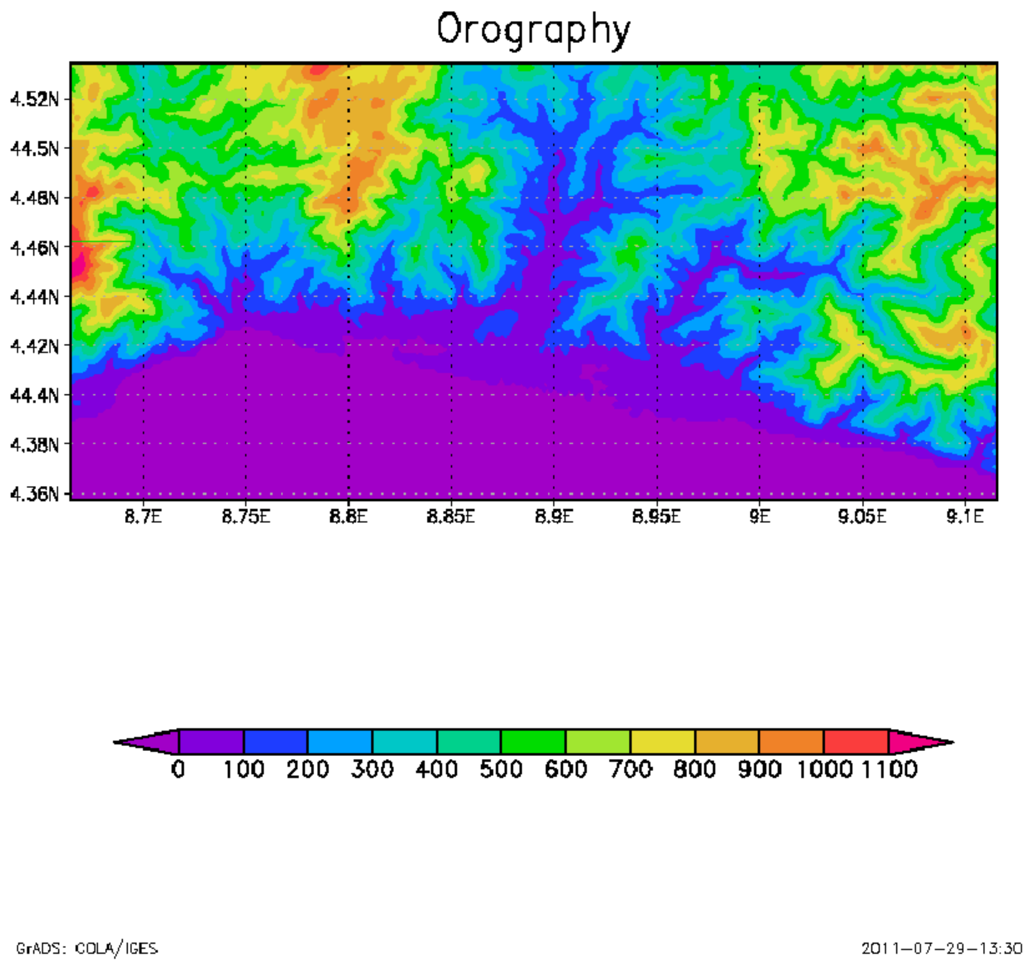

Figure 4.2: Orography of study domain.

- axis y: grid step = 185 m, total number = 107.

A model with surface from set of points is created (figure 4.5).
The output is saved in ascii format; in this way, it is imported easily in SOLID WORKS, by which the points are eliminated to render the system less heavy.
A single geometrical object is obtained by ICEM; it is divided in a limited number of areas (figure 4.5).
Land area is divided in inland part (mountains) and coastal area.
The coastal area is subdivided in:

- west;
- centre;
- port zone;
- east.

The sea is divided in four parts, corresponding to the relevant coastal zones:

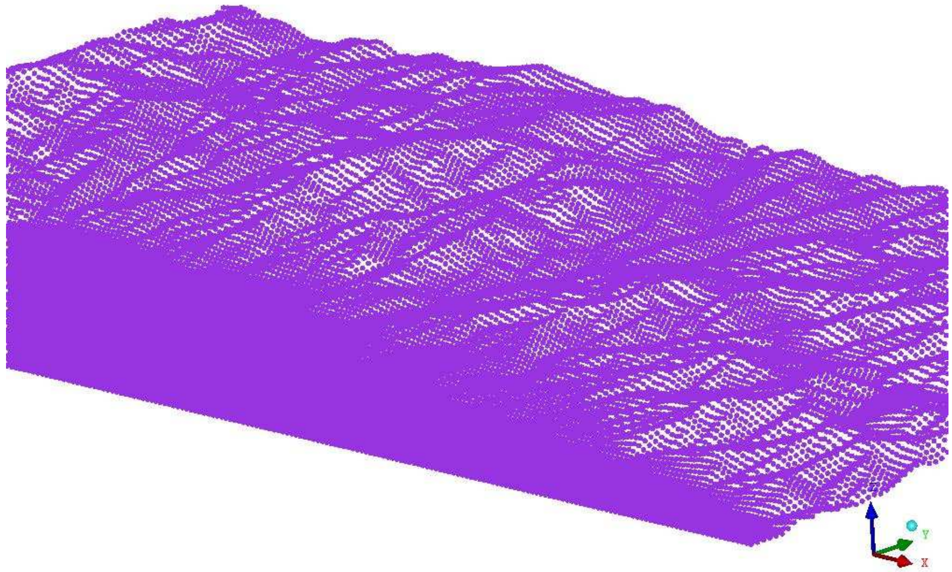

Figure 4.3: Points of orographic surface.

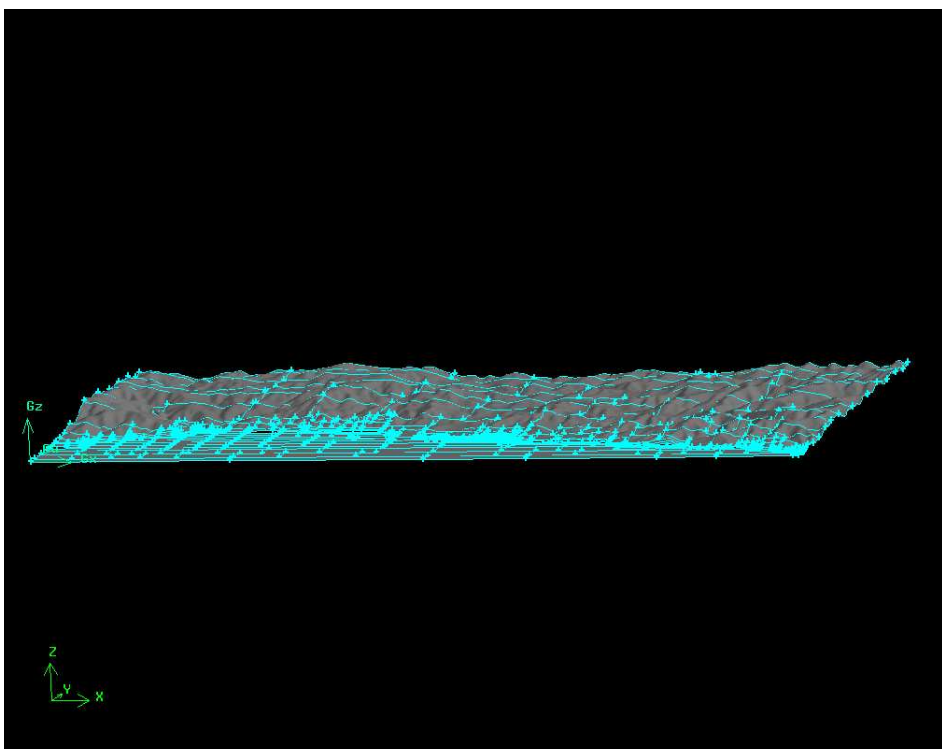

Figure 4.4: Model with surfaces of orography.

- sea west;
- sea centre;

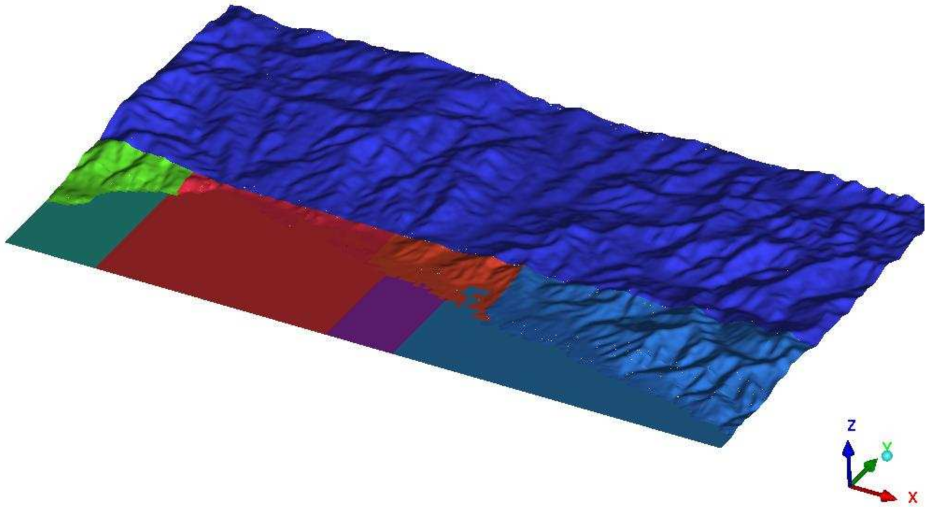

Figure 4.5: Model with areas of orographic surface.

- sea port;
- sea east.

A box with height of 3500 m (figure 4.6) is built.

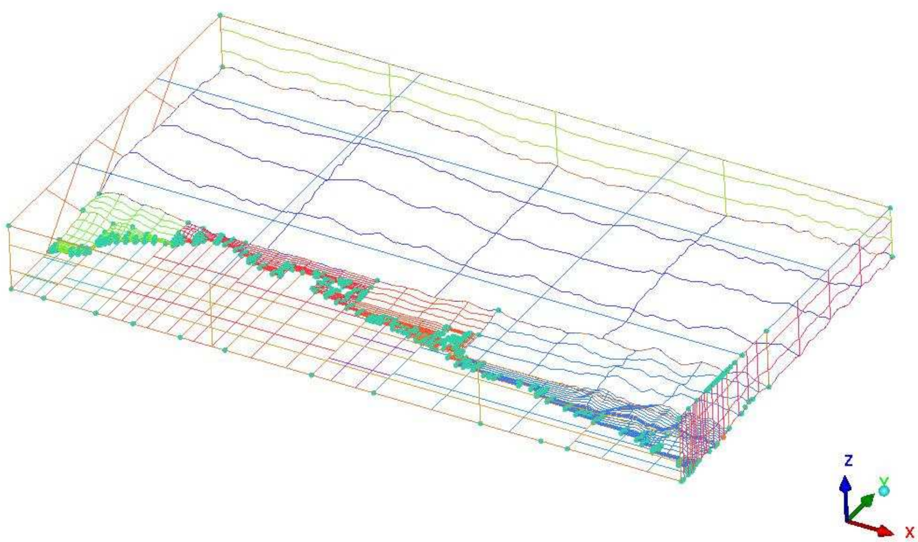

Figure 4.6: Box with height of 3500 m.

The position of the measurement station (section 4.2) is in the east zone of the coastal area (figure 4.6).

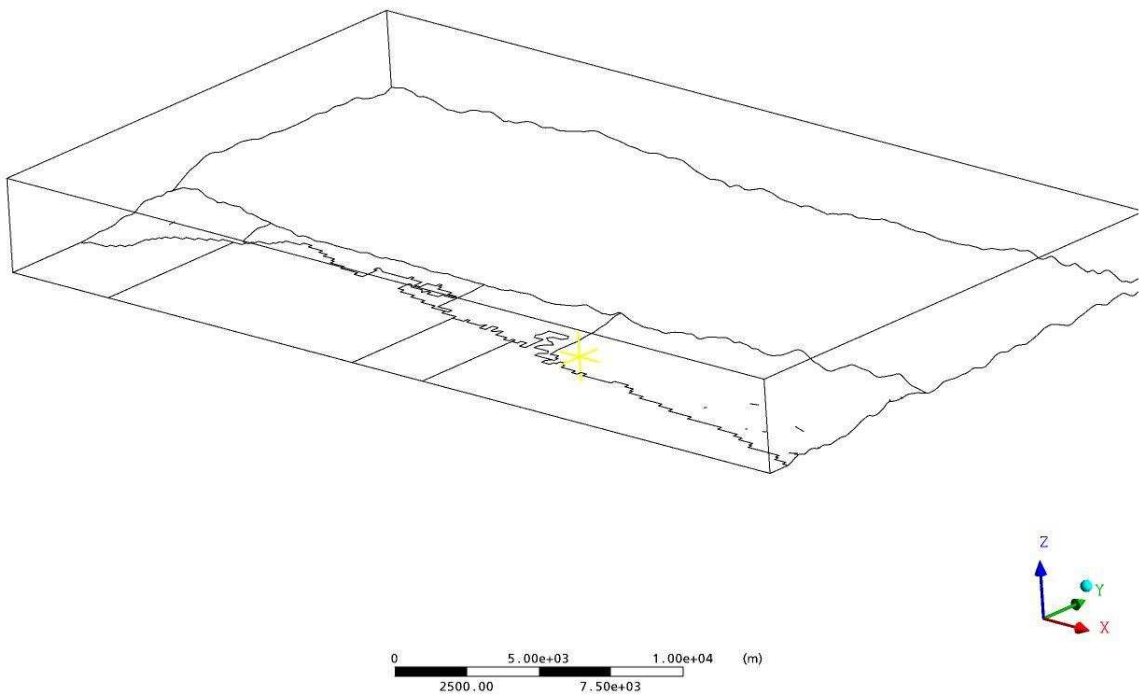

Figure 4.7: Position of meteorological station of Functional Center of ARPAL in box.

In the construction every lateral face has the name of the relative cardinal point (NORTH - EAST - SOUTH - WEST) and the upper face is named SKY.
Two grids with different spatial resolutions are built. They are unstructured meshes and their cells are tetrahedrons and prisms; the prisms are in layers near the land and sea surfaces. The number of layers is the same (10) with growth ratio of 1.1, so they enlarge up the surface for a height of 15.9 m.
The grid with lower resolution is built with the following characteristics:

- size of 80 m over the land and sea surfaces;
- size of 600 m over the lateral and upper faces.

The number of cells of coarse mesh is 6650057 (figure 4.8).
The grid with better resolution is built with the following characteristics:

- size of 80 m over the land and sea surfaces;
- size of 200 m over the lateral and upper faces.

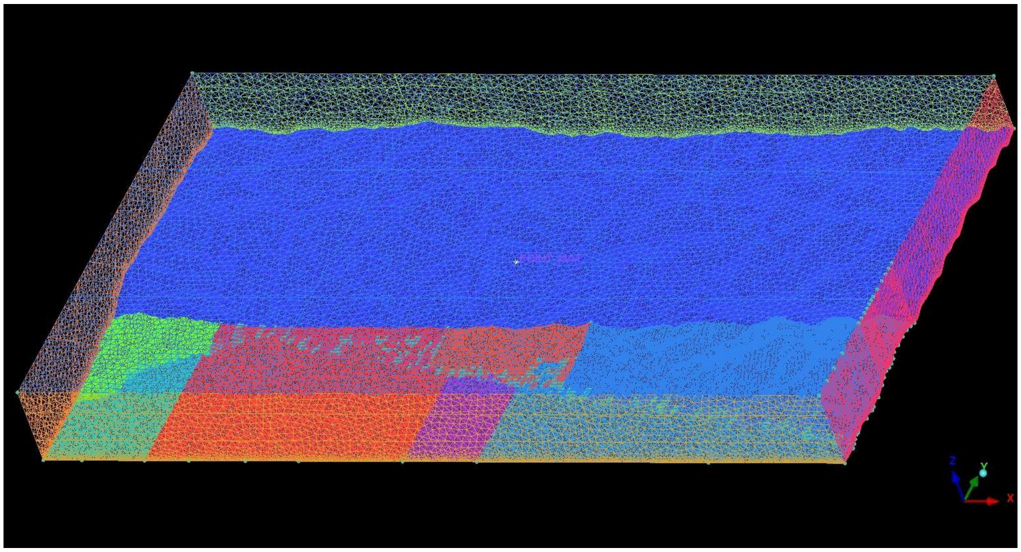

Figure 4.8: Global view of coarse mesh.

It is built with the same parameters of previous one and its number of cells is 13146002 (figure 4.9).

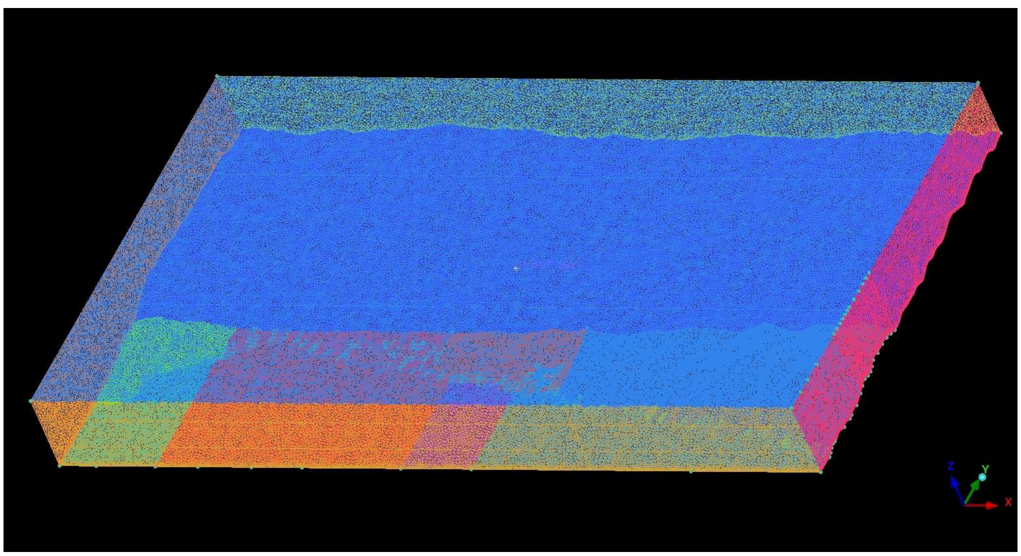

Figure 4.9: Global view of thick mesh.

The meshes have a good quality. Their resolution (figure 4.10) is good enough and it improves by means of prism layers (figure 4.11) close to surface.

4.5 Simulations

The simulations need model WRF and software CFX, as it was written in section 4.1.

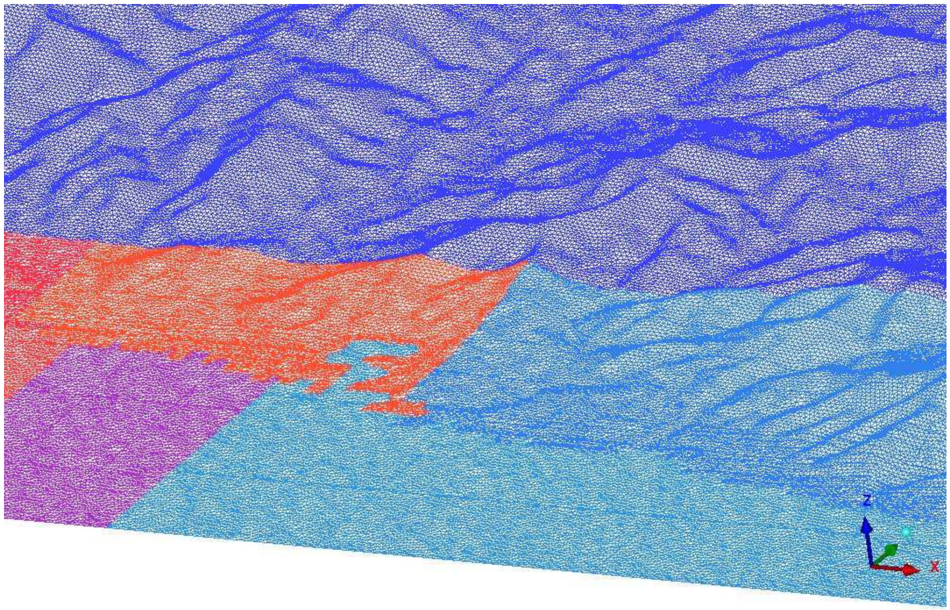

Figure 4.10: Detail of coarse mesh.

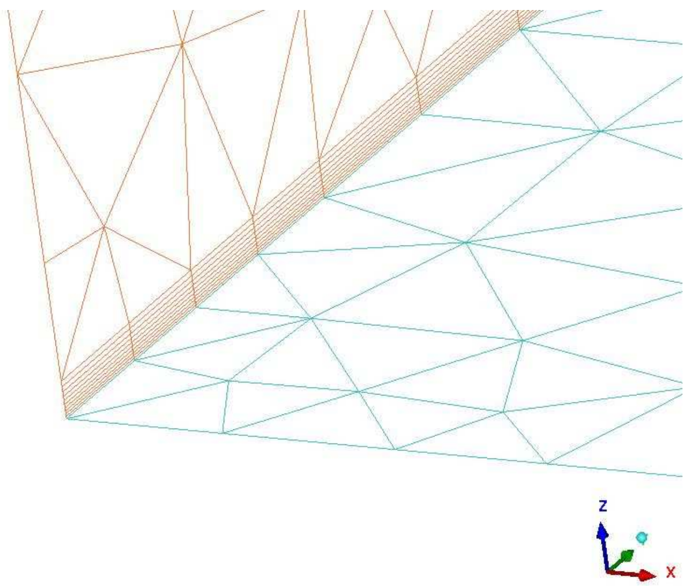

Figure 4.11: Prism layers of coarse mesh.

An hour of November 2009 (h 00 of 01/11/2009) is considered. It is characterized by wind coming from North-East direction. It is representative of meteorological configuration, that is typical of this month in Liguria.

4.5.1 Meteorological model

Using WRF, fields of meteorological variables with an hourly interval are obtained for November 2009.
At first the reanalysis for the whole Earth are obtained with grid step of 0.5 ° in latitude and longitude (about 50 km). A nesting system of the model is used:

- a "father" model with a resolution of about 10 km is used over a surface with continental scale (figure 4.12), that extends in longitude -2.6940 ° from to 21.1895 ° and in latitude from 34.3120 ° to 52.5847 °;
- a "son" model with resolution of about 2 km provides meteorological fields over a surface with a more reduced scale (figure 4.13), that extends in longitude 6.0570 ° from to 11.5078 ° and in latitude from 43.0710 ° to 45.6892 °.

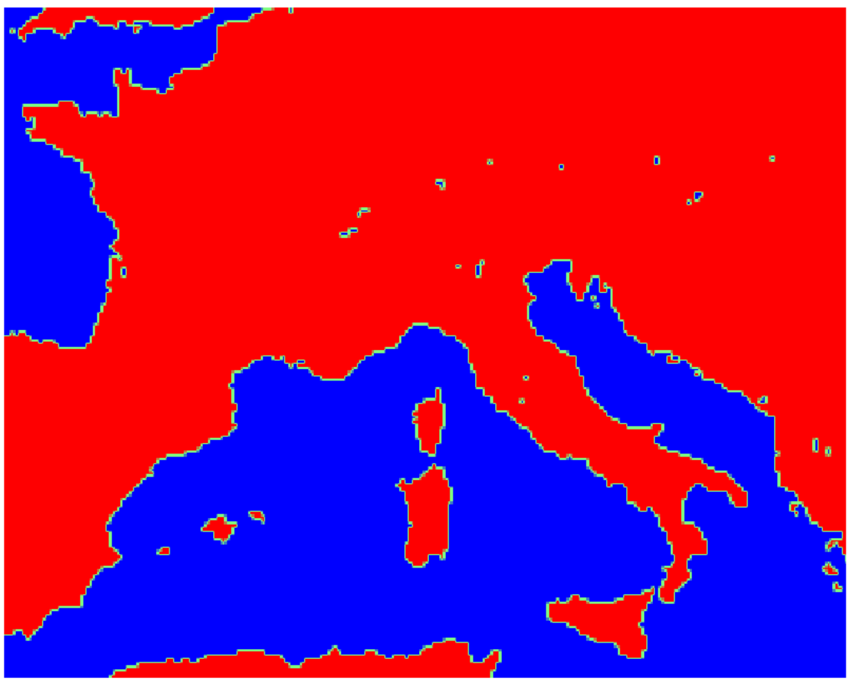

Figure 4.12: Domain for simulation of WRF. "Father" model.

Both models, "father" and "son", provide the meteorological fields over baric levels of 1000 hPa, 975 hPa, 950 hPa, 925 hPa, 900 hPa, 875 hPa, 850 hPa, 700 hPa, 500 hPa, 300 hPa, 200 hPa, 100 hPa. From the output of "son" model the information about the domain is extrapolated (figure 4.6).
In particular, for the examined events the following variables can be extracted:

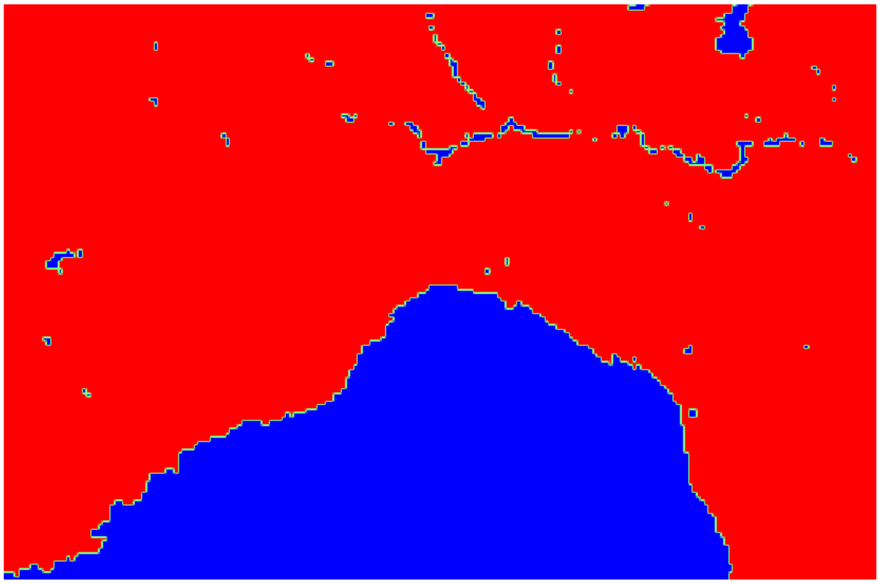

Figure 4.13: Domain for simulation of WRF. "Son" model.

- components of wind velocity;
- temperature;
- total pressure;
- density.

The resolution of these data is:

- 1976.4 m in longitude (axis x);
- 2022.3 m in latutude (axis y).

on the horizontal plane.
Along the vertical direction, the variables are calculated for the first eight levels of the domain.
The levels are nearer at low elevations, while the distance between the levels becomes larger at higher elevations. In this way, the data variability near the ground is known. The same levels are referred to sea altitude, therefore for the coastal and inland zones real values must be distinguished from not physical data. The model resolution does

not allow to consider the terrain complexity, in particular in a land, like Liguria, that has particular orographic features.
I calculated the values in the domain from WRF output by linear interpolations. I payed attention to the values on lateral faces (NORTH-EAST-SOUTH-WEST), used for following definition of boundary conditions in Computational Fluid Dynamics.

4.5.2 CFD

Different simulations by Computational Fluid Dynamics Package are executed. In this section I report the results about particular configurations of boundary conditions, permitted by CFX software. The values obtained by WRF are imposed on the lateral faces of the box. Meshes with different resolution are used.
Some conditions of computation are changed to improve the output of the simulation. Indeed, firstly I search for a realistic wind field over the terrain, secondly I define a statistical index to evaluate the result and finally the comparison with the measure of meteorological data is carried out.
In the first tests the values of wind velocity, obtained by meteorological model, are assigned as boundary conditions on lateral faces of the domain. I report the results of the following simulations:

- simulations with wind velocity assigned to four lateral faces, using both meshes;
- simulation with wind velocity assigned to three lateral faces, using coarse mesh;
- simulations with wind velocity assigned to two lateral faces, using both meshes.

The characteristics of the computations are specified for every case in the following sections.

4.5.2.1 Velocity on four lateral faces

I executed two simulations by CFX, using the meshes built before (section 4.4) and their results are reported, here following.
The same calculation model was applied. Both computations were stationary, isothermal with temperature of 280 K and incompressible. The fluid was set as air at 298 K and the turbulence model chosen is $k - \omega$.
The reference pressure was $p_0 = 89999.2$ Pa, and it corresponded to the minimun value of the wind intensity on lateral faces of domain.
Boundary conditions for NORTH, EAST, SOUTH and WEST lateral faces were the wind velocities (U, V, W components) in OPENING configuration (figures 4.14 and 4.15). SKY was set in OPENING configuration with relative static pressure of -29000 Pa.
The surfaces of sea and land (coastal zone and mountains) were WALLS with friction.
Both computations were structured with a high resolution scheme and the number of iterations made was 750.
The calculation with coarse mesh converged with order of residuals of 10^{-4}. It was obtained by observing flow rate going in and out the box. On the contrary, the

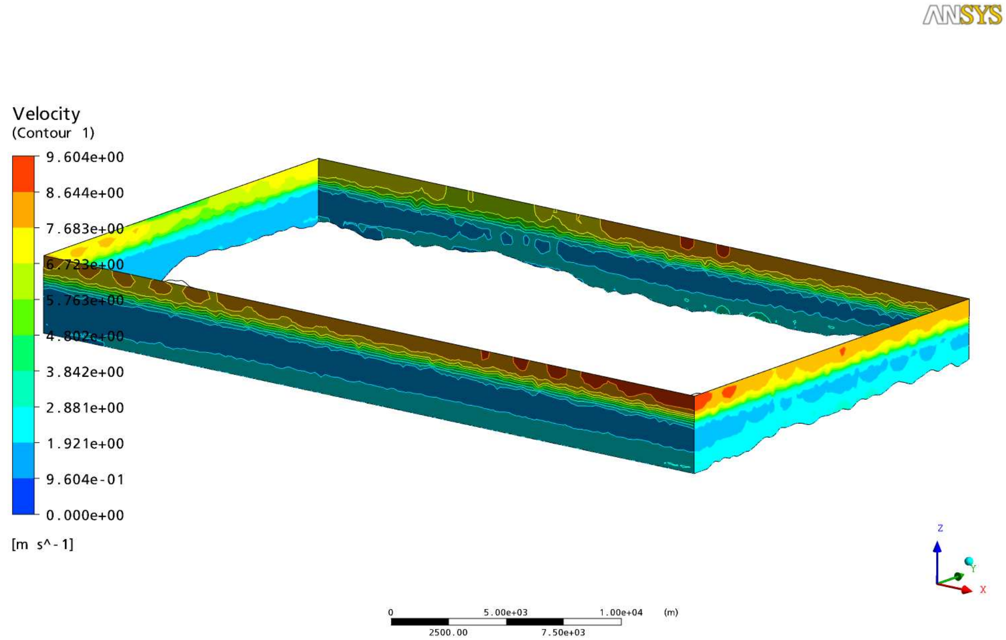

Figure 4.14: Simulation with wind velocity assigned to NORTH, EAST, SOUTH and WEST in OPENING configuration and coarse mesh - Boundary conditions: wind velocity on lateral faces of the domain.

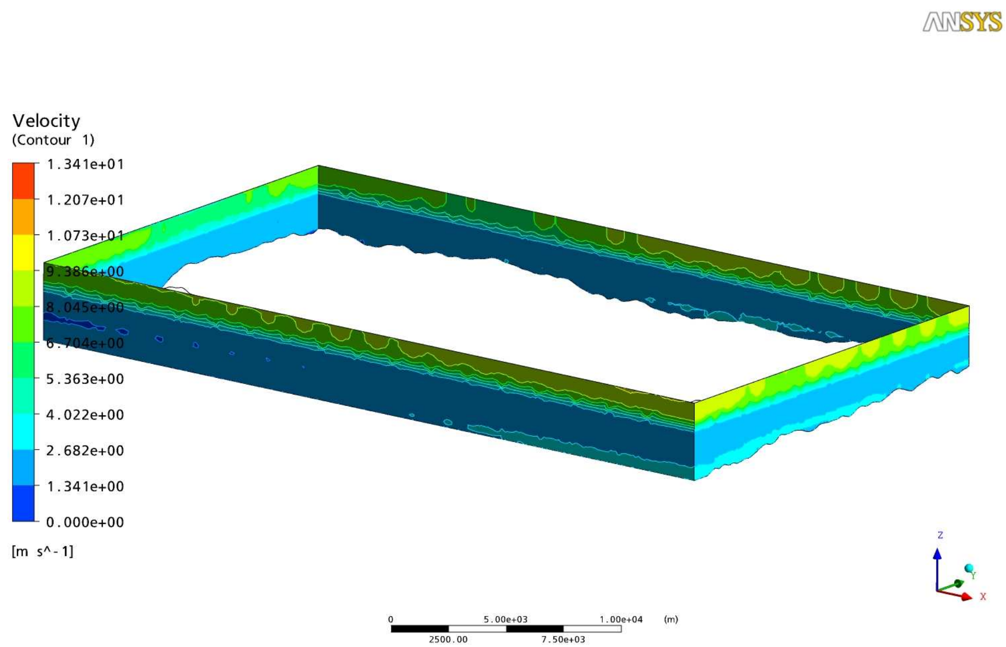

Figure 4.15: Simulation with wind velocity assigned to NORTH, EAST, SOUTH and WEST in OPENING configuration and thick mesh - Boundary conditions: wind velocity on lateral faces of the domain.

computation with thick mesh did not converge with the same number of iterations. I executed a qualitative control of wind fields, obtained in these simulations. For both the simulations I obtained the following wind fields at heights of 10 m, 30 m, 100 m and 1000 m (from figure 4.16 to figure 4.23).

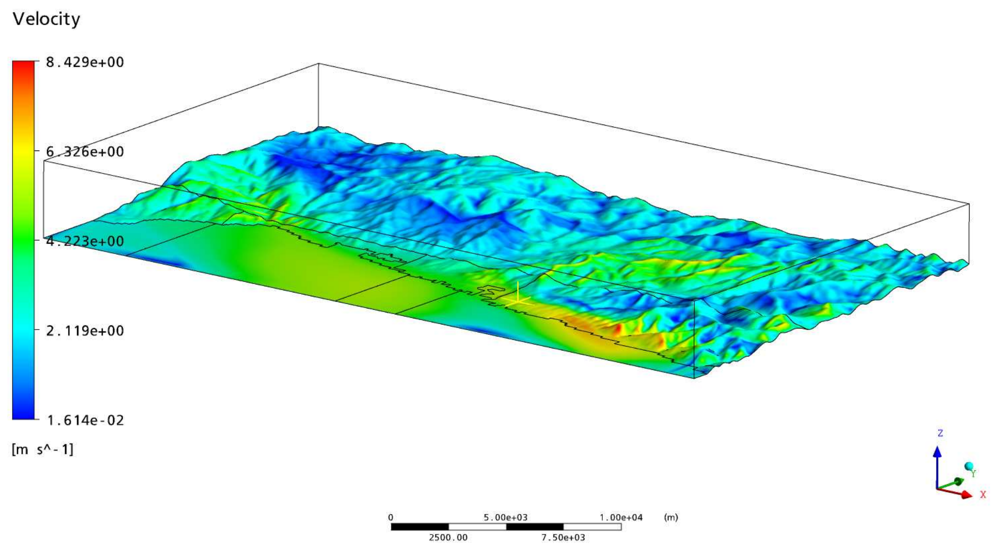

Figure 4.16: Simulation with wind velocity assigned to NORTH, EAST, SOUTH and WEST in OPENING configuration and coarse mesh. Wind field at 10 m.

The wind fields are similar all over the land (coastal zone and mountains) and they appear to be plausible; next to the sea the particular eddies are formed: in two large structures for the simulation with coarse mesh; in an intensive structure in the middle, and a little one in est sea in the case of a thick mesh.
Moreover, the first comparisons between CFX simulations and WRF outputs were executed. I paied attention to the points of lateral faces, where the boundary conditions were assigned by linear interpolation of WRF data, and to the points inside the domain, which are common between WRF grid (coarser) and CFX one (thicker).
The qualitative analysis was made using PARAVIEW software (figures 4.24 and 4.25).

In detail I calculated the normalized root mean square deviation (NRMSD) between WRF and CFX wind velocity components and intensity for each lateral face and for space inside the domain, considering WRF velocity as reference value in the calculation of NRMSD. The normalized root mean square deviation was chosen as index to show the discrepancy between the velocity provided by meteorological model and the one of computational fluid dynamics simulations.
The CFX data are calculated as an average of data around WRF nodes in space, having a pitch of WRF grid along coordinates x and y respectively of 1976.4 m and 2022.3 m (half pitch before the node and half pitch after the node in x and in y) and along z of 200 m.

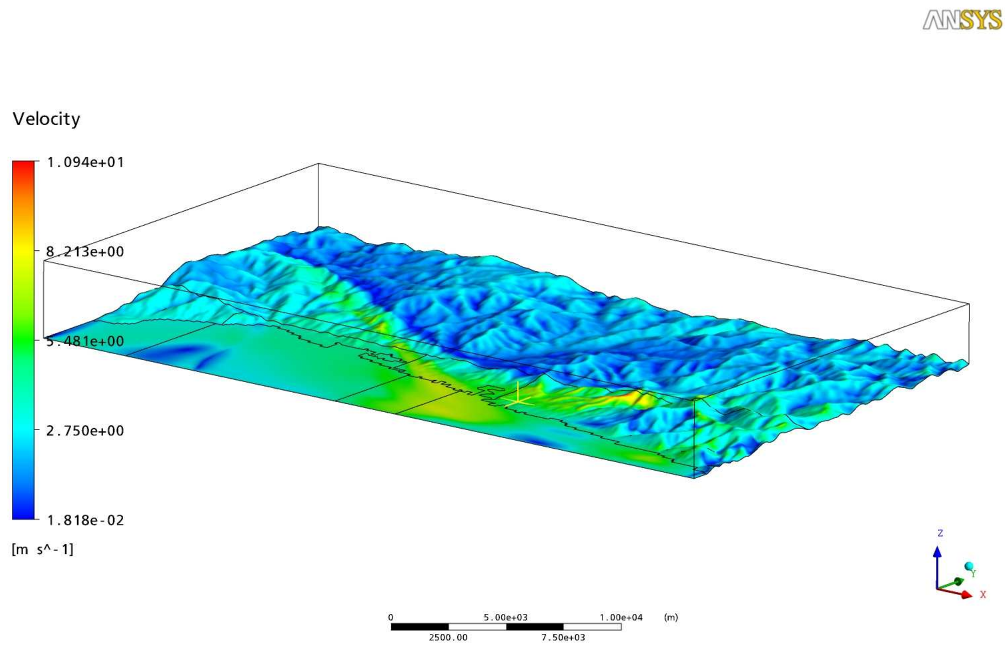

Figure 4.17: Simulation with wind velocity assigned to NORTH, EAST, SOUTH and WEST in OPENING configuration and thick mesh. Wind field at 10 m.

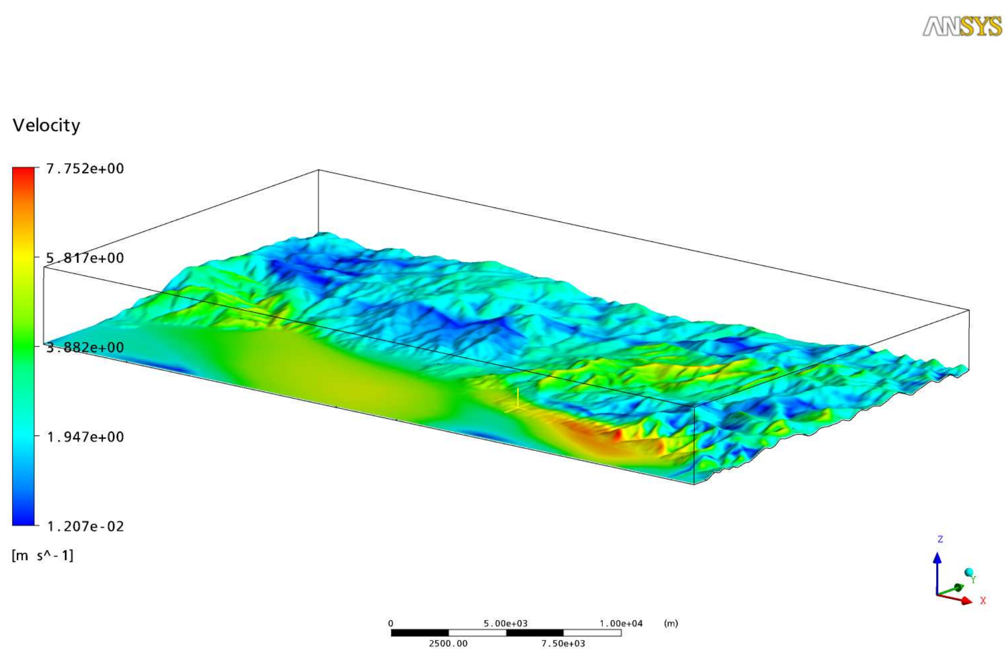

Figure 4.18: Simulation with wind velocity assigned to NORTH, EAST, SOUTH and WEST in OPENING configuration and coarse mesh. Wind field at 30 m.

I paied attention to velocities of points of lateral faces, where the boundary conditions are assigned by linear interpolation of WRF data, and to ones of points inside the domain, common between WRF grid (coarser) and CFX one (thicker).

Table 4.1: Simulation with wind velocity assigned to NORTH, EAST, SOUTH and WEST in OPENING configuration. U wind component. Normalized root mean square deviation (NRMSD) of U wind component on lateral faces and inside the domain of simulation.

region	U - NRMSD - coarse mesh	U - NRMSD - thick mesh
NORTH face	2.01	1.80
EAST face	0.11	0.11
SOUTH face	3.61	47.62
WEST face	7.17	7.23
INNER DOMAIN	8.73	18.29

Table 4.2: Simulation with wind velocity assigned to NORTH, EAST, SOUTH and WEST in OPENING configuration. V wind component. Normalized root mean square deviation (NRMSD) of V wind component on lateral faces and inside the domain of simulation.

region	V - NRMSD - coarse mesh	V - NRMSD - thick mesh
NORTH face	2.13	1.86
EAST face	0.34	0.32
SOUTH face	0.31	0.25
WEST face	2.16	2.17
INNER DOMAIN	3.21	3.17

Table 4.3: Simulation with wind velocity assigned to NORTH, EAST, SOUTH and WEST in OPENING configuration. W wind component. Normalized root mean square deviation (NRMSD) of W wind component on lateral faces and inside the domain of simulation.

region	W - NRMSD - coarse mesh	W - NRMSD - thick mesh
NORTH face	5.42	3.54
EAST face	10.64	5.31
SOUTH face	72600.93	101067.10
WEST face	633.23	1809.09
INNER DOMAIN	28022.94	26403.87

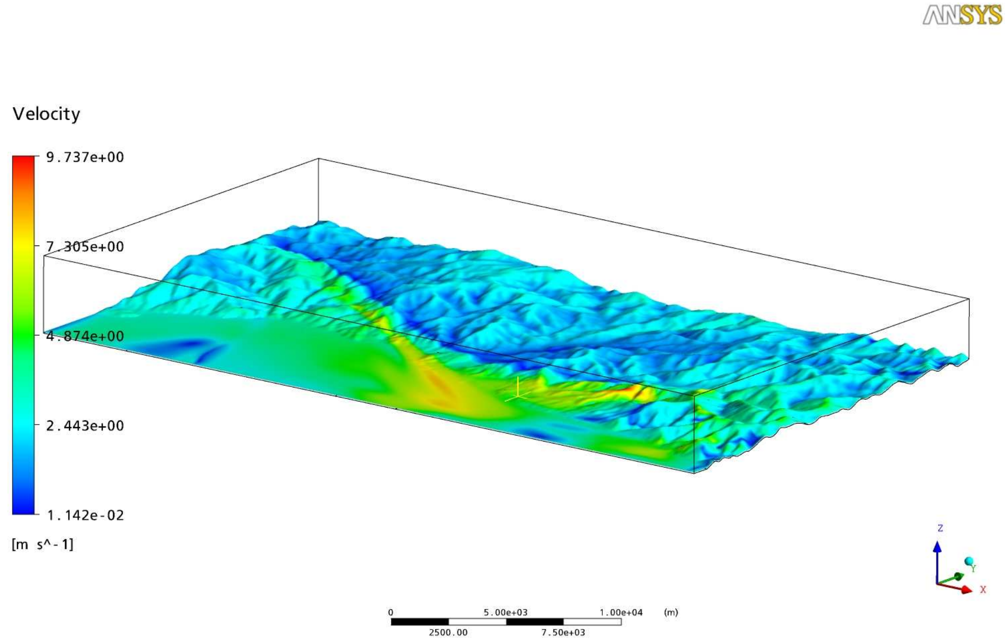

Figure 4.19: Simulation with wind velocity assigned to NORTH, EAST, SOUTH and WEST in OPENING configuration and thick mesh. Wind field at 30 m.

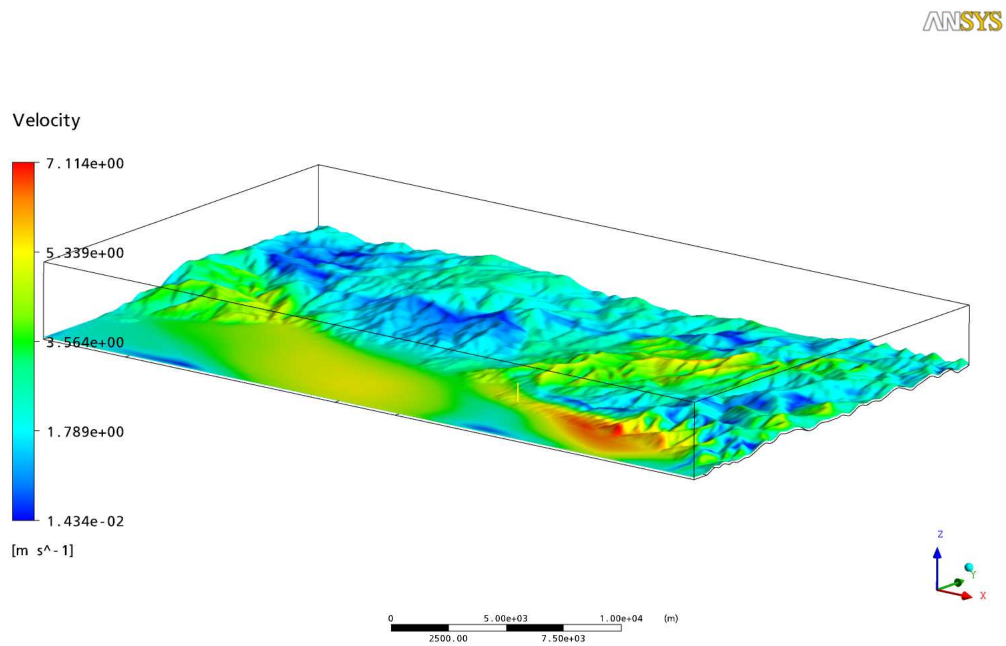

Figure 4.20: Simulation with wind velocity assigned to NORTH, EAST, SOUTH and WEST in OPENING configuration and coarse mesh. Wind field at 100 m.

Assessing the behaviour of the indicator (from table 4.1 to table 4.4), it is possible to observe that normalized root mean square deviation of wind components does not decrease noticeably passing from coarse grid to thick one; for W component its value

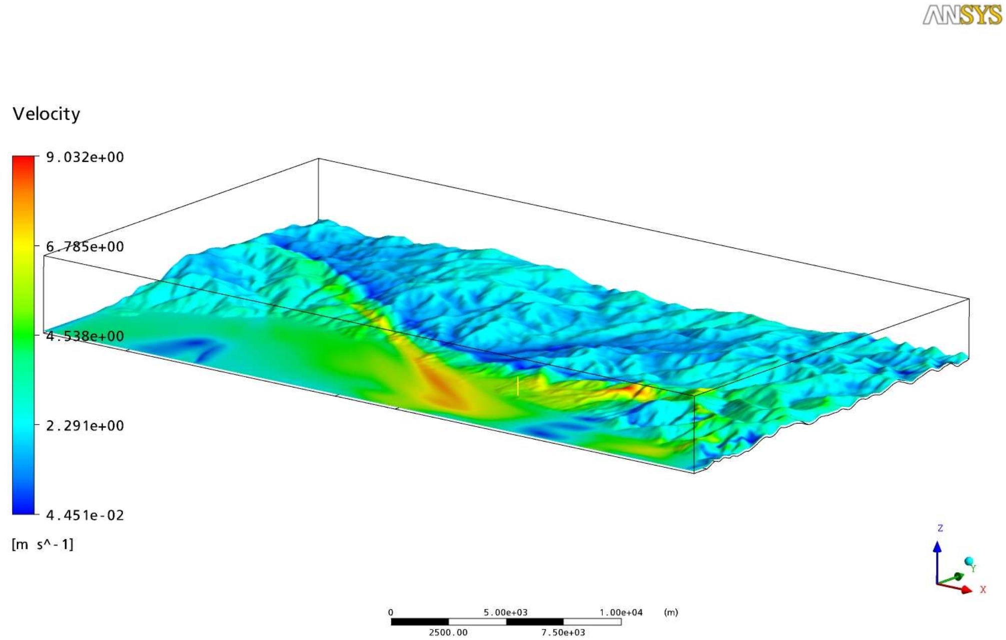

Figure 4.21: Simulation with wind velocity assigned to NORTH, EAST, SOUTH and WEST in OPENING configuration and thick mesh. Wind field at 100 m.

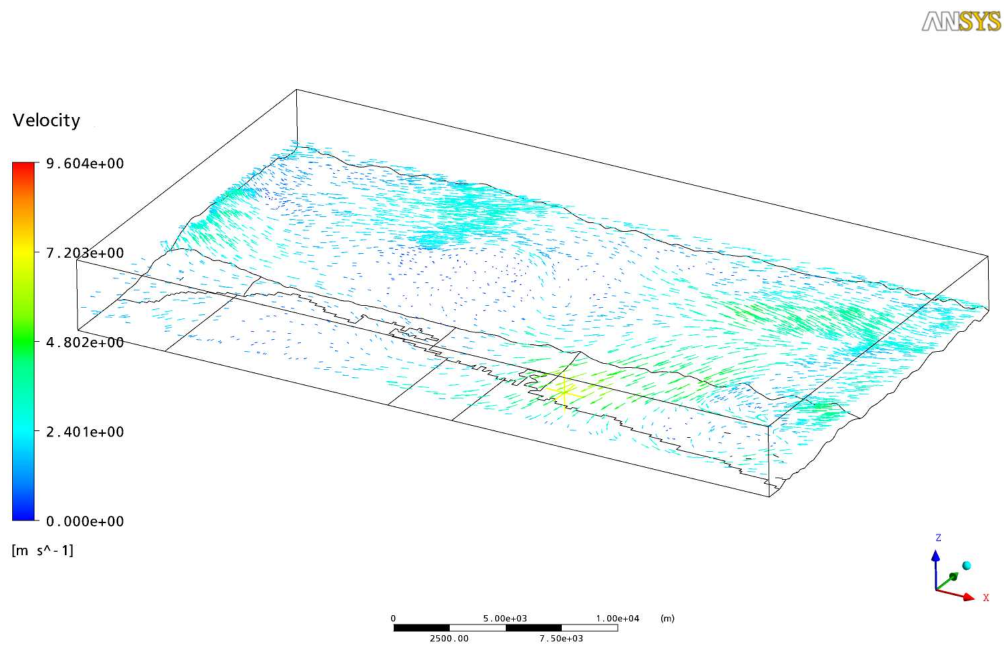

Figure 4.22: Simulation with wind velocity assigned to NORTH, EAST, SOUTH and WEST in OPENING configuration and coarse mesh. Wind field at 1000 m.

is very large. Moreover, the value of this indicator for wind intensity decreases in NORTH, EAST, WEST faces and inside the domain, where it becomes acceptable. In order to study more deeply the behaviour of the normalized root mean square

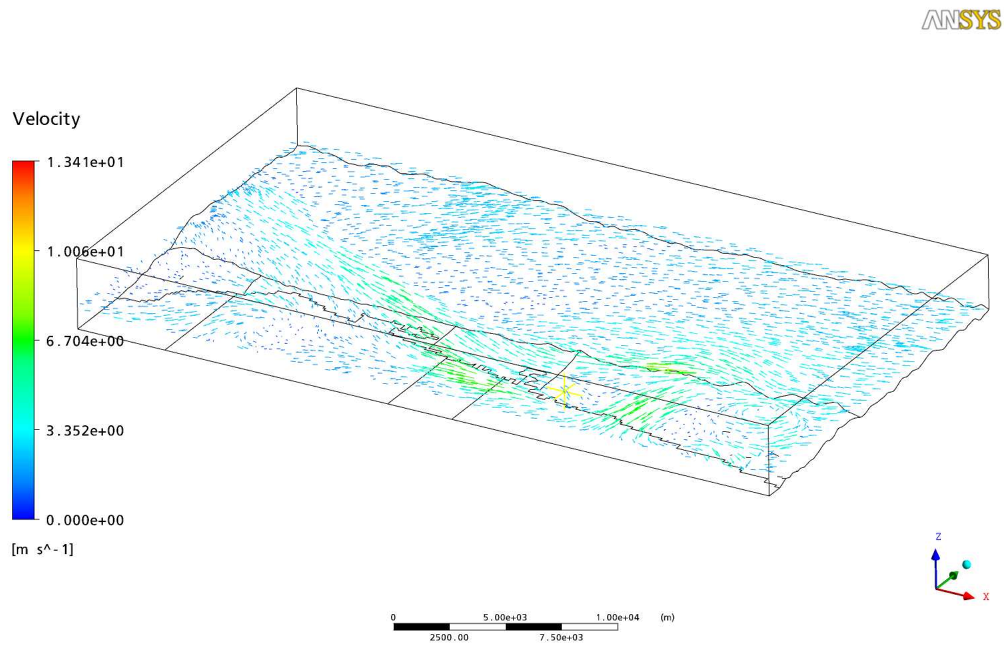

Figure 4.23: Simulation with wind velocity assigned to NORTH, EAST, SOUTH and WEST in OPENING configuration and thick mesh. Wind field at 1000 m.

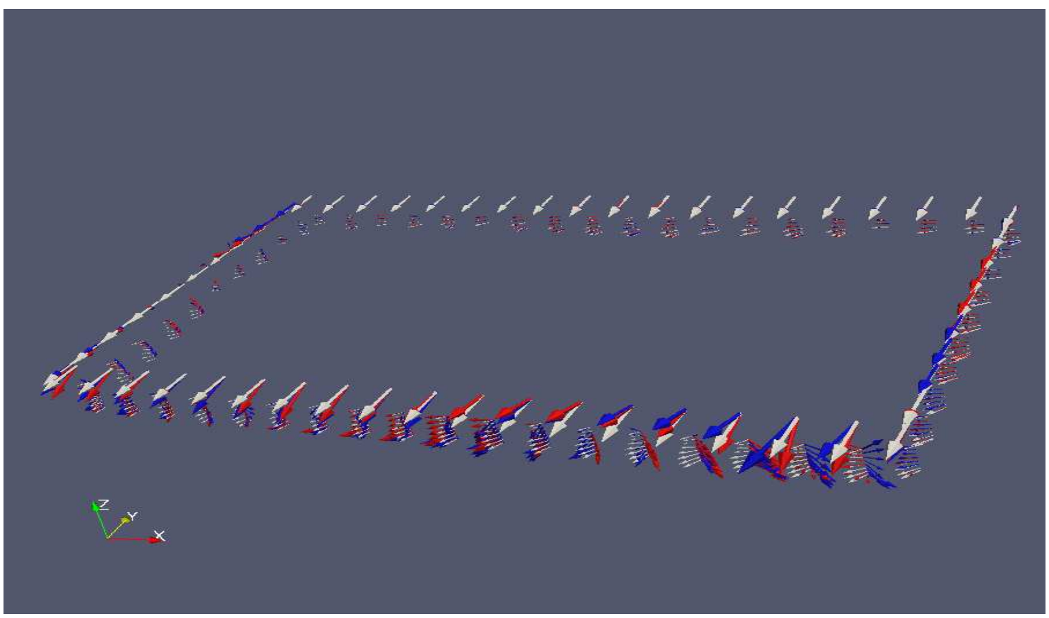

Figure 4.24: Simulation with wind velocity assigned to NORTH, EAST, SOUTH and WEST in OPENING configuration. Comparison between the velocity of CFX simulations and boundary conditions. Grey: WRF data. Red: results of simulation with coarse mesh. Blue: results of simulation with thick mesh.

deviation in the domain, I examined the trend of NRMSD for wind components and intensity in atmospheric layers; each atmospheric layer is 350 m deep.

Table 4.4: Simulation with wind velocity assigned to NORTH, EAST, SOUTH and WEST in OPENING configuration. Wind intensity. Normalized root mean square deviation (NRMSD) of wind intensity on lateral faces and inside the domain of simulation.

region	wind - NRMSD - coarse mesh	wind - NRMSD - thick mesh
NORTH face	0.13	0.12
EAST face	0.10	0.10
SOUTH face	0.73	0.90
WEST face	0.28	0.38
INNER DOMAIN	0.66	0.70

Table 4.5: Simulation with wind velocity assigned to NORTH, EAST, SOUTH and WEST in OPENING configuration. U wind component. Normalized root mean square deviation (NRMSD) of U wind component in atmospheric layers inside the domain of simulation. nn = missing data.

layer	U - NRMSD - coarse mesh	U - NRMSD - thick mesh
0 m - 350 m	1.29	1.26
350 m - 700 m	0.73	0.73
700 m - 1050 m	0.57	0.68
1050 m - 1400 m	0.53	0.82
1400 m - 1750 m	0.50	0.77
1750 m - 2100 m	nn	nn
2100 m - 2450 m	nn	nn
2450 m - 2800 m	nn	nn
2800 m - 3150 m	19.99	15.49
3150 m - 3500 m	32.86	92.16

Table 4.6: Simulation with wind velocity assigned to NORTH, EAST, SOUTH and WEST in OPENING configuration. V wind component. Normalized root mean square deviation (NRMSD) of V wind component in atmospheric layers inside the domain of simulation. nn = missing data.

layer	V - NRMSD - coarse mesh	V - NRMSD - thick mesh
0 m - 350 m	1.66	1.53
350 m - 700 m	1.34	1.39
700 m - 1050 m	1.51	1.98
1050 m - 1400 m	5.20	5.69
1400 m - 1750 m	4.60	2.69
1750 m - 2100 m	nn	nn
2100 m - 2450 m	nn	nn
2450 m - 2800 m	nn	nn
2800 m - 3150 m	0.30	0.37
3150 m - 3500 m	0.38	0.51

Table 4.7: Simulation with wind velocity assigned to NORTH, EAST, SOUTH and WEST in OPENING configuration. W wind component. Normalized root mean square deviation (NRMSD) of W wind component in atmospheric layers inside the domain of simulation. nn = missing data.

layer	W - NRMSD - coarse mesh	W - NRMSD - thick mesh
0 m - 350 m	7693.80	9751.06
350 m - 700 m	7862.79	8233.03
700 m - 1050 m	11470.68	12082.30
1050 m - 1400 m	46327.48	37507.18
1400 m - 1750 m	30021.06	26203.11
1750 m - 2100 m	nn	nn
2100 m - 2450 m	nn	nn
2450 m - 2800 m	nn	nn
2800 m - 3150 m	39.51	38.18
3150 m - 3500 m	55727.18	77982.70

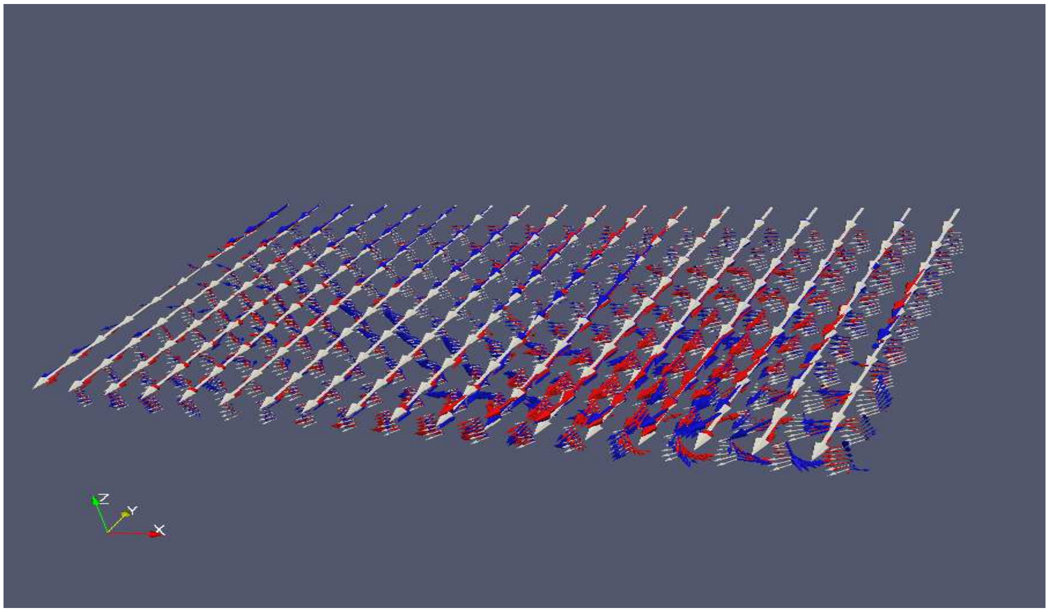

Figure 4.25: Simulation with wind velocity assigned to NORTH, EAST, SOUTH and WEST in OPENING configuration. Comparison between the velocity of CFX simulations and WRF data in inner domain. Grey: WRF data. Red: results of simulation with coarse mesh. Blue: results of simulation with thick mesh.

I used WRF with coarse resolution in z direction, there are not data (from table 4.5 to table 4.8) in halfway layers (from 1750 m to 2800 m). The values of normalized root mean square deviation are high again. The values are only partially satisfactory: for U component in bottom and middle layers, for V component in high layer; for the intensity of the wind the values of parameter are acceptable wherever.
At lower heights (from figure 4.26 to figure 4.28) the wind fields simulated by CFX computations are influenced by a complex orography and by a strong conditioning of lateral boundary conditions. Next to the sea the eddy configurations are shown. Besides there are some differences between the simulations with different mesh resolution. At higher elevations (figure 4.29) the wind fields simulated by CFX computations are similar, and there is a partial agreement between WRF data and simulation with coarse mesh, in the result of the simulation with thick mesh a singular wind configuration is highlighted over the sea.
Finally, I compared the output of simulations with direct measure, given by meteorological station (section 4.2).
The measurement of the station gave wind intensity of 3.9 m/s and wind direction of 45 °(calculated with respect to North).
The simulation with coarse grid gave:

- wind intensity = 5.6 m/s;
- wind direction = 182 °.

The simulation with thick grid provided:

- wind intensity = 5.1 m/s;

Table 4.8: Simulation with wind velocity assigned to NORTH, EAST, SOUTH and WEST in OPENING configuration. Wind intensity. Normalized root mean square deviation (NRMSD) of wind intensity in atmospheric layers inside the domain of simulation. nn = missing data.

layer	wind - NRMSD - coarse mesh	wind - NRMSD - thick mesh
0 m - 350 m	0.57	0.66
350 m - 700 m	0.42	0.47
700 m - 1050 m	0.42	0.56
1050 m - 1400 m	0.83	0.94
1400 m - 1750 m	1.08	0.95
1750 m - 2100 m	nn	nn
2100 m - 2450 m	nn	nn
2450 m - 2800 m	nn	nn
2800 m - 3150 m	0.29	0.31
3150 m - 3500 m	0.37	0.43

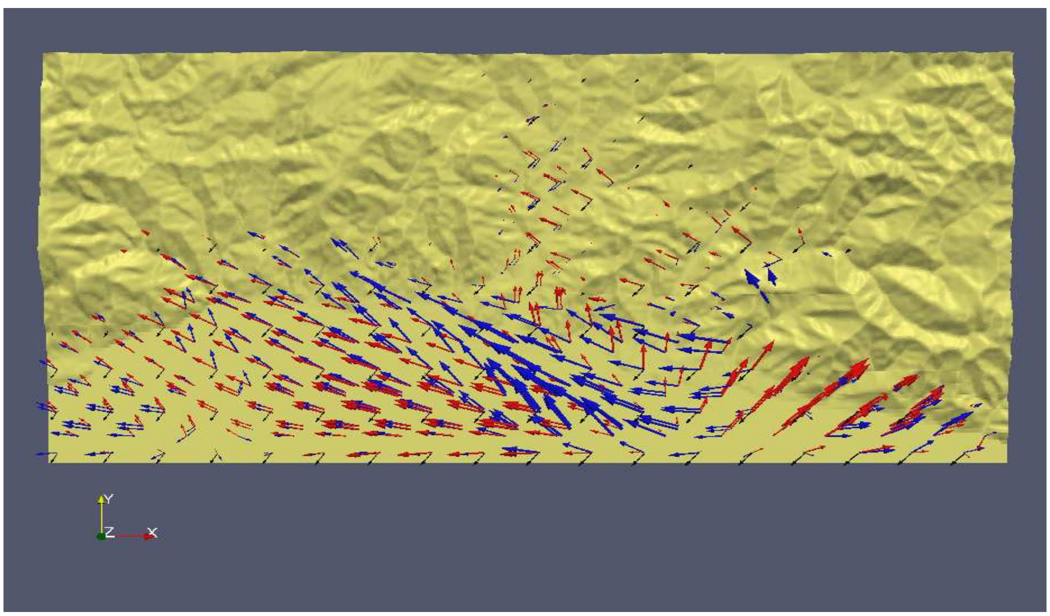

Figure 4.26: Simulation with wind velocity assigned to NORTH, EAST, SOUTH and WEST in OPENING configuration. Comparison between the velocity of CFX simulations and WRF data at height of 160 m. Black: WRF data. Red: results of simulation with coarse mesh. Blue: results of simulation with thick mesh.

- wind direction = 111 °.

Both simulations enable to detect the order of magnitude of wind intensity, overestimating the value; whereas there is a discrepancy between the computation and the

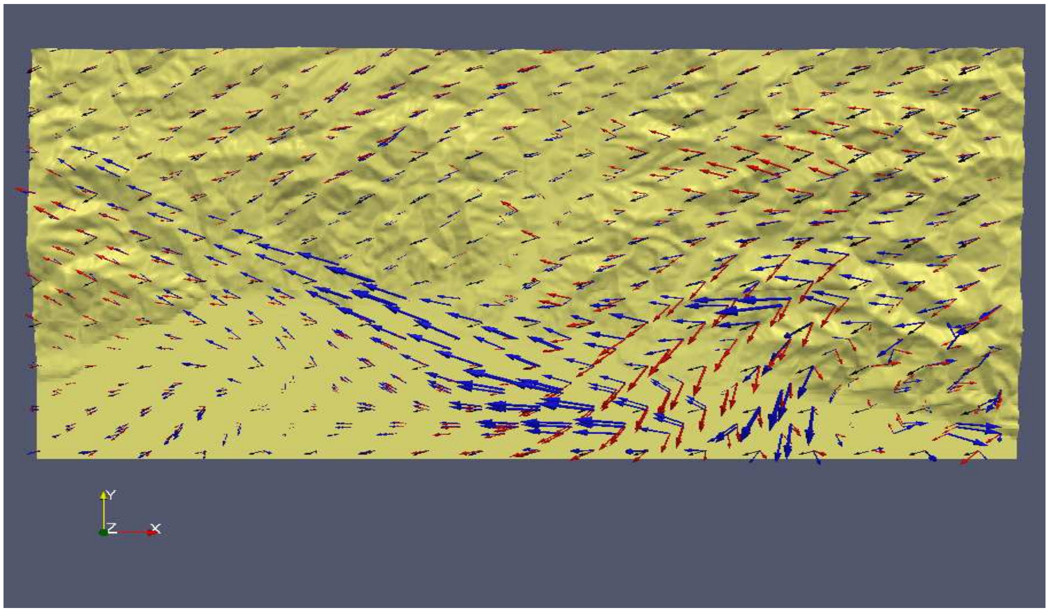

Figure 4.27: Simulation with wind velocity assigned to NORTH, EAST, SOUTH and WEST in OPENING configuration. Comparison between the velocity of CFX simulations and WRF data at height of 880 m. Black: WRF data. Red: results of simulation with coarse mesh. Blue: results of simulation with thick mesh.

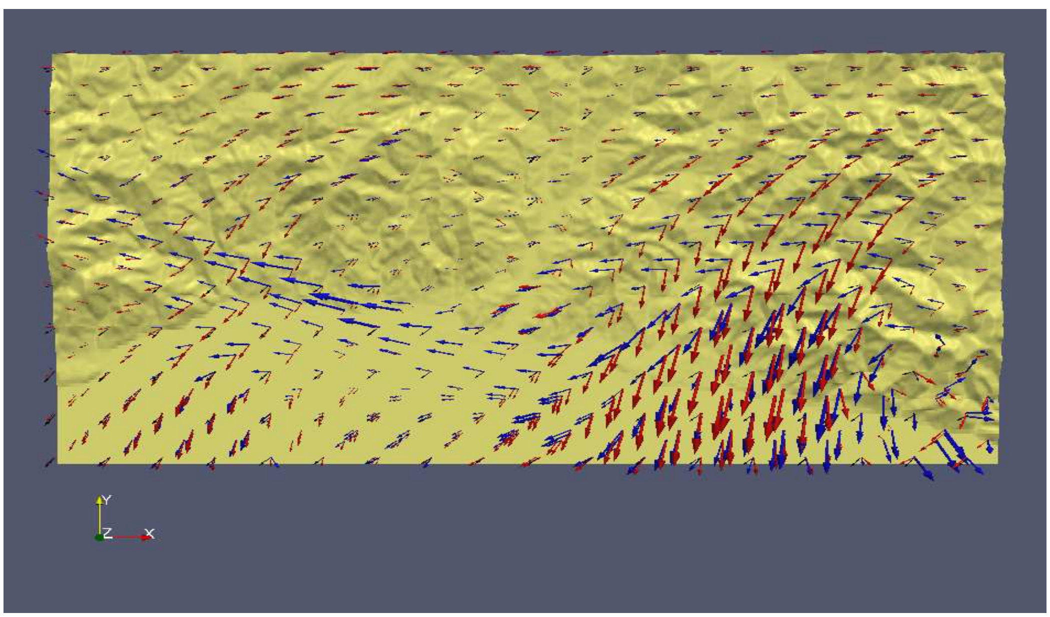

Figure 4.28: Simulation with wind velocity assigned to NORTH, EAST, SOUTH and WEST in OPENING configuration. Comparison between the velocity of CFX simulations and WRF data at height of 1520 m. Black: WRF data. Red: results of simulation with coarse mesh. Blue: results of simulation with thick mesh.

measure for the wind direction. Besides, a dependence of grid resolution, especially

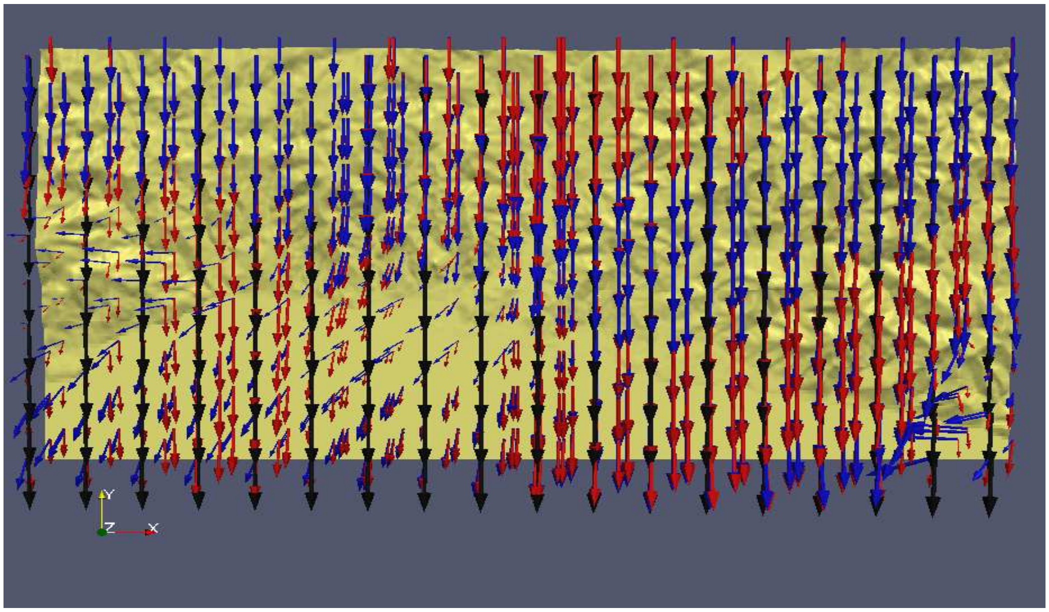

Figure 4.29: Simulation with wind velocity assigned to NORTH, EAST, SOUTH and WEST in OPENING configuration. Comparison between the velocity of CFX simulations and WRF data at height of 3100 m. Black: WRF data. Red: results of simulation with coarse mesh. Blue: results of simulation with thick mesh.

in direction of wind velocity, can be observed.

4.5.2.2 Velocity on three lateral faces

In this simulation I used only the mesh with coarse resolution to reduce the computational time.
According to the previous calculations (section 4.5.2.1), the computation was stationary, isothermal with temperature of 280 K and incompressible. The fluid was set as ideal gas and the turbulence model chosen was $k - \omega$.
The reference pression was $p_0 = 89999.2$ Pa, and it corrisponded to the minimun value of the wind intensity on the lateral faces of the domain.
Boundary conditions for NORTH, EAST and SOUTH lateral faces were the wind velocities (U, V, W components) in OPENING configuration. WEST lateral face and SKY were set in OPENING configuration with relative static pressure of -1000 Pa.
The surfaces of sea and land (coastal zone and mountains) were WALLS with friction.
The computation was structured with a high resolution scheme. It converged after 750 iterations and order of the residuals was 10^{-4}, obtained by observing rate of flow going in and out the box.
As the other cases, a qualitative control was carried out, examining the wind fields provided by CFX simulation at heights of 10 m, 30 m, 100 m and 1000 m (from figure 4.30 to figure 4.33).

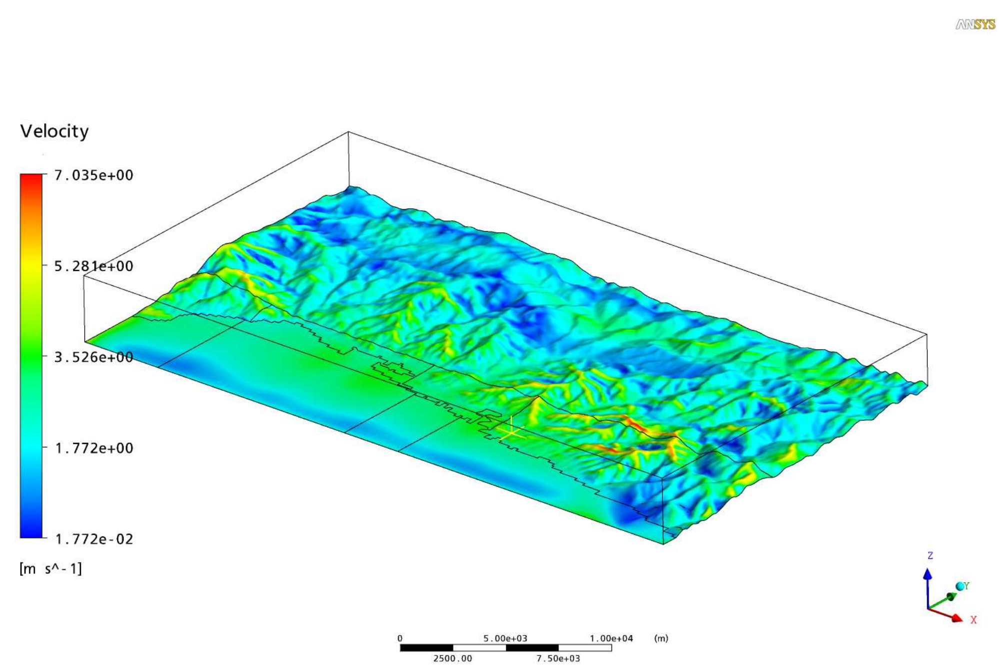

Figure 4.30: Simulation with wind velocity assigned to NORTH, EAST and SOUTH in OPENING configuration and coarse mesh. Wind field at 10 m.

The wind fields are plausible over the mountain and partially plausible next to the coastal zone and the sea, where there is a large area with a bigger velocity in comparison to surrounding zones.

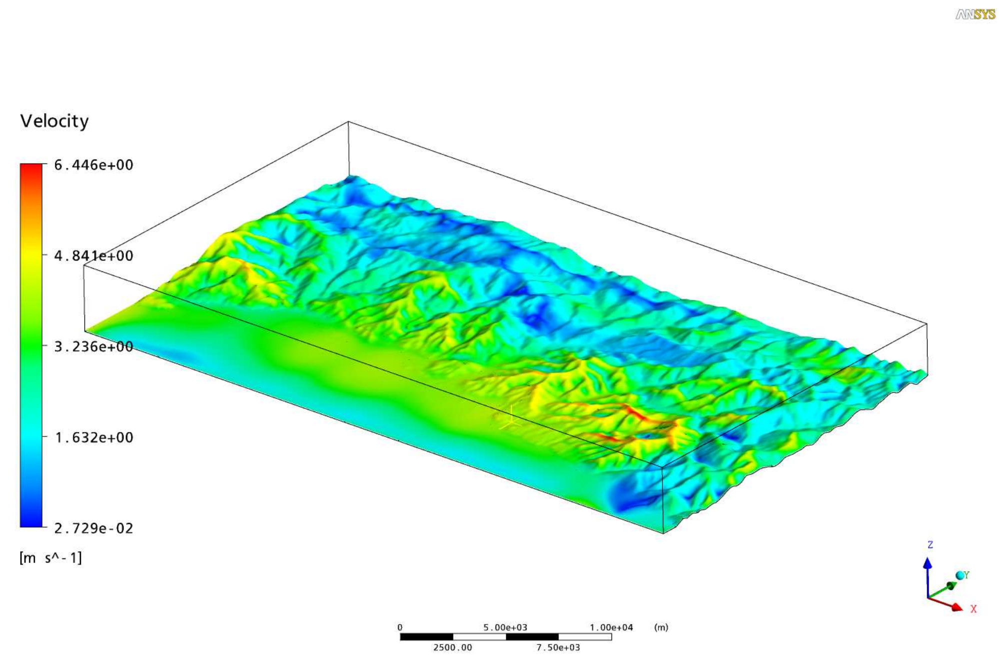

Figure 4.31: Simulation with wind velocity assigned to NORTH, EAST and SOUTH in OPENING configuration and coarse mesh. Wind field at 30 m.

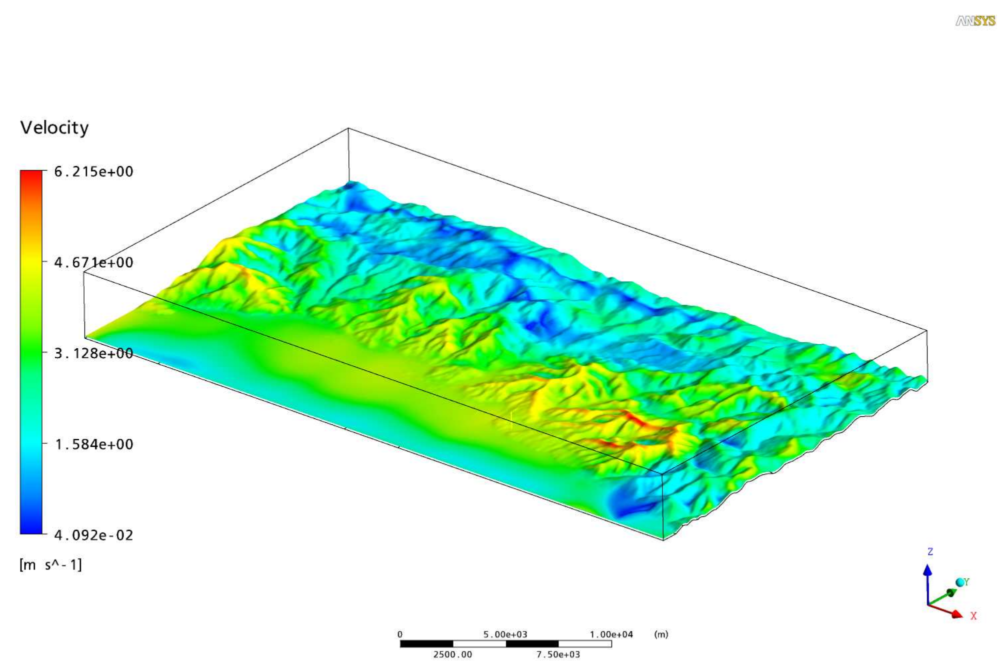

Figure 4.32: Simulation with wind velocity assigned to NORTH, EAST and SOUTH in OPENING configuration and coarse mesh. Wind field at 100 m.

Moreover, the first comparisons between CFX simulation and WRF output were executed. I paied attention to wind velocity on points of lateral faces and in inner

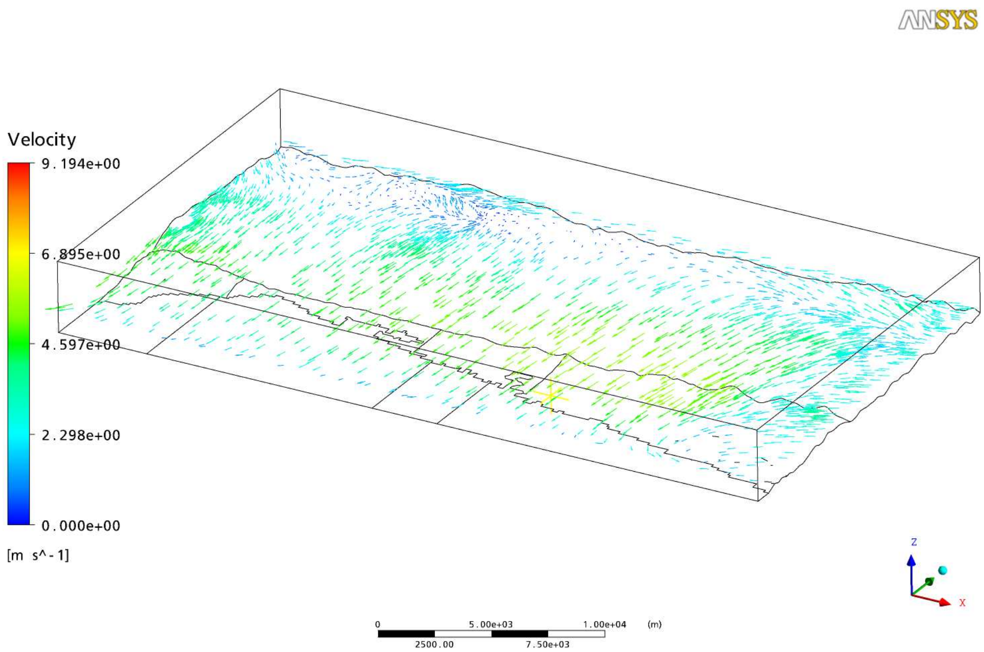

Figure 4.33: Simulation with wind velocity assigned to NORTH, EAST and SOUTH in OPENING configuration and coarse mesh. Wind field at 1000 m.

domain (figures 4.34 and 4.35).

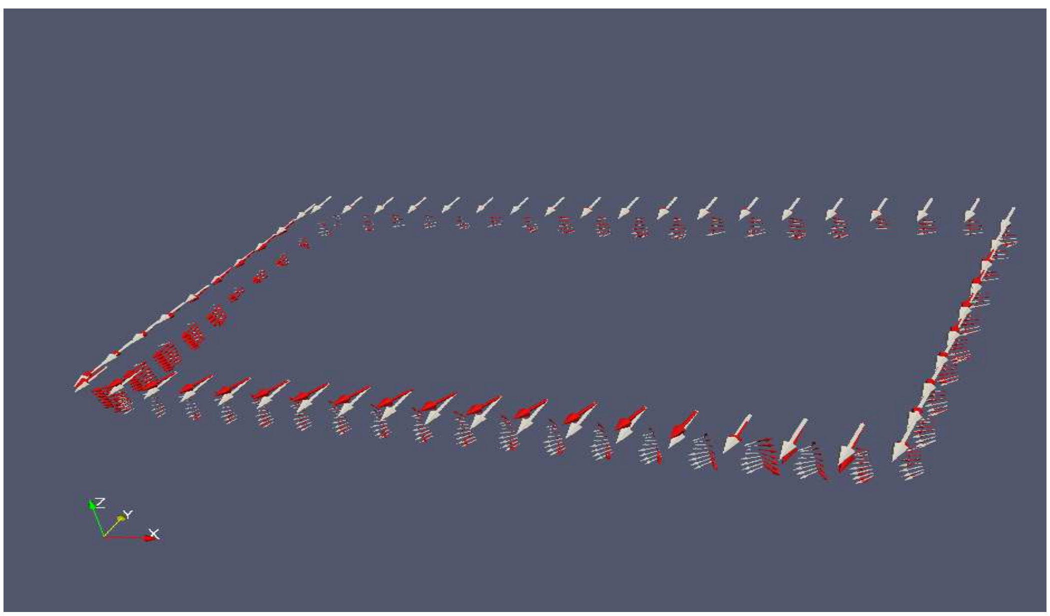

Figure 4.34: Simulation with wind velocity assigned to NORTH, EAST and SOUTH in OPENING configuration. Comparison between the velocity of CFX simulation and WRF data on lateral faces. Grey: WRF data. Red: results of simulation with coarse mesh.

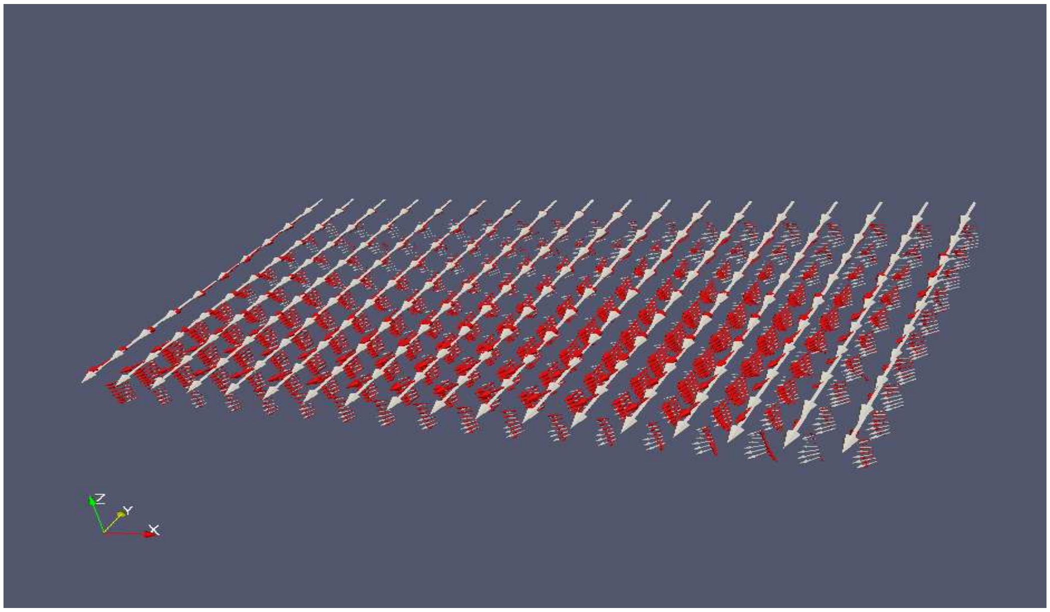

Figure 4.35: Simulation with wind velocity assigned to NORTH, EAST and SOUTH in OPENING configuration. Comparison between the velocity of CFX simulation and WRF data in inner domain. Grey: WRF data. Red: results of simulation with coarse mesh.

In detail, I calculated the normalized root mean square deviation (NRMSD) between WRF and CFX wind velocity components and intensity for each lateral face and for the space inside the domain.
The values of the normalized root mean square deviation of the wind components are high enough (from table 4.9 to table 4.12) with a few exceptions: only for U component on EAST face, for V component on EAST and SOUTH faces they are reasonable; for W component its values are very large. The parameter becomes acceptable for wind intensity in NORTH, EAST and SOUTH faces.
Then, I examined the trend of NRMSD for components and intensity of wind in atmospheric layers; each atmospheric layer is 350 m deep.
The values of normalized root mean square deviation are not acceptable everywhere (from table 4.13 to table 4.16), but only partially. For U component they are reasonable in bottom and halfway layers, for V component in higher layer and for the intensity of the wind they decrease in higher layer and they assume acceptable values.
At lower heights (from figure 4.36 to figure 4.38) the wind fields simulated by CFX computation are influenced by complex orography and by strong conditioning applied to the lateral boundary conditions. At higher elevations (figure 4.39) the wind fields simulated by CFX computation are in agreement with WRF data.
Finally, I compared the output of simulation with direct measure. The computation result was as follows:

- wind intensity = 4.0 m/s;
- wind direction = 6 °.

Table 4.9: Simulation with wind velocity assigned to NORTH, EAST and SOUTH in OPENING configuration. U wind component. Normalized root mean square deviation (NRMSD) of U wind component on lateral faces and inside the domain of simulation.

region	U - NRMSD - coarse mesh
NORTH face	2.16
EAST face	0.12
SOUTH face	12.50
WEST face	26.01
INNER DOMAIN	5.08

Table 4.10: Simulation with wind velocity assigned to NORTH, EAST and SOUTH in OPENING configuration. V wind component. Normalized root mean square deviation (NRMSD) of V wind component on lateral faces and inside the domain of simulation.

region	V - NRMSD - coarse mesh
NORTH face	1.64
EAST face	0.35
SOUTH face	0.38
WEST face	7.96
INNER DOMAIN	7.36

Table 4.11: Simulation with wind velocity assigned to NORTH, EAST and SOUTH in OPENING configuration. W wind component. Normalized root mean square deviation (NRMSD) of W wind component on lateral faces and inside the domain of simulation.

region	W - NRMSD - coarse mesh
NORTH face	15.65
EAST face	10.80
SOUTH face	58326.82
WEST face	213.61
INNER DOMAIN	35772.50

Table 4.12: Simulation with wind velocity assigned to NORTH, EAST and SOUTH in OPENING configuration. Wind intensity. Normalized root mean square deviation (NRMSD) of wind intensity on lateral faces and inside the domain of simulation.

region	wind - NRMSD - coarse mesh
NORTH face	0.19
EAST face	0.13
SOUTH face	0.33
WEST face	1.57
INNER DOMAIN	1.11

Table 4.13: Simulation with wind velocity assigned to NORTH, EAST and SOUTH in OPENING configuration. U wind component. Normalized root mean square deviation (NRMSD) of U wind component in atmospheric layers inside the domain of simulation. nn = missing data.

layer	U - NRMSD - coarse mesh
0 m - 350 m	0.82
350 m - 700 m	0.80
700 m - 1050 m	0.78
1050 m - 1400 m	0.74
1400 m - 1750 m	0.72
1750 m - 2100 m	nn
2100 m - 2450 m	nn
2450 m - 2800 m	nn
2800 m - 3150 m	13.06
3150 m - 3500 m	16.38

Table 4.14: Simulation with wind velocity assigned to NORTH, EAST and SOUTH in OPENING configuration. V wind component. Normalized root mean square deviation (NRMSD) of V wind component in atmospheric layers inside the domain of simulation. nn = missing data.

layer	V - NRMSD - coarse mesh
0 m - 350 m	0.98
350 m - 700 m	1.43
700 m - 1050 m	4.44
1050 m - 1400 m	12.60
1400 m - 1750 m	9.95
1750 m - 2100 m	nn
2100 m - 2450 m	nn
2450 m - 2800 m	nn
2800 m - 3150 m	0.24
3150 m - 3500 m	0.33

Table 4.15: Simulation with wind velocity assigned to NORTH, EAST and SOUTH in OPENING configuration. W wind component. Normalized root mean square deviation (NRMSD) of W wind component in atmospheric layers inside the domain of simulation. nn = missing data.

layer	W - NRMSD - coarse mesh
0 m - 350 m	948.25
350 m - 700 m	2735.56
700 m - 1050 m	17506.23
1050 m - 1400 m	42228.14
1400 m - 1750 m	60331.44
1750 m - 2100 m	nn
2100 m - 2450 m	nn
2450 m - 2800 m	nn
2800 m - 3150 m	55.07
3150 m - 3500 m	96590.33

Table 4.16: Simulation with wind velocity assigned to NORTH, EAST and SOUTH in OPENING configuration. Wind intensity. Normalized root mean square deviation (NRMSD) of wind intensity in atmospheric layers inside the domain of simulation. nn = missing data.

layer	wind - NRMSD - coarse mesh
0 m - 350 m	0.49
350 m - 700 m	0.52
700 m - 1050 m	0.84
1050 m - 1400 m	1.62
1400 m - 1750 m	1.77
1750 m - 2100 m	nn
2100 m - 2450 m	nn
2450 m - 2800 m	nn
2800 m - 3150 m	0.23
3150 m - 3500 m	0.31

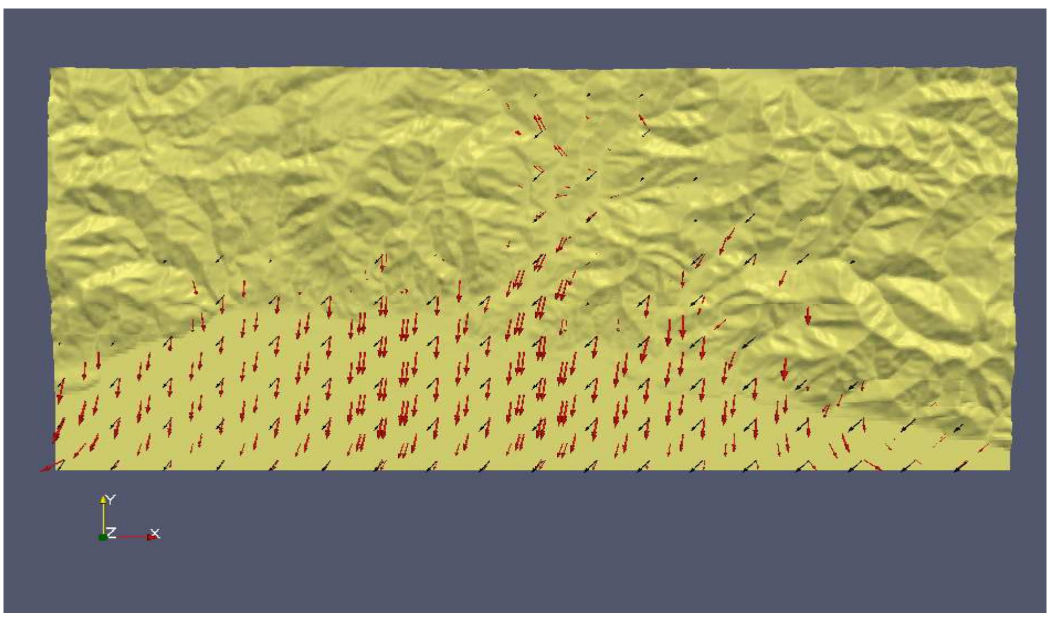

Figure 4.36: Simulation with wind velocity assigned to NORTH, EAST and SOUTH in OPENING configuration. Comparison between the velocity of CFX simulation and WRF data at height of 160 m. Black: WRF data. Red: results of simulation with coarse mesh.

The measurement of the station gave wind intensity of 3.9 m/s and wind direction of 45 °(calculated with respect to North), as written before. Therefore, the simulation enables to identify the wind intensity and the angular sector, from which the

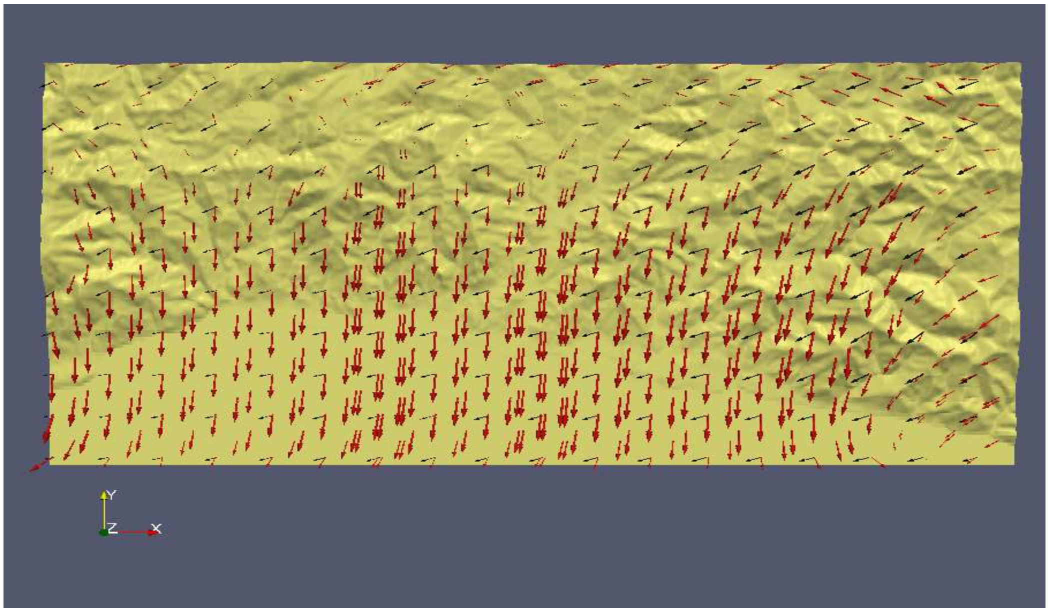

Figure 4.37: Simulation with wind velocity assigned to NORTH, EAST and SOUTH in OPENING configuration. Comparison between the velocity of CFX simulations and WRF data at height of 880 m. Black: WRF data. Red: results of simulation with coarse mesh.

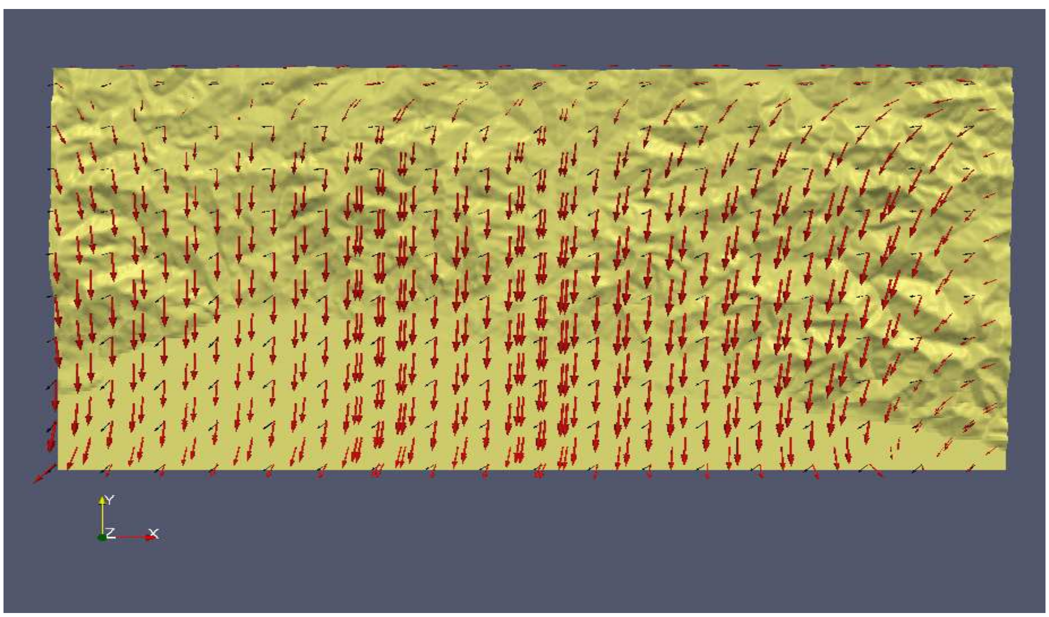

Figure 4.38: Simulation with wind velocity assigned to NORTH, EAST and SOUTH in OPENING configuration. Comparison between the velocity of CFX simulations and WRF data at height of 1520 m. Black: WRF data. Red: results of simulation with coarse mesh.

wind comes (North-East), is detected by simulation; but the discrepancy from the

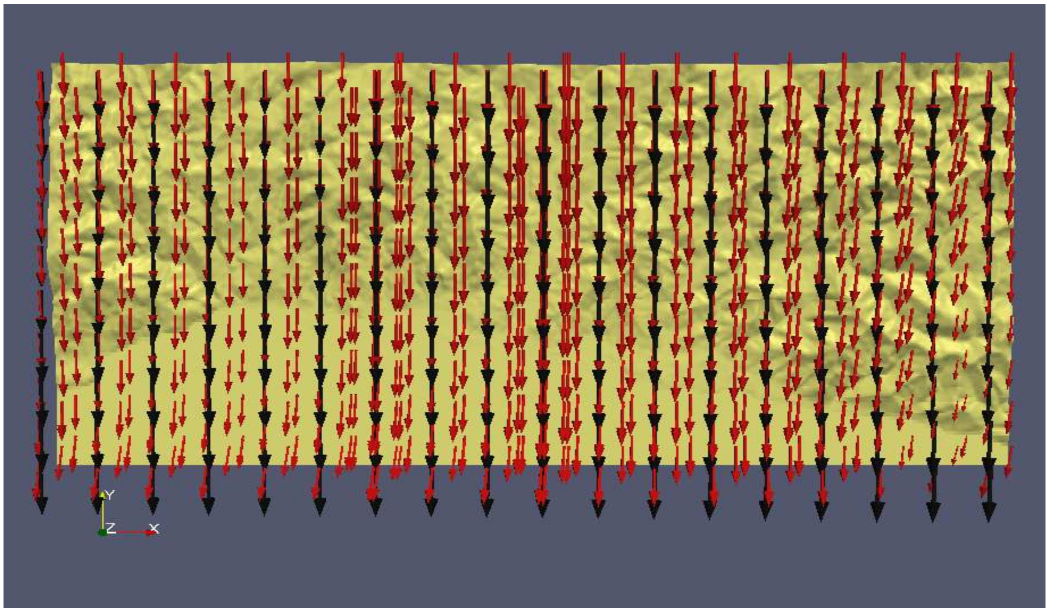

Figure 4.39: Simulation with wind velocity assigned to NORTH, EAST and SOUTH in OPENING configuration. Comparison between the velocity of CFX simulations and WRF data at height of 3100 m. Black: WRF data. Red: results of simulation with coarse mesh.

measurement is about 40 °.

4.5.2.3 Velocity on two lateral faces

In order to improve the precedent results (sections 4.5.2.1 and 4.5.2.2) and to verify another configuration of computational set, the boundary conditions in CFX simulation were changed. Both the meshes were used in order to compare CFX outputs, obtained by grids with different resolution, and WRF data.

Both computations were stationary, isothermal with temperature of 280 K and incompressible. The fluid was set as ideal gas and the turbulence model chosen was $k - \omega$.

The reference pression was $p_0 = 89999.2$ Pa, and it corrisponded to the minimun value of the wind intensity on the lateral faces of the domain.

The boundary conditions for NORTH and EAST lateral faces are the wind velocities (U, V, W components) in OPENING configuration. SOUTH, WEST lateral faces and SKY are set in OPENING configuration with relative static pressure of -1000 Pa.

The surfaces of sea and land (coastal zone and mountains) are WALLS with friction.

The computations were structured with a high resolution scheme. They converged after 750 iterations and the order of the residuals was 10^{-4}.

As the last cases, a qualitative control was made, examining the wind fields provided by CFX simulation at the heights of 10 m, 30 m, 100 m and 1000 m (from figure 4.40 to figure 4.47).

The wind fields are similar over the land (coastal zone and mountains) and they are

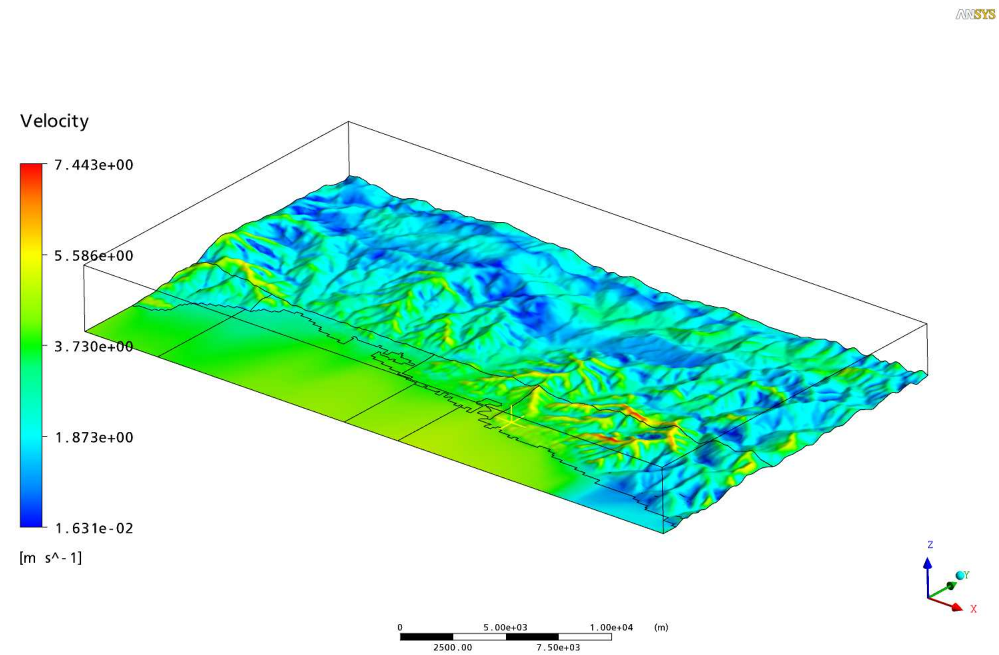

Figure 4.40: Simulation with wind velocity assigned to NORTH and EAST in OPENING configuration and coarse mesh. Wind field at 10 m.

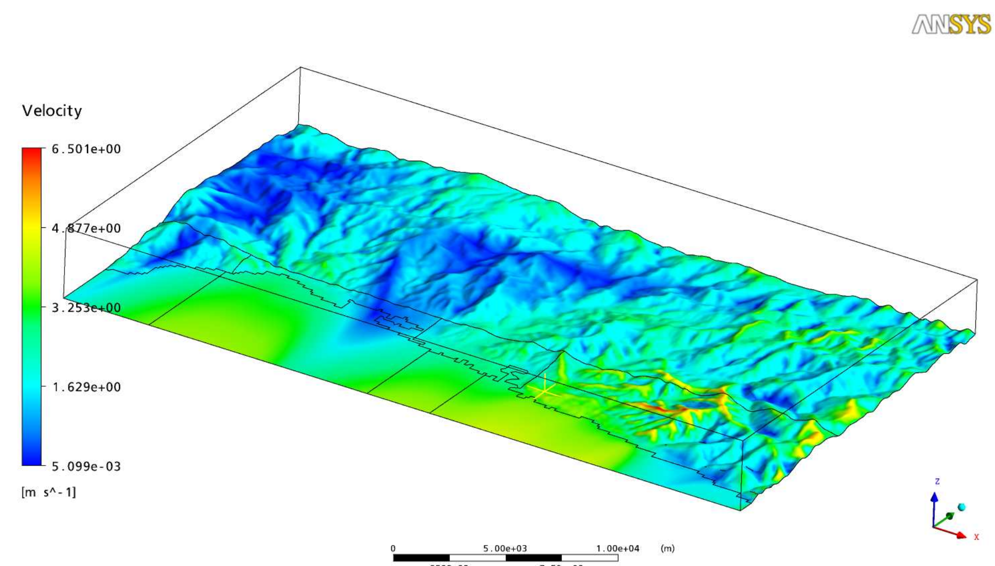

Figure 4.41: Simulation with wind velocity assigned to NORTH and EAST in OPENING configuration and thick mesh. Wind field at 10 m.

plausible; next to the sea the particular eddies are formed: in two large structures for the simulation with coarse mesh, in an intensive structure in the middle and in a small structure in est sea for the case with thick mesh, in similarity to simulation with the wind velocity assigned to all lateral faces (section 4.5.2.1).
Moreover, the first comparisons between CFX simulation and WRF outputs were

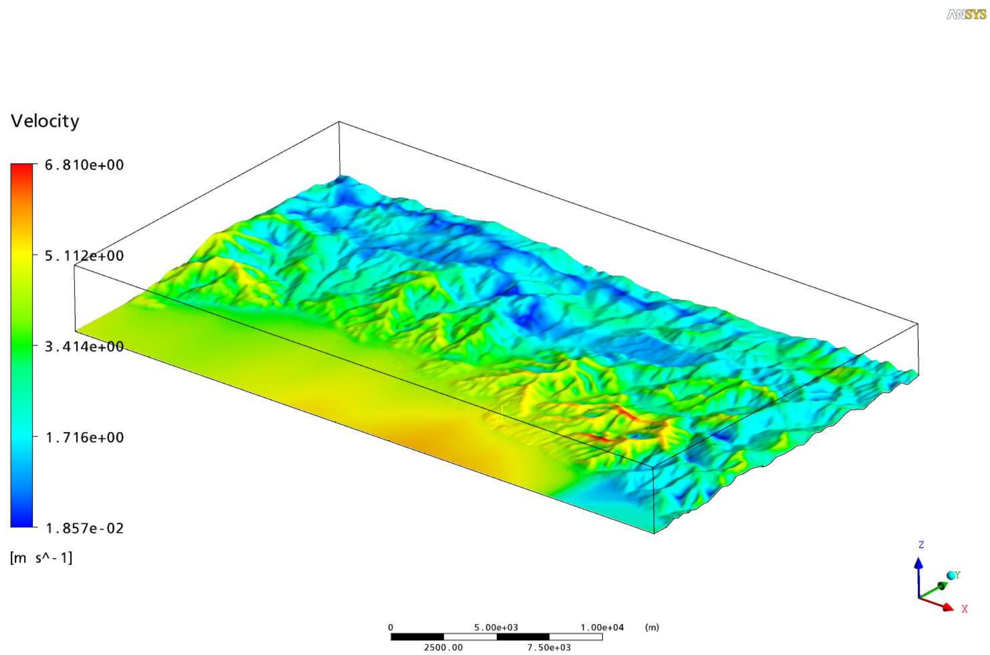

Figure 4.42: Simulation with wind velocity assigned to NORTH and EAST in OPENING configuration and coarse mesh. Wind field at 30 m.

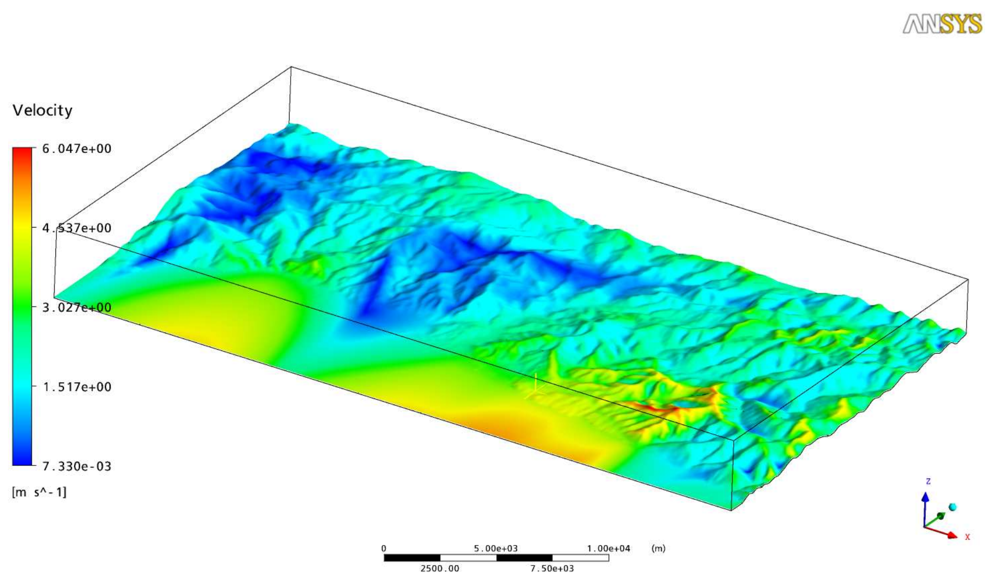

Figure 4.43: Simulation with wind velocity assigned to NORTH and EAST in OPENING configuration and thick mesh. Wind field at 30 m.

executed. I paied attention to wind velocity on points of lateral faces and in inner domain (figures 4.48 and 4.49).
According to previous simulations, I calculated the normalized root mean square deviation (NRMSD) between the WRF and CFX wind velocity components and the intensity for each lateral face and for the space inside the domain.

Table 4.17: Simulation with wind velocity assigned to NORTH and EAST in OPENING configuration. U wind component. Normalized root mean square deviation (NRMSD) of U wind component on lateral faces and inside the domain of simulation.

region	U - NRMSD - coarse mesh	U - NRMSD - thick mesh
NORTH face	2.16	1.81
EAST face	0.12	0.11
SOUTH face	4.15	0.72
WEST face	27.37	17.18
INNER DOMAIN	4.71	2.44

Table 4.18: Simulation with wind velocity assigned to NORTH and EAST in OPENING configuration. V wind component. Normalized root mean square deviation (NRMSD) of V wind component on lateral faces and inside the domain of simulation.

region	V - NRMSD - coarse mesh	V - NRMSD - thick mesh
NORTH face	1.64	1.87
EAST face	0.35	0.31
SOUTH face	7.35	7.01
WEST face	8.82	4.80
INNER DOMAIN	8.08	6.30

Table 4.19: Simulation with wind velocity assigned to NORTH and EAST in OPENING configuration. W wind component. Normalized root mean square deviation (NRMSD) of W wind component on lateral faces and inside the domain of simulation.

region	W - NRMSD - coarse mesh	W - NRMSD - thick mesh
NORTH face	15.64	4.27
EAST face	10.49	11.11
SOUTH face	3457.66	9345.06
WEST face	350.52	130.33
INNER DOMAIN	1350.38	8244.77

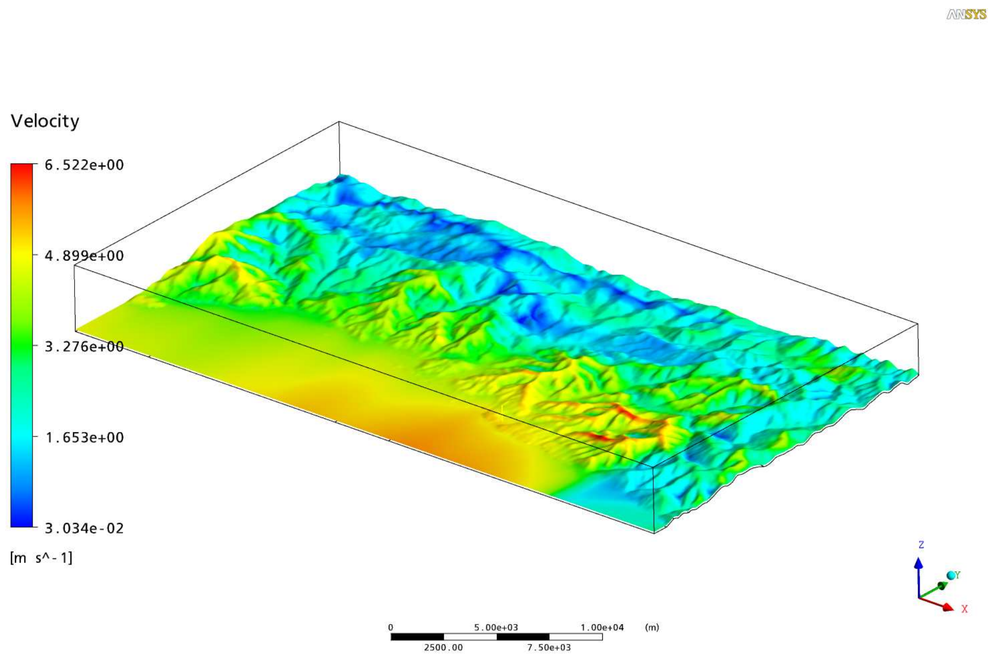

Figure 4.44: Simulation with wind velocity assigned to NORTH and EAST in OPENING configuration and coarse mesh. Wind field at 100 m.

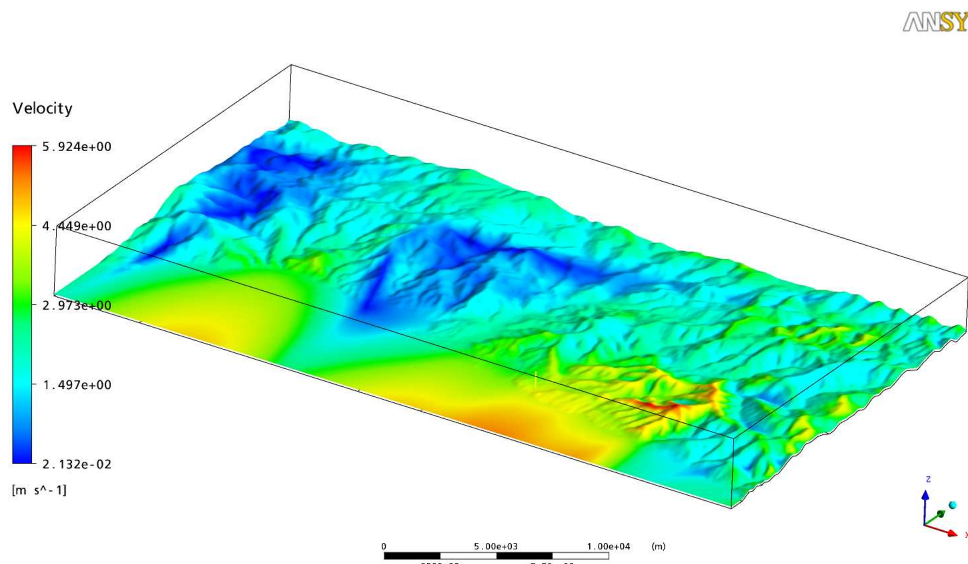

Figure 4.45: Simulation with wind velocity assigned to NORTH and EAST in OPENING configuration and thick mesh. Wind field at 100 m.

When assessing the behaviour of the indicator (from table 4.17 to table 4.20), it is possible to observe that the normalized root mean square deviation of the wind components and intensity decreases when passing from the coarse to the thick grid with some exceptions for the wind components. As the precedent simulations, the values of indicator for W component are very large. Besides, the values of indicator

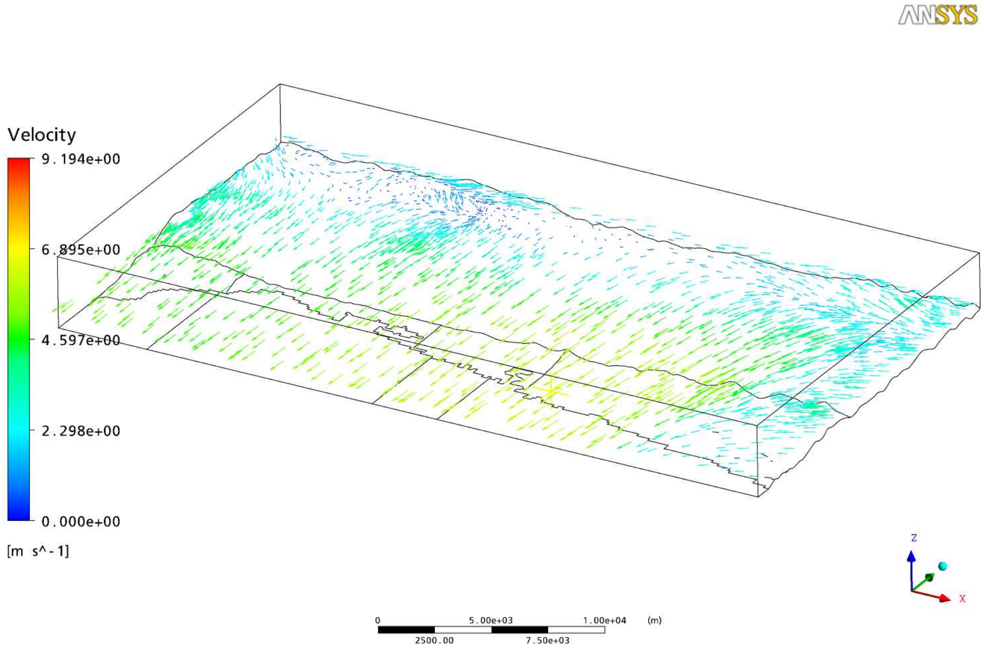

Figure 4.46: Simulation with wind velocity assigned to NORTH and EAST in OPENING configuration and coarse mesh. Wind field at 1000 m.

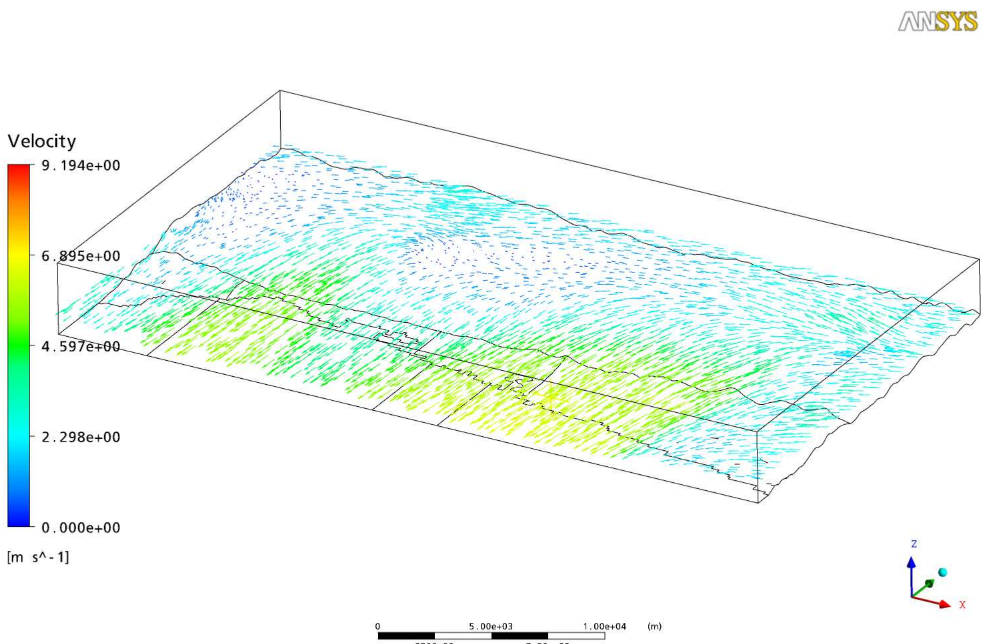

Figure 4.47: Simulation with wind velocity assigned to NORTH and EAST in OPENING configuration and thick mesh. Wind field at 1000 m.

are acceptable for the intensity of the wind only in NORTH and EAST faces.
Similarly to the previous situations, I examined the trend of NRMSD for the components and the intensity of wind in the atmospheric layers; each atmospheric layer

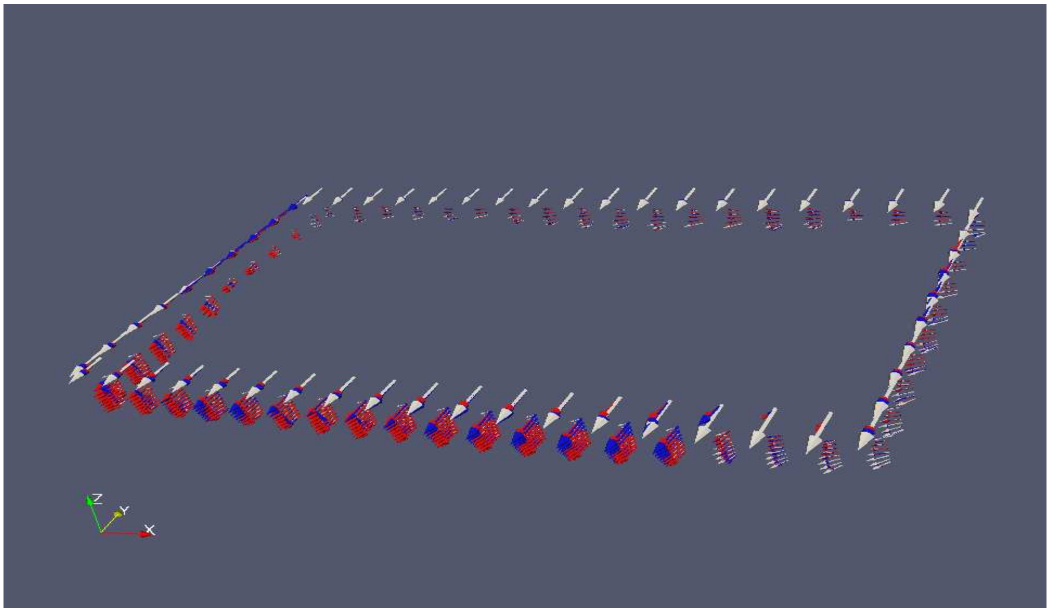

Figure 4.48: Simulation with wind velocity assigned to NORTH and EAST in OPENING configuration. Comparison between the velocity of CFX simulations and WRF data on lateral faces. Grey: WRF data. Red: results of simulation with coarse mesh. Blue: results of simulation with thick mesh.

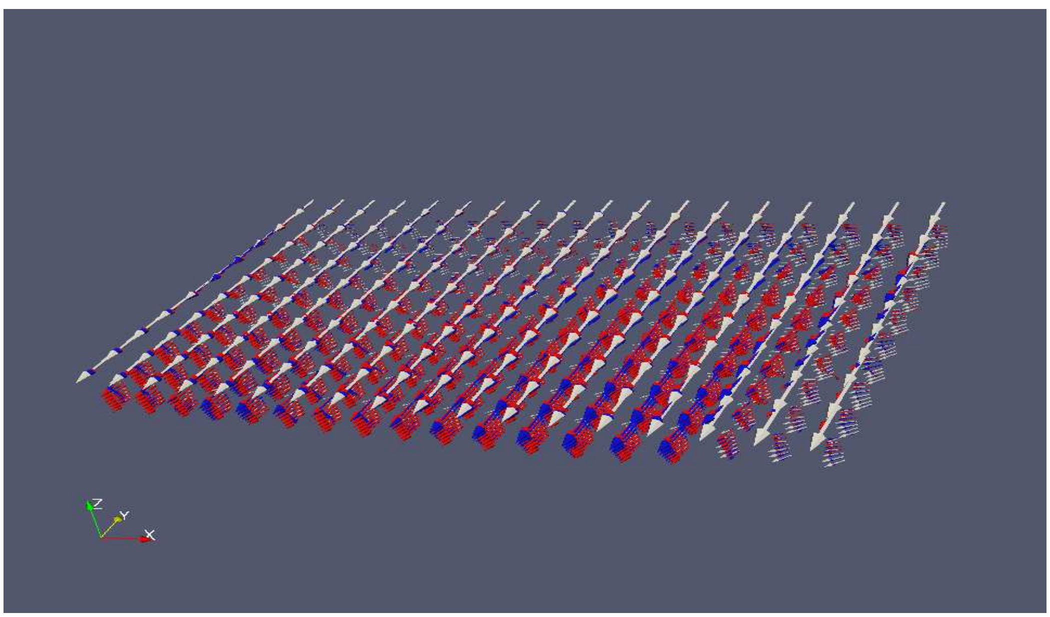

Figure 4.49: Simulation with wind velocity assigned to NORTH and EAST in OPENING configuration. Comparison between the velocity of CFX simulations and WRF data in inner domain. Grey: WRF data. Red: results of simulation with coarse mesh. Blue: results of simulation with thick mesh.

is 350 m deep.

Table 4.20: Simulation with wind velocity assigned to NORTH and EAST in OPENING configuration of OPENING. Wind intensity. Normalized root mean square deviation (NRMSD) of wind intensity on lateral faces and inside the domain of simulation.

region	wind - NRMSD - coarse mesh	wind - NRMSD - thick mesh
NORTH face	0.19	0.13
EAST face	0.13	0.11
SOUTH face	1.78	1.77
WEST face	1.67	0.79
INNER DOMAIN	1.38	1.20

Table 4.21: Simulation with wind velocity assigned to NORTH and EAST in OPENING configuration. U wind component. Normalized root mean square deviation (NRMSD) of U wind component in atmospheric layers inside the domain of simulation. nn = missing data.

layer	U - NRMSD - coarse mesh	U - NRMSD - thick mesh
0 m - 350 m	0.80	0.53
350 m - 700 m	0.80	0.55
700 m - 1050 m	0.78	0.58
1050 m - 1400 m	0.75	0.58
1400 m - 1750 m	0.73	0.62
1750 m - 2100 m	nn	nn
2100 m - 2450 m	nn	nn
2450 m - 2800 m	nn	nn
2800 m - 3150 m	12.99	7.33
3150 m - 3500 m	13.19	4.67

Table 4.22: Simulation with wind velocity assigned to NORTH and EAST in OPENING configuration. V wind component. Normalized root mean square deviation (NRMSD) of V wind component in atmospheric layers inside the domain of simulation. nn = missing data.

layer	V - NRMSD - coarse mesh	V - NRMSD - thick mesh
0 m - 350 m	1.25	0.85
350 m - 700 m	1.85	1.30
700 m - 1050 m	5.71	4.33
1050 m - 1400 m	13.92	11.18
1400 m - 1750 m	10.14	7.16
1750 m - 2100 m	nn	nn
2100 m - 2450 m	nn	nn
2450 m - 2800 m	nn	nn
2800 m - 3150 m	0.23	0.15
3150 m - 3500 m	0.31	0.21

Table 4.23: Simulation with wind velocity assigned to NORTH and EAST in OPENING configuration. W wind component. Normalized root mean square deviation (NRMSD) of W wind component in atmospheric layers inside the domain of simulation. nn = missing data.

layer	W - NRMSD - coarse mesh	W - NRMSD - thick mesh
0 m - 350 m	366.08	1090.40
350 m - 700 m	629.45	1512.84
700 m - 1050 m	1615.78	10243.27
1050 m - 1400 m	1616.32	10743.58
1400 m - 1750 m	1442.34	11340.87
1750 m - 2100 m	nn	nn
2100 m - 2450 m	nn	nn
2450 m - 2800 m	nn	nn
2800 m - 3150 m	55.57	46.74
3150 m - 3500 m	3485.97	15063.40

Table 4.24: Simulation with wind velocity assigned to NORTH and EAST in OPENING configuration. Wind intensity. Normalized root mean square deviation (NRMSD) of wind intensity in atmospheric layers inside the domain of simulation. nn = missing data.

layer	wind - NRMSD - coarse mesh	wind - NRMSD - thick mesh
0 m - 350 m	0.74	0.56
350 m - 700 m	0.74	0.57
700 m - 1050 m	1.15	0.88
1050 m - 1400 m	2.02	1.78
1400 m - 1750 m	2.02	1.90
1750 m - 2100 m	nn	nn
2100 m - 2450 m	nn	nn
2450 m - 2800 m	nn	nn
2800 m - 3150 m	0.23	0.15
3150 m - 3500 m	0.31	0.21

The values of normalized root mean square deviation are high enough (from table 4.21 to table 4.24), they decrease when passing from the computation with coarse mesh to the one with thick mesh, with the exception for W component. The indicator for U component is acceptable in bottom and middle layers, for V component in high layer and for wind intensity its values are reasonable in low and high layers, whereas for W component it is very large everywhere.
At lower heights (from table 4.50 to table 4.52) the wind fields simulated by CFX computations are influenced by the complex orography and by the strong conditioning on the lateral boundary conditions near NORTH face. Moreover, there are some differences between the simulations with different mesh resolution. At higher elevations (figure 4.53) the wind fields simulated by CFX computations are similar and there is an agreement with WRF data.
Finally, I compared the output of simulation with direct measure.
The simulation with coarse grid resulted as follows:

- wind intensity = 4.9 m/s;
- wind direction = 6 °.

The simulation with thick grid provided:

- wind intensity = 3.9 m/s;
- wind direction = 21 °.

The measurement of the station gave the wind intensity of 3.9 m/s and the wind direction of 45 °(calculated with respect to North), as written before; both simulations enable to detect the order of magnitude of wind intensity, in particular the

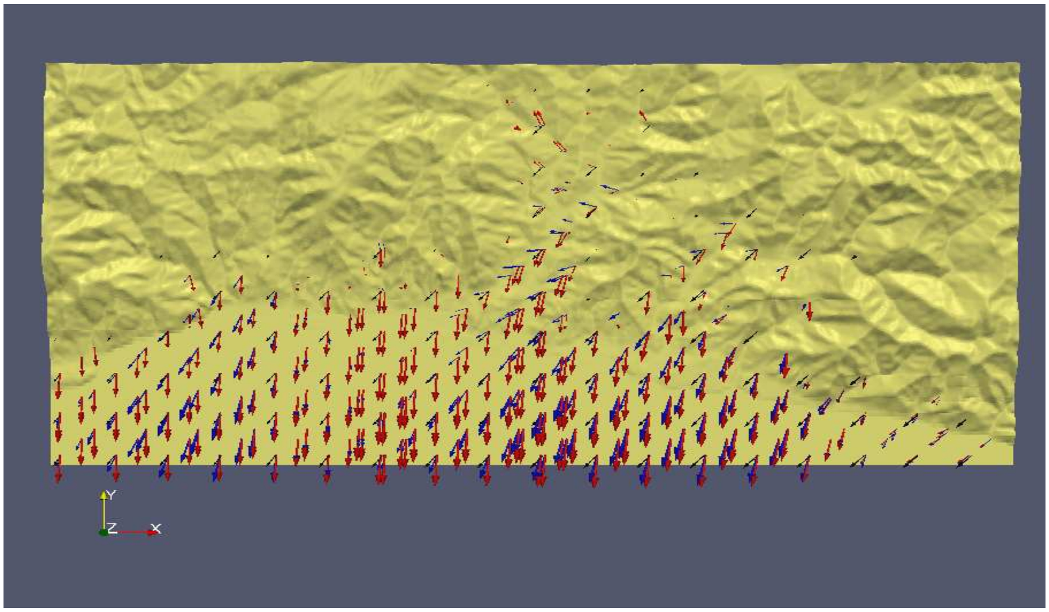

Figure 4.50: Simulation with wind velocity assigned to NORTH and EAST in OPENING configuration. Comparison between the velocity of CFX simulations and WRF data at height of 160 m. Black: WRF data. Red: results of simulation with coarse mesh. Blue: results of simulation with thick mesh.

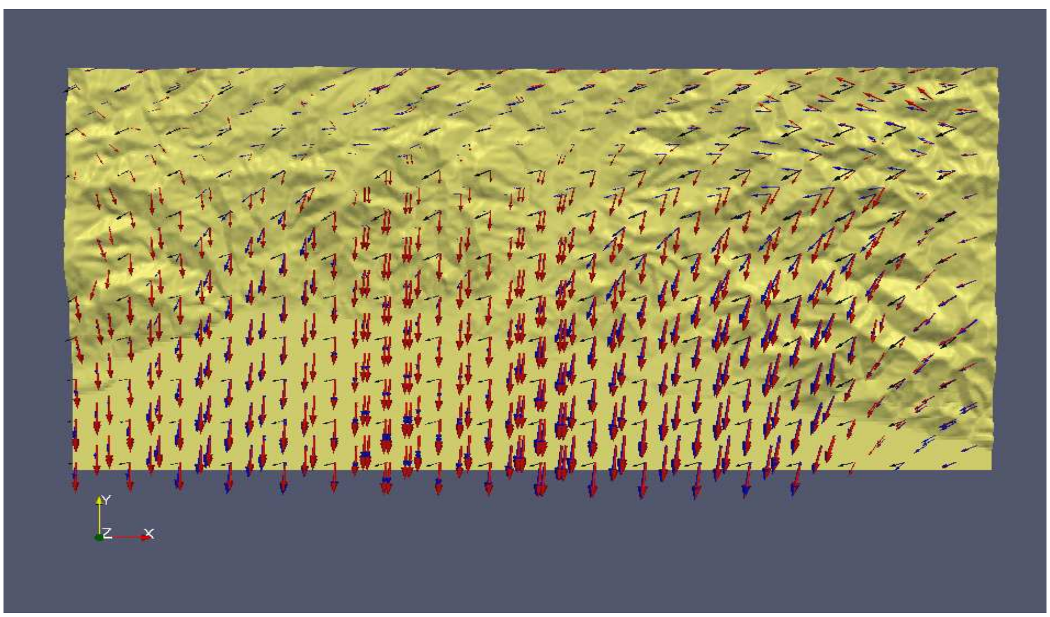

Figure 4.51: Simulation with wind velocity assigned to NORTH and EAST in OPENING configuration. Comparison between the velocity of CFX simulations and WRF data at height of 880 m. Black: WRF data. Red: results of simulation with coarse mesh. Blue: results of simulation with thick mesh.

simulation with thick mesh identifies the value equal to the measured one. The

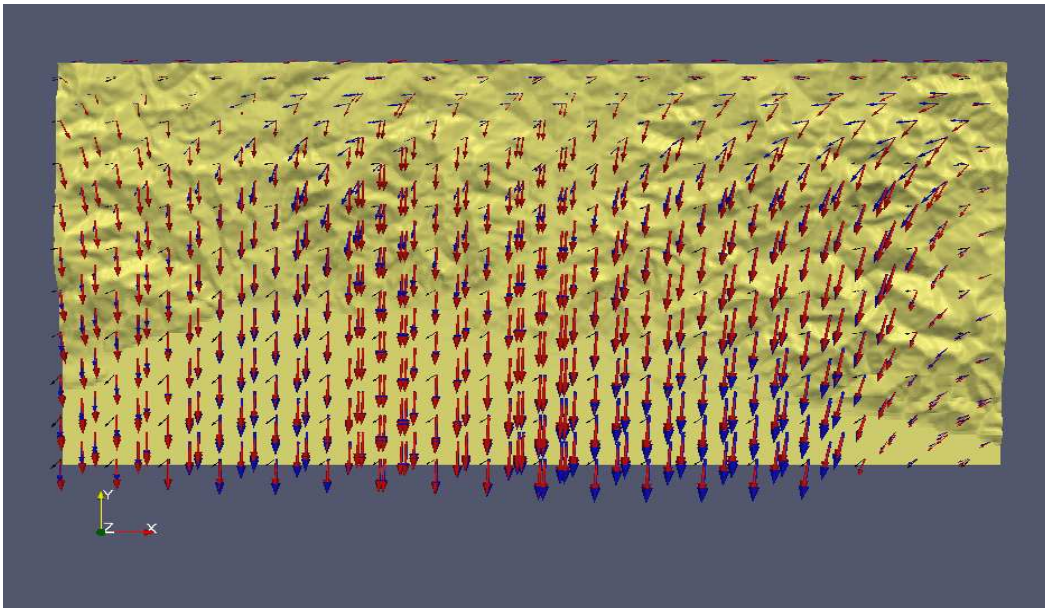

Figure 4.52: Simulation with wind velocity assigned to NORTH and EAST in OPENING configuration. Comparison between the velocity of CFX simulations and WRF data at height of 1520 m. Black: WRF data. Red: results of simulation with coarse mesh. Blue: results of simulation with thick mesh.

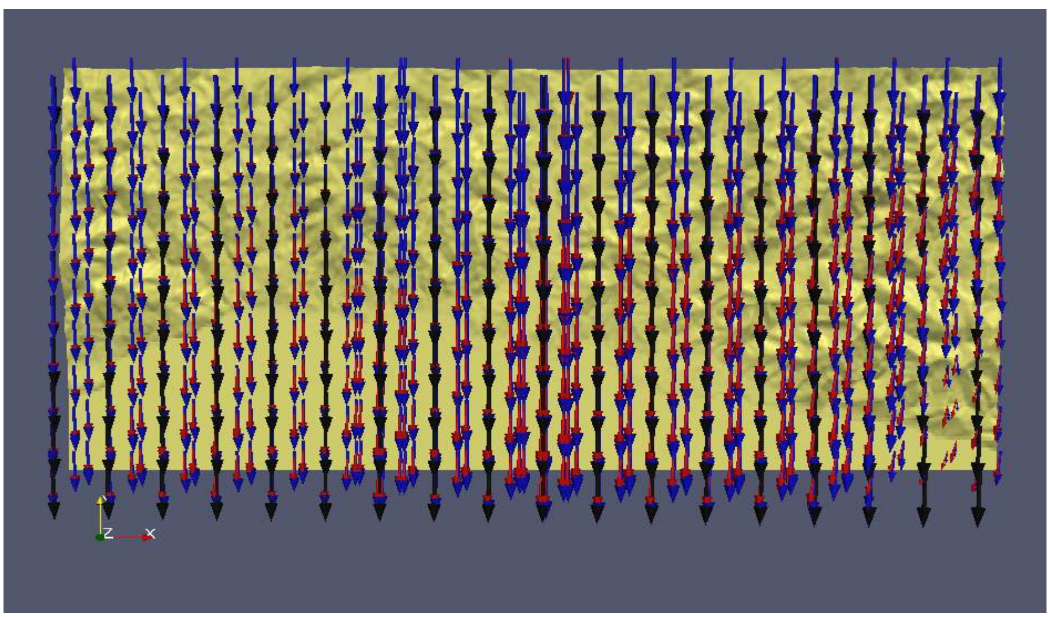

Figure 4.53: Simulation with wind velocity assigned to NORTH and EAST in OPENING configuration. Comparison between the velocity of CFX simulations and WRF data at height of 3100 m. Black: WRF data. Red: results of simulation with coarse mesh. Blue: results of simulation with thick mesh.

simulation with coarse mesh overestimates the measure, although the discrepancy can be included in the numerical errors propagation. For the wind direction the simulations allow to find the angular sector from which the wind comes. In detail, the simulation with coarse mesh distances itself of about 40 °, whereas the simulation with thick mesh gives a nearer value than the measured one, and the difference is equal to 24 °.

4.6 Conclusion

Evaluating the results, we can say that the boundary conditions corresponding to WRF velocities, are the strong constraints for the fluid dynamics computation. The algorithm reaches in all cases the numerical convergence, but it provides wind fields not always realistic.
In fact, it is possible to highlight the areas, corresponding to the sea and the coastal zone, where the flow convergences and the eddies are generated, but they are not physically acceptable. Instead, the configuration is reasonable near the mountains area. As expected, the CFD simulation allows to estimate partially the influence of orography on the wind flow, that is simulated by the meteorological model on a coarser grid than the ones used in Fluid Dynamics Computation.
In this chapter, I used two meshes for CFD calculation (coarse and thick), but there is not a pronounced improvement in the simulation with the thick mesh in comparison with the simulation with the coarse one and the computational time is very large if the grid with a great number of cells is used.
The statistical indicator, chosen to estimate the discrepancy between the output of computational fluid dynamics simulations and the output of meteorological model, takes partially acceptable values for U and V wind components, reasonable enough for wind intensity on the lateral faces and in the inner domain. However, in every case it is very large for W component: the simulation provides a wind flow with an upward or downward component, that is bigger than the one given by WRF.
A behaviour, analogous to the one described for all domain, occurs if different layers in inner domain are considered.
In the comparison among the different simulations, there are more reasonable results for computations with WRF wind velocity on two and three lateral faces than the one with WRF wind velocity on every face. The last one does not provide a physically acceptable flow, especially in parts of the domain near the sea.
Finally, I compared with direct measure the value of numerical simulations where the meteorological station is located. The wind intensity, simulated by all CFD computations, is in agreement with the measured value; the small variances between these values are attributable to the numerical errors propagation in the calculation.
For the wind direction, only the outputs of simulations obtained with WRF velocities assigned to three and two lateral faces are in agreement with the measured value.

Chapter 5

Variability of conditions in CFD simulations

5.1 Introduction

In order to improve the results of previous simulations (chapter 4), I performed other simulations with simpler boundary conditions.
The comparison between the WRF data and the output of CFD computations is performed in analogy to the above mentionated first analyses. Further, particular attention is given to the influences of orography on the flow.
After having chosen the best configuration of the boundary conditions, the simulations were implemented for ten following hours and the comparison between the results of numerical procedures and measurements of ARPAL station was carried out.
In order to try to reduce some spurious effects produced by CFX model, especially over the sea, I utilized another package (FLUENT). This software is particularly used in works concerning geophysical researches [18].
In these procedures, FLUENT, CFX and PARAVIEW softwares were used in different steps of computation and following analysis to improve the statement of the problem.
In particular, the simulation was set and executed by FLUENT, instead of CFX-PRE and CFX-SOLVER; then the analysis of the calculation results was studied by CFX-POST and PARAVIEW.

5.2 Simulations

The executed simulations have simpler boundary conditions than the ones described in chapter 4. They were set in order to obtain a more realistic wind field on the domain, considering the particular orography of the geographical area, and to have better agreement with measuments of ARPAL station. In this perspective, I executed two simulations as a test. I assigned to the lateral faces the average wind velocity, using the calculus of the data provided by the meterological model. The simulations are as follows:

- simulation with average wind velocity assigned to four lateral faces;
- simulation with average wind velocity assigned to two lateral faces.

Then, I repeated the simulation with the first statement for ten consecutive hours and in order to have more accurate computations I used WRF data with a bigger number of pressure levels. In addition to the layers of the previous simulations, I considered five pressure levels with a distance of 25 hPa between 850 hPa and 700 hPa, four pressure levels between 700 hPa and 500 hPa; in particular the last ones have values of 725 hPa, 700 hPa, 675 hPa, 625 hPa.
The used mesh is the coarser one, because there is not an evident improvement in comparison to the simulations with the thicker grid and the time requested for the computation with coarser mesh is shorter.
The set of computation is explained in every case and the methods of analysis concerning the study of Computation Fluid Dynamics is similar to the one described in section 4.5.2.

5.2.1 Average velocity on four lateral faces

The computation was stationary, isothermal with temperature of 280 K and incompressible. The fluid was set as ideal gas and the turbulence model chosen was k-ϵ. The parameters about turbulence were assigned by means of a turbulence intensity of 5 % and a turbulence length scale of 0.1 m.
The boundary conditions were the same for the lateral faces (NORTH, EAST, SOUTH, WEST) and for the top of the domain (SKY): they were set in VELOCITY-INLET configuration and the velocity is assigned by means of averaging the corresponding WRF velocities on the surfaces. In detail:

- NORTH: U = -1.51 m/s, V = -1.88 m/s, W = 0.03 m/s;
- EAST: U = -1.74 m/, V = -2.24 m/s, W = 0.06 m/s;
- SOUTH: U = -1.60 m/s, V = -1.29 m/s, W = 0.01 m/s;
- WEST: U = -1.04 m/s, V = -1.87 m/s, W = 0.03 m/s;
- SKY: U = 0.24 m/s, V = -9.10 m/s, W = 0.02 m/s.

On all the lateral faces, the intensity and the direction of the wind are similar: the wind intensity is low and the sector of wind coming is North-East. On the upper side of the box (SKY), the wind intensity is higher and the wind direction is North. The configuration of velocity on lateral faces is caused by the presence of many values at lower elevations and so the velocity of all faces is smaller than the one on the SKY.
The surfaces of sea and land (coastal zone and mountains) were WALLS with friction.
The solution method of the calculation was pressure-based and the spatial discretization was of second order upwind. The computation converged after 500 iterations and the order of the residuals was 10^{-6}.
A qualitative control was made in order to examine the wind fields provided by CFX

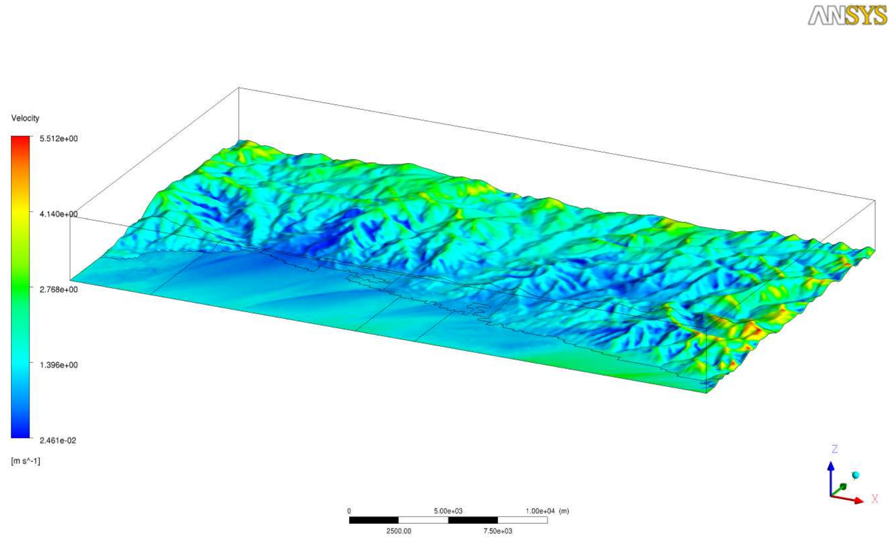

Figure 5.1: Simulation with average wind velocity assigned to NORTH, EAST, SOUTH, WEST and SKY in VELOCITY-INLET configuration and coarse mesh. Wind field at 10 m.

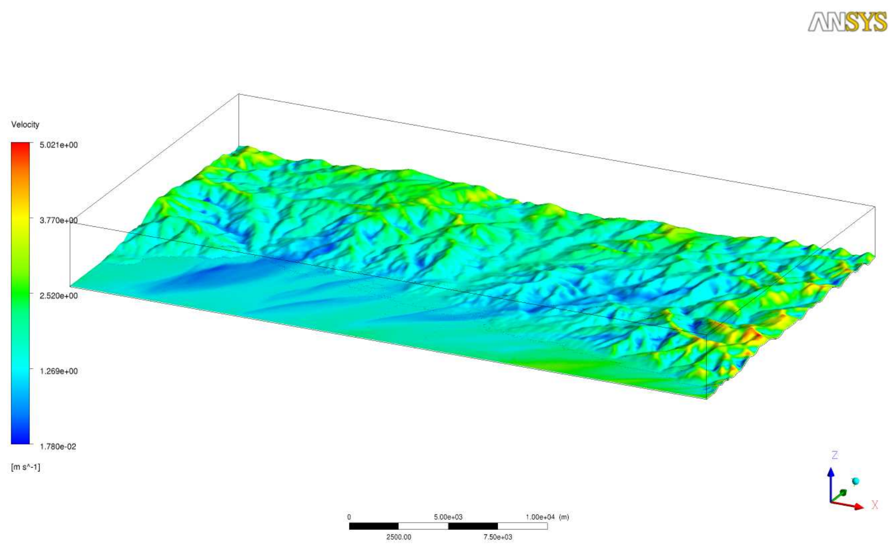

Figure 5.2: Simulation with average wind velocity assigned to NORTH, EAST, SOUTH, WEST and SKY in VELOCITY-INLET configuration and coarse mesh. Wind field at 30 m.

simulation at the heights of 10 m, 30 m, 100 m and 1000 m (from figure 5.1 to figure 5.4).

In detail, I calculated the normalized root mean square deviation (NRMSD) between WRF and FLUENT wind velocity components and intensity for the space inside the whole domain and in the atmospheric layers; each atmospheric layer is 350 m deep.

Table 5.1: Simulation with average wind velocity assigned to NORTH, EAST, SOUTH, WEST and SKY in VELOCITY-INLET configuration. Normalized root mean square deviation (NRMSD) of components and intensity of wind velocity inside the domain of simulation.

wind	NRMSD
U component	61.69
V component	12.44
W component	2469.83
intensity	0.53

Table 5.2: Simulation with average wind velocity assigned to NORTH, EAST, SOUTH, WEST and SKY in VELOCITY-INLET configuration. U wind component. Normalized root mean square deviation (NRMSD) of U wind component in atmospheric layers inside the domain of simulation. nn = missing data.

layer	U - NRMSD - coarse mesh
0 m - 350 m	0.63
350 m - 700 m	0.53
700 m - 1050 m	0.39
1050 m - 1400 m	0.27
1400 m - 1750 m	0.23
1750 m - 2100 m	nn
2100 m - 2450 m	nn
2450 m - 2800 m	nn
2800 m - 3150 m	178.93
3150 m - 3500 m	62.13

Table 5.3: Simulation with average wind velocity assigned to NORTH, EAST, SOUTH, WEST and SKY in VELOCITY-INLET configuration. V wind component. Normalized root mean square deviation (NRMSD) of V wind component in atmospheric layers inside the domain of simulation. nn = missing data.

layer	V - NRMSD - coarse mesh
0 m - 350 m	0.68
350 m - 700 m	0.49
700 m - 1050 m	1.10
1050 m - 1400 m	25.20
1400 m - 1750 m	4.50
1750 m - 2100 m	nn
2100 m - 2450 m	nn
2450 m - 2800 m	nn
2800 m - 3150 m	0.75
3150 m - 3500 m	0.73

Table 5.4: Simulation with average wind velocity assigned to NORTH, EAST, SOUTH, WEST and SKY in VELOCITY-INLET configuration. W wind component. Normalized root mean square deviation (NRMSD) of W wind component in atmospheric layers inside the domain of simulation. nn = missing data.

layer	W - NRMSD - coarse mesh
0 m - 350 m	1940.85
350 m - 700 m	1377.49
700 m - 1050 m	4833.61
1050 m - 1400 m	70097.76
1400 m - 1750 m	9399.76
1750 m - 2100 m	nn
2100 m - 2450 m	nn
2450 m - 2800 m	nn
2800 m - 3150 m	2.96
3150 m - 3500 m	18469.51

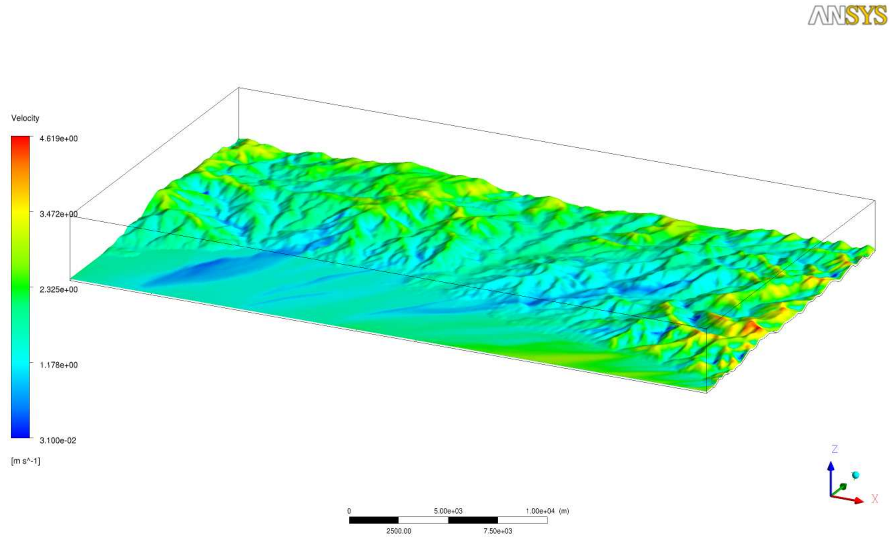

Figure 5.3: Simulation with average wind velocity assigned to NORTH, EAST, SOUTH, WEST and SKY in VELOCITY-INLET configuration and coarse mesh. Wind field at 100 m.

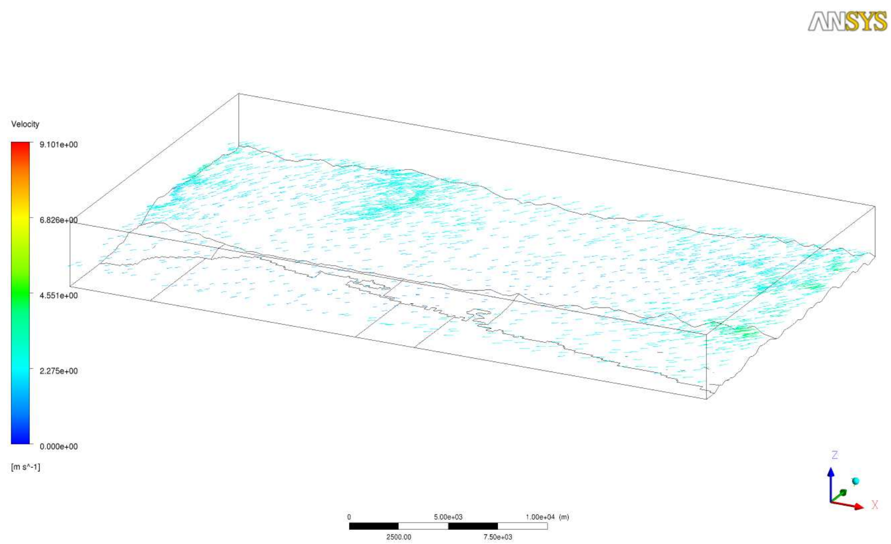

Figure 5.4: Simulation with average wind velocity assigned to NORTH, EAST, SOUTH, WEST and SKY in VELOCITY-INLET configuration and coarse mesh. Wind field at 1000 m.

The values of normalized root mean square deviation of wind components are very high in inner domain points, whereas its value for wind intensity is acceptable (table 5.1).

The values of normalized root mean square deviation are acceptable for U component in low layers, for V component in high layers and for the wind intensity in all elevations; on the contrary, for W component, the values of this indicator are very large in every layer (from table 5.2 to table 5.5).

Table 5.5: Simulation with average wind velocity assigned to NORTH, EAST, SOUTH, WEST and SKY in VELOCITY-INLET configuration. Wind intensity. Normalized root mean square deviation (NRMSD) of wind intensity in atmospheric layers inside the domain of simulation. nn = missing data.

layer	wind - NRMSD - coarse mesh
0 m - 350 m	0.63
350 m - 700 m	0.49
700 m - 1050 m	0.24
1050 m - 1400 m	0.30
1400 m - 1750 m	0.40
1750 m - 2100 m	nn
2100 m - 2450 m	nn
2450 m - 2800 m	nn
2800 m - 3150 m	0.71
3150 m - 3500 m	0.70

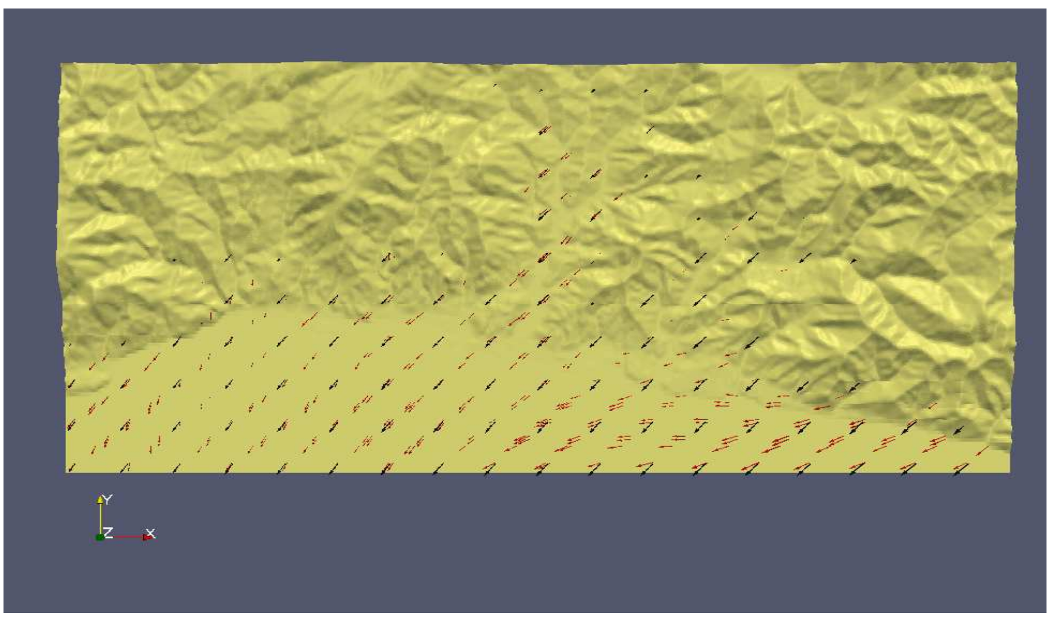

Figure 5.5: Simulation with average wind velocity assigned to NORTH, EAST, SOUTH, WEST and SKY in VELOCITY-INLET configuration. Comparison between the velocity of FLUENT simulation and WRF data at height of 160 m. Black: WRF data. Red: results of simulation.

At lower heights (figure 5.5) the wind field simulated by FLUENT is influenced by the complex topography and by strong conditioning of the lateral boundary conditions in the different areas of the domain. At midway elevations (figures 5.6

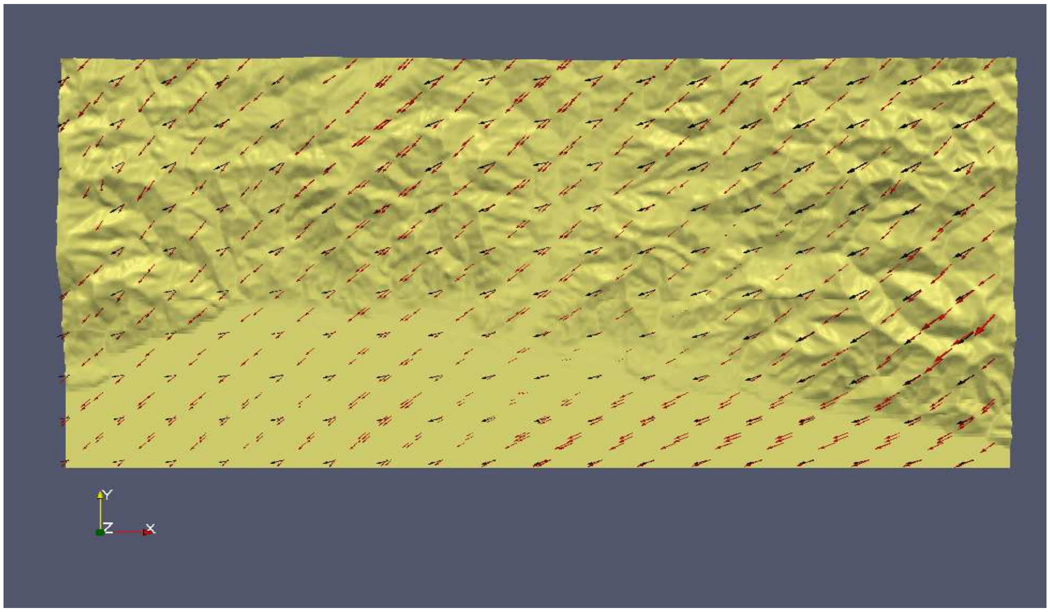

Figure 5.6: Simulation with average wind velocity assigned to NORTH, EAST, SOUTH, WEST and SKY in VELOCITY-INLET configuration. Comparison between the velocity of FLUENT simulation and WRF data at height of 880 m. Black: WRF data. Red: results of simulation.

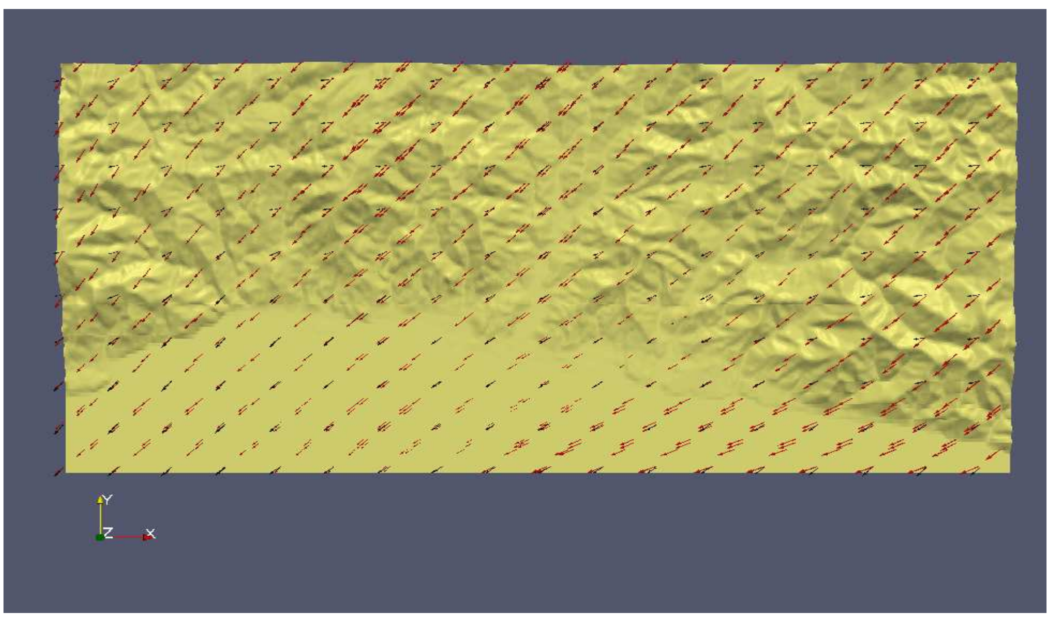

Figure 5.7: Simulation with average wind velocity assigned to NORTH, EAST, SOUTH, WEST and SKY in VELOCITY-INLET configuration. Comparison between the velocity of FLUENT simulation and WRF data at height of 1520 m. Black: WRF data. Red: results of simulation.

and 5.7), the wind fields simulated by FLUENT computations and the ones of WRF

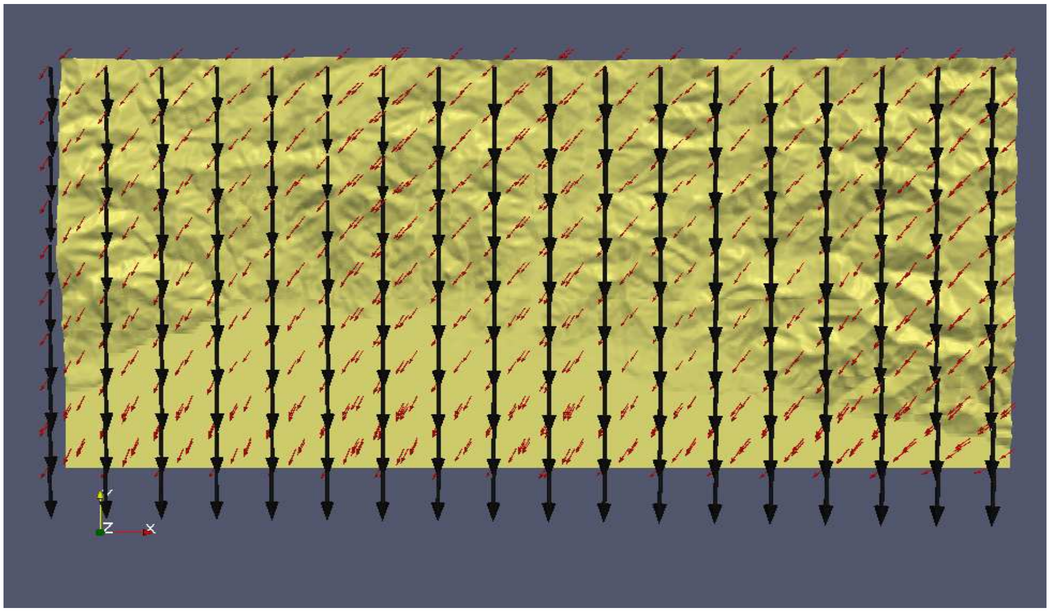

Figure 5.8: Simulation with average wind velocity assigned to NORTH, EAST, SOUTH, WEST and SKY in VELOCITY-INLET configuration. Comparison between the velocity of FLUENT simulation and WRF data at height of 3100 m. Black: WRF data. Red: results of simulation.

data are similar. In the high elevations (figure 5.8) the wind fields are homogeneus, but there is a variance between FLUENT simulation and WRF data regarding the intensity and the direction of the wind.
Finally, I compared the simulation output with direct measure. The computation provided:

- wind intensity = 1.3 m/s;
- wind direction = 77 °.

The measurement of the station gave a wind intensity of 3.9 m/s and a wind direction of 45 °(calculated with respect to North). There is a discrepancy between the simulation and the measure for wind intensity, that is underestimated by the simulations, but there is a good agreement for the direction of wind; in fact, the simulation identifies the angular sector of the wind origin.

5.2.2 Average velocity on two lateral faces

The computation was stationary, isothermal with temperature of 280 K and incompressible. The fluid was set as ideal gas and the turbulence model chosen was k-ϵ. The parameters about turbulence were assigned by means of profiles of turbulent kinetic energy and its dissipation rate.
The boundary conditions were the same for NORTH, EAST lateral faces and for the top of the domain (SKY): they were set in VELOCITY-INLET configuration with assigned velocity. On NORTH and EAST lateral faces, the assigned velocity

was the average value calculated distinctly for the faces; for SKY face the value was an average of these faces values. In particular:

- NORTH: U = -1.51 m/s, V = -1.88 m/s, W = 0.03 m/s;
- EAST: U = -1.74 m/s, V = -2.24 m/s, W = 0.06 m/s;
- SKY: U = -1.63 m/s, V = -2.06 m/s, W = 0.05 m/s.

SOUTH and WEST lateral faces were set in OUTFLOW configuration, so that no particular constraint was applied.
The surfaces of sea and land (coastal zone and mountains) were WALLS with friction.
The solution method of the calculation was "simple" and the spatial discretization was of second order upwind. The computation converged after 500 iterations and the order of the residuals was 10^{-6}.
The analysis of the solution was studied with the same method as the previous simulation.
A qualitative control was made in order to examine the wind fields provided by FLUENT simulations at the heights of 10 m, 30 m, 100 m and 1000 m (from figure 5.9 to figure 5.12).

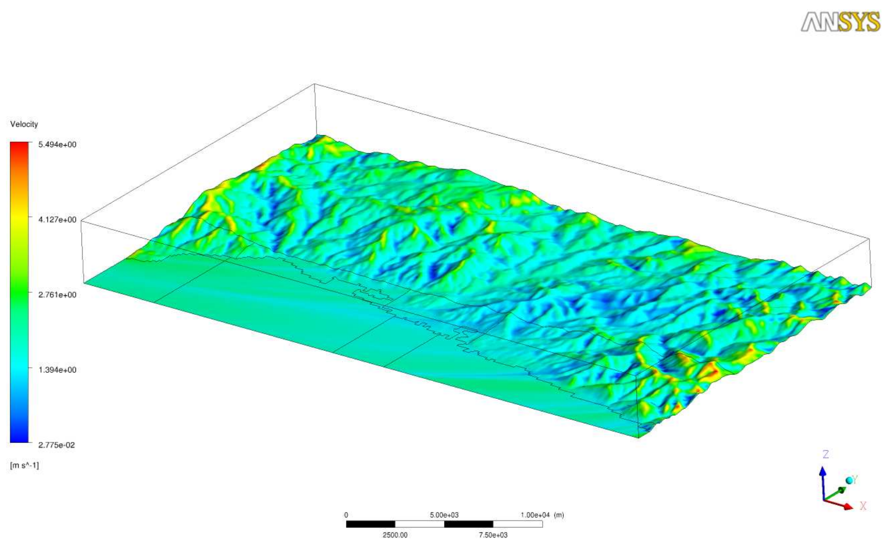

Figure 5.9: Simulation with average wind velocity assigned to NORTH, EAST and SKY in VELOCITY-INLET configuration and coarse mesh. Wind field at 10 m.

In detail, I calculated the normalized root mean square deviation (NRMSD) between WRF and FLUENT wind velocity components and intensity for the space inside the whole domain and in the atmospheric layers with depth of 350 m.
The values of the normalized root mean square deviation (NRMSD) of wind components are very large in inner domain points, whereas the value of NRMSD for the wind intensity is acceptable (table 5.6).
The values of the normalized root mean square deviation are acceptable for U component in low and middle layers, for V component in layers next to surface and for

Table 5.6: Simulation with average wind velocity assigned to NORTH, EAST and SKY in VELOCITY-INLET configuration. Normalized root mean square deviation (NRMSD) of components and intensity of wind velocity inside the domain of simulation.

wind	NRMSD
U component	61.44
V component	12.44
W component	2813.10
intensity	0.52

Table 5.7: Simulation with average wind velocity assigned to NORTH, EAST and SKY in VELOCITY-INLET configuration. U wind component. Normalized root mean square deviation (NRMSD) of U wind component in atmospheric layers inside the domain of simulation. nn = missing data.

layer	U - NRMSD - coarse mesh
0 m - 350 m	0.76
350 m - 700 m	0.48
700 m - 1050 m	0.36
1050 m - 1400 m	0.41
1400 m - 1750 m	0.45
1750 m - 2100 m	nn
2100 m - 2450 m	nn
2450 m - 2800 m	nn
2800 m - 3150 m	189.04
3150 m - 3500 m	116.94

Table 5.8: Simulation with average wind velocity assigned to NORTH, EAST and SKY in VELOCITY-INLET configuration. V wind component. Normalized root mean square deviation (NRMSD) of V wind component in atmospheric layers inside the domain of simulation. nn = missing data.

layer	V - NRMSD - coarse mesh
0 m - 350 m	0.72
350 m - 700 m	0.49
700 m - 1050 m	0.94
1050 m - 1400 m	24.88
1400 m - 1750 m	4.79
1750 m - 2100 m	nn
2100 m - 2450 m	nn
2450 m - 2800 m	nn
2800 m - 3150 m	0.78
3150 m - 3500 m	0.84

Table 5.9: Simulation with average wind velocity assigned to NORTH, EAST and SKY in VELOCITY-INLET configuration. W wind component. Normalized root mean square deviation (NRMSD) of W wind component in atmospheric layers inside the domain of simulation. nn = missing data.

layer	W - NRMSD - coarse mesh
0 m - 350 m	280.96
350 m - 700 m	576.56
700 m - 1050 m	4118.12
1050 m - 1400 m	3025.92
1400 m - 1750 m	3067.15
1750 m - 2100 m	nn
2100 m - 2450 m	nn
2450 m - 2800 m	nn
2800 m - 3150 m	1.89
3150 m - 3500 m	1681.04

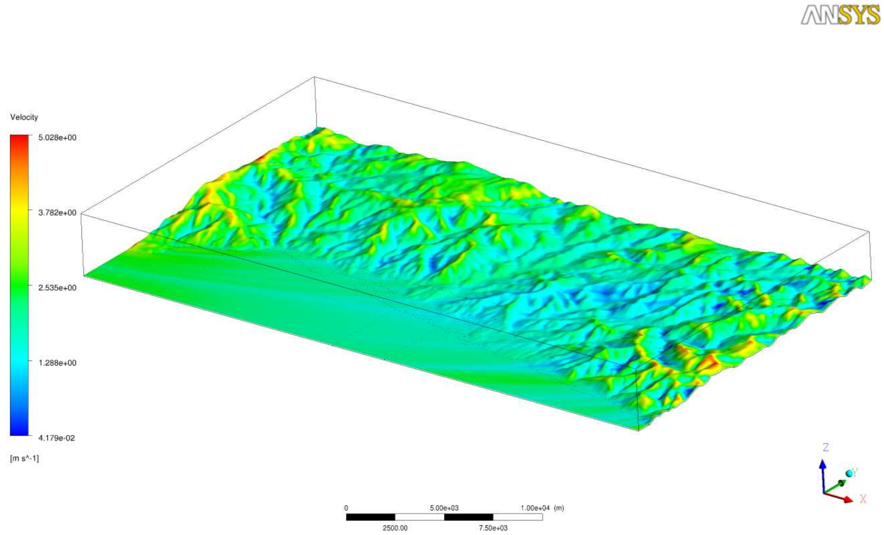

Figure 5.10: Simulation with average wind velocity assigned to NORTH, EAST and SKY in VELOCITY-INLET configuration and coarse mesh. Wind field at 30 m.

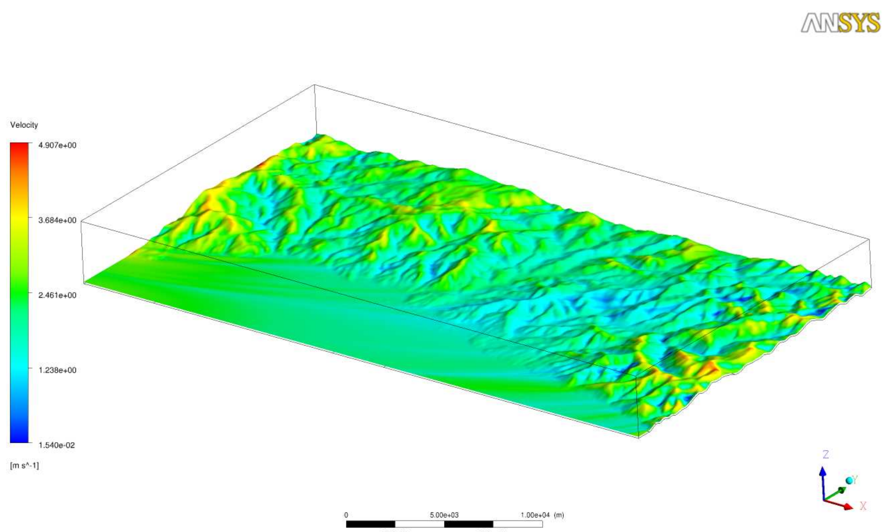

Figure 5.11: Simulation with average wind velocity assigned to NORTH, EAST and SKY in VELOCITY-INLET configuration and coarse mesh. Wind field at 100 m.

the wind intensity in all elevations; on the contrary, for W component the values of this indicator are very large in every layer (from table 5.7 to table 5.10).

At low heights (figure 5.13) the wind field simulated by FLUENT is influenced by the complex topography of the domain. At intermediate elevations (figures 5.14 and 5.15) this influence decreases and at higher elevations (figure 5.16) the wind fields simulated by FLUENT are not subject to orography. There is a partial agreement between FLUENT simulation and WRF data in atmosheric layers at intermediate elevations. Next to the SKY (figure 5.16) there is an evident variance between

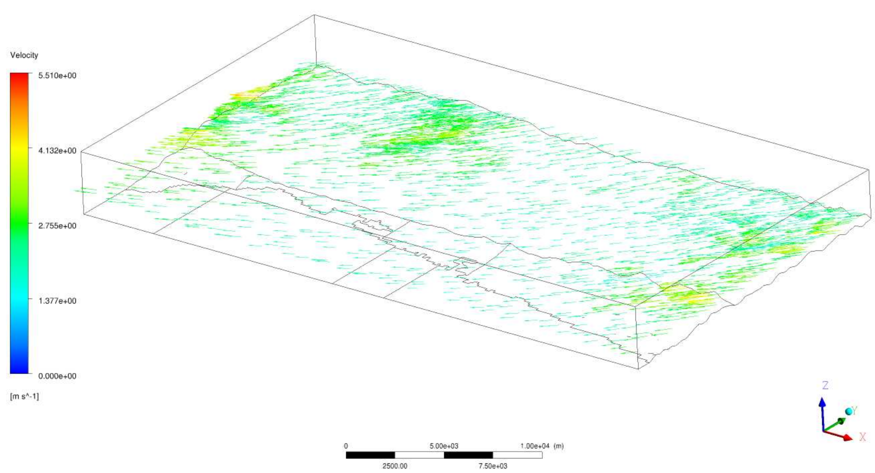

Figure 5.12: Simulation with average wind velocity assigned to NORTH, EAST and SKY in VELOCITY-INLET configuration and coarse mesh. Wind field at 1000 m.

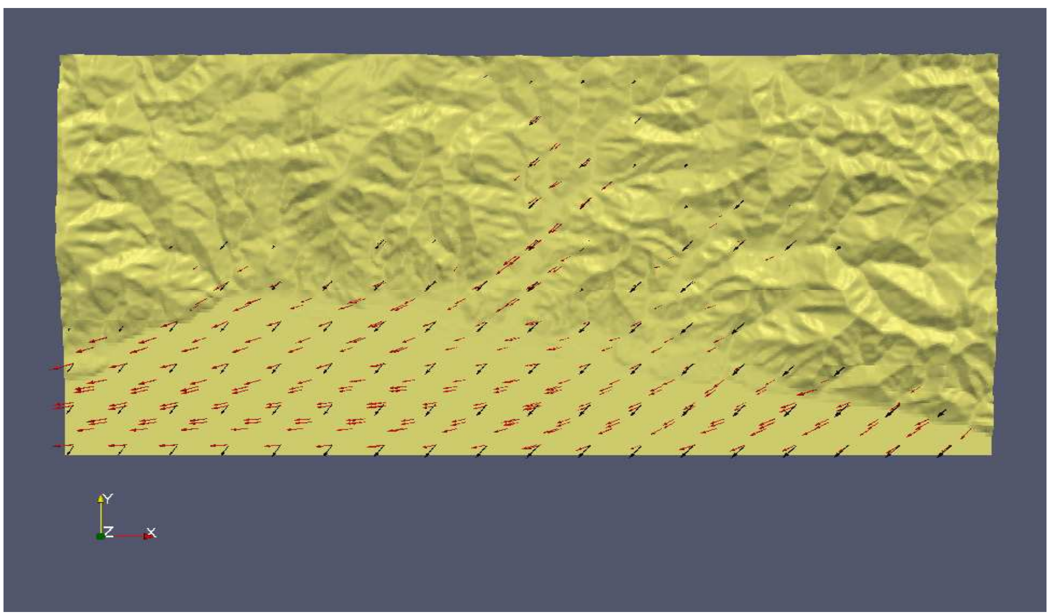

Figure 5.13: Simulation with average wind velocity assigned to NORTH, EAST and SKY in VELOCITY-INLET configuration. Comparison between the velocity of FLUENT simulation and WRF data at height of 160 m. Black: WRF data. Red: results of simulation.

FLUENT simulation and WRF data regarding the intensity and the direction of the wind.
Finally, I compared the simulation output with direct measure. The computation provided:

- wind intensity = 1.6 m/s;

Table 5.10: Simulation with average wind velocity assigned to NORTH, EAST and SKY in VELOCITY-INLET configuration. Wind intensity. Normalized root mean square deviation (NRMSD) of wind intensity in atmospheric layers inside the domain of simulation. nn = missing data.

layer	wind - NRMSD - coarse mesh
0 m - 350 m	0.58
350 m - 700 m	0.44
700 m - 1050 m	0.31
1050 m - 1400 m	0.55
1400 m - 1750 m	0.57
1750 m - 2100 m	nn
2100 m - 2450 m	nn
2450 m - 2800 m	nn
2800 m - 3150 m	0.70
3150 m - 3500 m	0.71

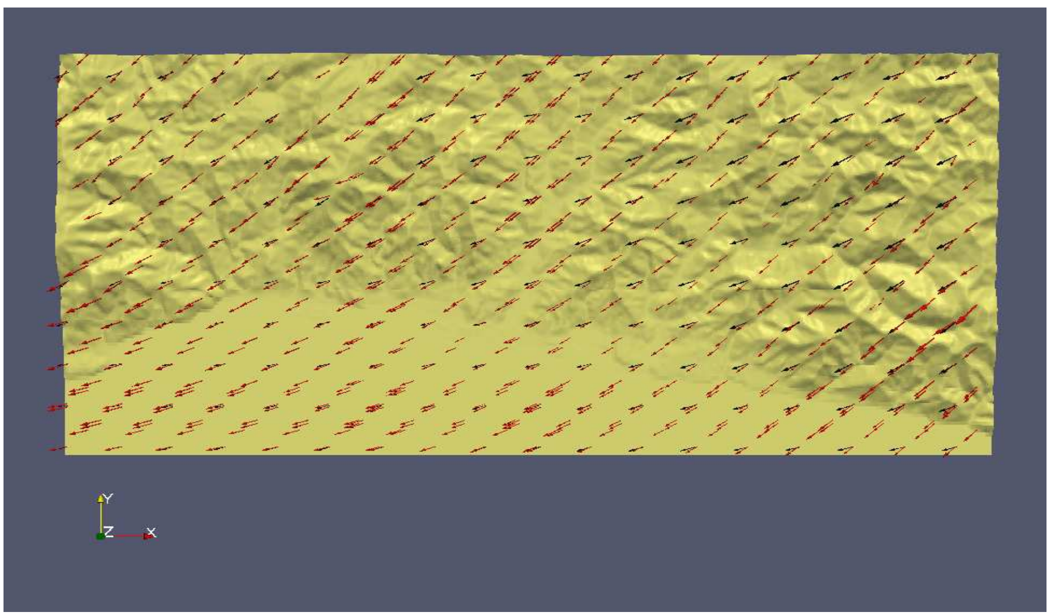

Figure 5.14: Simulation with average wind velocity assigned to NORTH, EAST and SKY in VELOCITY-INLET configuration. Comparison between the velocity of FLUENT simulation and WRF data at height of 880 m. Black: WRF data. Red: results of simulation.

- wind direction = 60 °.

The measurement of the station gave a wind intensity of 3.9 m/s and a wind direction of 45 °(calculated with respect to North). There is a good agreement between the

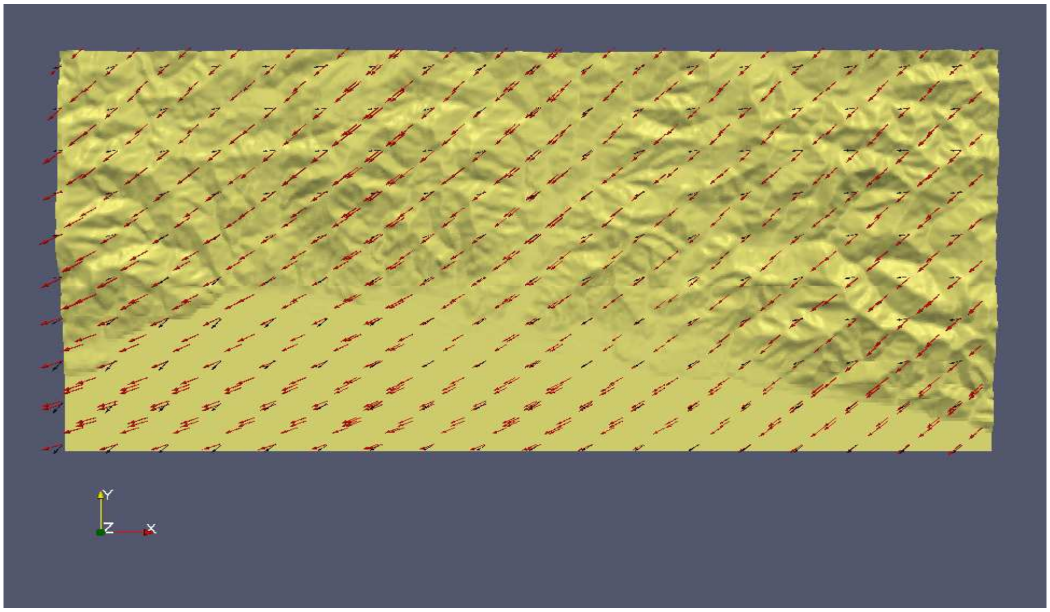

Figure 5.15: Simulation with average wind velocity assigned to NORTH, EAST and SKY in VELOCITY-INLET configuration. Comparison between the velocity of FLUENT simulation and WRF data at height of 1520 m. Black: WRF data. Red: results of simulation.

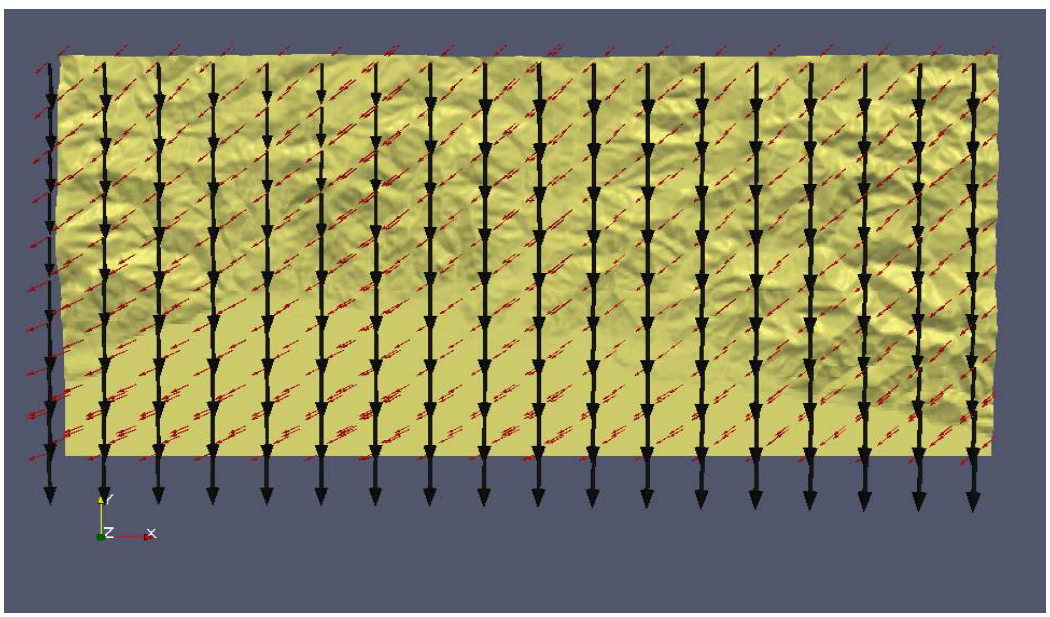

Figure 5.16: Simulation with average wind velocity assigned to NORTH, EAST and SKY in VELOCITY-INLET configuration. Comparison between the velocity of FLUENT simulation and WRF data at height of 3100 m. Black: WRF data. Red: results of simulation.

simulation and the measure for wind direction and the sector of wind origin is identified by simulation; there is a little discrepancy between the measurement and the simulation, that underestimates the measured value of about 2 m/s.

5.2.3 Average velocity on four lateral faces with variation of velocity values of boundary conditions

I repeated the simulation with the same numerical model described in section 5.2.1, but with more details in boundary conditions.
The lateral faces and the top face were VELOCITY-INLET, but in addition to the precedent case, I considered the data with a greater number of pressure levels. In this way, the values of velocity assigned by boundary conditions were modified, and they were:

- NORTH: U = -1.51 m/s, V = -3.36 m/s, W = 0.03 m/s;
- EAST: U = -1.28 m/, V = -3.61 m/s, W = 0.05 m/s;
- SOUTH: U = -1.06 m/s, V = -3.52 m/s, W = 0.01 m/s;
- WEST: U = -0.79 m/s, V = -3.17 m/s, W = 0.02 m/s;
- SKY: U = 0.24 m/s, V = -9.10 m/s, W = 0.02 m/s.

On all the lateral faces, the intensity and the direction of the wind are similar: the values of wind intensity are low in absolute reference scale, but they are greater than the case described in section 5.2.1, because I considered a larger number of velocity values at higher elevations.
The sector of wind coming is North-East, but the absolute value of V component is greater than the precedent case, because it is a predominant component in higher altitudes. In fact, in the top of the box (SKY) the wind intensity is higher and the wind direction is North.
The surfaces of sea and land (coastal zone and mountains) were WALLS with friction.
The solution method of the calculation was "simple" and the spatial discretization was of second order upwind. The computation converged after 500 iterations and the order of the residuals was 10^{-6}.
A qualitative control was made to examine the wind fields provided by CFX simulation at the heights of 10 m, 30 m, 100 m and 1000 m (from figure 5.17 to figure 5.20).
The figures provide the acceptable wind fields. In detail, I calculated the normalized root mean square deviation (NRMSD) between WRF and FLUENT wind velocity components and intensity for the space inside the whole domain and in the atmospheric layers, each atmospheric layer is 350 m deep.
The values of the normalized root mean square deviation (NRMSD) of wind components are very high in inner domain points, whereas the value of NRMSD for wind intensity is acceptable (table 5.11).
The values of the normalized root mean square deviation are acceptable for U component in layers at middle elevations, for V component in high layers and for the

Table 5.11: Simulation with average wind velocity assigned to NORTH, EAST, SOUTH, WEST and SKY in configuration of VELOCITY-INLET with more velocity values at higher elevations. Normalized root mean square deviation (NRMSD) of components and intensity of wind velocity inside the domain of simulation.

wind	NRMSD
U component	45.28
V component	17.27
W component	30473.03
intensity	0.76

Table 5.12: Simulation with average wind velocity assigned to NORTH, EAST, SOUTH, WEST and SKY in VELOCITY-INLET configuration with more velocity values at higher elevations. U wind component. Normalized root mean square deviation (NRMSD) of U wind component in atmospheric layers inside the domain of simulation.

layer	U - NRMSD - coarse mesh
0 m - 350 m	0.87
350 m - 700 m	0.80
700 m - 1050 m	0.64
1050 m - 1400 m	0.43
1400 m - 1750 m	0.25
1750 m - 2100 m	0.18
2100 m - 2450 m	0.78
2450 m - 2800 m	12.40
2800 m - 3150 m	101.55
3150 m - 3500 m	105.63

Table 5.13: Simulation with average wind velocity assigned to NORTH, EAST, SOUTH, WEST and SKY in VELOCITY-INLET configuration with more velocity values at higher elevations. V wind component. Normalized root mean square deviation (NRMSD) of V wind component in atmospheric layers inside the domain of simulation.

layer	V - NRMSD - coarse mesh
0 m - 350 m	0.69
350 m - 700 m	0.82
700 m - 1050 m	3.26
1050 m - 1400 m	45.82
1400 m - 1750 m	10.05
1750 m - 2100 m	1.77
2100 m - 2450 m	0.25
2450 m - 2800 m	0.40
2800 m - 3150 m	0.51
3150 m - 3500 m	0.37

Table 5.14: Simulation with average wind velocity assigned to NORTH, EAST, SOUTH, WEST and SKY in VELOCITY-INLET configuration with more velocity values at higher elevations. W wind component. Normalized root mean square deviation (NRMSD) of W wind component in atmospheric layers inside the domain of simulation.

layer	W - NRMSD - coarse mesh
0 m - 350 m	1689.11
350 m - 700 m	4221.85
700 m - 1050 m	5816.73
1050 m - 1400 m	16742.88
1400 m - 1750 m	15874.14
1750 m - 2100 m	14154.80
2100 m - 2450 m	4847.88
2450 m - 2800 m	10485.75
2800 m - 3150 m	92455.99
3150 m - 3500 m	8533.96

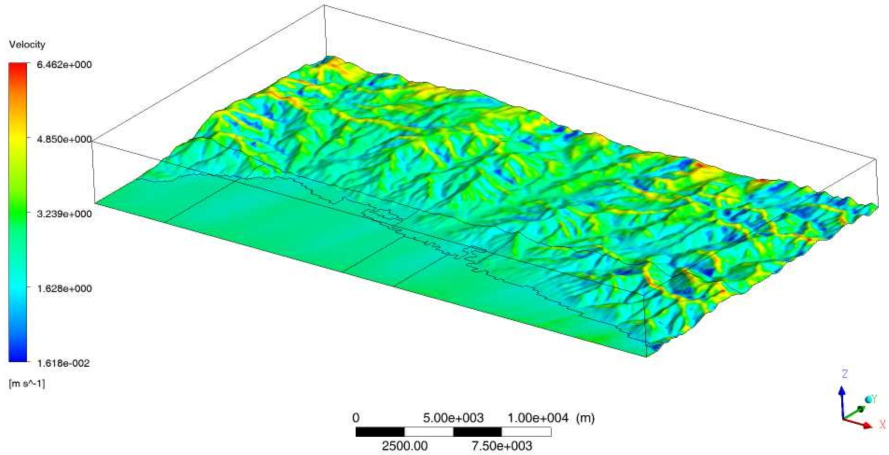

Figure 5.17: Simulation with average wind velocity assigned to NORTH, EAST, SOUTH, WEST and SKY in VELOCITY-INLET configuration with more velocity values at higher elevations and coarse mesh. Wind field at 10 m.

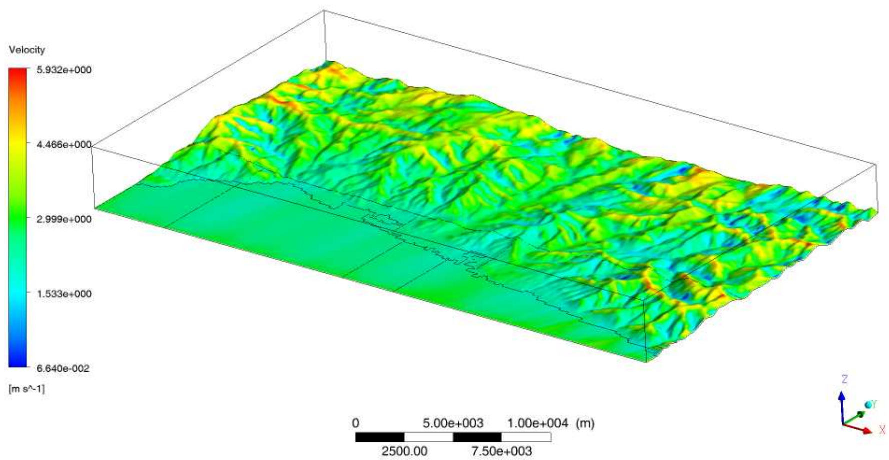

Figure 5.18: Simulation with average wind velocity assigned to NORTH, EAST, SOUTH, WEST and SKY in VELOCITY-INLET configuration with more velocity values at higher elevations and coarse mesh. Wind field at 30 m.

wind intensity in the most of elevations. Similarly to precedent simulations, for W component the values of this indicator are very large in every layer (from table 5.12 to table 5.15).

At lower heights (figures 5.21 and 5.22) the wind field simulated by FLUENT is influenced by the complex topography and by the strong conditioning of lateral boundary conditions. At midway elevations (figures 5.23 and 5.24) the wind fields simulated by FLUENT computations and the ones of WRF data are similar, espe-

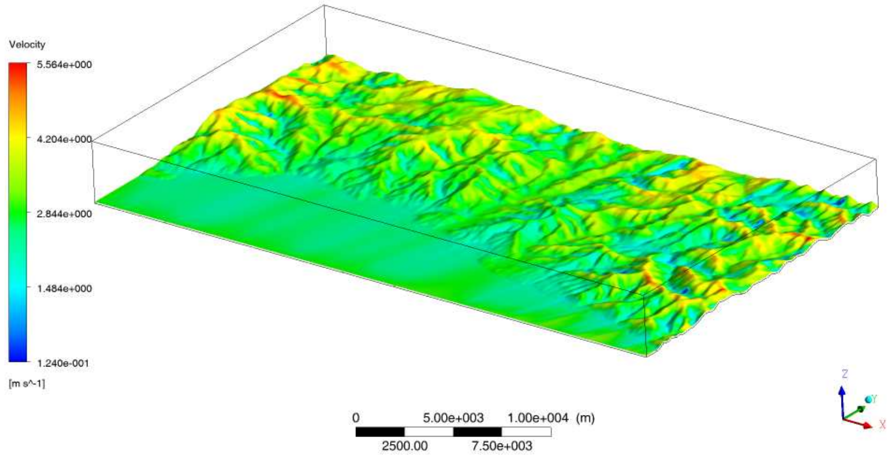

Figure 5.19: Simulation with average wind velocity assigned to NORTH, EAST, SOUTH, WEST and SKY in VELOCITY-INLET configuration with more velocity values at higher elevations and coarse mesh. Wind field at 100 m.

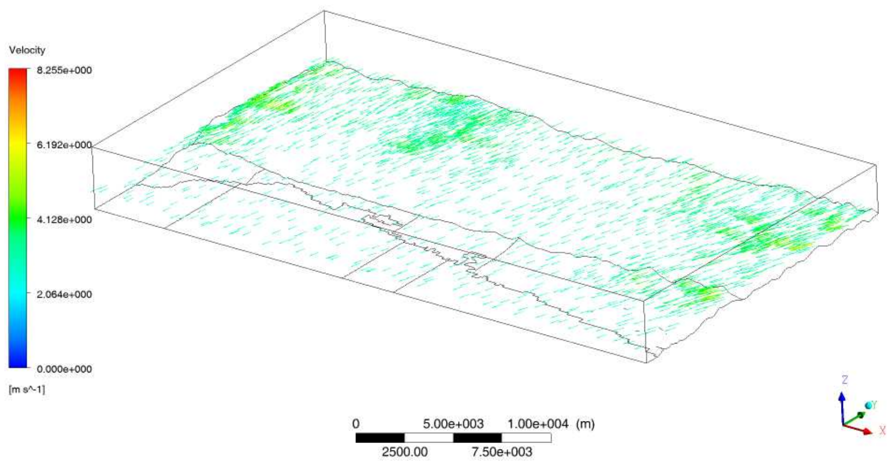

Figure 5.20: Simulation with average wind velocity assigned to NORTH, EAST, SOUTH, WEST and SKY in VELOCITY-INLET configuration with more velocity values at higher elevations and coarse mesh. Wind field at 1000 m.

cially at the elevation of 2050 m: at this height there is an agreement between results of FLUENT simulation and WRF data. In the highest altitudes (figures 5.25 and 5.26) the wind fields are homogeneus, but there is a little variance between FLUENT simulation results and WRF data regarding the intensity and the direction of the wind; nevertheless this discrepancy is smaller than the previous simulation (section 5.2.1).
In this case, I examined in particular the influence of orography on velocity fields at

Table 5.15: Simulation with average wind velocity assigned to NORTH, EAST, SOUTH, WEST and SKY in VELOCITY-INLET configuration with more velocity values at higher elevations. Wind intensity. Normalized root mean square deviation (NRMSD) of wind intensity in atmospheric layers inside the domain of simulation.

layer	wind - NRMSD - coarse mesh
0 m - 350 m	0.70
350 m - 700 m	0.53
700 m - 1050 m	0.52
1050 m - 1400 m	1.21
1400 m - 1750 m	1.41
1750 m - 2100 m	0.74
2100 m - 2450 m	0.23
2450 m - 2800 m	0.37
2800 m - 3150 m	0.49
3150 m - 3500 m	0.36

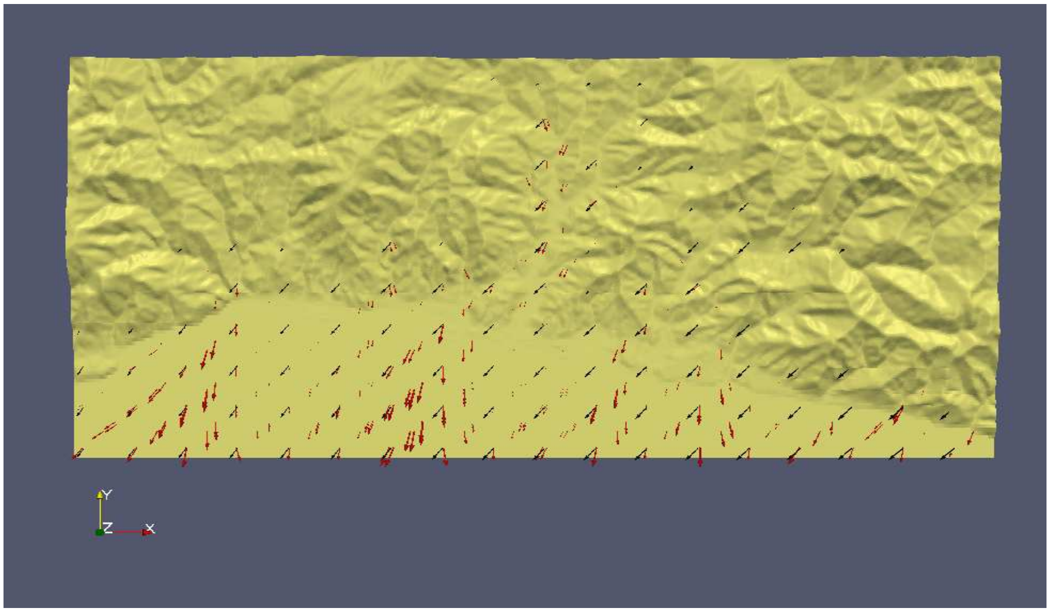

Figure 5.21: Simulation with average wind velocity assigned to NORTH, EAST, SOUTH, WEST and SKY in VELOCITY-INLET configuration with more velocity values at higher elevations. Comparison between the velocity of FLUENT simulation and WRF data at height of 160 m. Black: WRF data. Red: results of simulation.

lower elevations, shown in following figures (from figure 5.27 to figure 5.29).
The influence of orography is evident for velocity fields provided by FLUENT simulation at low elevations, especially in Bisagno and Polcevera valleys (figures 5.27

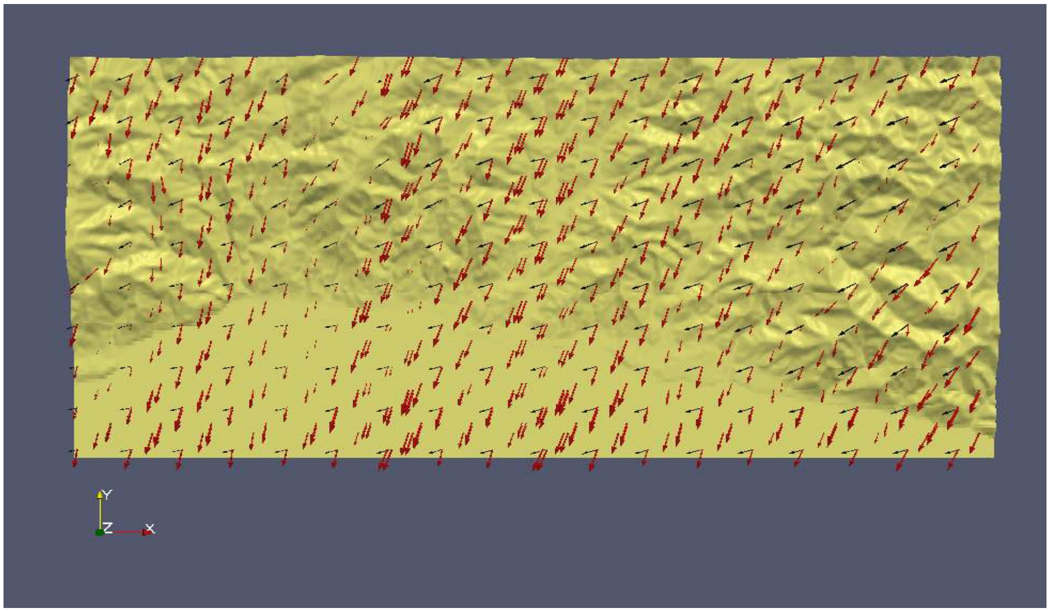

Figure 5.22: Simulation with average wind velocity assigned to NORTH, EAST, SOUTH, WEST and SKY in VELOCITY-INLET configuration with more velocity values at higher elevations. Comparison between the velocity of FLUENT simulation and WRF data at height of 880 m. Black: WRF data. Red: results of simulation.

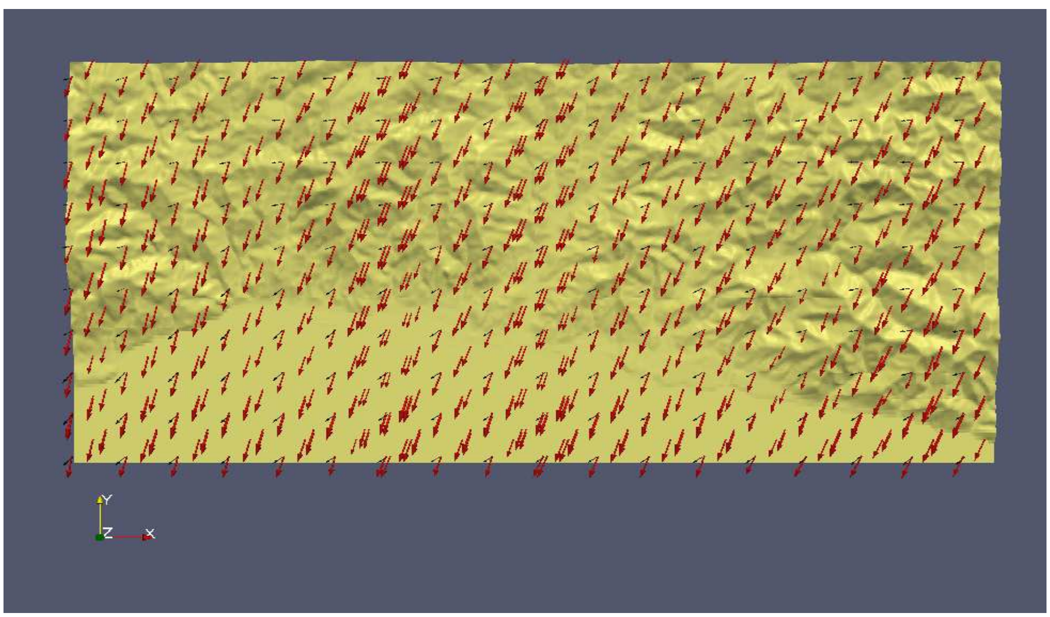

Figure 5.23: Simulation with average wind velocity assigned to NORTH, EAST, SOUTH, WEST and SKY in VELOCITY-INLET configuration with more velocity values at higher elevations. Comparison between the velocity of FLUENT simulation and WRF data at height of 1520 m. Black: WRF data. Red: results of simulation.

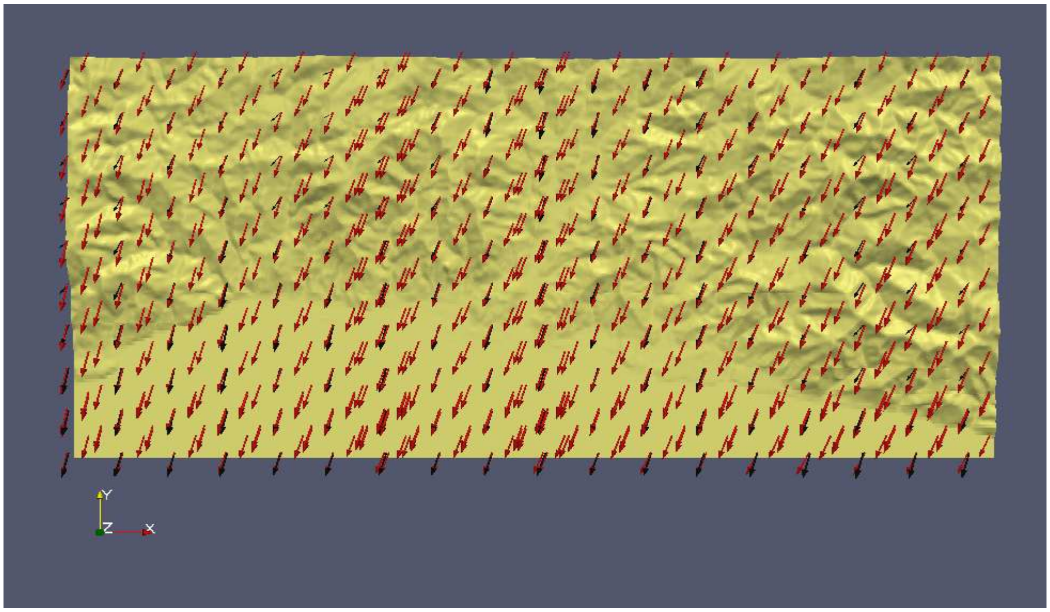

Figure 5.24: Simulation with average wind velocity assigned to NORTH, EAST, SOUTH, WEST and SKY in VELOCITY-INLET configuration with more velocity values at higher elevations. Comparison between the velocity of FLUENT simulation and WRF data at height of 2050 m. Black: WRF data. Red: results of simulation.

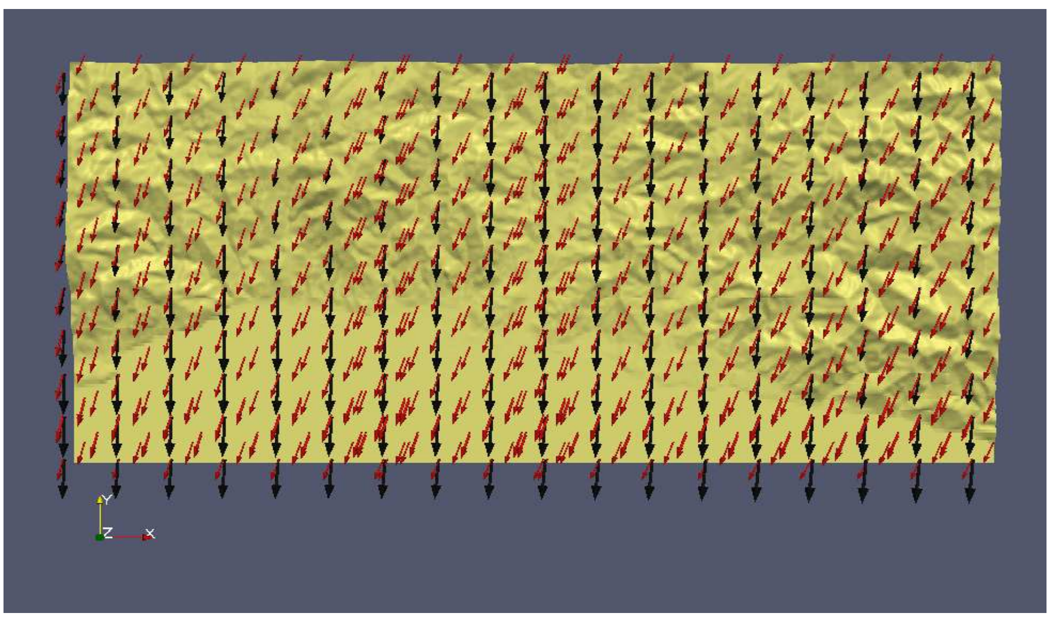

Figure 5.25: Simulation with average wind velocity assigned to NORTH, EAST, SOUTH, WEST and SKY in VELOCITY-INLET configuration with more velocity values at higher elevations. Comparison between the velocity of FLUENT simulation and WRF data at height of 2510 m. Black: WRF data. Red: results of simulation.

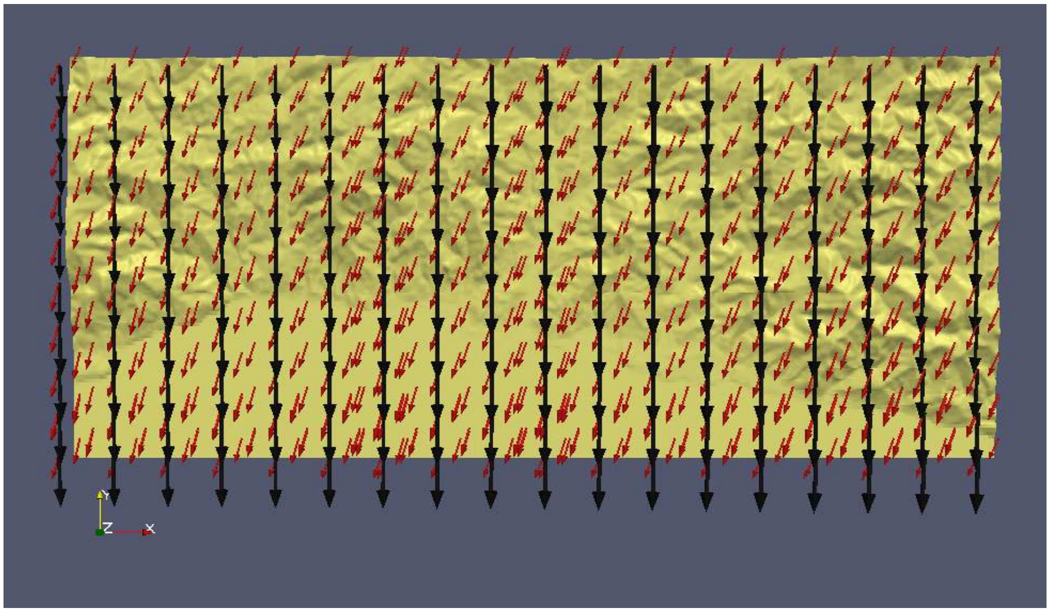

Figure 5.26: Simulation with average wind velocity assigned to NORTH, EAST, SOUTH, WEST and SKY in VELOCITY-INLET configuration with more velocity values at higher elevations. Comparison between the velocity of FLUENT simulation and WRF data at height of 3100 m. Black: WRF data. Red: results of simulation.

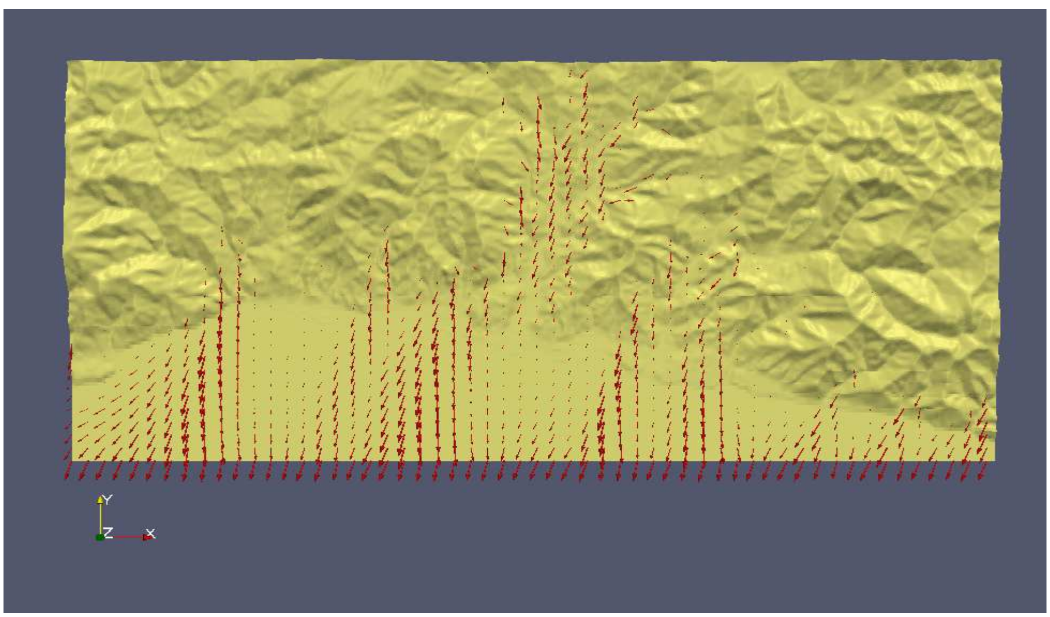

Figure 5.27: Simulation with average wind velocity assigned to NORTH, EAST, SOUTH, WEST and SKY in VELOCITY-INLET configuration with more velocity values at higher elevations. Influence of orography on the velocity fields provided by FLUENT simulation at height of 240 m.

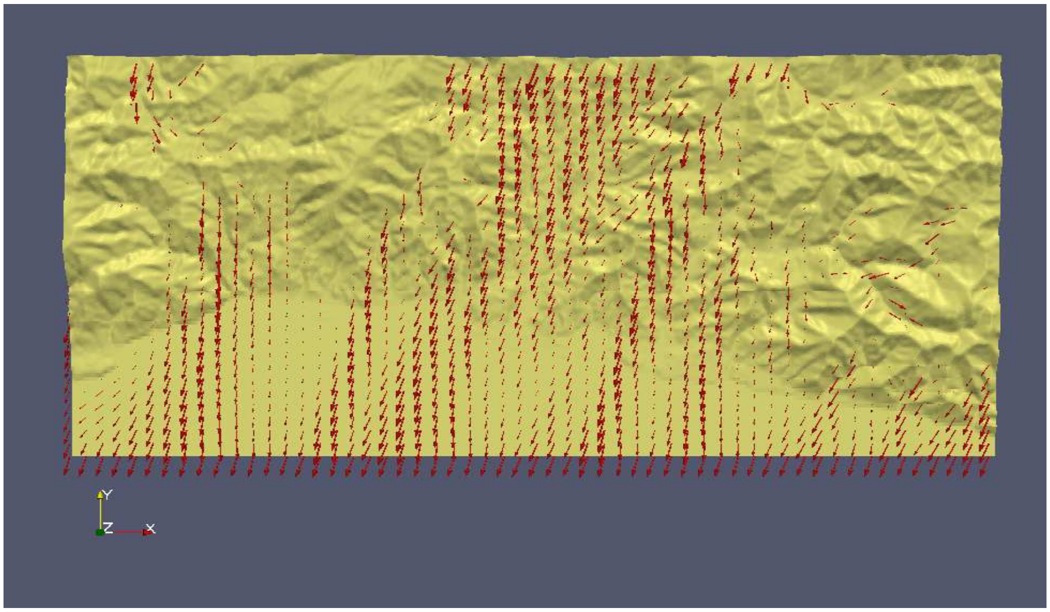

Figure 5.28: Simulation with average wind velocity assigned to NORTH, EAST, SOUTH, WEST and SKY in VELOCITY-INLET configuration with more velocity values at higher elevations. Influence of orography on the velocity fields provided by FLUENT simulation at height of 480 m.

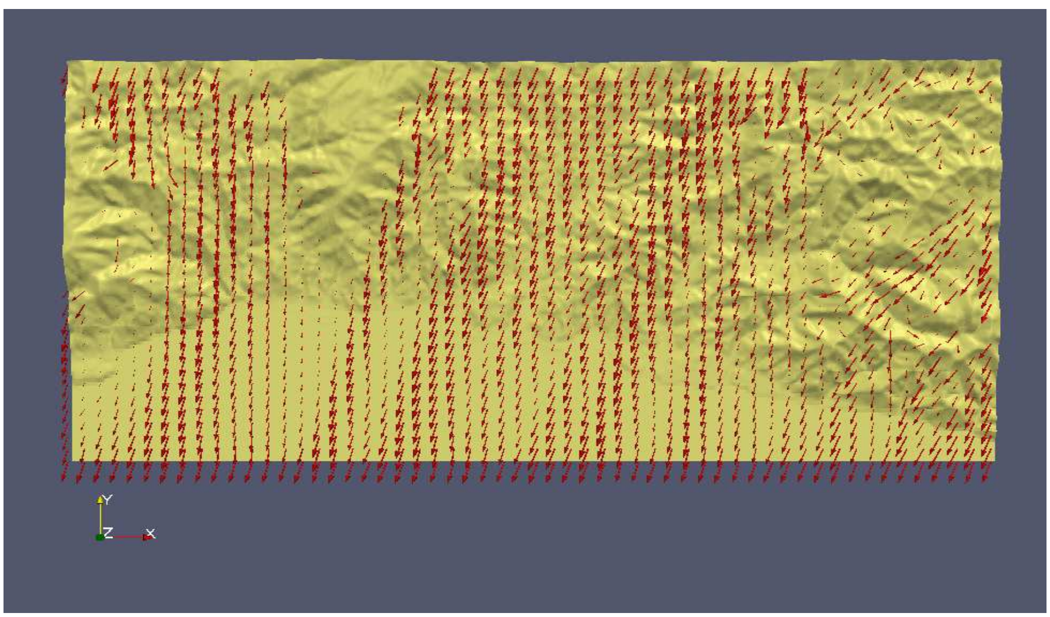

Figure 5.29: Simulation with average wind velocity assigned to NORTH, EAST, SOUTH, WEST and SKY in VELOCITY-INLET configuration with more velocity values at higher elevations. Influence of orography on the velocity fields provided by FLUENT simulation at height of 720 m.

and 5.28) and in the easter areas of the domain in study (figure 5.29).
Finally, I compared the simulation output with direct measure. The computation provided:

- wind intensity = 2.2 m/s;
- wind direction = 15 °.

The measurement of the station gave a wind intensity of 3.9 m/s and a wind direction of 45 °(calculated with respect to North). There is a discrepancy between the simulation and the measure of the wind intensity, that is underestimated by simulations, but there is a good agreement for the direction of wind; in fact, the simulation identifies the angular sector of wind origin. In comparison to the simulation with few velocity data assigned in boundary conditions, there is an analogous agreement for the wind intensity, while the behaviour of wind direction changes. In the first case, the measurement of angle of wind direction is lower than the value obtained by numerical computation; whereas in the last case, the measure provided a bigger value than the simulated one.

5.2.4 Simulations of consecutive time instants

I repeated the simulation with a statement equal to the one shown in section 5.2.3 for ten consecutive hourly time instants. In these cases, the behaviour of wind velocity is similar to the one of the first examined hour.
The data of meteorological model and the outputs of computational fluid dynamics simulations are in partial agreement. The direction of wind velocity is North-East in lower atmospheric layers and it rotates to North direction in higher atmospheric layers, but there are discrepancies in the values of wind velocity intensity. For this reason, the indicator of the normalized root mean square deviation (NRMSD) of the components and the intensity of wind velocity has values which are not always acceptable in the atmospheric layers and in the inner of the domain. It occurs especially for W component.
In all cases I studied, there is a good agreement between the fields of wind velocity simulated by FLUENT and WRF data in the higher layers of atmosphere. However, in the lower layers there is an evident influence of orography in the field of wind velocity. Similar to the behaviour of the first hourly time instant, the complex topography of the main valleys influences the wind velocity under an elevation of about 1000 m.
Finally, I compared the results of the numerical simulations with the values measured by the meteorological station of ARPAL.
The variance between the values of wind intensity and direction, provided by the numerical simulations and the ones obtained by direct measurements of ARPAL station, is acceptable in every case I examined (figures 5.30 and 5.31). It is possible to observe that the agreement among FLUENT procedures and measured data is good and the simulations of Fluid Dynamics Computational provide more accurate results than ones obtained by the data of WRF simulations.
Likely, the discrepancy between FLUENT outputs and measurements might be due

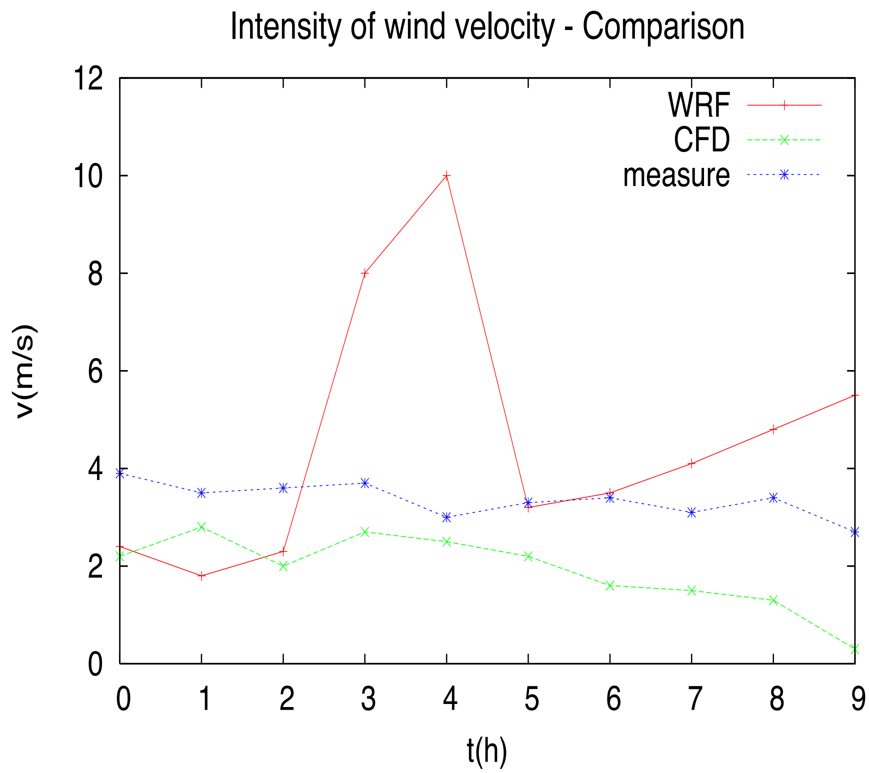

Figure 5.30: Intensity of wind velocity. Comparison among WRF data, results of FLUENT simulations and direct measurements at location of ARPAL meteorological station.

to the numerical errors of the computations and the random errors of the direct measures. Further, connected to the operation of measurement, the position of the measure instrument can be the reason of systematic errors. The errors in simulations are inborn in every numerical approach, and the ones of the measurement are due to the interference of wind velocity with complex terrain near the measure device. In detail, the instrument position is decisive, because the measured values of intensity of wind velocity are always bigger than simulated ones. The meterological station is located at the end of Bisagno valley, towards the sea. Therefore, the channelling effects are predominant in the measurements. Besides, the measure device is located on the roof of a palace and the FLUENT simulations do not consider the urban configuration, but only the orography and the characterization of the terrain is generally represented by an average roughness, that determines an understimated value of intensity of wind velocity in comparison with the measured one.

5.3 Conclusion

In the study of the variability of boundary conditions, I examined again the first hour of the available sequence. The numerical set obtained by assigning an average

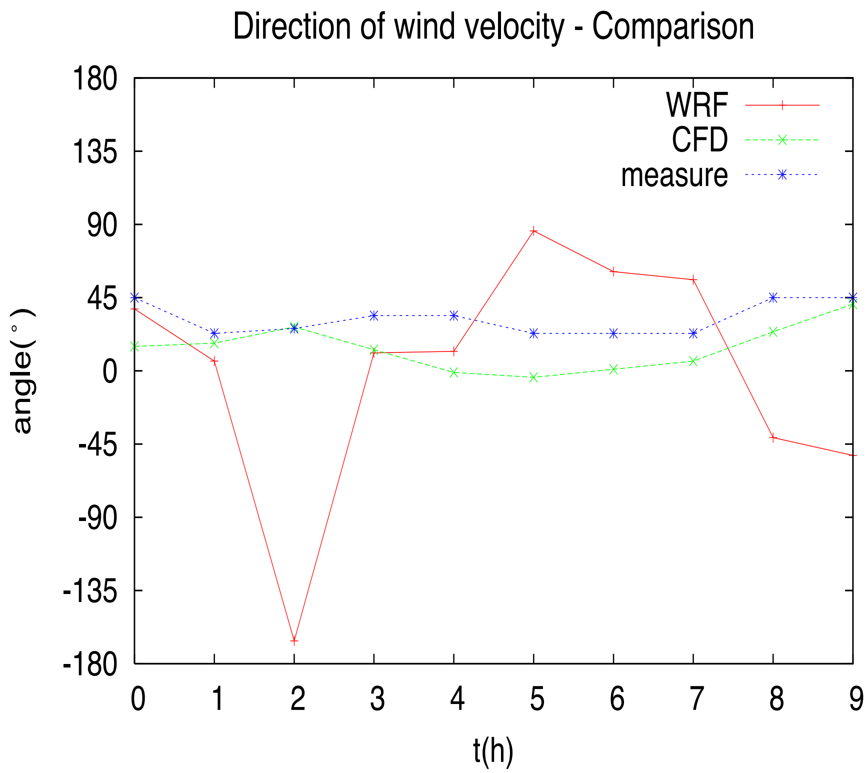

Figure 5.31: Direction of wind velocity. Comparison among WRF data, results of FLUENT simulations and direct measurements at location of ARPAL meteorological station. The angle of vertical axis is calculated in reference to North direction.

velocity on the lateral faces and on the top face of the domain provides acceptable outputs. The wind fields are realistic enough, both at higher and at lower altitudes. These considerations are correct for the simulation with velocity assigned to two lateral faces too, but the results are better in the case of the simulation with velocity assigned to every lateral face.
Moreover, the addition of more vertical levels at higher altitudes in the calculation of the average velocity enables to obtain better wind velocity fields. They have a good agreement with the data of the meteorological model at higher elevations. At lower altitudes, the wind fields are influenced by orography, in particular in the main valleys of Genoa.
The statistical indicator, chosen in order to estimate the discrepancy between the outputs of computational fluid dynamics simulations and the outputs of meteorological model, takes partially acceptable values for U and V wind components, reasonable enough for wind intensity in various atmospherical layers of the domain. However, it is very large for W component: the simulation provides a wind flow with upward or downward component, that is bigger than the one given by means of WRF.
I extended the analysis to the following hours in order to have a trend of wind fields, and I obtained a similar configuration for wind velocity. The examined ten

hours are characterized by an average wind with North-East direction. Therefore, they permit to verify the procedure in similar meteorological cases. This study is important, because this meteorological configuration is frequent in Genoa area.
Finally, it is possible to observe the agreement beetwen the results of FLUENT simulations and ARPAL measurements. The CFD procedures provide more accurate values than the ones calculated by meteorological model. It occurs both for the intensity and the direction of the wind velocity. The discrepancies noticed are due to the numerical errors or to the position of the device of measure, that is influenced by the complexity of the contiguous topography.

Conclusion

I searched different aspects about the examined subjects and I obtained significant results concerning them.
Regarding the study of the atmospheric turbulence in urban area, I studied the daily trends of the meteorological variables of Reynolds number and temperature, as well as of the atmospheric stability indicators. I chose the index to show conditions of atmospheric stability and subsequently I examined the statistics of temperature fluctuations.
As decided, I studied the features of the temperature fluctuations in relation with the conditions of atmospheric stability and I identified the scaling of weak and strong temperature fluctuations.
The meteorological variables of Reynolds number and temperature, and the atmospheric stability indicators show that the solar daily cycle influences these physical greatnesses.
The Reynolds number increases passing from the measures of anemometer at 5 m to the ones obtained by instruments at 9 m and 25 m and permits to notice that the turbulence is characterized by two aspects, mechanical and thermal. Both of them are mainly connected with the daily trend of this variable. This is more evident if the measure of the instrument at the highest elevation is utilized.
On average, the values of the temperature decrease passing from the measurements of anemometers at 5 m to the ones obtained by instruments at 9 m and 25 m, with few exceptions. Events of thermal inversion occur in some periods (March 2007 and April 2007). It is possible to notice that in summer months the difference among the temperatures measured at different elevations are small, probably because in this period the atmosphere is more mixed.
The temperature follows a behaviour analogous to that of Reynolds number. The differences among these variables, obtained from the measurements of anemometers at different heights, decrease partially in the spring and summer months; during these periods the atmosphere is particularly mixed and it is possible to observe larger values of Reynolds number.
The atmospheric stability index, chosen to characterize the atmospheric stratification, uses the temperatures at 9 m and 25 m. The values of this indicator are lower during the hours around midday and in the first hours of the afternoon, especially during the spring and autumn months. Besides, the index allows to notice that the events of unstable atmospheric stratification are more frequent than the ones of stable atmospheric stratification.
Moreover, it is possible to notice that the conditions of atmospheric stability are connected with the atmospheric turbulence. In particular, the turbulence of ther-

mal origin, that is more frequent than the one of mechanical nature, is identified by lower values of stability index during the hours around midday and in the first hours of the afternoon. It is verified especially during the spring and summer months.

In the analysis of temperature fluctuations, I considered the distinction of the configuration between the atmosphere with stable stratification and the one with unstable stratification. The statistics for the study of stable atmosphere counts a number of smaller events than the one of unstable atmosphere; but the dataset is very large and this allows to use enough data for a statistical study of both configurations of atmospheric stratification.

In my research, I studied the statistics of the temperature fluctuations, when the atmospheric stability changes. I found the scaling properties for the weak and strong temperature fluctuations in unstable and stable atmospheric stratification. In particular, for the weak temperature fluctuations I verified the linear behaviour of scaling exponents and for the strong temperature fluctuations I identified the saturation of the intermittency. I could verify that the scaling exponents do not depend on the different conditions of the atmospheric stability.

These results are not only interesting in theoretical tractation, but also in applicative fields. In fact, they could be useful in the meteorological sector, for example in the parameterizations of the turbulence: they could permit to obtain the behaviour of the atmospheric flow at small spatial lenght scales, if the behaviour of the atmospheric flow is known at large spatial lenght scales.

Regarding to the study of the behaviour of the wind over a complex orography, I examined a particular meteorological configuration that interests Genoa area. In this case, the wind direction come from North-East sector at low elevations and it is frequent in autumn and in winter in the studied zone.

I used a data obtained by meterological model in order to define the boundary conditions of Computational Fluid Dynamics (CFD) model. I executed simulations with different statements to identify the procedure that allowed to obtain more realistic wind fields.

I used two meshes for CFD calculation (coarse and thick), but there is not a pronounced improvement in the simulation with the thick mesh in comparison with the simulation with the coarse one, and the computational time is very large when using the grid with a great number of cells.

I assigned the WRF velocity to the domain, changing the number of lateral faces on which the punctual data of meteorological model are set. Evaluating the simulation results, it was possible to say that these boundary conditions are the strong constraint for the fluid dynamics computation. This last one converged numerically, but it provided wind fields not always realistic. In fact, it is possible to highlight the areas corresponding to the sea and the coastal zone, where the flow convergences and the eddies are generated, but they are not physically acceptable. On the contrary, the configuration is reasonable near the mountains area.

In order to compare the output of CFD and meteorological model simulations, I calculated the normalized root mean square deviation for the components and the intensity of the wind. The statistical indicator took partially acceptable values for U and V wind components, but not acceptable for W component: the computational fluid dynamics simulation provided a wind flow with an upward or downward

component, that is bigger than the one given by meterological model.
Other simulations were carried out, changing the boundary conditions. The average velocities, obtained by meteorological model, were assigned to lateral faces and to the upper side. The wind fields, provided by this simulation, resulted physically acceptable.
Therefore it was possible to repeat this last calculation for the following hours, characterized by similar meteorological conditions, in order to verify the elaborated model.
I compared the results of CFD simulations with the data of meteorological model and direct measures, provided by ARPAL station, located at the Functional Center (Genoa).
Hence, it was possible to observe the agreement beetwen the outputs of CFD simulations and ARPAL measurements for wind intensity and direction. Besides, the CFD simulations provided more accurate results than the ones calculated by meteorological model.
My research could be applied to other meteorological configurations in order to obtain an operative model chain. This last one could have many applications, not only in the meteorological sector, but also in the evaluation of wind energy potential, in the study of pollutant dispersion or in the examination of fire propagation.

Bibliography

[1] J. D. Anderson, G. Degrez, E. Dick, R. Grundmann. *Compuational Fluid Dynamics*. Springer Press. 1995

[2] ANSYS-CFX. *Solver/Modelling Guide*. Realise 11.0. 2006.

[3] ANSYS-FLUENT. *Solver/Modelling Guide*. Realise 13.0. 2011.

[4] ANSYS-ICEM. *User Manual*. Realise 11.0. 2007

[5] M. Antonelli, A. Mazzino, U. Rizza. *Statistics of temperature fluctuation in a buoyancy-dominated boundary layer flow simulated by a large eddy simulation model*. Journal of the Atmospheric Sciences. Volume 60, 215-224. 2003.

[6] M. Antonelli, M. Martins Afonso, A. Mazzino, U. Rizza. *Structure of temperature fluctuation in turbulent convective boundary layer*. Journal of turbulence. Volume 6, No. 35, 1-34. 2005.

[7] C. D. Arhens. *Meteorology today: an introduction to weather, climate and the environment*. Cengage Learning. 2007

[8] S. Pal Arya. *Introduction to Micrometeorology*. Academic Press. 2001

[9] R. G. Barry, R. G. Chorley. *Atmoshere, Weather and Climate*. Routladge. 2003.

[10] S. Di Sabatino, R. Buccolieri, B. Pulvirenti, R. E. Brittere. *Flow and pollutant dispersion in street canyons using FLUENT and ADMS-urban*. Environmental model assessment. Volume 13, 369-381. 2007.

[11] P. G. Duynkerke. *Application of the $k - \epsilon$ turbulunce closure model to neutral and stable atmospheric boundary layer*. American meteorology society. Volume 45, No. 5, 865-880. 1988.

[12] E. Ferrero, D. Anfossi, R. Richiardone, S. Trini Castelli, L. Mortarini, E. Carretto, M. Muraro, S. Bande, D. Bertone. *Urban turbulence project. The field experimental campaign*. Internal Report ISAC-TO, 1-37. 2009.

[13] J. H. Ferziger, M. Peric. *Computational Methods for Fluid Dynamics*. Springer Press. 2010.

[14] U. Frisch. *Turbulence. The legacy of A. N. Kolmogorov*. 120-194. Cambridge University Press, United Kingdom. 1995.

[15] J. R. Holton. *An introduction to Dymanics Meteorology*. Academic Press. 2004.

[16] H. G. Kim, V. C. Patel. *Test of turbulence models for wind flow over terrain with separation and recirculation*. Boundary Layer Meteorology. Volume 94, 5-21. Kluwer Academic Publishers, Netherlands. 1999.

[17] P. K. Kundu, I. M. Cohen. *Fluid Mechanics-Third Edition*. Elsevier Academic Press. United States of America. 2004.

[18] L. Li, L. Zhang, F. Hu, Y. Jiang, W. Jiang. *Application of Fluent on fine-scale simulation of wind field over complex terrain*. Science in cold and arid regions. Volume 2, No. 5, 411-418. 2010.

[19] J. M. McDonough. *Introductory. Lecture on turbulence. Physics, Mathematics and Modeling*. Scientific Literature Digital Library and Search Engine. United States. 2004.

[20] C. H. Moeng, J. Dudhia. J. Klemp, P. Sullivan. *Examing two-way grid nesting for Large Eddy Simulation of the PBL using the WRF model*. American Meteorolical Society. Volume 135, 2295-2311.

[21] L. Mortarini, E. Ferrero, S. Falabino, S. Trini Castelli, R. Richiardone, D. Anfossi. *Low-frequency processes and turbulence structure in a perturbed boundary layer*. Quaterly Jpurnal of the Royal Mateorological Society (in press).

[22] S. B. Pope. *Turbulent flows*. Cambridge University Press. 2001.

[23] P. Sagaut. *Large eddy simulation for incompressible flows*. Springer Press. 2006.

[24] S. Schneiderbauer, S. Pirker. *Resolving unsteady micro-scale atmospherci flows by nesting of CFD simulation into wide range numerical weather prediction model*. Internationale Journal af Computational Fluid Dynamics. Volume 24, No.1, 51-68. 2010.

[25] W. C. Skamarock, J. B. Klemp, J. Dudhia, D. O. Gill, D. M. Barker, X. Z. Huang, W. Wang, J. G. Powers. *A Description of the Advanced Research WRF Version 3*. Technical report, Mesoscale and Microscale Meteorology Division, NCAR, Boulder, Colorado. 2008.

[26] Z. Sorbjan. *Structure of the Atmospheric Boundary Layer*. 69-81. Prentice-Hall, Inc. United States of America. 1989.

[27] V. Stocca. *Development of a large eddy simulation model for the study of pollutant dispersion in urban areas*. PhD. Thesis. Trieste University. 2010.

[28] R. Stull. *An introduction to boundary layer meteorology*. 75-95. Kluwer Academic Publisher, Netherlands. 1988.

[29] J. C. Tannehill, D. A. Anderson, R. H. Pletcher. *Computational Fluid Mechanics and Heat Transfer*. Springer Press. 1997.

[30] J. M. Wallace, P. Hobbs. *Atmospheric sciences: an introductory survey*. Academic Press. 2006.

[31] Z. Zhang, W. Zhanga, J. Zhaib, Q. Y. Chena. *Evaluation of various turbulence models in predicting airflow and turbulence in enclosed environments by CFD: Part 2 Comparison with experimental data from literature*. HVAC & R Research. Volume 13, No. 6. 2007.

List of Figures

List of Tables